Cure and Conductivity: Investigation of Thermal Processing of Silver Nanobelt - Epoxy Composites

by

Geoffrey Rivers

A thesis
presented to the University of Waterloo
in fulfillment of the
thesis requirement for the degree of
Doctor of Philosophy
in
Mechanical and Mechatronics Engineering (Nanotechnology)

Waterloo, Ontario, Canada

© Geoffrey Rivers 2017

Examining Committee Membership

The following served on the Examining Committee for this thesis. The decision of the Examining Committee is by majority vote.

External Examiner	Dr. Marianna Kontopoulou PhD, Associate Head and Professor Queens University
Supervisors	Dr. Pearl Sullivan PhD, P.Eng, Professor Mechanical and Mechatronics Engineering
	Dr. Boxin Zhao PhD, Associate Professor Chemical Engineering
Internal Member	Dr. Shahrzad Esmaeili PhD, P.Eng, Professor Mechanical and Mechatronics Engineering
Internal-external Member	Dr. Michael Pope PhD, Assistant Professor Chemical Engineering
Other Member	Dr. Hyock Ju (HJ) Kwon PhD, P.Eng, Associate Professor Mechanical and Mechatronics Engineering

Author's Declaration

This thesis consists of material all of which I authored or co-authored: see Statement of Contributions included in the thesis. This is a true copy of the thesis, including any required final revisions, as accepted by my examiners.

I understand that my thesis may be made electronically available to the public.

Statement of Contributions

Chapter 4 of this thesis contains material for which I was not first author. In that study, I was the member primarily responsible for the construction and validation of the numerical pH model, including the collection of literature data for its construction. I also was primarily responsible for utilizing the model to guide and analyze studies. I performed literature review relating to the synthesis of silver nanoparticles in advance of the studies, attempting to identify the critical factors that would be worth investigation. I also performed approximately one third of the synthesis experiments, contributed significantly in the analysis of all results from synthesis experiments, took part in SEM microscopy sample preparation and imaging sessions, and was significantly involved in planning of recipes to investigate throughout the study. This includes the second and third round of recipes, which were selected based on the results of previous formulations. I was also substantially involved throughout the preparation and revision of the manuscript.

In all other chapters I was first author of the comprising work.

Abstract

Electrically conductive adhesive (ECA) composites based on diglycidyl ether of bisphenol-A / triethylenetetramine (DGEBA/TETA) epoxy, including a hybrid nanocomposite containing newly developed silver nanobelts, have been investigated for the relationships between the cure process and the evolving electrical properties. When nanobelt-filled electrically conductive composites are fully developed their advantages may include: 1) reduced total filler content compared to microcomposites, resulting in reduced cost; 2) improved final conductivity; 3) improved longevity due to high nanobelt stability.

The current work is focused on several studies of electrically conductive composites, and of silver nanobelts: 1) Traditional investigations, *via* differential calorimetry, of the effect that the filler additions had on the composite cure behavior. 2) Development of nanobelt synthesis methods to provide consistent and repeatable production of high quality one-dimensional silver nanobelt fillers. 3) Characterization of the particle joining process exhibited by silver nanobelts when heat treated without being inside a polymer matrix. 4) *In-situ* characterization of the evolving electrical conductivity throughout the cure progression of a microcomposite containing only silver microflake fillers. 5) Similar *in-situ* electrical characterization of conductivity throughout the cure of several hybrid nanocomposites containing silver nanobelts and silver microflakes.

The primary results and scientific contributions from this work are: 1) Determination that addition of silver nanobelts to a composite influences cure and glass transition behavior less than or equal to the presence of small quantities of solvents, demonstrating that traditional cure analysis methods alone are not sufficient for characterizing these conductive nanocomposites. 2) Improvements in the particle aspect ratio and the batch repeatability when synthesizing silver nanobelts in gram-quantities, with the determination that the dominant factors controlling final morphology are the reaction mixture pH and the concentration of the dissolved silver salt in the precursor solution. 3) Identification of a non-diffusional joining process that occurs between silver nanobelts outside of a composite, during heat treatment between 75°C and 180°C, allowing reductions in network electrical resistance without the detrimental effects of the activation of diffusion. 4) and 5) First observations of path-dependency during cure displayed by the evolving electrical conductivity of hybrid nanocomposites and a microcomposites, due to the onset of vitrification when partially cured.

In addition, a number of other contributions were also made, mainly: 1) Design, construction, and verification a custom curing mold with inlaid reusable 4-wire electrical probe integrated with a specimen curing mold, designed to obtain *in-situ* electrical measurements throughout cure during high precision temperature control. 2) A table-top vacuum-mixing system that mounts onto a common model of vortex mixer, allowing solvent blending by continuous stirring under vacuum of up to 6 simultaneous batches of nanocomposites, to obtain composite batches with low final solvent contents. 3) Demonstration that small additions of high aspect ratio nanoparticles, such as silver nanobelts, into a hybrid

nanocomposite has the potential to substantially alter the distribution of fillers, causing standard models of electrical percolation in hybrid systems to be potentially inaccurate.

Although the hybrid nanocomposites filled with silver nanobelts has a lower conductivity than anticipated, it is thought that this is due to the path-dependent and resistance-increasing effect of its high glass transition temperature, and the resulting highly significant vitrification during cure. It is hypothesized that additions of solvent will substantially reduce vitrification effects, and improve conductivity further. This system shows potential of desirably high conductivity at filler contents as low as 55 wt% silver. Further, these demonstrations of the influence of vitrification on the evolving electrical properties during cure represent a significant source of bias or variation for research conducted on new conductive composites. Similarly, this may also significantly impact the utilization of conductive adhesives in industry, since industry prefers multi-stage cure treatments that feature significant amounts of vitrification.

Acknowledgements

I would like to thank my advisers Dr. Pearl Sullivan and Dr. Boxin Zhao for their technical advice and financial assistance.

I would like to thank Dr. Norman Y. Zhou for his technical expertise, and his interest in my professional development.

I would like to thank my friends and colleagues, Dr. Allan Rogalsky and Dr. Ehsan Marzbanrad, for a collaboration filled with expertise, back-of-the-envelope diagrams, and theoretical debates.

I gratefully acknowledge my Co-op Research Assistants: Mr. Maximilian Reed, and Mr. Yeshwanth Kesavan, for impressing me with their dedication, careful work, and insightful inputs.

I would like to thank the many specialists and technicians of the University of Waterloo's MME and Chem Eng departments for their support.

I would also like to thank my family: Bill Rivers, Robin Brown, Dawn Rivers, Brian Cullen, and my sister Heather. They've always been there for me.

I would like to thank my wonderful partner Carrie McNabb and the ever-gracious Penny Monster, for being awesome and understanding while I prepared this manuscript.

Dedication

Science, my lad, is made up of mistakes, but they are mistakes which it is useful to make, because they lead little by little to the truth.

Jules Verne
A Journey to the Center of the Earth

I will set up my name in the place where the names of famous men are written, and where no mans name is written yet I will raise a monument to the gods.

Anonymous
The Epic of Gilgamesh

"The best thing for being sad," replied Merlin, beginning to puff and blow, "is to learn something. That's the only thing that never fails. You may grow old and trembling in your anatomies, you may lie awake at night listening to the disorder of your veins, you may miss your only love, you may see the world about you devastated by evil lunatics, or know your honour trampled in the sewers of baser minds. There is only one thing for it then - to learn. Learn why the world wags and what wags it. That is the only thing which the mind can never exhaust, never alienate, never be tortured by, never fear or distrust, and never dream of regretting. Learning is the only thing for you. Look what a lot of things there are to learn."

T.H. White
The Once and Future King

Table of Contents

List of Figures

List of Tables

List of Symbols

α_i Degree of conversion (or degree of cure)

ΔH_{tot} Total heat of reaction

ΔT_{DSC} Temperature difference between the specimen and the reference

$\dot{\alpha}_{L-ASB}$ Normalized relative rate of reaction of Silver Nitrate and L-Ascorbic Acid

$\dot{Q}$ or $\frac{dQ}{dt}$ Rate of heat flow

$\dot{Q}_{NRFH}$ Non-reversing heat flow

$\dot{T}$ Heating rate

$\langle V_{ex} \rangle$ Predicted average excluded volume of a particle (assuming uniform shape)

$\langle V_{ex}^{crit} \rangle$ Critical total average excluded volume

$\ln(\frac{d\alpha}{dt})$ or $\ln(\dot{\alpha})$ Effective preexponent for Arrhenius model at some α

μ_I Ionic strength

ω Temperature modulation frequency

Φ_0 Percolation threshold for the filler in question

Φ_0^{η} Percolation threshold for nanocomposite

$\Phi_0^{\mu+\eta}$ Percolation threshold estimate for hybrid composite

Φ_0^{μ} Percolation threshold for microcomposite

Φ_{η} Volume fraction of nanoparticle

Φ_{μ} Volume fraction of microfiller

Φ_f Volume fraction of the filler

Φ_i Volume Fraction of some component i

Φ_m Volume fraction of the matrix

ρ Electrical Resistivity

V_i Volume of some component i

V_p Volume of a single particle

$C_{f'}$ Amplitude of kinetic thermal response to applied sine wave modulation

c_i Molar concentration of ionic species i

C_p or $RevC_p$ Reversing heat capacity

C_{square} Geometric correction factor for square specimens with corner-located probe pins

d_μ/d_η Diameter ratio of microfiller to nanofiller

$E_{a,\alpha}$ Effective activation energy at some α

$f(\alpha)$ Functional form of reaction at some α

$f'(t,T)$ Underlying kinetic function of time and temperature that governs the thermal response associated with a physical or chemical transformation

$I_{1,2}$ Applied electrical current between probe contacts 1 and 2

k_0 Rate constant of Silver Nitrate and L-Ascorbic Acid reaction

m_i Mass of some component i

M_p Total mean curvature of a particle

m_{resin} Mass of reference (or resin) in mixture

m_{total} Total mass of the mixture

P_c Some physical property value for the composite

P_f Some physical property value for the filler

P_m Some physical property value for the matrix

pK' Apparent pK at test conditions

pKa' Degree of dissociation of acid units

$R_{2\Omega}$	Measured Resistance (for 2-contact probes)
R_{disk}	Thermal resistance of the heat-flow path in DSC
R_s	Electrical Sheet Resistance
s_1	Distance between probe pin I^+ and V^+
s_2	Distance between probe pin I^+ and V^-
s_3	Distance between probe pin I^- and V^+
s_4	Distance between probe pin I^- and V^-
S_p	Surface area of a particle
T_R	Temperature of the reference
T_S	Temperature of the specimen
t_s	Thickness of thin film specimen's gauge section
$V_{3,4}$	Measured electrical voltage between probe contacts 3 and 4
W_i	Weight percent of some component i
z_i	Absolute value of the charge of ionic species i
B	Temperature modulation amplitude
I	Applied electrical current
L	Length of thin film specimen's gauge section
phr	"Per Hundred Reference" (or "Per Hundred Resin")
R	Gas constant
V	Measured electrical voltage
W	Width of thin film specimen's gauge section
n	Analytically obtained exponent
pH	Decimal logarithm of the reciprocal of the hydrogen ion activity
pK	Acid dissociation constant

Chapter 1

Introduction

1.1 Motivation

Thermosetting ECAs are composites filled with conductive fillers, and have properties that are desirable for replacing conventional interconnect materials in industry. The most well-established interconnect material, eutectic lead solder alloy, is no longer accepted due to the environmentally toxic nature of the lead wastes. However, replacement alloys are typically expensive, and melt at prohibitively higher temperatures. Thus there is an opportunity for conductive adhesive composites to fill this need. Studied in primitive forms since the late 1960's, ECAs can be applied to electronic packaging at room temperature and then solidified by thermoset curing at temperatures below the melting point of metallic solders. Different combinations of fillers and polymer binders produce different process and final properties, allowing the material to be tuned to an application. However, until recently these ECAs have been prohibitively expensive and typically less conductive than desired, relying on microparticle silver contents as high as 90 wt% to achieve useful conductivities. These high filler contents lead to high viscosities, difficult mixing and dispensing, inflated costs from expensive fillers, and relatively large minimum dispensing sizes. The combination of these factors have limited the widespread adoption of ECAs, leading to much research directed at overcoming these limitations.

Advancements in conductive fillers, such as the recent development of high aspect ratio silver nanoparticles, have the potential to reduce the filler content necessary to obtain useful conductivity, reducing cost. One such high aspect ratio nanoparticle, silver nanobelts, has been developed by this group, and demonstrate exceptional stability to degradation, beneficial to ECA applications. The final processing step of a thermoset ECA is the solidification of the composite by the chemical curing of the polymer binder. This is a time and temperature sensitive process, and its progression evolves the final physical and electrical properties of the composite. Similarly, during the heat treatment of a curing process, silver nanoparticles can join, further improving composite conductivity by reducing

the contact resistance between particles. However, the scientific aspects of both of these processes is poorly known, especially in relation to the newly developed silver nanobelts. Therefore, an understanding of the relationships between the composite formulation, its curing conditions and behaviours, and the evolution of its properties throughout the cure are all crucial to the future widespread implementation of thermoset ECAs.

1.2 Thesis Layout

Below is a flowchart, Figure 1.1, presenting the logical progression of this thesis as it relates to topics and chapters. The arrows demonstrate the flow of information between studies used in planning and decision making.

The chapters of this thesis are, in many cases, constructed from manuscripts that have either been published, or prepared for publication. Table 1.1 provides a breakdown of the chapters, their associated manuscripts, and the status of the manuscripts.

In Chapter 2 the literature regarding conductive composites and silver nanoparticles is reviewed. There I discuss methods of characterization by calorimetry and electrical resistivity, clarify theory regarding curing of thermosets and the onset of conductive percolation in composites, and discuss the thermally induced joining of metallic nanoparticles.

In Chapter 3, traditional methods of calorimetry were employed to investigate the effect that the addition of fillers, including an early variety of silver nanobelts, had on the cure behaviour of a thermosetting composite. This included modeling of the cure kinetics in an attempt to identify changes in the model parameters produced by the addition of silver microflakes or nanobelts. Alongside this, a literature review was performed, identifying potential sources of systematic error for traditional cure studies. The combined results

Table 1.1: Thesis chapters and their related manuscripts

Thesis Chapter	Reference	Status
3		
· 3.1	[1]	Published
· 3.2	Unpublished	
4		
· 4.1	[2]	Published
· 4.2	[3], Unpublished work	Presented; Prepared
5	[4]	Published
6	[5], Unpublished work	In-publication; In-review
7	Unpublished work	Prepared

Figure 1.1: Research plan flowchart and chapters associated with the work.

strongly inform the remainder of the research path and methodologies in all subsequent studies. From this work it was determined that it would be more valuable to employ additional analytical methods alongside traditional calorimetry of cure, to investigate the influence of applied cure conditions and cure progression on the silver nanobelts and the developing properties of their hybrid nanocomposite ECAs.

To investigate silver nanobelt composite ECAs, and to allow their eventual adoption by industry, the synthesis of nanobelts must be well-controlled and understood. In two studies, presented in Chapter 4, I demonstrate improved selection of the developed nanoparticle morphology, identifying the two most dominant factors controlling the morphology of the nanobelts. This allows the repeatable synthesis of gram-quantities of silver nanobelts, with improved particle length and linearity. The synthesis studies also demonstrate that silver nanobelts and their precursor particles easily join at room temperature when the capping agent coating is not able to protect the surfaces.

In Chapter 5 I investigate the behaviour of silver nanobelts during heat treatment, when they are not embedded in composite. This study is necessary prior to studying the evolving conductivity throughout cure of nanocomposites containing silver nanobelts. Literature reporting discussed in Chapter 2 demonstrates that the joining of filler particles substantially lowers electrical resistance of a composite, and the results of Chapter 4 demonstrate that the nanobelts join readily when their polymeric capping agent coating is unable to protect them. Therefore it is expected that the activation of joining and the related evolution of electrical conductivity in nanobelts on their own may have a substantial influence on the planned nanocomposites studies. This is especially vital, because the previously reported silver nanoparticles are far less stable than silver nanobelts, indicating that the joining of silver nanobelts would require a different mechanism.

In Chapter 6 I present a study in which the electrical conductivity of simple silver-filled epoxy microcomposites is measured *in-situ* throughout cure, during which cure is characterized by calorimetry. This was intended to produce a baseline of the expected conductivity vs cure behaviour without the nanoparticles or their low-temperature joining behavior. The results demonstrate that the development of conductivity in a curing composite is path-dependent, and that the vitrification of a composite during cure can produce lasting reductions to final conductivity.

In Chapter 7 I present a study which builds upon those of Chapters 5 and 6. In this study, hybrid nanocomposites containing silver microflakes and nanobelts in varying contents were characterized by *in-situ* electrical resistance measurements throughout cure. Here calorimetry, electrical resistivity, and dimensional measurements and compared in order to draw final conclusions of the complex relationship between the composite formulation, the degree of conversion, contraction, and the resulting electrical conductivity.

In Chapter 8 I present concluding remarks, summarizing the main conclusions of this thesis. In addition, I provide recommendations of future work that could be performed based on this thesis, which are intended to further improve the knowledge of the field of electrically conductive adhesives.

Chapter 2

Background and Literature Review

In this chapter I present a review of literature relevant the nature of composites, and composite theory as it relates to electrically conductive adhesive (ECAs). Additionally, I present a review of the literature and theory relevant to conductive fillers, with an emphasis on silver nanoparticles, and a novel nanoparticle the "silver nanobelt". The nature of thermosetting polymers will be discussed, including theory regarding their curing and thermophysical properties. Finally, a review of the preparation methods and characterization tools available all these topics will be presented.

2.1 Conductive composites

Conductive interconnect materials are used to bond electronic components to the circuit board, providing electrical, thermal, and mechanical connections. Traditionally, electrical connection has achieved using homogeneous metal solders, the most common of which was lead/tin alloy. These materials were advantageous due to low cost, low temperature processing, and durability. However, the known toxic impact of lead to the environment and the increasing trends of consumer electronic waste generation have led to increasing pressure in the industry to replace lead solders with less toxic alternatives[6–9].

One alternative is electrically conductive adhesives (ECAs), typically in the form of composites: conductive filler particles bonded together by an adhesive polymer matrix, as illustrated in Figure 2.1. The network of fillers act as an electrical or thermal bridge, and in some cases a mechanical stiffening agent, while the polymer adhesive provides adhesion and toughness. A thermosetting composite does not require melting prior to application, unlike metallic alloy interconnect materials. Instead they start as a fluid and undergo a solidification based on chemical reactions. Since the new generation of low-toxicity metallic alloy interconnect materials typically have higher melting points, this means lower or more gently applied processing temperatures may be possible with thermosetting composites. ECA composites have existed as "silver paste" and similar formulations since the 1960s, but

were not as broadly applicable as Pb-Sn solders, in part due to relatively poor conductivity, high costs from high filler contents, and relatively poor adhesion or mechanical properties. As such, much work is being done in the current climate to improve the properties of these composites to achieve widespread use.

2.2 Composites Theory for ECAs

In general, a composite's properties are derived from the properties of its filler and matrix components, their interactions at their contact surfaces, the relative volume fractions of each component, and their distribution or orientation within the composite[10–20].

The volume fraction of a component (Φ_i) is one of the most influential factors of a composite, and is defined by Equation 2.1, where V_i is the volume of one component or phase of the composite, and $\sum_j V_j$ is the summation of all component or phase volumes[21]. The Rule of Mixtures is a weighted mean that uses the various volume fractions of components to arrive at a theoretical upper- and lower- bound estimation for the final composite properties, and is described in Equation 2.2 for a simple 2-component example. There, Φ_f and Φ_m respectively represent the volume fractions of the filler and matrix, while P_f, P_m, and P_c respectively represent some physical property value for the filler, matrix, and composite. While the Rule of Mixtures was originally developed for estimation of the Young's modulus in composites (the upper and lower bounds respectively representing loading either parallel or perpendicular to fiber direction [22]), it can be used to provide reasonable engineering estimates of other properties.

The relative component quantities of a composite can also be described indirectly us-

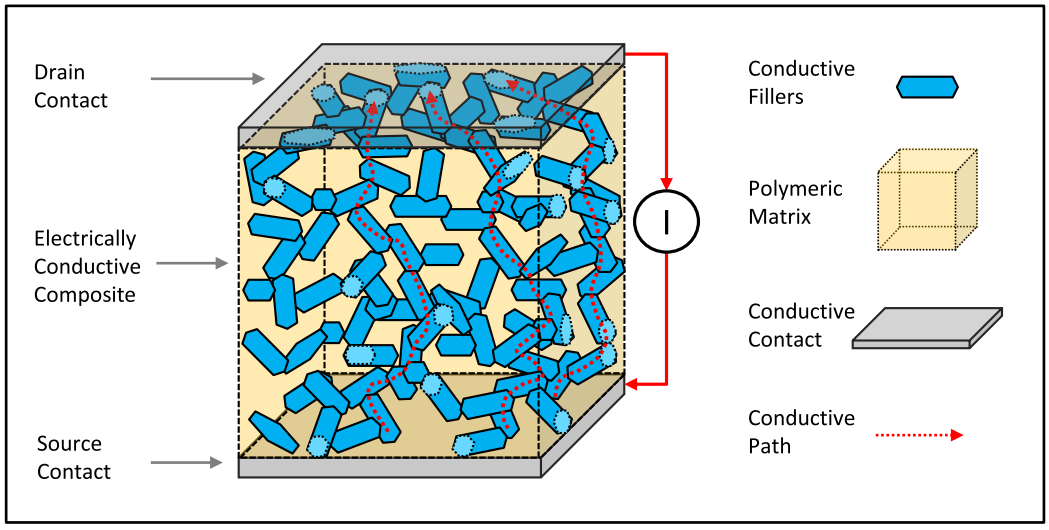

Figure 2.1: Illustration of an electrically conductive adhesive.

ing "weight percentage" ("W_i", units wt%), or "per hundred reference" ("*phr*", units *phr* or 1/1) [21, 23]. These are defined mathematically in equations 2.3 and 2.4, respectively. There, m_i, m_{resin}, and m_{total} respectively represent the masses of the component of interest, the resin, and the total mixture. Weight percent is useful for describing composite formulations based on final mass. In contrast, *phr* originally was used to describe the mix ratio of hardener to resin (the original common names are "parts hardener per hundred resin" and "parts per hundred rubber"[23]). As such it relates the mass of each additive as a fraction to the reference component, commonly the matrix resin, independent of the other components. This can sometimes be useful when describing a composite as a "recipe", especially when testing involves varying the content of one additive while holding all other contents relatively constant.

$$\Phi_i = \frac{V_i}{\sum_j V_j} \tag{2.1}$$

$$(\frac{\Phi_f}{P_f} + \frac{\Phi_m}{P_m})^{-1} \leq P_c \leq \Phi_f P_f + \Phi_m P_m \tag{2.2}$$

$$W_i = \frac{m_i}{m_{total}} \times 100\% \tag{2.3}$$

$$phr = \frac{m_i}{m_{resin}} \tag{2.4}$$

The main controlling factors for expected electrical conductivity are the relative volume fractions and filler distribution, for a given conductive filler. To achieve bulk conductivity through the composite, there must be a high enough filler volume fraction to obtain conductive pathways in a given distribution and orientation[6, 20, 24]. The volume fraction needed for a particular filler in a particular orientation to achieve a conducting network is called the percolation threshold. In the scientific literature, there are several definitions of a percolated network, and investigation of this general problem *via* mathematical modeling is an extensive field. An extensive and recent summary of many of the electrical conduction percolation models was published by Taherian[24].

The electrical percolation threshold can be considered in practical terms to be the range of filler volume fractions over which the conductivity of the composite sharply increases. Below the percolation threshold range, there are too few particles to establish a conductive network. Above the percolation threshold there are enough particles to ensure sufficient particle-particle contacts to allow conductivity. Once the composite is percolated, there are diminishing returns: adding additional particles to the composite improves the conductivity, but each increment of improvement requires ever greater particle volume fractions.[24–28]. Since the conductive fillers are typically more expensive than the polymer matrix, and less beneficial to mechanical bonding, it is therefore desirable to produce composites with

as low a percolation threshold as possible and to only fill them to that point. Prediction of this percolation range based on the filler morphology is a major topic in the aforementioned literature, and many models exist for particular cases[24–28].

With regards to filler orientation, ECAs generally fall into two main categories: isotropic ECAs (ICAs) and anisotropic ECAs (ACAs)[6, 20, 24]. ICAs conduct equally well in all directions, and are filled with a spatially isotropic 3-dimensional network of filler particles, which are typically randomly oriented[20]. For an arbitrary particle morphology, there will be some particle volume fraction that produces enough random contacts, and thus random conductive pathways, in the composite to guarantee a percolated network. This is illustrated in Figure 2.2. On the other hand, ACAs are anisotropic, and are designed to conduct well in along selected-for directions. For these applications, the fillers can be purposely oriented in a preferential manner, which allows ACAs to achieve percolation along the intended axis at lower particle volume fractions than ICAs.[20]. For this thesis, focus will be placed on the general case of ICA composites.

2.3 Fillers in Conductive Composites

For ECAs, a variety of particle shapes have been used to varying success[29–35]. Percolation models generally agree that high-aspect ratio particles are better for minimizing filler volume fraction at percolation compared to low-aspect ratio particles, since rod-like and sheet-like particles can reach farther through the composite per-unit-volume than a spheroid particle could[28]. One model of percolation that describes this is excluded volume theory presented by Balberg *et al.*, Saar *et al.*, Sreenivasan *et al.* and others[24–28].

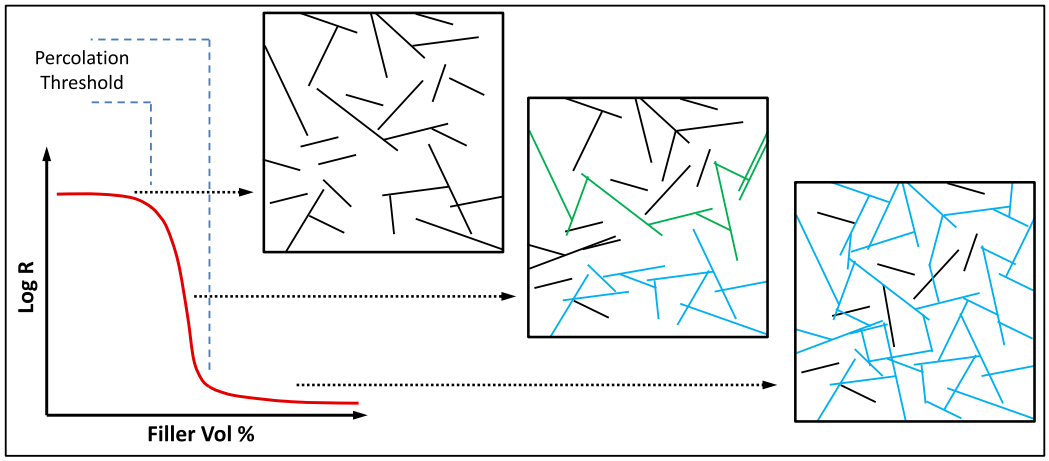

Figure 2.2: Illustration of percolation onset in a network of random sticks. Note the transition from non-conductive, to anisotropically conductive (left-to-right direction), to isotropically conductive as filler content is increased.

The excluded volume ($\langle V_{ex} \rangle$) definition used here, published by Sreenivasan *et al.*, is presented in Equation 2.5, where total mean curvature, $M_p = \pi(l_1 + l_2 + l_3)$, and V_p and S_p are the estimated volume and surface area of the particle, respectively, and particle shape and size are considered to be uniform rectangular prisms[27]. For this, l_1, l_2, and l_3 are the three side lengths of the rectangular prism. The critical volume fraction for percolation for some particle (Φ_0, or Φ_0^i for some particle i) can then be calculated according to the model in equation 2.6, where it is assumed the critical total average excluded volume, $\langle V_{ex}^{crit} \rangle$ is 1.4, based on literature findings[36]. Balberg *et al.*'s theoretical work obtains a percolation estimate for high aspect ratio randomly arrayed rods, listed in Equation 2.7[36].

$$\langle V_{ex} \rangle = 2(V_p + (M_p S_p)/4\pi) \tag{2.5}$$

$$\Phi_0 = 1 - exp(-\frac{\langle V_{ex}^{crit} \rangle}{\langle V_{ex} \rangle} V_p) \tag{2.6}$$

$$\Phi_0 = \frac{0.5}{(AspectRatio)} \tag{2.7}$$

A composite containing microparticle fillers only is considered a microcomposite, while a composite containing only nanoparticles is considered a nanocomposites. If two or more types of fillers of differing size, or morphology, are used in combination, the resulting material is a "hybrid composite". In this case, the composite is considered a "hybrid nanocomposite" if any of the fillers are nanoparticles, even if the remaining material is microscale[30, 31, 34, 35, 37, 38]. Hybrid ECAs are often reported to have significantly better conductivity than mono-filler ECAs, due to synergistic interactions between fillers[30, 31, 34, 35, 37, 38]. Chen *et al.* presents a model to estimate the percolation of a hybrid ECA, listed as Equation 2.8 [26], where Φ_0^μ, Φ_0^η, and $\Phi_0^{\mu+\eta}$ represent the estimated critical volume fraction for percolation of a microparticle, a nanoparticle, and the mixture of micro- and nanoparticles, respectively. To evaluate the model's prediction requires knowledge of d_μ/d_η, the diameter ratio of microfiller to nanofiller, and Φ_μ, Φ_η, the respective volume fractions of microfillers or nanofillers . This equation assumes that the fillers are distributed and oriented in the hybrid without a bias applied to them by the presence of the other fillers.

$$\Phi_0^{\mu+\eta} = \Phi_0^\eta \{1 - [1 - (1 - \frac{\Phi_\mu}{\Phi_0^\mu})^{0.622+0.0531(d_\mu/d_\eta)}]^{0.690}\} \tag{2.8}$$

In recent years, much work has been directed at implementing various nanofillers into conductive adhesives, producing significant improvements to electrical properties and reduced filler content[7, 15, 16, 30, 31, 34, 37–61]. Previously, classical ECAs are filled with

micro-particles. However, the aspect ratio of microfillers have practical limits, otherwise the particle length would become excessive for the application. As such, microcomposite ECAs filled with silver microflakes might require filler contents in excess of 80 wt% to achieve reliably low conductivity, making them prohibitively expensive, and difficult to work with due to high viscosity[62].

ECAs filled with high-aspect ratio nanoparticles achieve percolation at much lower volume fractions[28, 37]. Additionally, many nanoparticles have exceptional properties due to their nanoscale nature[63–65]. Finally, since the matrix and filler interact mechanically and chemically at their shared interface, the high specific surface area of nanoparticles means that even at low volume fractions the nanofillers can produce very significant reinforcement to the mechanical properties, or significant changes to chemical reactions in the composite, the possibility of which will be discussed later.

The synergistic effect in hybrid composites is caused because the electrical resistance of a percolated isotropic network of fillers is dependent on the resistance of each particle in the conduction path, and the contact resistances between them[38]. The contact resistance is a summation of the tunnelling and constriction resistances. Tunneling resistance occurs at locations where direct particle-particle contact is not available and the electrons must tunnel across an energy barrier of a small gap[38]. Constriction resistance occurs when the free flow of electrons is constrained by small contact areas at sharp contacts between fillers[38]. Mixing different size scales allows the nanoparticles to act as bridging material at the microparticle contact points, enlarging the contact areas with only minor increases in total filler volume fraction[37, 38].

2.3.1 Silver as Conductive Fillers and Nanoparticles

Silver has long been widely used as a filler in ECAs, in spite of its prohibitive cost, because of its exceptionally high electrical conductivity (6.25×10^7 S/cm [66]) and resistance to oxidation. Silver microflakes are typically mechanically processed flakes, while the available nano-silvers come in a variety of morphologies. Silver nanoparticles have several advantages compared to other electrically conductive nanofillers investigated in the ECA literature. In nanoparticles, where the high specific surface areas and high surface energies promote oxidation, this is a major advantage over other metallic nanofillers. However, several non-metallic nanofillers, such as graphene and carbon nanotubes are also of interest to ECA research. However, the bulk conductivity of graphene ($\approx 9.6 \times 10^5$ S/cm)[67] is lower than that of silver, with no significant improvement at this time to cost or difficulty of processing. Therefore, silver is one of the most competitive nanofillers available, and worth further investigation in ECA composites.

An FCC crystal, silver is capable of forming single crystal nanoparticles of a variety of morphologies, illustrated in Figure 2.3 a). There are few high-aspect silver nanoparticles available at this time, the most common being pentagonal silver nanowires (PSNWs),

illustrated in 2.3 b) [68–71]. There are also silver "nanosheets", illustrated in Figure 2.3 c), which are flat hexagonal or triangular plates with stacking faults, with majority [111] surfaces[72–78]. Silver nanosheets can be high aspect ratio due to their 2-dimensional nature, but are relatively small and therefore not particularly useful. However, as will be discussed below, it has been demonstrated that these sheets can be assembled into larger and higher aspect-ratio nanomaterials with beneficial properties and applicability to ECA composites[37, 72–74].

Silver nanoparticles are often synthesized by reduction of silver salts, such as $AgNO_3$[75, 80]. A wide variety of reducing agents are reported for use, including poly(vinyl pyrrolidinone) (PVP), or ascorbic acid[72, 74]. Typically, it is reported that small low aspect-ratio nanoparticles are produced using rapid syntheses, while large or high-aspect ratio nanoparticles (such as PSNWs), are obtained by slow syntheses processes[73, 74]. Growth of particles and stabilization is typically mediated by various capping agents that bond to the surfaces and are capable of select particle sizes, morphologies, and preferred crystallographic planes[55, 72, 75–77, 80, 81]. These capping agents can then stabilize the particles in solvent suspensions, allowing introduction to composites, and in some cases allowing chemical bonding to the matrix[1, 31, 55, 82–85].

2.3.2 Resistance reduction by metallic nanoparticle joining

Contact resistance between particles is often a major limiting factor to the network conductivity of an ECA (and other fabricated nanoparticle network devices)[86], amplified by the large number of nanoparticles typically in-series within a network[51]. Use of high aspect ratio particles also help mitigate this, by reducing the number of particle-particle junctions required along a given path[87]. This can also be mitigated by triggering joining mechanisms between particles, causing them to merge and eliminate the resistive junction.

Diffusional Sintering

One method of joining is sintering, wherein particles join via long-range diffusion of surface atoms, illustrated in Figure 2.4. Silver nanoparticles typically have a high surface strain energy, which reduces the energy barrier to the diffusion of their surface atoms. For sintering this is beneficial, since it allows the silver nanoparticles, and other metallic nanoparticles with similar high energy surfaces, to easily sinter *via* diffusion at temperatures well below their melting point and below temperatures that would be required to sinter microparticles of the same material[29, 53, 54, 70, 88–92]. Much of the work with both low- and high-aspect ratio silver nanoparticles has been directed at obtaining this beneficial sintering under workable low-temperature conditions for device and ECA manufacture, including during the curing of a host thermosetting polymer in composite applications. Methods of interest to date include thermal annealing[87, 92–97], localized

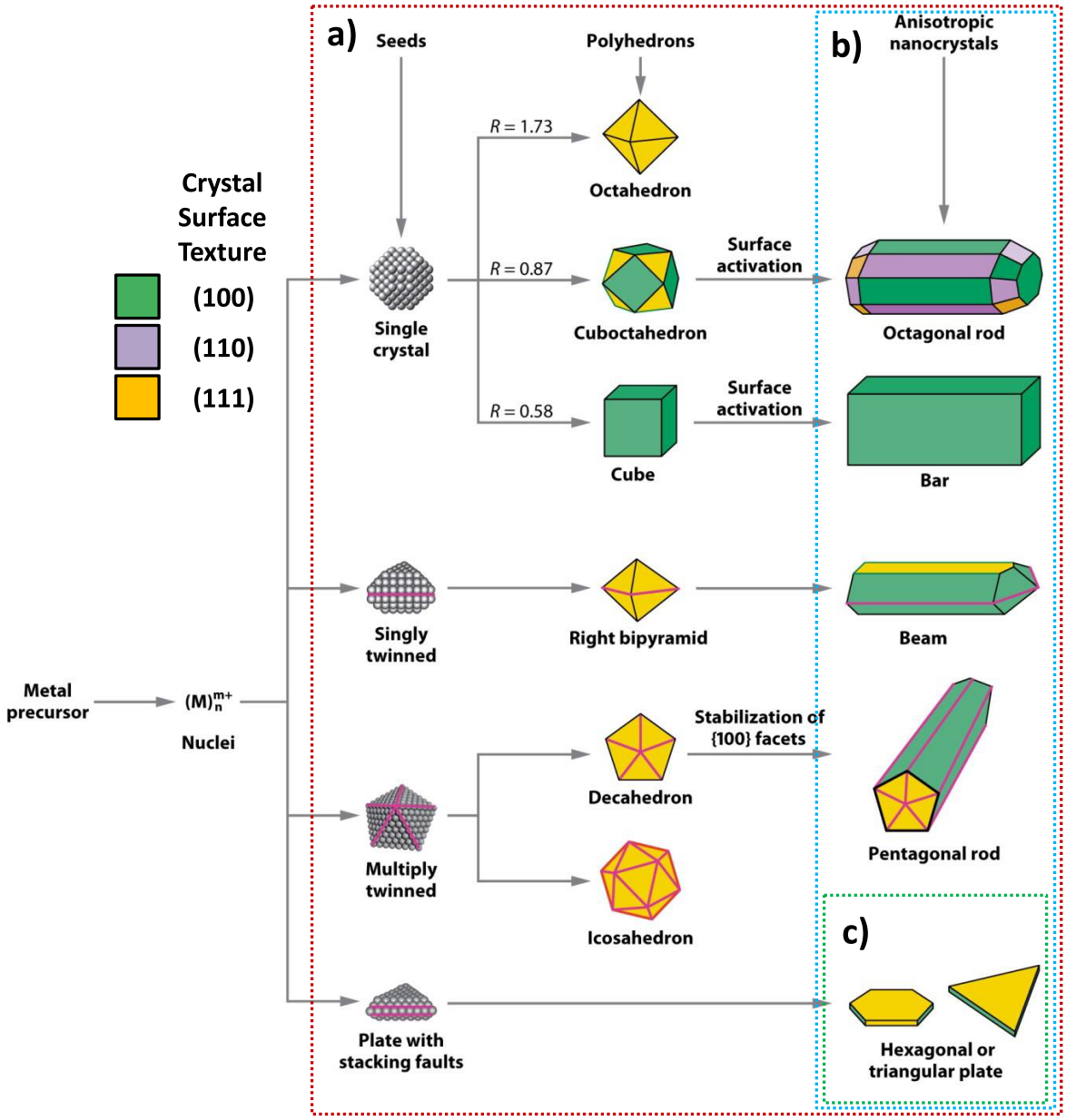

Figure 2.3: Illustration of common nanoparticle shapes for silver. a) Common morphologies, b) high-aspect morphologies, c) flat "nanosheet" morphologies. Adapted with permission from reference [79].

plasmonic heating by light or laser[98, 99], chemical or solvent treatment[94], and pressure[96, 100]. It is considered advantageous to device fabrication and ECA application if this merging can occur below 200 °C, preferably even less[87, 92–97].

Oriented Attachment

An alternate joining mechanism is oriented attachment, sometimes called "nanojoining", illustrated in Figure 2.5, a non-classical crystallization mechanism that does not rely on diffusion of surface atoms, and is able to occur at exceptionally low temperatures when uninhibited[69, 101, 102]. In oriented attachment, nanoscale crystals spontaneously reorient to align with one adjoining particles, and meld their contact surfaces to form larger assemblies, exothermally reducing their strain energy by eliminating their surfaces[72, 103]. Limited examples of silver nanoparticles undergoing oriented attachment have been reported in the literature, in most cases during the particle synthesis[73, 74, 102–104]. No examples were found of a conductive network of high-aspect ratio metallic nanoparticles undergoing oriented attachment while dry.

Limitations of Sintering Due to Diffusional Degradation

However, due to the nature of diffusion, low temperature diffusional sintering is inherently intertwined with particle instability, and therefore with failure by degradation during operation[29, 39, 69–71, 92, 97, 98, 105–109]. Along with forming sintered joints, diffusing surface atoms also form small clusters on the nanoparticle surface, or may diffuse away from the particle if driven by an externally applied potential gradient such as an electric

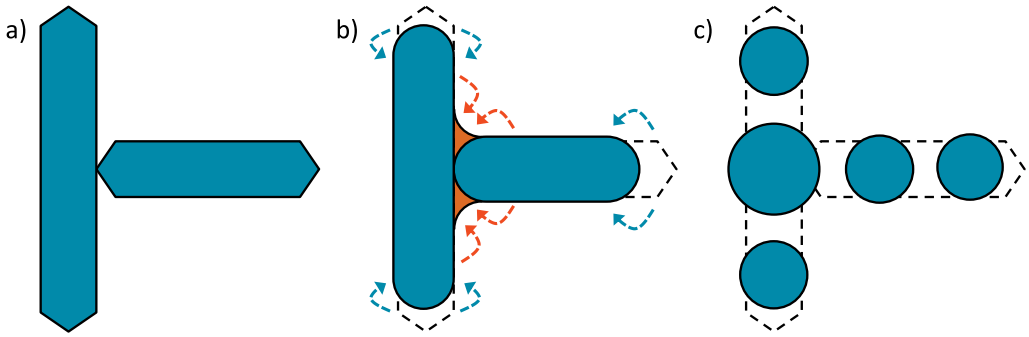

Figure 2.4: Progression of sintering for high aspect ratio nanoparticles. a) sharp-tipped nanoparticles in contact, b) surface diffusion produces desired intermediate-phase neck structure (orange), as well as undesirable degradation such as blunting or shortening, c) end state of diffusion is degradation into a compacted mass or several spheroid particles based on Rayleigh instability.

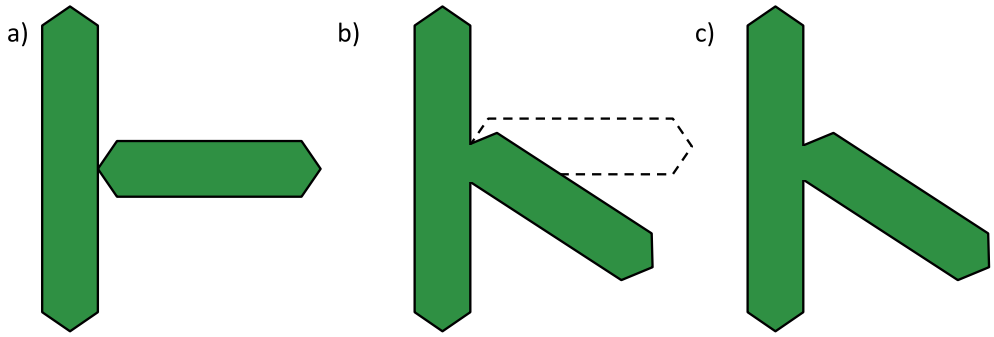

Figure 2.5: Progression of nanojoining for high-aspect ratio nanoparticles. a) Sharp-tipped nanoparticles in contact. b) Spontaneous reorientation of particle, alignment and oriented attachment of mutual crystallographic surfaces. Completed joint has no grain boundary. c) No further progression.

field[39, 71]. Given sufficient diffusional mass transfer, the reorganization of surfaces will completely remodel a high nanoparticle's shape, as seen in Figure 2.4[71, 110]. High-aspect ratio nanoparticles proceed towards reorganization into spheres to minimize surface area, breaking up into separate particles as dictated by Rayleigh instability[105]. This inherent instability has been demonstrated for pentagonal silver nanowires[71], and so for the most common high-aspect ratio silver nanoparticle is limited in its applicability. By similar terms, any nanoparticle with high enough stability to avoid degradation would be expected to be too stable to sinter by diffusion at acceptably low temperatures for use in ECAs, requiring other mechanisms to be explored.

In comparison, oriented attachment does not require atoms to diffuse from their lattice locations, and thus does not require the nanoparticle to be unstable to achieve joining at low temperatures, including room temperature when joining is not inhibited by capping agents (see Section 2.3.3) or unresolvable poor alignment[69, 101, 102]. As such, it is expected that a nanoparticle with low enough surface energy to be desirably stable will be capable of undergoing nanojoining under relatively mild conditions. Unlike sintering, oriented attachment reaches completion very rapidly at each joint once activated[72], and then is expected to progress no further for that joint. Therefore, under isothermal conditions the progression and rate of progression of oriented attachment would not be expected to be significantly influenced by time.

2.3.3 Protection of nanoparticle surfaces by polymer capping agents

To prevent particle instability by diffusion, or joining by oriented attachment, polymeric capping agents are often used to protect the surfaces. For silver these commonly include poly(vinyl pyrrolidinone) (PVP),[70, 92], thiocarboxylates[55], or poly-carboxylic acids, such as poly(methacrylic) acid (PMAA)[2, 4, 39, 72]. As a capping agent, carboxylic acids form co-ordination bonds with silver atoms, stabilizing nanoparticle surfaces[39]. This increased stabilization reduces the driving force for degradation by diffusion, but this consequently increases the barrier to sintering by diffusion. In these cases, neither oriented attachment or sintering can be achieved until the capping agent is rendered at least partially ineffective[29, 70, 92]. This limits both the fabrication and operation conditions for pentagonal silver nanowires, demonstrating a need for a more stable alternative nanoparticle.

Capping agents have their own behaviors that add to the nature of their host nanoparticles, which must be considered. Nanoparticle dispersion into solvents and polymers is often mediated and stabilized by the capping agent[1, 31, 55, 82, 83, 85]. For example, silver nanobelts are coated in PMAA, a polyelectrolyte weak acid, meaning it is sensitive to solution pH. Thus it would not be unexpected if pH influenced the nanobelts strongly when in aqueous suspension, as will be seen in Chapter 4. Early varieties of silver nanobelts, produced using the methods described by Amoli *et al.* [37] are considered to be "Generation 1" nanobelts. Studies of the synthesis methodology, discussed in Chapter 4, will introduce new "Generation 2" nanobelts, with improved lengths and linearity.

2.4 Silver Nanobelts

Silver nanobelts are a newly developed high aspect ratio silver nanoparticle, illustrated in Figure 2.6, which are typically 25 - 40 nm thick, and 75 - 200 nm wide. The length of the nanobelts has a broad distribution, which has been improved during the study discussed in Chapter 4. Originally, the length of nanobelts typically ranged from 1 μm to 15 μm (generation 1 nanobelts, median $\approx$ 6 μm) [37], but after synthesis studies lengths between 1 μm and as much as 100 and 150 μm were obtained (generation 2 nanobelts, median not yet determined, estimated to be $\approx$ 30 μm).

Applying the percolation models described in Section 2.3, the predicted percolation threshold of nanobelts can be estimated. Equations 2.5 and 2.6 obtain 0.3 Vol% (2.5 wt%), and 0.06 Vol% (0.5 wt%) for Generation 1 and Generation 2, respectively. Estimates using Equation 2.7 obtain 0.4 Vol% (3.25 wt%), and 0.08 Vol% (0.67 wt%) for Generation 1 and Generation 2, respectively. It has been shown that adding small quantities (approximately 1 - 3 wt%) of the silver nanobelts to microcomposites filled with 60 wt% $\approx$ 10 μm silver

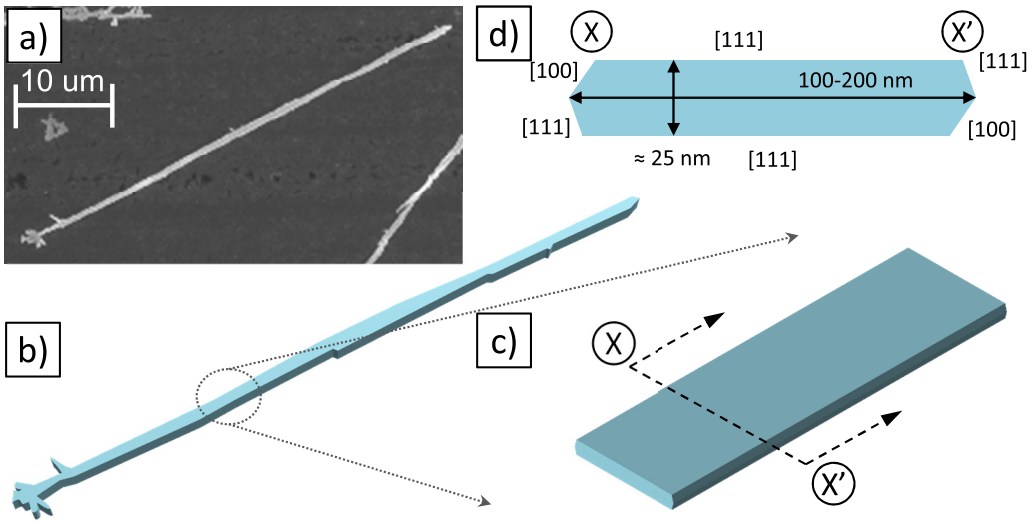

Figure 2.6: a) SEM micrograph and b) sketched trace of a highly linear silver nanobelt. c) Short segment, showing bar-like nature, and d) cross-section X-X' showing surface crystal textures, and approximate dimensions.

microflakes produces a significant improvement in conductivity, thanks to the synergistic hybrid filler effect of the mixed scale and morphology[37, 38]. It was hypothesized that the nanobelts were acting as bridges between microparticles, reducing their contact resistance by reducing the current constriction[37, 38]. The experimentally-determined percolation threshold of the silver microflakes was over the range of 60 wt% to 85 wt% (15.2 Vol% to 40.3 Vol%)[62], and from this data the hybrid percolation model by Chen *et al.* predicts the hybrid percolation threshold to be the relationship presented in Figure 2.7, using the Balberg *et al.* percolation estimate for generation 1 nanobelts and 85 wt% for micro-silver.

Silver nanobelts have been shown to have exceptionally high resistance to degradation by diffusion, owing to its predominately [111] crystallographic surface texture[71]. This improved stability allows silver nanobelts to resist degradation up to 400 °C, unlike PSNWs which begin to degrade by 100 °C and degrade rapidly by 200 °C. This high stability makes them ideal candidates for a variety of applications[71]. In spite of this stability, it is believed that nanobelts are synthesized at room temperature through assembly of the silver nanoplates described in Section 2.3.1 *via* oriented attachment[72], which is a method of nanoparticle manufacture currently under investigation in the literature[69, 101–103]. Similar silver nanobelts, reported in the literature and synthesized by a high temperature process, grow in a slow and kinetically controlled reaction.[74, 103]. However, as will be discussed in Chapter 4, the nanobelts under discussed here were syntehsized in a rapid, room temperature, kinetically-insensitive syntehsis process.

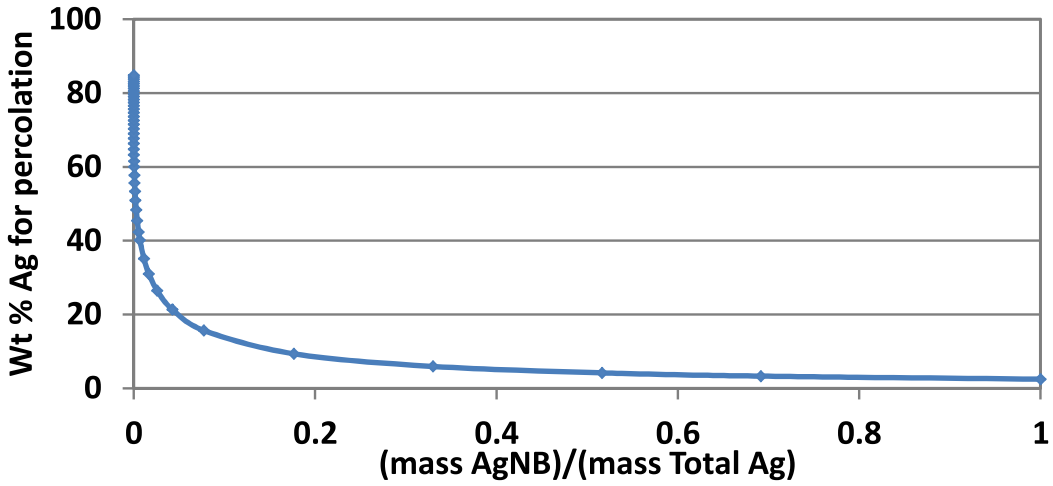

Figure 2.7: Plot of predicted percolation for hybrid composites of silver nanobelts and silver microflakes).

2.5 Thermoset polymers as composite matrices

The matrix of an ECA is composed of polymeric binder, selected based on the requirements of the application. Although they are one of many options, epoxy-based adhesives are very common in the literature, due to their low cost, well understood chemistry, and good adhesion and mechanical properties[20, p. 83]. Epoxies are a "thermoset" polymer, solidifying through an irreversible and exothermic covalent cross-linking of monomers or short ligands through the reaction of their epoxide side groups with some selected hardening agent[111]. The reaction is referred to as "curing", and results in a volume-spanning molecular network when taken to completion[111].

At first the thermoset reaches the "gel-point" where the continuous network forms, preventing fluid-like flow[111]. It is common to perform a pre-cure, curing at reduced temperature and progressing only to slightly more than gelled. This has the following advantages: minimizing the time spent exposing electronic components to high temperature, reducing the dimensional distortion of the parts, minimizing self-heating in parts too large to conduct away their exothermal heat, and producing a mid-step in processing where the composite cannot flow away if the work-piece is moved.

Progressing beyond the gel-point to completion involves the formation of additional crosslinks, further constricting network mobility, until all available reactions have occurred[111]. It is throughout this curing process that the final properties of the thermoset composite will develop, discussed below. Discussion of the equipment, mathematics, and methodologies for quantifying the cure progression can be found in Section 2.6.1.

The continued cross-linking of the thermoset develops the mechanical properties, steadily increasing the viscosity of the polymer resin. Once cured beyond the gel-point, the polymer

behaves as a solid, and begins to contract, known as "cure-shrinkage"[112–118]. The gelled polymer network is constrained by itself and any surfaces it is interacting with, and so is now limited in its ability to relieve stresses produced by the cure shrinkage, though some relaxation continues based on its molecular mobility[113–116].

2.5.1 Thermoset Chemistry of Cure: DGEBA - Amine Epoxies

Epoxies come in a wide variety of chemistries, differing based on the backbone segment, and can react with a wide variety of hardening agents. Reactions can be catalysed chemically, thermally, or through exposure to UV light, opening a wide range of options for reaction initiation. In the interest of simplifying the studies performed here, the epoxy selected for use in the studied composites is a very common and simple difunctional diglycidyl ether of bisphenol-A (DGEBA) epoxy from DOW chemicals, "D.E.R. 331" (Epoxide Equivalent Weight 182 - 192 (g/eq) [119]). For use as a hardener, triethylene tetramine ("TETA") was selected, which is effectively a tetra functional hardener (Amine Hydrogen Equivalent Weight $\approx$ 24 (g/eq) [120]). The chemical structure of each is presented in Figure 2.8. The stoichiometric ratio by mass is 12.8 *phr* TETA, resin as reference. For simplification, this is typically considered to be 13 *phr* [23].

The cure process is illustrated in Figure 2.9. This reaction is "autocatalytic": the consumption of a epoxide group by an amine produces both a cross-link and a hydroxyl side-group, and the hydroxyl side-group can then go on to consume another epoxide to produce another cross-link and another hydroxyl group. Thus, as the readily available amines are consumed, they are replaced by a stable population of hydroxyls that compete for epoxides.

Additives are often introduced into thermosetting polymers, to tailor the developed properties or the cure behavior. For example, a catalyst may accelerate the cure initiation to a lower temperature, while an inhibitor may prevent or impede curing until a

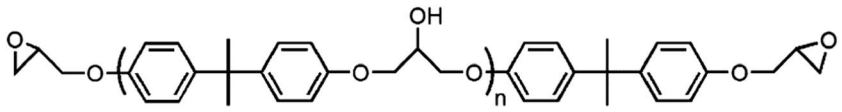

Diglycidyl ether of bisphenol A (DGEBA)

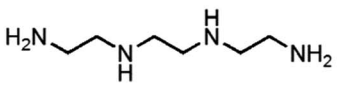

Triethylenetetramine (TETA)

Figure 2.8: Illustration of DGEBA epoxy and TETA hardener. Reproduced from reference [121] with permission from The Royal Society of Chemistry

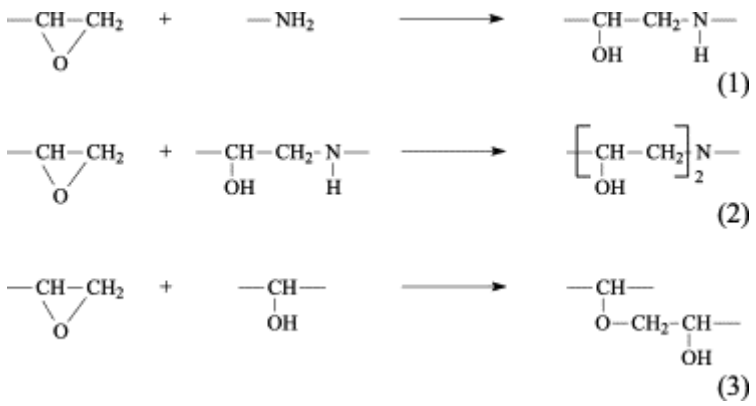

Figure 2.9: Illustration of (1) primary and (2) secondary epoxide-amine reaction, and (3) epoxide-hydroxyl autocatalytic reaction. Reproduced with permission from Elsevier, from reference [118].

temperature has been reached that degrades the inhibitor. Similarly, capping agents or nanoparticles that supply reactive functional groups can alter the cure process and developed properties of the final material[122–126]. Solvents with reactive groups (such as ethanol or isopropanol) may contribute to changes in the chemistry, either during the cure process or during the preceding mixing process, which may unintentionally have an effect on cure and final properties[127, 128]. Analysis of these sources of alteration can be investigated by quantifying the cure progression and kinetics, fitting the observations to descriptive models for analysis, which will be discussed below in Section 2.6.1

2.5.2 Glass Transition: General, and Throughout Cure

The glass transition is a feature of the cooperative mobility of the cross-linked polymer network, and in many ways its nature is an open question in the literature. At temperatures below the glass transition temperature range, the network does not have enough energy to undergo cooperative chain motions on the time-scale of the experiment, and behaves as a stiff glassy solid. Above the glass transition temperature, cooperative movement is activated, and the polymer can respond to applied stresses, behaving as a rubbery solid, leathery solid, or viscous fluid (and a number of other rheometric options not under study here) depending on the molecular weight and degree of cross linking of the polymer. The range of temperatures defining this transition is often simplified to a single "glass transition temperature" (T_g). The determination of this value discussed in Section 2.6.1.

The more densely cross-linked the polymer is, the higher the range of temperatures needed to activate the cooperative movement. As such, as a thermoset cures its instantaneous T_g at that degree of conversion ($T_{g\alpha}$) will increase to its "maximum", "final", or "ultimate" T_g ($T_{g\infty}$). For clarification of the definition of degree of conversion, see

Section 2.6.1. When cured below its ultimate ($T_{g\infty}$), the cure will proceed until the instantaneous ($T_{g\alpha}$) begins to approach the temperature of the composite, at which point the increasingly difficult molecular motion slows the cure rate. This causes the cure to asymptotically slow to a stop as the material approaches the glassy state ("vitrifies")[114]. Under these circumstances, stresses are developed within the polymer or composite that are different than those in the fully mobile state, partially due to the inability to relieve the cure shrinkage forces[114]. Also, in this semi-vitrified cure state the low mobility of the chains produces a different cross-linked structure than would have formed if the material was more mobile, which is an irreversible change to the polymer architecture[113, 114, 116].

For ECAs, the glass transition is important from several practical standpoints. Firstly, for dimensional stability as a connective adhesive, the T_g can be considered the softening temperature of the composite and its maximum operating temperature, above which mechanical stiffness is lost. It would be wise, however, to remember that the glass transition occurs over a range of temperatures: when the operating temperature is within 30 °C, or even 50 °C, below the T_g, the softening from the glass transition to the rubbery state may produce the same detrimental losses in mechanical stiffness when the composite is considered on longer timescales of months or years.

The glass transition is dependent on the cooperative mechanical mobility of the polymer network, and so composites containing fibers or particles that are stiffer than the polymer and in good contact with it can reinforce the matrix network, raising the T_g. Since nanoparticles have high specific surface areas, a larger fraction of the composite matrix is in close proximity to the filler surfaces than would be in a microcomposite, and therefore more strongly reinforced by the nanoparticle surfaces[129]. As such it is expected from theory that well-dispersed nanoparticle fillers such as silver, graphene, or boron nitride in a conductive adhesive would raise the T_g of the composite, and would do so to a greater degree than a microcomposite at the same filler wt%.

Similarly, additives that improve mobility of the composite, such as absorbed solvents, will lower the T_g. A literature review of this topic, discussed in Section 3.1 found mixed reporting of this effect, with a number of authors attributing reductions in T_g to the addition of nanofillers, (though, in Section 3.1 I will also cast doubt on some of these results). Finally, internal stresses in the composite network can also shift the glass transition, and once the glass transition is approached or exceeded these stresses will relax, potentially shifting the T_g again.

2.5.3 Conductivity Throughout Curing

Prior to curing, thermoset ECAs are typically non-conductive, due to a thin insulating polymer layer separating the conductive particles, and only "over-filled" composites that represent a nearly close-packed filler content are conductive even when uncured. As mentioned above, during cure the polymer network contracts, a process known as "cure shrinkage"[113–118, 130], shown in Figure 2.10.

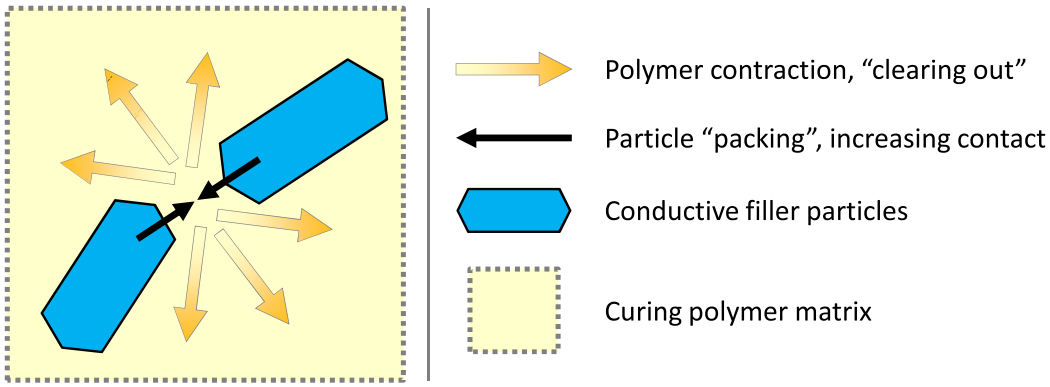

Figure 2.10: Illustration of literature-proposed process of polymer contraction developing composite conductivity, adapted from [117].

This shrinkage process causes the formation of the conductive properties of ECAs, either caused by the contracting particles being forced into contact, or the contraction acting to "clear out" the polymer from the inter-particle spaces, illustrated in Figure 2.10[117, 130]. It should be noted that the inter-particle spacing portrayed in Figure 2.10 is highly exaggerated. The resistance of the ECA is typically thought to reduce following an approximate power-law, though few in-situ studies were found in the open literature[130].

2.6 Analytical Methodologies

2.6.1 Calorimetry: Theory and Analysis

Calorimetry is a widely-used method of determining thermoset cure rate and progression, the specific heat of the cure reaction, and the glass transition temperature range. It is also significant to this thesis, and therefore discussed in detail. These topics have been discussed in detail by Turi and Prime [111, 131, 132]. Differential scanning calorimetry (DSC) obtains the heat-flow ($\dot{Q}$ or $\frac{dQ}{dt}$) between a specimen and its temperature-controlled environment. Heat-flux DSC does this by comparing the temperature of a pan containing a specimen to a pan that is empty, seen in Figure 2.11, according to Equation 2.9. Here,

ΔT_{DSC} represents the temperature difference between the sample and reference pans, while R_{disk} represents the calibrated-for value of the thermal resistance of the heat-flow path.

$$\frac{dQ}{dt} = \frac{\Delta T_{DSC}}{R_{disk}} = \frac{T_S - T_R}{R_{disk}} \tag{2.9}$$

Modulation of temperature during DSC (MTDSC) allows disassembly of the heat-flow into the non-reversing ($\dot{Q}_{NRHF}$) and reversing heat-flows ($\dot{Q}_{RHF}$), according to Equation 2.10[132, 133]. One term is controlled by the absolute temperature, the other by the heating rate, allowing deconvolution of the signal. For the interests of this thesis, these two heat flow components are related, respectively, to chemical reactions and heat capacity, though they are also representative of other phase transitions and material processes. The methods used here are applicable to calorimetric time-temperature-transition processes in more than just thermoset cure, such as exothermic sintering of nanoparticles[29]. In Equation 2.10, C_p is equivalent to $RevC_p$, the reversing heat capacity of the specimen, while $\dot{T}$ represents the underlying heating rate of the experiment. B and ω are the amplitude and frequency of the applied temperature modulation, respectively, while $f\prime(t,T)$ represents the underlying kinetic function of time (t) and temperature (T) that governs the thermal response associated with a physical or chemical transformation. Finally, $C_{f\prime}$ is the amplitude of kinetic thermal response from the specimen caused by the applied sine wave temperature modulation.

$$\frac{dQ}{dt} = C_p(\dot{T} + B\omega\cos\omega t) + f'(t,T) + C_{f'}\sin\omega t \tag{2.10}$$

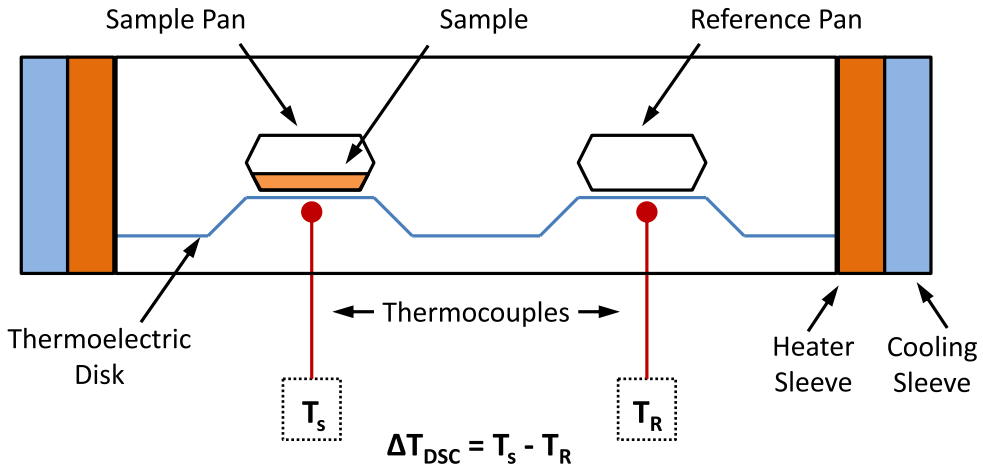

Figure 2.11: Illustration of DSC/MTDSC experimental chamber.

Calorimetry: Cure Progression and Kinetics

For cure rate and progression, the heat flow of interest is the non-reversing heat flow ($\dot{Q}_{NRFH}$). This is integrated over the full reaction to obtain the estimated total heat of reaction (ΔH_{tot}). An integral between time t=0 and time t=i obtains the heat produced over that period, and the degree of cure or degree of conversion at that time (α_i) is evaluated with Equation 2.11. The derivative of α_i is the instantaneous rate of conversion at some time and temperature. Integration of $\dot{Q}_{NRFH}$ requires selection of a baseline. The simplest is a straight-line baseline from the onset to the apparent end of the reaction. Analysis of the cure progression, rate, and heat-flow can reveal a wealth of information on their own, especially when comparing multiple heating conditions or material formulations.

$$\alpha_i = \frac{\int_{t=0}^{t=i} \dot{Q}_{NRFH} dt}{\Delta H_{tot}} \tag{2.11}$$

Further analysis is possible by processing the cure data into phenomenological kinetic models. A summary of some models used for epoxy thermosets, which are autocatalytic reactions, are listed in Table 2.1. Fitting these models required substantial data from multiple heating rates, and methods exist to apply these to isothermal conditions.

Methods of deriving kinetics that do not assume the functional form of the reaction also exist, most commonly in the Flynn/Wall/Ozawa model-free isoconversional method. In this, it is assumed that the reaction has some functional form $f(\alpha)$ that is constant at each degree of conversion regardless temperature or heating rate. Therefore, the reaction kinetics should obey the basic Arrhenius model put forth in Equation 2.12 (presented at some arbitrary α). Sets of $\ln(\dot{\alpha})$ and $1/T$ for multiple values of α are obtained from calorimetry of cure, performed at multiple heating rates. Plotting the sets as "isoconversion lines" (sets of $\ln(\dot{\alpha})$ and $1/T$ at a shared α), the slope and intercept of the plotted line obtains an estimate of the "effective activation energy" ($E_{a,\alpha}$) and "effective preexponent" ($ln(A)_\alpha$) at that α. This is valid, because for each isoconversional line $f(\alpha)$ is unique and constant, and therefore factors out[139–142].

Table 2.1: Collection of phenomenological cure kinetics models from the literature

Model Name	Model Equation $\frac{d\alpha}{dt} =$	Reference
Kamal and Sourour 1	$k\alpha^m(1-\alpha)^n$	[134]
Kamal and Sourour 2	$(k_1 + k_2\alpha^m)(1-\alpha)^n$	[135]
Lee *et al.*	$k_1(1-\alpha)^{n_1} + k_2\alpha^m(1-\alpha)^{n_2}$	[136]
Nunez *et al.*	$\frac{(k_1+k_2\alpha^m)(1-\alpha)^n}{1+exp[C_k(\alpha-\alpha_c)]}$	[137]
Rogers and Lee-Sullivan	$\frac{k_1(1-\alpha)^{n_1}+k_2\alpha^m(1-\alpha)^{n_2}}{1+exp[C_k(\alpha-\alpha_c)]}$	[138]

$$\ln(\frac{d\alpha}{dt}) = \ln(Af(\alpha)) - \frac{E_{a,\alpha}}{R}\frac{1}{T} \tag{2.12}$$

Calorimetry: The Glass Transition

For investigating the T_g range, and the changes in heat capacity throughout thermoset cure, the heat flow of interest is the reversing heat-flow, which is product of the specific heat-capacity (*RevCp*) of the material and the underlying heating rate. Throughout cure, the rising molecular weight causes the specific heat capacity of a thermoset to rise. The glass transition is a second-order phase change, and therefore appears as a sigmoidal step in *RevCp*. The onset start and end temperatures, the span of the T_g can be obtained using ASTM E1356 - 08, in which the temperature at (1/2 ΔC_p) is used as the representative T_g.

2.6.2 Conductivity and Resistance Measurements

Resistance Measurement Theory

To obtain reliable measurements of electrical resistivity (ρ), the material property of electrical resistance, requires careful selection of the method applied. While it is simple to relate resistivity and sheet resistance in general theory (Rs, the thickness-dependent area-normalized measure of resistance and resistivity), as seen in the first equality of Equation 2.13, the practicalities of obtaining accurate sheet resistance measurements complicate the matter. This is discussed in detail by Schroder[143], and Weiss *et al.*[144, 145]. Sheet resistance is defined for uniform thin-layers with a unit of ohm-per-square ($\Omega/square$), and is the special case of resistivity for sheets of uniform thickness.

Sheet resistance measurements are typically taken using the 4-wire (or Kelvin) method, which separates leads carrying the applied current and measured voltage signals. This removes the lead resistance from the system, and allows separate circuits to supply and measure, allowing more precise control of each. The resistance measurement (R_{obs}) obtained by the 4-wire method must be processed to obtain the sheet resistance, since the relative sizes and geometries of the specimen and probe will influence the measurement of R_{obs}. Sheet resistance in the literature is typically obtained by Equation 2.13, where the specimen geometry is factored out by width W and length L[143].

$$R_s = \frac{\rho}{t_s} = R_{obs}\frac{W}{L} = \frac{V}{I}\frac{W}{L} \tag{2.13}$$

However, this is the simplified solution and in most cases requires extensive correction factors based on probe geometry, specimen thickness, and probe location; the general solution, for arbitrary probe geometry and a specimen with known thickness and infinite geometry sheet perimeters, is shown in Equation 2.14[143]. Here, t_s represents the thickness of the specimen, while s_1, s_2, s_3, and s_4 represent the distances between the following pairs of probe pins, respectively: I^+ and V^+, I^+ and V^-, I^- and V^+, and I^- and V^-.

Adding finite lateral geometry constricts the electrical field, requiring the addition of correction factors dependent on probe and specimen relative geometry[143]. Certain probe and specimen geometries produce special cases that simplify the sheet resistance calculation, and introduce correction factors only applicable to that geometry case. For example, a square specimen with probe pins in the corners is a special symmetrical case that only needs to apply corrections based on the ratio between the specimen side length and the probe contact size[143].

$$V = V_{1,2} - V_{3,4} = \frac{I\rho}{2\pi t_s} \ln \frac{s_2 s_3}{s_1 s_4} \tag{2.14}$$

2.6.3 Thermo-Gravimetric Analysis

Mass loss from thermal effects (evaporation, chemical reaction, outgassing) can be a valuable source of data, as a measurement of both thermo-chemical stability and the fractional content of different components[131, 139, 146]. Specimens are heated, or held at elevated temperature, under oxidizing or noble gas atmospheres, while measured by a sensitive mass balance[131, 132]. The intersection of the initial baseline and the steepest slope of the mass loss represents the onset temperature or time, depending on the applied conditions[131, 139, 146]. This has been used in literature for analysis of composite filler fractions, or investigating the nature of capping agents on filler particles[38].

2.6.4 Scanning Electron Microscopy

For detailed morphological analysis, silver nanoparticles can be easily imaged by scanning electron microscopy (SEM), owing to the efficient scattering of electrons by silver due to its high atomic weight. SEM is widely used in the literature to observe nanoparticles , including silver nanoparticles[29, 68–71, 94]. This obtains data for discussing morphology, and effects of applied treatments, as seen in Chapters 4 and 5, respectively.

2.6.5 Dilatometry

Dilatometry, in the form of a linear or volumetric dimensional change over a temperature range, is valuable as a measure of thermo-mechanical properties (coefficient of thermal expansion, and relatedly T_g), which can be measured by Thermo-Mechanical Analysis (TMA) [131, 132]. Since the cure contraction of the composite is of interest to this thesis, this method is expected to provide useful data. The method used has been previously published by Shah and Schubel, as well as Lu and Wong, in which an uncured composite specimen is dispensed between two glass microscope side covers and cured while being measured by the TMA[112, 147]. This is shown in Figure 2.12. The heating program set to match the DSC and Probe-Mold programs, and the pair of glass slides were measured by the TMA prior to the composite being loaded, so their paired thickness could be estimated and removed from the measured dimensions.

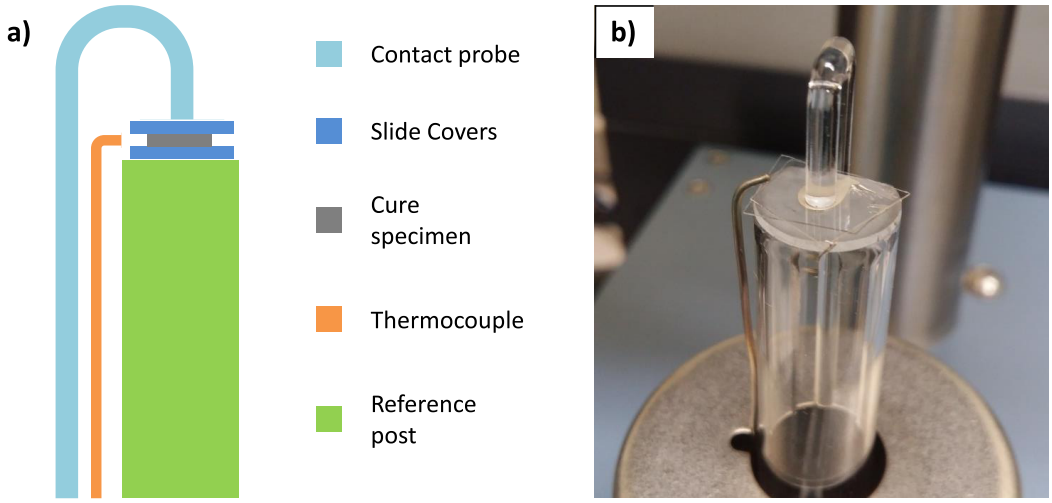

Figure 2.12: Images of TMA setup for monitoring cure contraction. a) schematic, b) photograph.

2.6.6 Mixing and Dispersion Methodologies

Nanoparticle Dispersion

The dispersion of nanoparticles into a polymeric matrix is often difficult, with the nanoparticle often aggregating or agglomerating strongly due to the high van der Waals attraction of their proportionally large surface areas. Capping agents protect and separate the surfaces from one another to reduce agglomeration, and can improve the particle's compatibility with polymers. However, mechanically dispersing even capped nanoparticles directly into a polymer is often difficult, in part because polymers typically have a relatively high viscosity, which increases as nanoparticles are added, and reduced the ability to disperse by shearing. Typically, compatible solvents are used to lower the viscosity of the polymer resin, or as a medium to disperse and suspend the nanoparticles so that they can be added to the resin as a colloidal mixture. Since this typically requires a quantity of solvent that drastically dilutes the resin, the solvent must then be removed from the mixture once the polymer and nanoparticles are well-intermingled. However the solvent must be either removed thoroughly, or quantifiably, since (as discussed above in Section 2.5.2, and later in Section 3.1) residual solvents can have a strong influence on the developed properties of nanocomposites that can overshadow or misrepresent the influences of other components and treatments if not well-controlled.

Common methods of removing the solvent include heating and stirring, heating under airflow, and vacuum evaporation. One concern with any heated or time-consuming method is that reactive solvents may have enough time to alter the chemistry of the resin, compounding the above-mentioned influence of the solvent. Stirring throughout solvent removal assists both maintaining the dispersion of the nanoparticles, and speeding the solvent removal by preventing the formation of a diffusion-controlled gradient of solvent once the viscosity of the mixture begins to rise.

Vortex Shear Mixing

Simple mixing, typically with relatively low viscosity mixtures, can be performed on a tabletop vortex mixer. These have been used in the literature for a wide variety of mixtures, and operate by orbital oscillation of a container at high rate, such that the momentum of the contents sets up a wave in the fluid around the perimeter of the container, producing shear mixing.

The maximum shear rates produced by this form of non-rotary mixing are difficult to estimate, and a review of the open literature did not find a general model that can be applied. The nearest models found describe bioreactor shaker-tables used in biological sciences, intended to minimize applied shear while maximizing mass transfer of diffused gas and nutrients[148–151], with the most applicable work performed by Zhang *et al.*[152].

In those cases the model was dependent on RPM of the orbital oscillation, the viscosity and density of the mixture, the volume of the mixture, the dimensions of the container, and in some cases the surface tension of the mixture. Unfortunately, in the work by Zhang *et al.*, shear was part of a numerical simulation of the container under study, and a similar simulation for the research and equipment at hand is beyond the scope of this thesis. As such, no estimates of mixing shears generated by the vortex mixing regime, applicable to this thesis, are currently available.

Planetary Centrifugal Mixing

Mixing can be very difficult once there is a high viscosity component, or large differences in density, which are both significant features of silver-filled ECAs. It is desirable to minimize variation in cure conversion estimates or material properties caused by undesired curing prior to loading specimens into analytic equipment. Therefore, rapid and thorough mixing of the amine hardener into a prepared composite is critical, since initiation of the cure reaction occurs at room temperature.

A planetary centrifugal mixer (PCM) is designed to mix high viscosity composite mixtures very rapidly. A drum containing the specimen is spun rapidly, and revolved at an angle around a central axis, as seen in Figure 2.13. The resulting superposition of centrifugal forces produces very high toroidial shear forces, allowing rapid laminar mixing of the specimen. The nature of the vortex, with stable subduction zones, allows rapid and consistent dispersion of differing components, even with substantially differing viscosities and densities, including nanocomposites mixing[153].

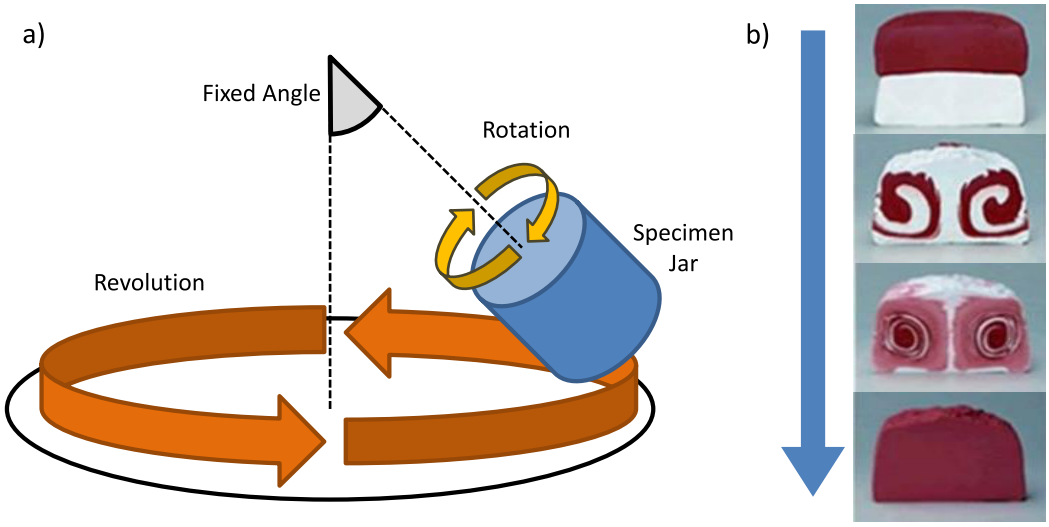

Figure 2.13: Illustration of planetary centrifugal mixer operation. a) Rotation/revolution method to obtain shear vortex, and b) sequential PCM mixing of two pieces of oil-based modeling clay, provided by manufacturer sales literature.

Ultrasonication

One aggressive method of nanoparticle dispersion is ultrasonication, in which the suspension media is agitated by high power ultrasonic-frequency vibrations. The vibrations produce pressure-induced cavitation, generating small-scale shear-stress fields that delaminate the nanoparticles from one another[82].

Ultrasonication is widely used in nanocomposites fabrication[15, 16, 37, 38, 55, 126, 154–159]. However, a concern arises that there is evidence that ultrasonication is intense enough that it can fracture nanoparticles during dispersion; even the very stiff carbon nanotube[82, 155]. As such, ultrasonication is highly effective, but should be used with caution as it may act to lower the aspect ratio of silver nanobelts through fracturing.

2.7 Summary

Literature suggests that silver nanobelts may significantly reduce the critical filler volume fraction of hybrid nanocomposite ECAs, using only a small addition of silver nanobelt fillers, owing to their high aspect ratio. These silver nanobelts appear to have significant advantages from their high-aspect ratio morphology, and their apparent high thermal stability. This may translate into the capacity to enhance conductivity by merging at relatively low temperatures (below 200 °C), *via* oriented attachment or a similar non-diffusional joining process, once the PMAA capping agent is thermally disabled. This could lead to

resistance reductions from particle joining and thermoset cure temperatures, potentially obtaining a single-step cure and sintering process. The literature also indicates that thermoset ECAs display continuously changing conductivities throughout the cure process due to alterations of the filler contact conditions driven by polymer physics effects. How this may effect a composite containing silver nanobelts is unknown, and should be studied.

Chapter 3

Effect of Addition of Fillers on Composite Properties and Cure Kinetics Studied by Differential Scanning Calorimetry

3.1 Solvent Influence: Demonstration, and Meta-Analysis of Nanocomposite Literature

3.1.1 Overview

In Sections 2.5.1 and 2.5.2, a brief overview was discussed for the literature of the effect that added nanoparticles has on the curing and thermo-mechanical properties of epoxy-matrix composites. In that section, I expressed concern with some of the conclusions, for reasons that will be discussed here.

The following sections (Section 3.1.2 to Section 3.1.7) present and discuss: results from a meta-analysis of the nanocomposites literature that identifies a flaw in methodologies that conflates effect from solvents with the effects of added nanoparticle; a set of experiments that demonstrate the discussed erroneous effect attribution; and a set of recommendations to future studies to limit the potential for this mis-attribution. These sections are taken from a manuscript published in the Journal of Thermal Analysis and Calorimetry, as listed in Table 1.1. That manuscript is co-authored by G. Rivers, A. Rogalsky, P. Lee-Sullivan, and B. Zhao[1].

In this work, analysis of the nanocomposite literature revealed that in many cases the changes in $T_{g\infty}$, typically attributed to the addition of nanoparticles to the composite, were more strongly correlated with whether or not solvent-blending methods were used for

filler dispersal. It was noted that no studies found were using control groups to separate the influence of nanoparticles from that of residual solvent content. An experiment was performed using microparticles, wherein it was demonstrated that failure to include solvent content as a controlled-for factor could produce the same apparent reductions in $T_{g\infty}$, producing the perception the reduction was caused by the addition of the microparticles. This study influenced methodologies used in the remainder of the thesis composite studies, ranging from the inclusion of baseline-control groups and emphasizing the importance of comparing multiple measurable properties of a composite in order to draw meaningful conclusions.

3.1.2 Solvent Effect in the Nanocomposites Literature

To explore the hypothesis that solvent effects may be incorrectly attributed to the nanoparticle addition in the nanocomposite literature, T_g data from mechanically mixed studies (no possible solvent effect) [96, 157, 160–164] was compared with T_g data from solvent blended studies (solvent effects possible)[82, 124–126, 156, 165–171], (Figure 3.1). As can be seen, there is a large difference in both the number and severity of negative T_g trends between the two groups; 7 out of 14 solvent blended studies reported $T_{g\infty}$ reductions with a maximum drop of 50 °C [124, 126, 167–171] compared to 2 out of 8 in the mechanically mixed group with no more than a 15 °C decrease[163, 164].

Comparing the sample preparation procedures of the solvent blended studies with T_g decreases [124, 126, 167, 170] to those with clear increases[82, 156, 165, 166, 172, 173], it can be seen that T_g decreases are generally associated with vacuum degas at lower temperatures and without mixing. Increases in $T_{g,\infty}$ are associated with studies that degassed their mixtures using agitation at higher temperatures. The correlation between degassing procedure and outcome can be taken as further evidence for a solvent effect, particularly as one author in the decreased T_g group noted significant solvent remained after degassing[167].

The absence of solvent controls in any of the reviewed papers does not allow us to delineate solvent from other effects. It is fair to infer that solvent blended studies that correlate their $T_{g,\infty}$ decreases with aggregation[124, 169, 171, 173] or chemical ratio interference [124, 125, 174] may be incorrectly attributing the cause due to overlooked solvent. Even those studies with positive trends may have the magnitude of the nano-particle effect masked by the presence of residual solvent.

3.1.3 Incomplete Cure

In the solvent blended group, several authors [125, 126, 165, 167, 169–171] report T_g values near or above their maximum cure temperature with only two of these reports verifying that crosslinking was not prematurely terminated by vitrification[169, 171]. It

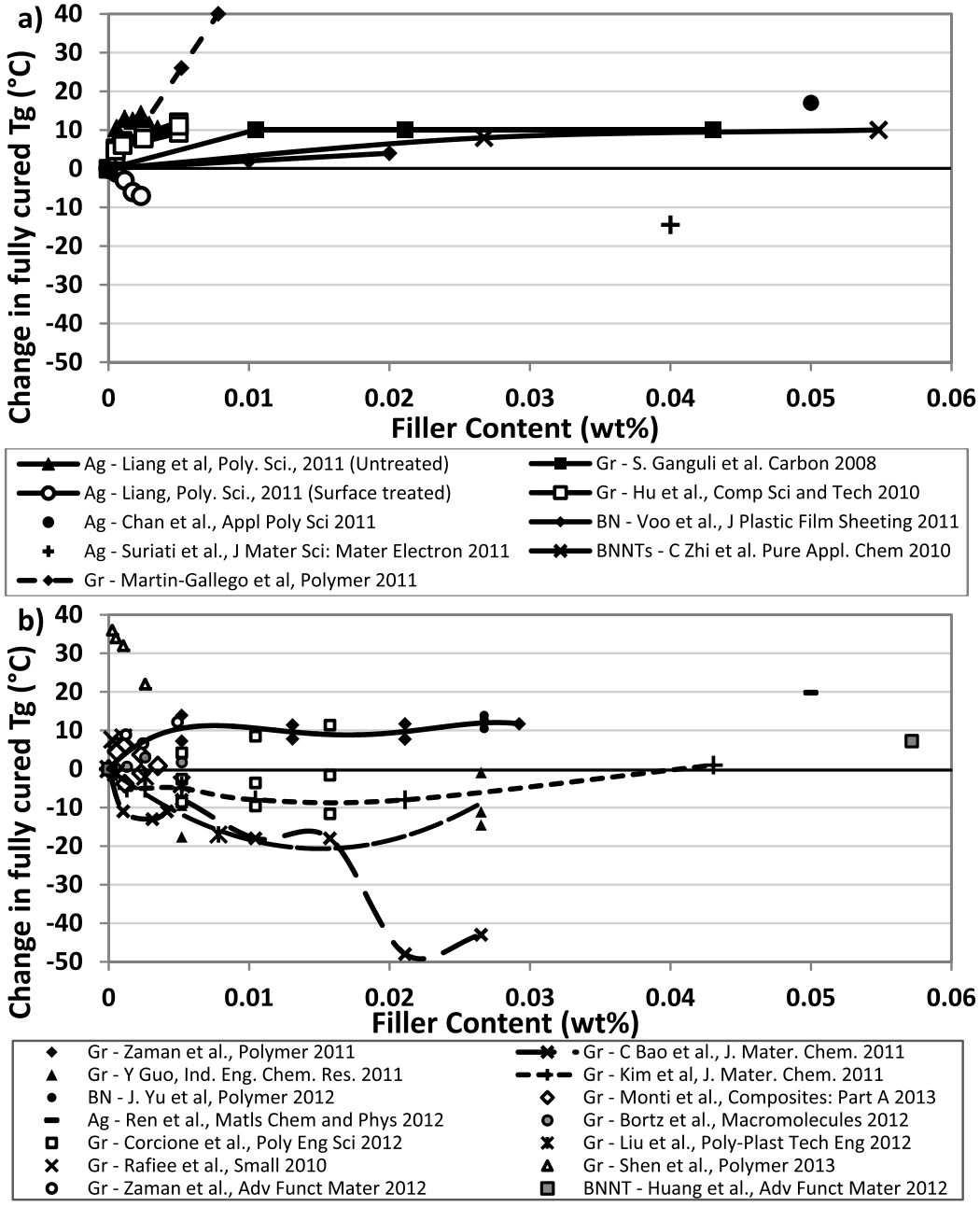

Figure 3.1: Final T_g data from open literature, normalized to provided final T_g of neat epoxy, grouped by a) studies that did not use solvent (mechanically mixed) and b) solvent blended studies. The prefixes used in the legend (Ag, BN, BNNT, Gr) represent the chemistry of the filler under study (Silver, Boron Nitride sheets, Boron Nitride nanotubes, and Graphene sheets

was also noted that decreased reaction rates are correlated with increased filler loadings for both silver [31, 175] and graphene [157, 174, 176]. Therefore, the addition of nanofillers may lead to incomplete cure that varies with nanoparticle content. Under these circumstances, a nanoparticle that is expected to increase final T_g by restricting molecular motion within the matrix will actually lower T_g, due to the sensitivity of instantaneous T_g to the degree of cure [177].

3.1.4 Discernible Nanoparticle Effects

Despite the potential interferences from solvent and incomplete cure, conclusions can be drawn regarding the existence of nanoparticle effects caused by aggregation, non-stoichiometric chemistry and nanoparticle surface interactions. In general these conclusions are consistent with the established cure literature.

Aggregation of nanofillers has been correlated with a reduction in $T_{g\infty}$[124, 161, 164, 169, 171, 173] and no significant cure rate change [45]. Although in many cases the exact magnitude of the effect may be obscured by solvent, the balance of evidence indicates that aggregation does cause reductions in T_g. The reduction has been shown to occur in the absence of solvent[164] and as a change in T_g trend associated with the onset of aggregation at high filler loadings[173]. The mechanism responsible for reducing T_g is speculated to be related to the aggregates acting as a flexible second phase. Similarly the lack of cure rate impact might be due to a significant fraction of the nanoparticle surfaces becoming occluded within the aggregates, including reactive surface groups.

Non-stoichiometric chemistry is known to lead to reductions in $T_{g\infty}$ [122, 123]. Unfortunately all reports relevant to this review that attributed this effect to the nanoparticles occur within the solvent blended group[124–126]. In two of these cases, non-stoichiometric chemistry due to solvent can be identified as a likely cause of the observed effect. An alcohol was used, and significant reaction between the solvent and the matrix are expected based on either initial solvent concentration [126] or conditions of the degas cycle [125].

For well-dispersed nanoparticles with epoxy-reactive surface chemistry, where the reactants added by the fillers did not significantly impact the epoxy stoichiometry, both final T_g and cure rate were reported to increase. This is applicable to nanoparticles with short functional groups that coat the surface plentifully [15, 16, 59, 65, 96, 161, 166, 168, 176, 178, 179], or nanoparticles sparsely coated with longer polymer chains capable of reacting with the epoxy matrix. This was associated with an increase in cure enthalpy when normalized to the mass of resin and hardener[82, 165, 174, 180]. The acceleration of cure rate was attributed to the increased concentration of reactive groups, dependent on the type of reactive group decorating the nanoparticle[111, 127, 168, 174, 176, 178–180]. In cases where the altered stoichiometry did not degrade the epoxy crosslink density appreciably, $T_{g\infty}$ was increased by the crosslinking the matrix to the rigid nanoparticles, which reduced

molecular mobility only after the particle-matrix cross-links were formed[82, 96, 125, 161, 165, 166, 168, 178].

Nanoparticles sparsely coated in non-reactive polymers that weakly interacted with the epoxy matrix through hydrogen bonding or van der Waals force increased $T_{g\infty}$ of the final nanocomposites [172], while dense coatings produce a polymer brush effect, introducing a flexible particle-matrix interface and lowering $T_{g\infty}$ [163].

Well-dispersed nanoparticles with bare nonreactive surfaces were reported to produce an increase in $T_{g\infty}$, and a reduction in cure rates. Both of these effects were attributed to steric hindrance of the epoxy chains by physical interactions with the nanoparticle surfaces during curing and in fully cured epoxy, by either high surface energy and a reduction in void free-volume [175], or π-π stacking interactions between nanoparticle π-bond networks and epoxy resin aromatic groups [96, 156, 160, 166, 169].

3.1.5 A Proposed Methodology for Accurate Data Interpretation

I hereby propose a simple methodology, and demonstrate how it can be used to avoid potential misinterpretation of thermal analysis results. In this approach, a set of solvent controls representative of the residual solvent content of the composite is used. The method has focused on characterizing $T_{g\infty}$ because it is the most frequently reported property in the literature for epoxy nanocomposites containing silver, graphene, or boron nitride. Although $T_{g\infty}$ characterization by DMA is valid, here $T_{g\infty}$ was characterized by DSC, because this affords the opportunity to confirm complete cure within the same experiment.

Materials and Methods

The composite system consisted of DEGBA epoxy resin (DER331 Dow Chemical) filled with silver micro-flake (Sigma Aldrich 327077). The silver microflakes are 10 μm, and are expected to have significantly lower aspect-ratio than the nanoparticles. As such, the filer contents of these composites have very high weight percentages compared to the nanofiller reported in the literature. They were solvent blended using either acetone (Sigma Aldrich 270725) or isopropanol (IPA, Sigma Aldrich 34863) and hardened by triethylenetetramine (TETA, DEH 24 Dow Chemical). A limited set of composite compositions ranging between 0 and 70 wt% silver, with additions of up to 1.2 wt% IPA and 2.5 wt% acetone, respectively, were studied. Note that solvent wt% is presented as the matrix wt%, which neglects filler mass. The solvent content of the silver-filled composites is the equilibrium content after degassing to constant mass. For the IPA-blended composite, a solvent control group was diluted to match as closely as possible the calculated residual solvent contents. For the acetone-blended composites, two solvent control groups without silver were produced, bracketing the composite residual solvent contents.

The epoxy resin was diluted with 10 wt% solvent. Weighed quantities of silver filler were incorporated by vortex-mixing for 5 minutes (Corning LSE) and dispersed by using an ultrasonic mixer for 1 hour (Fisher-Scientific FS20). Samples were degassed under ˜28 inHg vacuum with agitation at room temperature. Samples were periodically weighed, and degassing continuing until the mass stopped changing. After degassing, TETA hardener was added at a stoichiometric 13:100 hardener-to-resin ratio by mass, and the material vortex-mixed an additional 5 minutes.

Differential Scanning Calorimetry

DSC samples were encapsulated in hermetically sealed aluminum pans, and cured during a 3 °C/min ramp to 175 °C in a TA4600 differential scanning calorimeter. The area under the exothermal peak was taken as the reaction enthalpy. Samples were cooled and a second-heating scan performed to 200 °C, using an underlying rate of 3 °C/minute with modulation of ±0.477 °C every 60 seconds. No residual cure signal was observed, confirming that the samples were fully cured during the first scan. $T_{g\infty}$ was determined from the reversing heat capacity (Rev Cp) signal of the second scan, using the methodology described by ASTM D7426-08. Typical second-scan Cp data is shown in Figure 3.2.

3.1.6 Results and Discussion

The final T_g results for the tested composites are shown in Figure 3.3. When compared with neat epoxy but not solvent control groups, Figure 3.3 (a) and (b), it would appear that the addition of silver micro-flakes has a strong negative impact on $T_{g\infty}$. As bare silver micro-flakes are chemically inert towards epoxy, the only potential filler influence on T_g would be due to physical interaction. However, physical interaction is expected to be negligible because the micro-flakes have a low specific surface area ($1.16 m^2/g$, Sigma Aldrich). Work by Utracki indicates that localized polymer reinforcement by a surface, capable of altering the glass transition temperature, is restricted to a range of approximately 15 nm [129] from the surface. At ideal microflake dispersion, the formulations prepared here (60 to 70 wt% silver microflakes) are expected to have a maximum of 5% of the matrix volume within the ≈ 15 nm [129] region adjacent to particle surfaces. Therefore, the silver micro-flakes used are not expected to have a measurable effect on the T_g. When composite $T_{g\infty}$ results are presented alongside those of solvent control groups without silver, Figure 3.3 (c) and (d), the correct interpretation becomes apparent: the reduction in $T_{g\infty}$ is almost wholly due to the presence of solvent.

The enthalpy results for the tested composites are shown in Figure 3.4. These results have been normalized using the epoxy system mass (resin + hardener). From the normalized enthalpy data, it is clear that the silver fill has no statistically significant effect on the crosslinking density, and that if any effect exists it is primarily due to the solvent.

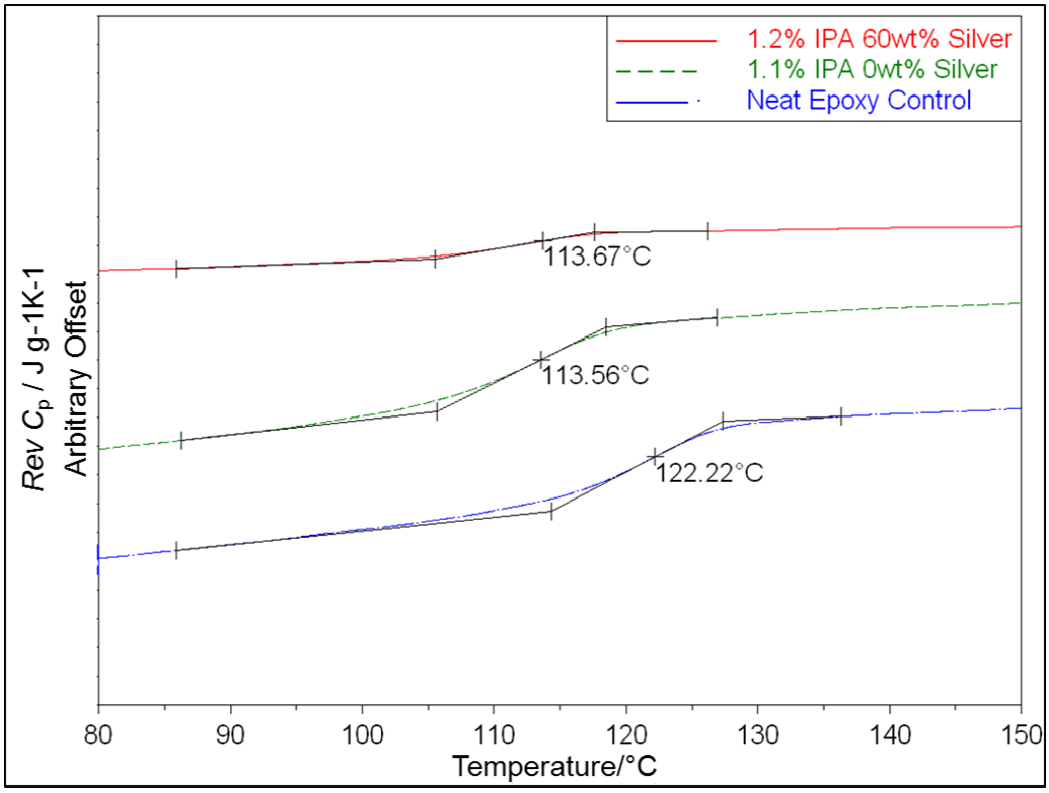

Figure 3.2: Final T_g data from open literature, normalized to provided final T_g of neat epoxy, grouped by a) studies that did not use solvent (mechanically mixed) and b) solvent blended studies.

Although there is high scatter for the 1.3 % acetone 70 wt% silver composite sample, the trends suggest that solvent contents beyond 1.3 % can result in decreased cross-linking density. This is consistent with previous results reported by Loos et al.[181]. At low solvent contents there is no statistically significant difference in enthalpy, indicating that the observed $T_{g\infty}$ decreases are most likely due to plasticization.

3.1.7 Summary

The literature on nanocomposite cure studies to date has almost always attributed all observed cure effects in epoxy-based silver, graphene, and boron nitride nanocomposites to the nanoparticles with little consideration of incomplete cure or residual solvent as potential sources of error. Some authors are aware that incomplete cure can affect results but no attempts were made to correlate results with the final degree of cure. In general, residual solvent effects are poorly addressed and unaccounted for in data analysis. As far as the authors are aware, studies in the literature have not included solvent control groups.

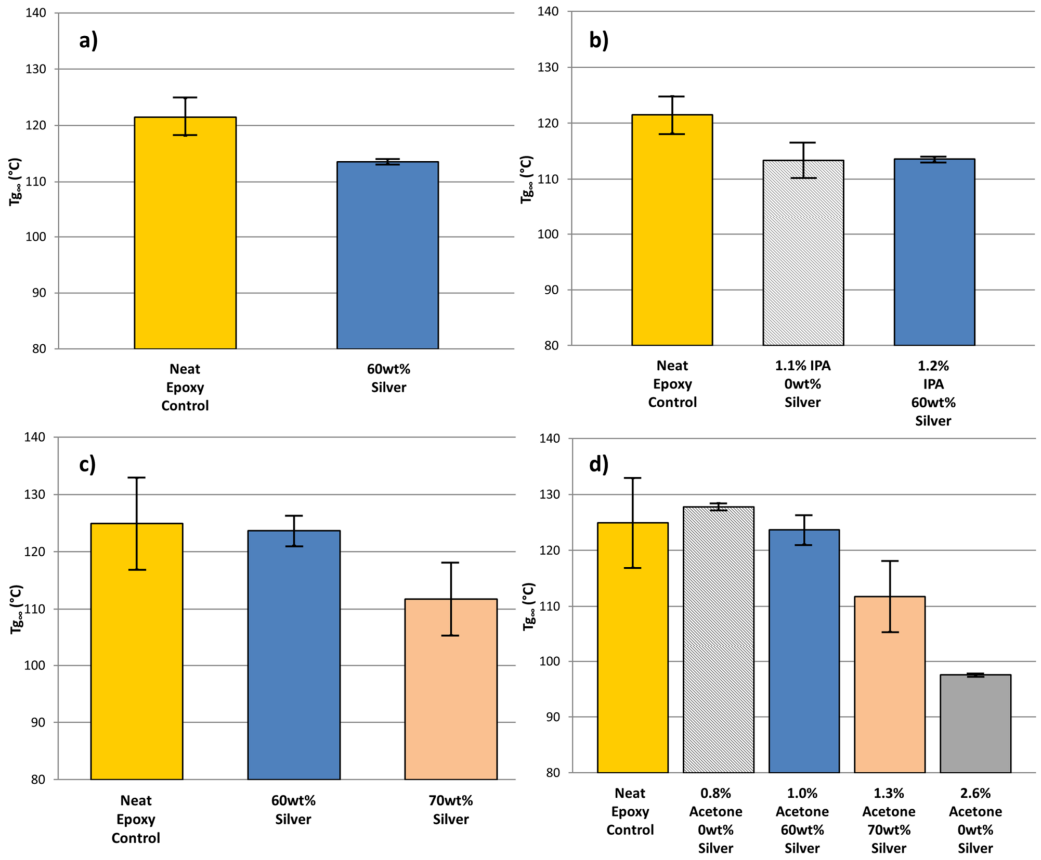

Figure 3.3: Final T_g data from open literature, normalized to provided final T_g of neat epoxy, grouped by a) studies that did not use solvent (mechanically mixed) and b) solvent blended studies.

This limits the ability to draw conclusions; although enough data without solvent effects was available to enable analysis.

The current literature on silver, graphene and boron nitride nanocomposites is consistent with established knowledge regarding T_g and cure rate. Chemically inert, well-dispersed, and rigid nanoparticles slowed cure kinetics but increased final T_g, while those with flexible surface coatings lowered the final T_g of the composite. Nanoparticles with reactive surface chemistry had the potential to raise T_g and accelerate cure depending on the functional groups available and the bonding between nanoparticle and matrix. Aggregated nanoparticles, regardless of surface chemistry, reduced final T_g and displayed an insignificant effect on cure rates.

Using solvent control groups to differentiate solvent effects from filler effects, DSC experiments were performed to demonstrate the ease of erroneous interpretations when solvent-containing control groups are not included. When $T_{g,\infty}$ results are analyzed accounting for

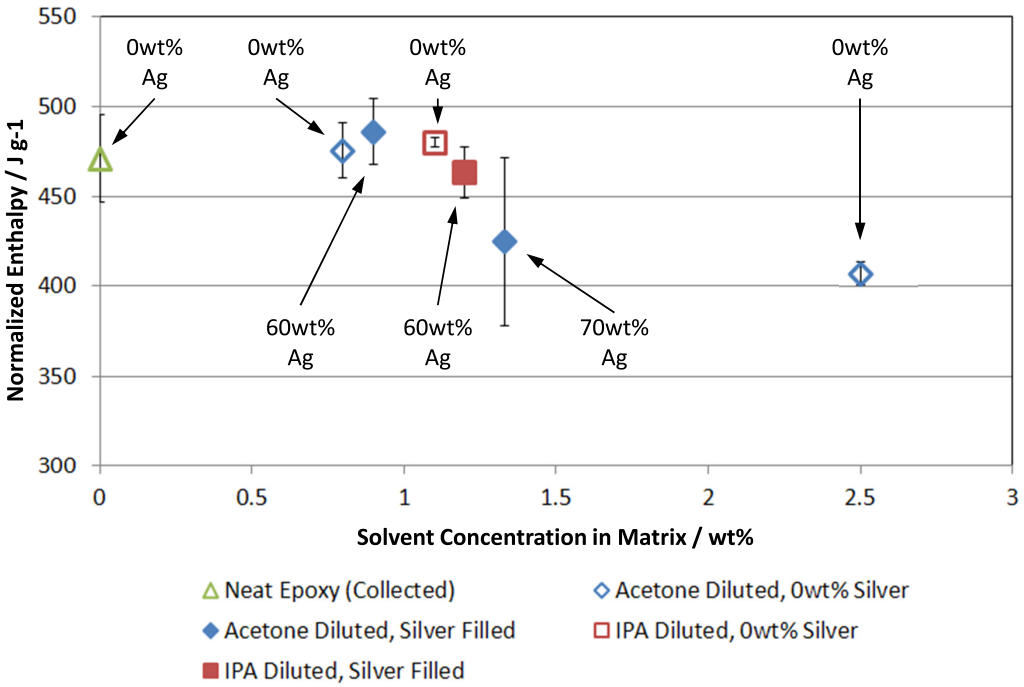

Figure 3.4: Final T_g data from open literature, normalized to provided final T_g of neat epoxy, grouped by a) studies that did not use solvent (mechanically mixed) and b) solvent blended studies.

the presence of solvent, the microparticles had no statistically significant effect on T_g. Solvent effects were statistically significant. At relatively low residual solvent contents, $T_{g\infty}$ decreases due to solvent plasticization were observed. At higher solvent contents, $T_{g\infty}$ decreases can be attributed to both plasticization and decreased crosslinking. When solvent controls are not included in the analysis, the erroneous apparent microparticle effect is very similar to reported effects for nanoparticles in the literature.

Given the high likelihood for misinterpretation, any study using solvent-blending should quantify the residual solvent present in their nanocomposites before cure, and separate its effect from that of the nanoparticles using solvent-only control groups. For T_g analysis, complete cure should be confirmed and methods reported, particularly if final T_g is near or above the cure temperature. In nanocomposite studies using reactive nanoparticles, there is the concern that sufficient addition of nanoparticles may alter the chemical ratio of the matrix, leading to reduced crosslinking density and T_g. Although it is not possible to draw a conclusion from the available literature, this concern warrants further study.

3.2 Experimental Investigations of Effects on Composite Properties and Curing

3.2.1 Overview

Initial studies in this thesis investigated the influence that the addition of silver nanobelts would have on the cure properties and kinetics of a thermoset ECA composite. As discussed previously in Section 2.5.1, it is known that adding functional groups such as those supplied by the PMAA capping agent of silver nanobelt can alter the cure behavior of composites, by competing in or enhancing their chemical cure process. In addition to this, methodologies involving production, handling, testing, and analysis of ECAs needed to be verified, and decisions made regarding which materials to test. For this purpose, preliminary studies largely focused on the thermosetting matrix polymers, solvent additives, and micro-silver based composites were necessary.

Sections 3.2.2 to 3.3 investigate these aspects of the planned testing, and the results informed decisions that strongly directed the remainder of the thesis. Sections of this work were previously presented in the initial project proposal of this dissertation.

In the work presented in this section, calorimetry methods were used to characterize a commercial thermosetting microcomposite ECA, mixtures of DEGBA/TETA epoxy in the form of dilutions and microcomposites, and a nanocomposite densely filled with silver nanobelts. Along with analysis of the glass transition and enthalpic properties of the cure, reaction kinetics methods were applied to investigate the viability of further research, and the validity of the methods used for these materials. The results determined that although it was possible to measure the influence of the filler content on cure and glass transition behaviour, the change to cure behavior and $T_{g,\infty}$ was less significant than that of small quantities of residual solvent left behind by the solvent blending process of composite production. Investigation of the mixing and solvent extraction methods were performed to determine the reasonable limits of solvent removal and the subsequent influence of the residual solvent concentration on the cure properties. The combined results strongly inform the remainder of the research path of the presented thesis, directing investigations toward the influence of cure progression on the electrical properties of various composites, and the use of correlating results from various analytical methods with one another to understand observed behaviours.

3.2.2 Methodology

Calorimetry was performed on a variety of composites and epoxy formulations, as well as epoxies with varying amounts of added solvent, all of which are listed in Table 3.1. In some cases cure kinetic studies were performed using five heating rates (1,2,3,4 and 5 °C)

with appropriate modulations selected to produce a heat-only condition at each heating rate (± 0.159 °C, ± 0.318 °C, ± 0.477 °C, ± 0.637 °C, ± 0.796 °C, respectively). Glass transition data was obtained using the methods detailed in Section 2.5.2.

For cure kinetic studies, model "Kamal and Sourour 1" from Table 2.1 was applied, as was the model-free isoconversional methods discussed in Section 2.6.1. The limitations of this model, and justification for limiting the study to only this model, will be discussed below in Section 3.2.3.

The commercial ECA (Anisotropic ECA "Hysol ECCOBOND CE3126") is a one-part mixture, and did not require mixing or alteration before testing. Custom-prepared epoxy and ECA formulations were prepared using DGEBA epoxy resin (D.E.R. 331, Dow Chemical), hardened by 13 *phr* triethylenetetramine ("TETA", DEH 24, Dow Chemical), and containing selected additions of acetone (Sigma Aldrich 270725), as listed in Table 3.1. The silver microflakes used were 10 micron mesh silver flakes (Sigma Aldrich, 327077), while the "Generation 1" variety of nanobelts used were produced in-house using the same methods described in previous work by Amoli *et al.* [37]. Mixing was performed by various methods, utilizing vortex mixing, manual mixing by stir-rod, and bath ultrasonication.

For solvent removal studies, vacuum extraction was performed at room temperature under 64 cm**.**Hg. In most cases this was performed in a vacuum desiccator chamber. In other cases this was performed in modified 50 ml centrifuge vials that had been fitted with hose fittings to allow vacuum application or air-stream injection, designed to allow solvent extraction during vortex mixing. In some cases mass measurements were taken at prescribed times using a Sartorius CP1245 digital mass balance. For the nanocomposite, the changing mass of the mixture was recorded throughout the degassing process, allowing the calculation of the final solvent content. This value of solvent concentration was then used to produce a solvent-diluted epoxy without fillers for use as a control group.

Table 3.1: Formulations of composites and epoxy mixtures for preliminary calorimetry experiments

Formula Code	Formula Name	Thermoset Polymer	Microfiller Wt%	Nanofiller Wt%	Solvent *phr*
CE3126	Commercial ECA	Unknown	Unknown	0	Unknown
P-A	Neat DER-331	DER-331 + TETA	0	0	Unknown
P-B	Low Acetone	DER-331 + TETA	0	0	0.8
P-C	High Acetone	DER-331 + TETA	0	0	2.6
P-D	60wt% Ag μ-flake	DER-331 + TETA	60	0	0.9
P-E	70wt% Ag μ-flake	DER-331 + TETA	70	0	1.33
P-F	50wt% Ag Nanobelt	DER-331 + TETA	0	50	6.2
P-G	Control for P-F	DER-331 + TETA	0	0	6.2

Mixed thermosets intended for kinetics analysis were stored in sub ambient temperatures (-35 °C for the Commercial ECA, -80 °C for others), to minimize progression of the cure prior to testing in the DSC. These temperatures were below the initial uncured T_g of the composites. Dispensing was performed based on mass, using either glass pipette or micro-pipette (Eppendorf Research Plus 123149B).

3.2.3 Results and Discussion

Commercially available ECA

The Commercial ECA was studied by calorimetry, including preforming comparisons of the cure behaviour under various heating rates and performing analysis by fitting cure kinetic models to the resulting data. The original intent was that nanobelts could be incorporated into the commercial ECA to improve its conductivity, altering it from an anisotropic conductor to an isotropic conductor. In turn, calorimetry would be used to determine how the addition of silver nanobelts alters the cure behavior. Figure 3.5 presents the cure rates determined for various heating rates, exhibiting the following common features: a sharp exothermal peak, a high initiation temperature, and a long shoulder on the high temperature side of the reaction peak. Figure 3.6 presents the degree of conversion under various heating rates, obtained by integration of the cure rates.

Applying the isoconversional model-free method of kinetics, obtained isoconversional

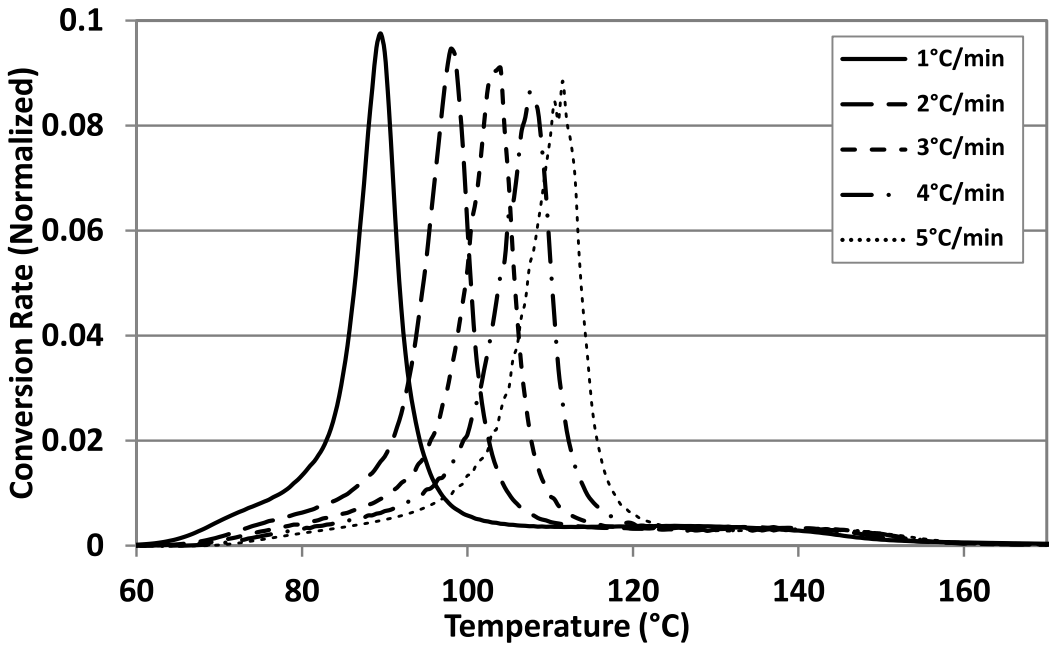

Figure 3.5: Plot of cure rates for Commercial ECA Hysol Eccobond CE3126.

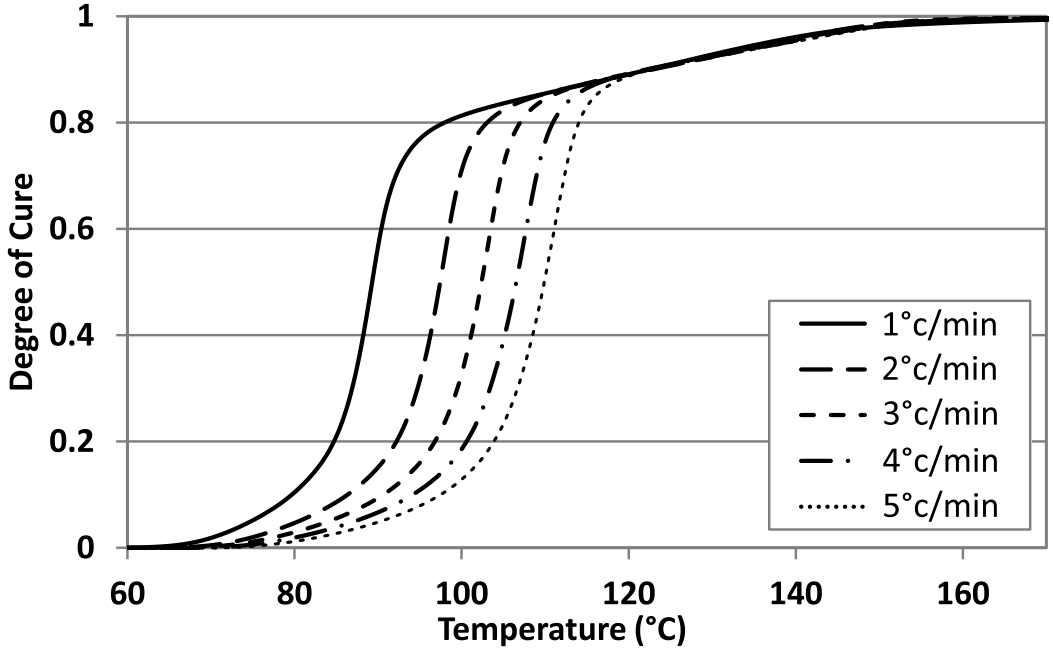

Figure 3.6: Plot of cure conversion for Commercial ECA Hysol Eccobond CE3126.

curves presented in Figure 3.7 and the determined effective Arrhenius constants presented in Figure 3.8. The derived values present a very high effective activation energy and time constant between 0% and 10% cure, followed by a plateau, then a sharp increase again between 65% and 80%. Beyond 80% cure the values become extreme and oscillate between positive and negative values. This will be discussed in greater detail below.

Negative values of activation energy and time constant are not valid from a physical standpoint. Related, the isoconversion curves are not valid, crossing over themselves throughout the reaction, and even displaying positive slopes. This indicates that at least one assumption of the Flynn/Wall/Ozawa isoconversional method was violated, especially at high degrees of conversion, though the values obtained are likely descriptive of the true behavior. There are two potential sources of assumption violation in this study: severe thermal lag throughout the specimen that is dependent on heating rate, or that $f(\alpha)$ is not constant at a given degree of conversion under differing heating rates.

Thermal lag dependent on heating rate is caused by an interaction of the specimen mass, specimen thermal conductivity, and the applied heating rates. When significant, this lag violates an assumption that the measured behavior of the specimen is representative of the applied conditions. This produces a distortion in the isoconversional curves, non-linearly dependent on applied heating rate at all degrees of conversion. In studies involving microcomposites in the literature this effect is occasionally misinterpreted, because the addition of metallic fillers increases thermal conductivity, altering the accuracy of the test, and producing what initially appears to be a catalytic effect from the filler. In reality it

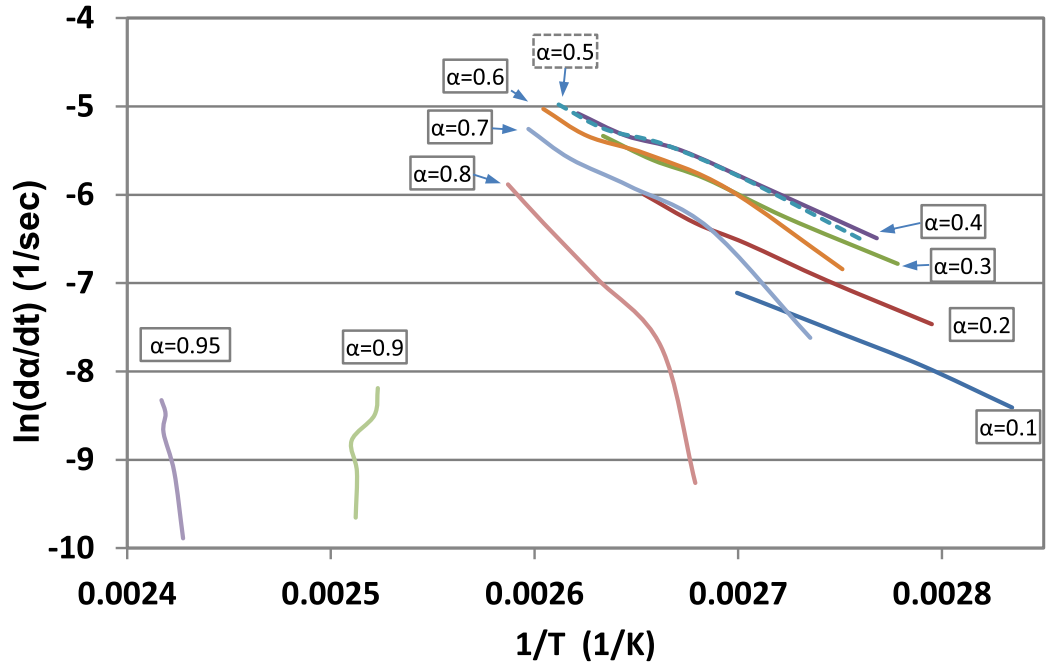

Figure 3.7: Plot of cure isoconversion lines for Commercial ECA Hysol Eccobond CE3126.

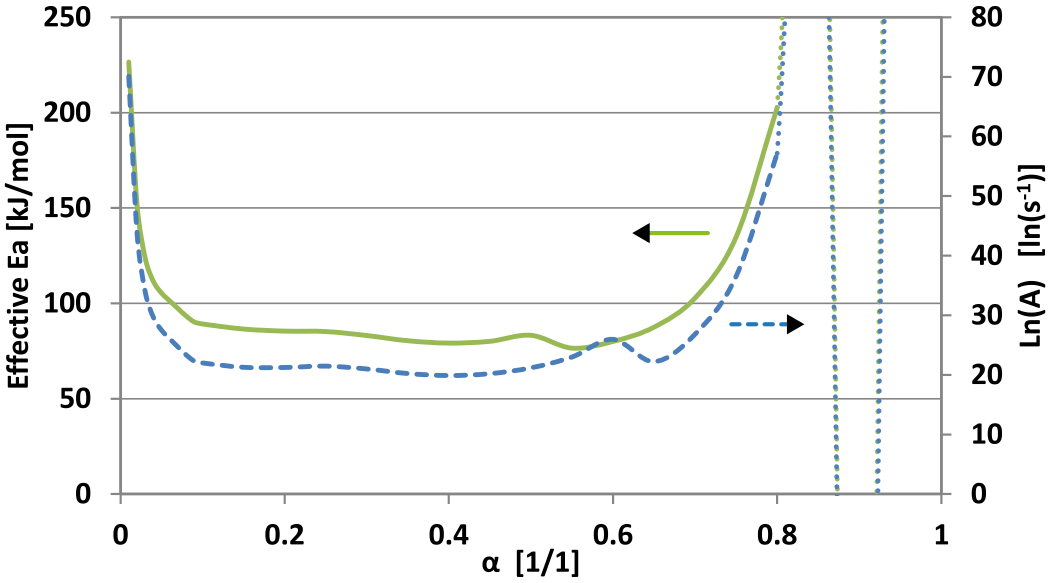

Figure 3.8: Plot of Ea and ln(A) Isoconversion-method parameters obtained for Commercial ECA Hysol Eccobond CE3126. Regions of non-physical response above 80% conversion are included as dotted lines, and exceed the plotted range in both directions.

is only a measure of applying the intended test conditions adequately. It is for this reason that use of the Flynn/Wall/Ozawa model-free method is not recommended at heating rates beyond 5 °C/min [139, Chapter 2, p. 140-142][140, p. 79-81][141, p. 148][142]. In Figure 3.7 a non-linear response across all conversions is not seen, and therefore poor thermal communication is not likely the cause of the atypical cure behavior in this study.

This leaves the violation of the assumption that $f(\alpha)$ is constant at a given degree of conversion regardless of reaction form. Since this is the case, between 0% and 80% degrees of conversion the calculated behaviors are likely representative of the physical process. Likely the aberrant behavior is being caused by additives in the commercial ECA. There is likely a cure inhibitor that slows onset of curing until a certain degree of conversion or temperature is reached: a common alteration made to thermosets to increase their working time. There may also be a catalyst that becomes active when the inhibitor deactivates, allowing a rapid gelification, though there is no direct evidence other than the rapid cure at all heating rates. At high degrees of conversion, the model becomes violated by the onset of vitrification, which would be dependent on the interaction of time, temperature, and conversion, and therefore $f(\alpha)$ would not be constant at a given degree of conversion. It is due to this non-linearity that the values obtained between 80% and 100% cure are non-physical.

The high residency time at the start of cure, followed by the very rapid 10% to 80% cure, makes this Commercial ECA not desirable for further study. Although the apparent inhibitor would allow greater time to disperse the nanofillers into the microcomposite, the strong influence of this unknown chemistry and the partial violation of model assumptions, would make analysis of the resulting hybrid nanocomposites almost impossible, and would likely overwhelm any effect that the nanobelts have on cure at any filler content. For these reasons further study of the Commercial ECA was suspended, and focus was shifted to the two-part epoxy mixture used for the remainder of this thesis.

Solvent Extraction

A study of the rate of solvent extraction using various methods was performed, and results are presented in Figures 3.9, 3.10, 3.11, and 3.12. These are presented in *phr* of the solvent, so that the addition of fillers in Figure 3.12 does not alter the representation of the solvent concentration. Specimens contained in 50 ml centrifuge vials with modified lids were stirred continuously throughout degassing *via* vortex mixing. "Jet" degassing was performed by directing a stream of air at the surface of the mixture. Vacuum degassing was performed by continuously drawing a vacuum. Final solvent concentrations in Figure 3.9 is ≈ 0.4 *phr*, while in Figure 3.12 is ≈ 1 *phr*, and Figure 3.10 and Figure 3.11 is ≈ 5 *phr*.

The results from solvent extraction provide guidelines for anticipated behavior during later studies. Much of the literature, mentioned in Section 2.6.6 and Chapter 6, only perform solvent extraction for short periods of time, and assumed that enough solvent had

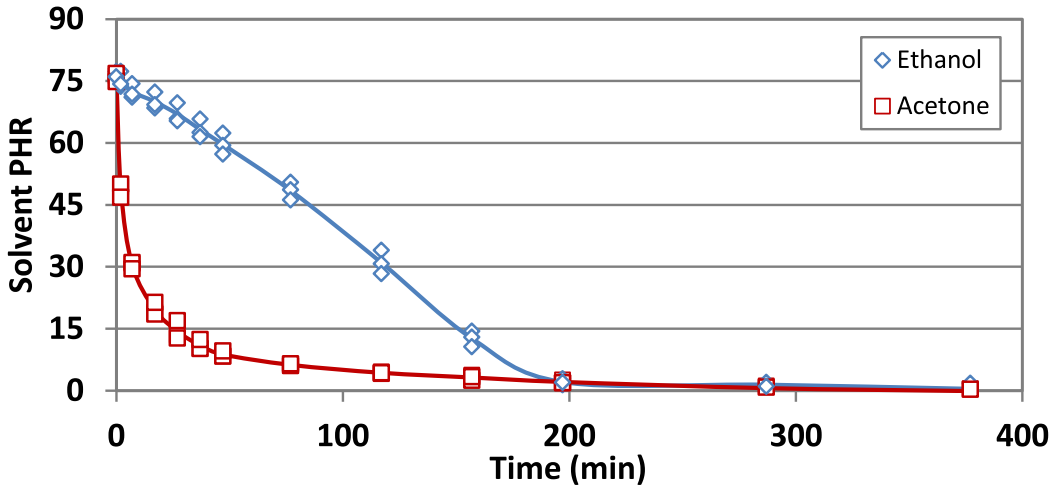

Figure 3.9: Plot of solvent extraction from DER-331 resin, performed under vacuum for acetone and ethanol.

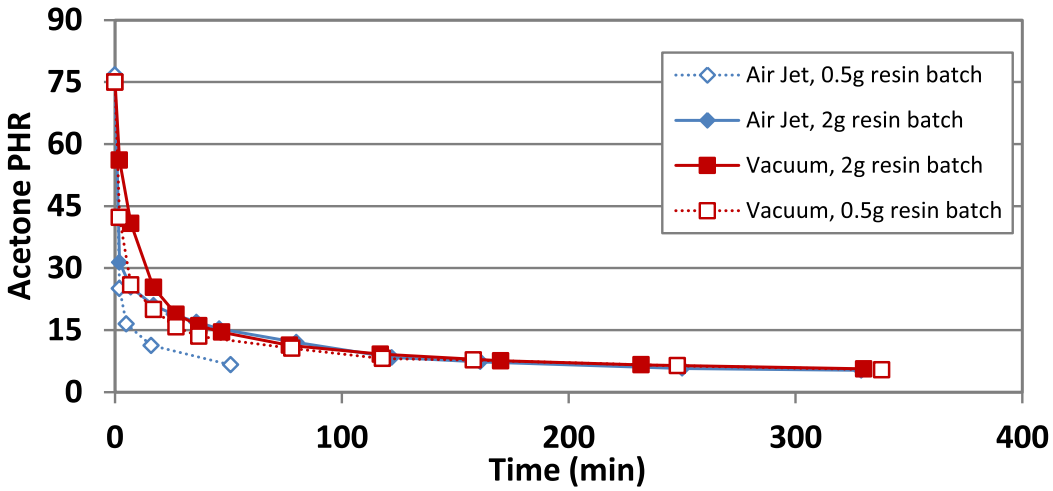

Figure 3.10: Plot of acetone extraction from epoxy resin *via* vacuum and air-jet extraction.

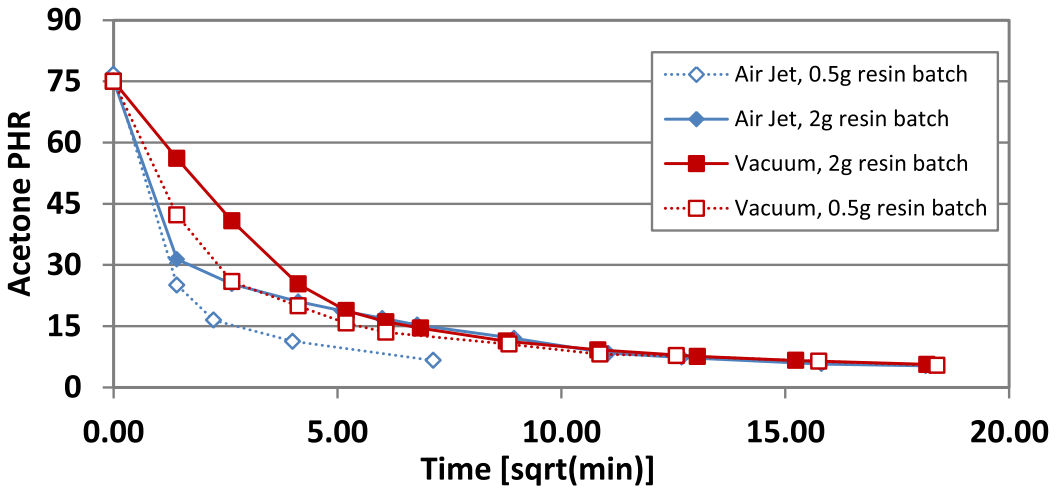

Figure 3.11: Square-root time domain plot of acetone extraction from epoxy resin *via* vacuum and air-jet extraction.

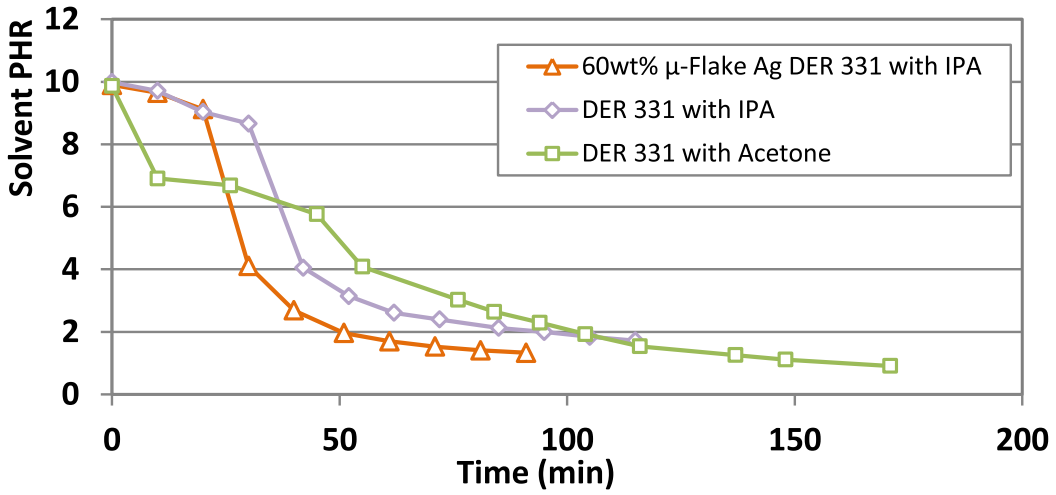

Figure 3.12: Plot of solvent extraction from DER-331 resin, performed under vacuum for acetone and isopropanol, in mixtures containing no fillers or 60 wt% silver microflakes.

left to be inconsequential to their further studies[82, 124–126, 156, 165–173]. Here it is seen that significant quantities of solvent (isopropanol, ethanol, and acetone) remain in DER-331 epoxy resin even after 5 hours of extraction during mixing. Figure 3.9 demonstrates that acetone can be extracted far more quickly than ethanol, due to acetone's higher volatility[182], though their equilibrium concentrations appear to be very near one another based on their displayed asymptotes after 6 hours.

Similarly, Figure 3.12 demonstrates that isopropanol leaves more slowly than acetone at first, then displays a faster profile after the initial concentration drop. This is likely because the rapid initial loss of acetone produced a reduction in temperature substantial enough to increase the viscosity of the mixture, reducing its ability to mix and degas. In the formulation containing micro-flake the initial onset of degassing was accelerated, likely due to the high thermal mass and conductivity providing heat to speed the evaporation. However, the asymptote that is approached is very similar to the other formulations.

Figures 3.11, and 3.12 demonstrate that for low-volume specimens, extraction by air jet appears more effective than vacuum extraction especially early in the extraction, but this advantage is lost with larger specimens. With larger specimens (and thus a lower surface area to volume ratio), the two methods are equivalent in mass loss, though jet drying carries an added risk of introducing contaminants.

This study demonstrates that long periods of solvent extraction will not be sufficient to remove all solvent, contrary to the claims often made in the literature [82, 124–126, 156, 165–173]. Further studies will be made to investigate how this may the effecting the literature claims, and methods by which this can be mitigated. Due to the long extraction times, composite production including solvent extraction must be made parallelizable. It was this conclusion that lead to the development of the custom-designed solvent extraction and mixing equipment reported in Section 7.2.1.

Effect of Addition of Silver Microflakes on Cure Kinetics and Glass Transition Temperature

A cure study on five formulations (named P-A through P-E) was performed, and cure kinetics calculated from the results. Figure 3.13 presents an example of the average cure rates measured for each formulation at one heating rate (1 °C/min). Critical values from the analysis can be found in Table 3.2, and the model parameters determined from Kamal and Sourour Model 1 are presented in Table 3.3. Comparisons of the cure model developed and the averaged experimental data can be found in Figure 3.14, demonstrating good fit between 0% and 80% conversion. The inaccuracy of the model above 80% conversion appears to be dependent on heating rate for all compositions.

Model-free isoconversional methods were also applied, and the resulting effective activation energy (Ea) and preexponential factor ln(A) are plotted in Figure 3.15. The derived

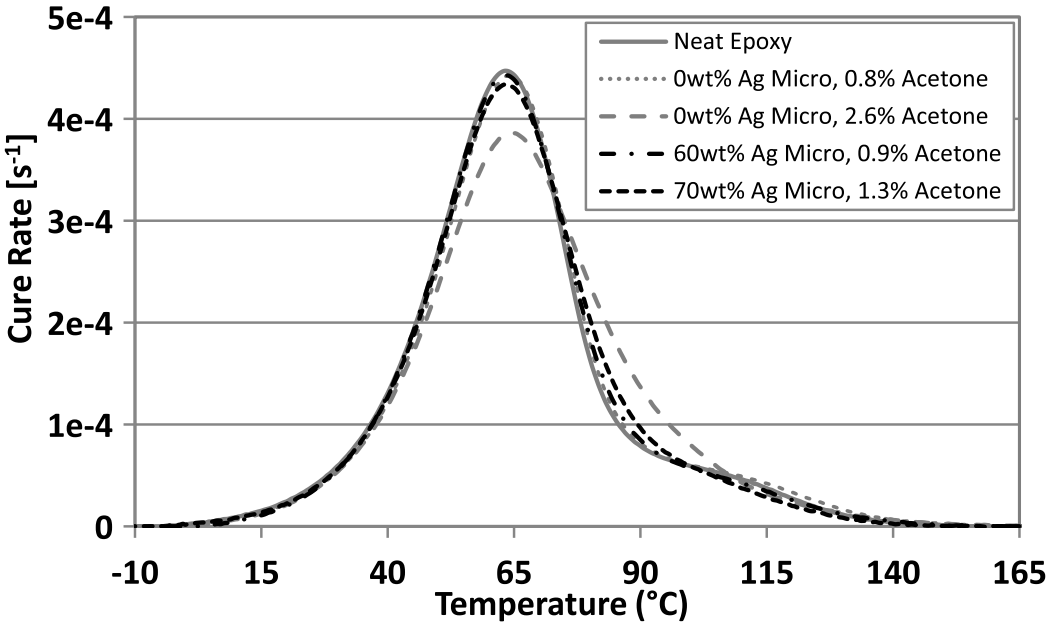

Figure 3.13: Example of cure rates for five DER-331 based mixtures and composites under 1 °C/min heating rate.

Table 3.2: Critical calorimetry values obtained from composites or epoxy mixtures used for preliminary calorimetry experiments

Formula Code	Formula Name	Composite-Normalized ΔH_{total} J/$g_{composite}$	Matrix-Normalized ΔH_{total} J/g_{matrix}	$T_{g\infty}$ °C
P-A	Neat DER-331	481 (28)	481 (28)	125 (4)
P-B	Low Acetone	487 (19)	491 (19)	128 (4)
P-C	High Acetone	194 (6)	484 (16)	124 (1)
P-D	60wt% Ag μ-flake	129 (9)	431 (29)	112 (3)
P-E	70wt% Ag μ-flake	409 (18)	419 (19)	98 (1)

Table 3.3: Model parameters determined from Kamal and Sourour Model 1 for composites or epoxy mixtures used for preliminary calorimetry experiments

Formula Code	Formula Name	Kamal and Sourour Model 1 Parameters n -	m -	E kJ/mol	A s^{-1}
P-A	Neat DER-331	1.68	0.43	58.2 (0.06)	14.5 (0.1)
P-B	Low Acetone	1.75	0.42	59.1 (0.06)	14.9 (0.1)
P-C	High Acetone	1.84	0.30	56.7 (0.06)	14.0 (0.1)
P-D	60wt% Ag μ-flake	1.74	0.43	56.8 (0.06)	14.0 (0.1)
P-E	70wt% Ag μ-flake	1.67	0.42	60.8 (0.06)	15.2 (0.1)

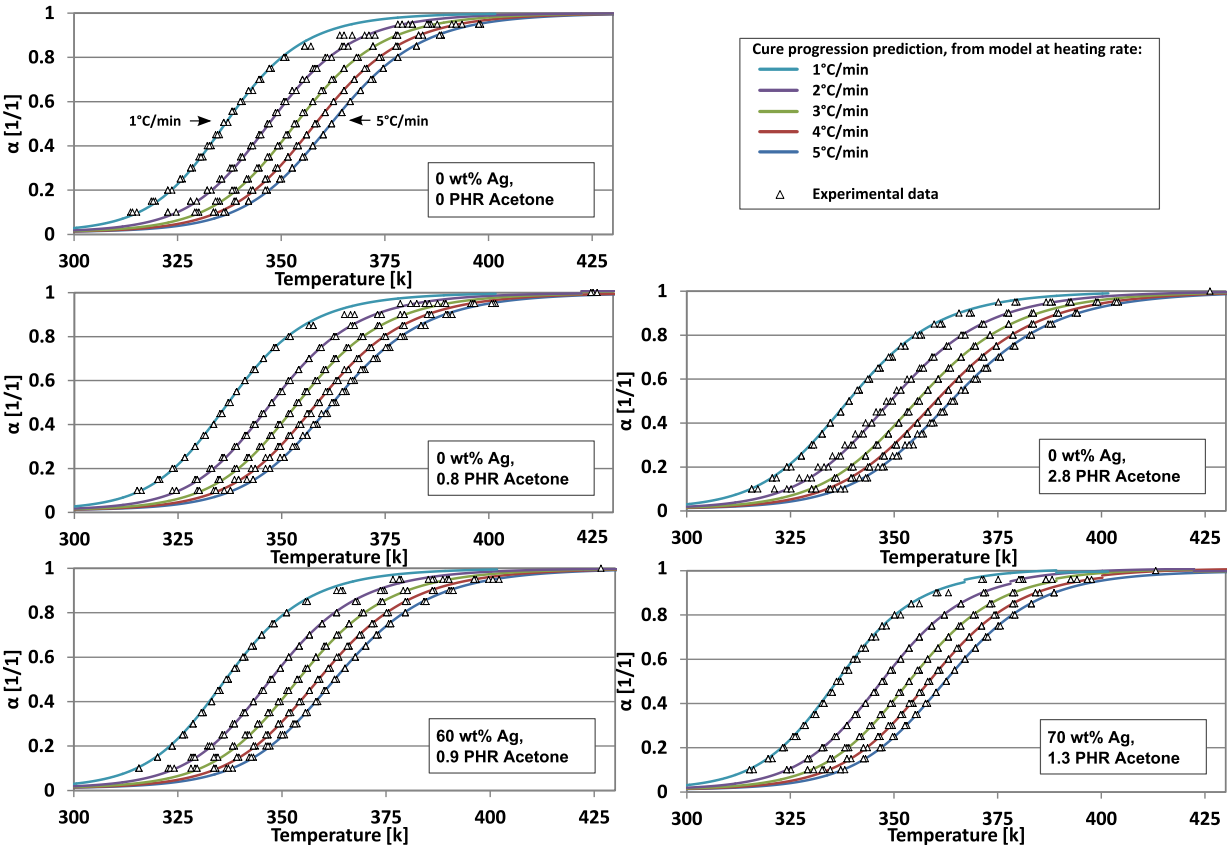

Figure 3.14: Comparison of predicted cure conversion (α) from calculated models to experimental data for five DER-331 based mixtures and composites, differing in solvent and microsilver filler content.

values are, in all cases, fairly constant between 0% and 80% conversion, then sharply increase at high conversion. In some cases the values became negative, which is a physically invalid response.

Cure analysis of multiple formulations of DER-331 epoxy containing various solvent and silver microflake contents (Section 3.2.3, Figures 3.13 to Figure 3.15) demonstrate that between 0% and 80% conversion the simplest Kamal and Sourour model fits very well, and nearly constant estimates of Ea and ln(A) can be obtained. Above 80% the models are violated by the onset of diffusion-controlled cure from the steadily increasing $T_{g\alpha}$. Similar to the commercially available ECA discussed above, the microcomposites produce poor fits and non-physical values at high conversions when fit by these methods.

The models can be adjusted, for example by use of the model "Nunez *et al.*" listed in

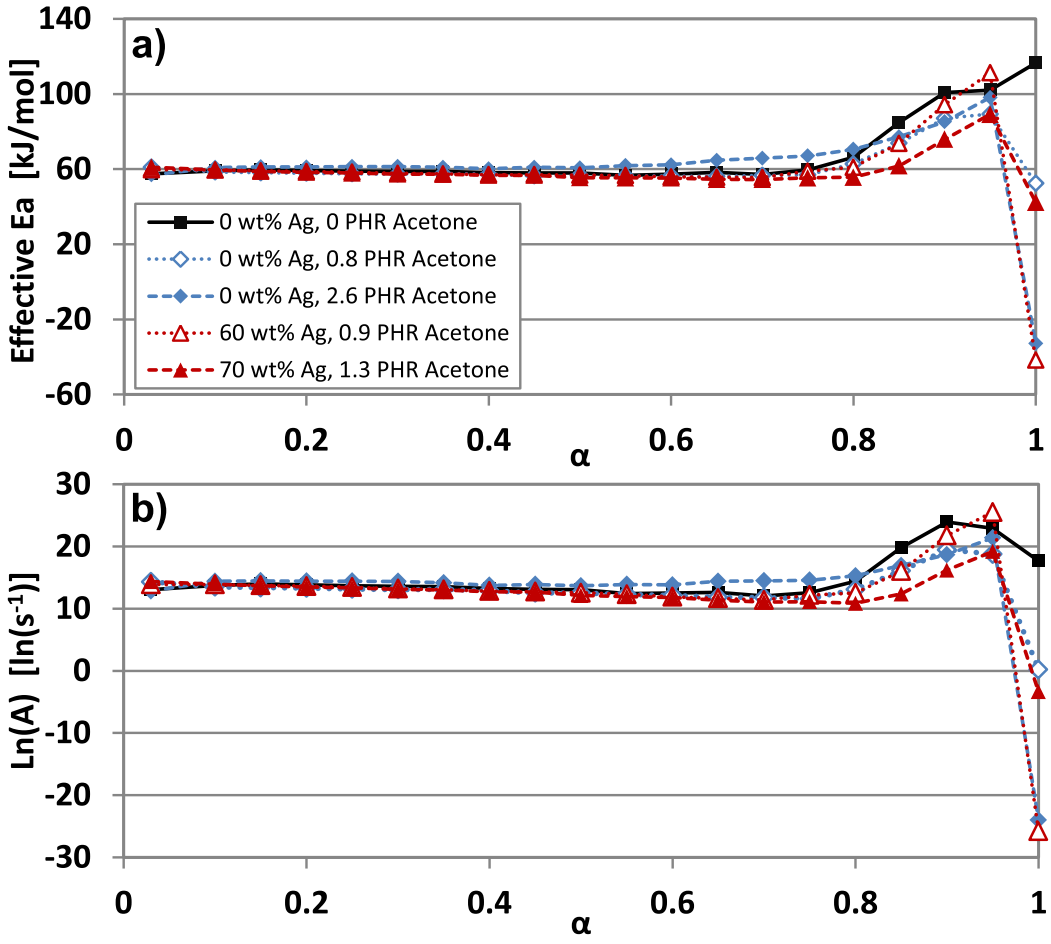

Figure 3.15: Plot of descriptive cure kinetic parameters vs degree of conversion (α) for five DER-331 based mixtures and composites, derived from model-free isoconversion method. a) Effective activation energy, b) effective pre-exponential constant (Ln(A)).

Table 2.1, which is the "Kamal and Sourour 2" model with an additional factor that scales for the onset of a diffusion-controlled regime. However, this requires significant additional experiments to fit since this model has three additional control constants. As can be seen from Tables 3.4 and 3.3, there is no practically significant change in the cure behavior or $T_{g\infty}$ from the addition of the silver microflake. The acetone content has a more notable effect, especially in improving the fit of the models by reducing $T_{g\alpha}$ and thus reducing the amount of curing controlled by diffusion. The control of solvent content is therefore likely significant to all future studies undertaken in this thesis.

Effect of Addition of Silver Nanobelts in High Concentration on Cure Behavior and Glass Transition Temperature

Calorimetry was performed on a 50 wt% silver nanocomposite, to check for any significant influence on cure behavior resulting from the addition of a very high loading of nanofillers, compared to a control epoxy mixture containing the same concentration of solvent without fillers. Due to a limitation in filler production at that time the large quantities necessary for a cure kinetic modeling study were not available. For that reason a direct comparison of conversion to that of a representative control group under the same conditions was performed, shown in Figure 3.16 and 3.17. The critical values for the cures are shown in Table 3.4.

The calorimetry results demonstrate an influence on the cure of the composite from the nanobelts, narrowing the reaction and shifting the peak temperature lower, indicating a mild reaction-accelerating behavior. This is likely because a fraction of the carboxylic acids of PMAA capping agent are contributing to the cure reaction of the composite, or due to

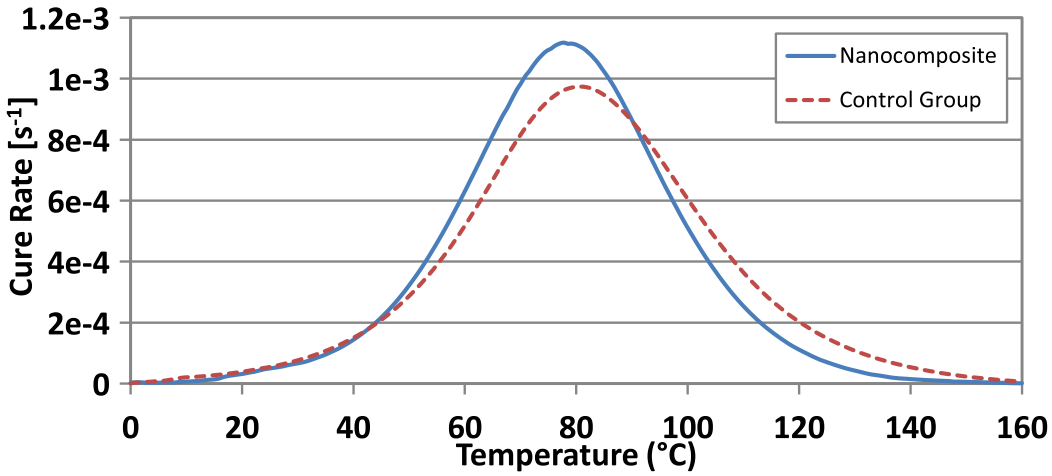

Figure 3.16: Plot of the cure rates of 50 wt% silver nanobelt composite and its control group.

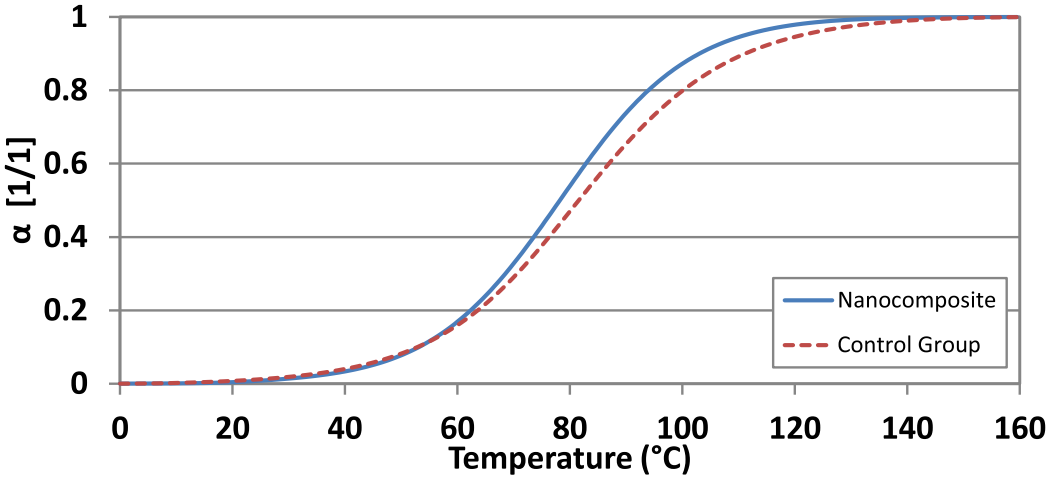

Figure 3.17: Plot of the cure conversion of 50 wt% silver nanobelt composite and its control group.

Table 3.4: Critical calorimetry values obtained from 50 wt% silver nanobelt composite and its control group

Formula Code	Formula Name	Matrix Normalized ΔH_{total} J/g_{matrix}	Onset Temp. T_o °C	Peak Temp. T_P °C	$T_{g\infty}$ °C
P-F	50wt% Ag Nanobelt	502	43.0	77	116.3
P-G	Control Group for P-F	491	45.3	80.67	99.7

a mild catalytic effect from the silver surface[127, 183]. However, although the nanobelts have a detectable effect, it is not practically significant: in spite of the high filler content, the nanobelts caused the peak temperature to be reduced by only 3 °C, and an even smaller reduction in the onset of the reaction peak. A 16 °C increase in $T_{g\infty}$ was noted compared to the control groups, agreeing with basic composite theory. This is the same scale scale of changes as those produced by less than 3 *phr* acetone, as seen in Figure 3.13.

However, high concentrations of nanobelts drastically increase viscosity, far more than similar weight percentages of silver microflakes. Therefore, a practical hybrid nanocomposite would contain far lower concentrations of nanobelts for practical reasons, likely less than 10 wt%. Therefore it can be expected that the change in cure behavior would be proportionally less in those formulations than in the one studied here. In that case, the effect from nanobelts on cure and $T_{g,\infty}$ of their composite, are less significant than the effect from small variations in solvent content. As such the work necessary to investigate the effect on cure produced by the nanobelts *via* further kinetic modeling studies is not

sufficiently justified by the results obtained.

3.3 Concluding Remarks

Investigations of the mixing methodologies used for nano- and micro-composite production in the literature have been performed, and revealed a strong correlation between the reported "nanoparticle" effect on the composite glass transition temperature and whether solvent was used to disperse the filler content. Similarly, literature studies focused on cure kinetics and activation energies also lacked the control groups necessary to rule out solvent effects, but also did not exist in sufficient numbers for a reasonable meta-analysis. This study influenced methodologies in all subsequent composite studies, ranging from the inclusion of baseline-control groups to emphasizing the importance of comparing multiple measurable properties of a composite in order to draw meaningful conclusions. As a result, great care was taken to minimize and quantify residual solvent content, whenever possible, and comparison between the properties of interest and the developed $T_{g\infty}$, a strong indicator of solvent effects or incomplete cure.

Cure kinetic analysis demonstrated that solvent content can have a significant influence over observed behavior. However, these cure kinetic studies also determined that, although there was measurable influence from the silver nanobelts on the cure and glass transition properties, it was small even at large nanoparticle contents, and less significant than the influence caused by small quantities of residual solvent.

Therefore characterizing the effect of the silver nanobelt filler on the cure behavior of its composites, is not worthwhile due to the effort necessary and the large variation produced by solvents. At this point the thesis plan was reviewed, and redirected to focus on process-property relationships of the composite cure, nanoparticle behaviour, and final composite properties. It was also decided that it was most valuable to utilize a several independent characterization methods, so that behaviours under multiple conditions and composite formulations could be correlated to understand how cure processes influence the conductivity of the composite.

Chapter 4

Silver Nanobelts: Synthesis

4.1 Obtaining Repeatability and Shape-Control of Silver Nanobelts

4.1.1 Overview

It is necessary that the process for silver nanobelt production be consistent and repeatable to conduct further research to scale manufacturing and achieve wide utilization by industry. However, during initial experiments in the publications by Marzbanrad *et al.* and Amoli *et al.*, it was observed that the assembled morphology was highly sensitive to experimental procedure, making repeatable synthesis by this method a challenge[37, 72].

Section 4.1 presents investigations of the relationship between the synthesis mixture chemistry and handling on the silver nanobelt synthesis, and is adapted from a manuscript published in the Journal of Nanotechnology, as listed in Table 1.1. That manuscript is co-authored by E. Marzbanrad, G. Rivers, A. Rogalsky, P. Lee-Sullivan, B. Zhao, and Y. N. Zhou,[2], reproduced with permission from The Royal Society of Chemistry. A clarification of the contributions by the author of this thesis is presented at the end of this section.

In this work, mathematical modeling and experimental observation was applied to investigate the influence of the synthesis factors on the resultant nanostructure morphologies. First, chemical reaction modeling techniques were applied to correlate the changing pH of the mixture to the progression of the synthesis reaction, which was verified by experimental observation. This model was employed to predict the pH of formulations prior to testing, to compare to *in-situ* pH measurements taken during synthesis as a predictor of conversion and reaction kinetics, and to discuss the effect of pH on the shape of the generated super-crystals. Next, the morphology of the silver super-crystals that were produced by various synthesis recipes, correlating the selected changes to the formulation with the resulting morphology and model-predicted changes in pH. Finally, the progress of

the reaction using various recipes was characterized through measurement of the optical transmittance of the solution by a simple photo detector, to investigate if reaction kinetics correlated with morphology. Combined, the results reveal that pH and the concentration of the silver nitrate precursor solution are the dominant factors in controlling the final morphology of the fabricated nanostructures. Also, the synthesis of the silver nanobelts is not kinetically controlled, with is contrary to the knowledge in the literature for similar silver nanostructures synthesized by different methods. This study resulted in improvements to the nanobelt morphology, resulting in "Generation 2" nanobelts. Compared with earlier nanobelts, Generation 2 nanobelts exhibit improved linearity, fewer large side-branches, and increased average and maximum particles sizes observed.

In this study, I was the member primarily responsible for the construction and validation of the pH model, including the collection of literature data for its construction, programming, and utilizing the model to guide and analyze studies. I performed literature review relating to the synthesis of silver nanoparticles in advance of the studies, attempting to identify the critical factors that would be worth investigation. I also performed approximately one third of the synthesis experiments, contributed significantly in the analysis of all results from synthesis experiments, took part in SEM microscopy sample preparation and imaging sessions, and was significantly involved in planning of recipes to investigate throughout the study. This includes the second and third round of recipes, which were selected based on the results of previous formulations.

4.1.2 Experimental Procedure

First, 0.68 g L-ascorbic acid (Alfa Aesar, 50-81-17) was dissolved into 200 mL H_2O. In another beaker, 1 mL of a poly-(methacrylic acid) sodium salt, 40 wt% solution in water (PMAA · Na) (Aldrich Chemistry) and 100 mL deionized water were mixed by gently shaking (Solution B). Then, 1.6 mL of this solution was added to ascorbic acid solution and mixed to prepare reducing solution (solution B). Then, 2.1 g of $AgNO_3$ (Sigma-Aldrich) was poured in a 500 mL beaker and 60 mL of $AgNO_3$ (except for recipe 9) added to it and gently sway the container to dissolve $AgNO_3$ and prepare the silver nitrate solution (Solution A). When the silver nitrate crystals disappeared, the solution B was poured into this 500 mL beaker. After five minutes (10 minutes for recipe 9 and 10), the synthesized silver nanoparticles were collected by Bchner funnel vacuum filtration.

For SEM observations, two minutes after synthesis (exactly before vacuum filtration), 500 μl of nanoparticles suspension was collected by a micropipette and added to a 3 mL of H_2O. This suspension was shaken for around one minute. 150 μL of this dilute suspension was poured on a clean silicon wafer and dried at 70 °C for SEM observation.

To measure transmittance of the solution during reaction, a photoconductive cell (Parallax Inc., 350-00009) and a LED (Lumex Opto/component Inc., SML-XL1110SOC-BTR) were used. They installed in two standard cuvettes (LIGHTLAB, C-6001) and the cuvettes

are fix in a way that the gap between the photodetector and LED was 5 mm. The setup was connected to a data logger to record the data. This setup was placed in the reactor and transmittance of the solution was measured every 5 ms.

Modeling

A predictive model of the pH developed throughout the silver reduction was constructed. The reacting mixture is assumed to be well mixed, and to be at pH equilibrium for every point of the reaction, where the equilibrium point will shift as the relative concentrations and activity of each contributing species changes throughout the reaction. It is also assumed that every species that is in the mixture throughout the progression of the reaction is contributing to the pH equilibrium without sequestration; which is to say that it is assumed that the adsorption of the PMAA by the silver surface has a negligible effect on its buffering capacity, and that the developed dehydroascorbate is stable on the timescale of the synthesis. Ionic strength, μ_I, is calculated as shown in Equation 4.1, where c_i represents the molar concentration of an ionic species, and z_i represents the absolute value of its charge. Counter ions related to the PMAA are considered to be localized near the polymer chain and do not contribute to the overall ionic strength, and the self-ionization of water was included in the model. Strong acids and bases are treated as fully dissociated. Ascorbic acid and PMAA $\cdot$ Na are weak acids expected to act as buffers, and both are expected to have their dissociation pK values influenced by the solution ionic strength μ_I. For ascorbic acid, Ball demonstrated that across the applicable range of total ionic strengths the Henderson-Hasselbalch equation is acceptable when the apparent dissociation constant is varied with ionic strength according to the equation proposed by Ball (Eq. 4.2), with a pK constant of 4.21 at zero ionic strength[184]. PMAA $\cdot$ Na is a polyelectrolyte, and was treated according to the Katchalsky model (Eq. 4.3)[185].

$$\mu_I = \frac{1}{2} \sum_{i=1}^{n} c_i z_i^2 \tag{4.1}$$

$$pK' = pK \; - \; 0.5 \sqrt{\mu_I} \, / \, (1 \; + \; 0.5 \sqrt{\mu_I}) \tag{4.2}$$

$$pH = pKa' \; + \; n \, \log \left((1 \; - \; a) / \, a \right) \tag{4.3}$$

For PMAA, Katchalsky and Spitnik reported analytical titration curves of across the range of interest, linearized independently for five ionic strengths[186]. The data presented in a figure by Katchalsky and Spitnik was digitized by image analysis, where it was assumed that distortions by rotation, stretch and shear were applied uniformly to the figure, and the axes were used for scale calibration. The resulting dataset was fit by a linear regression

of the form shown in Equation 4.4, to be performed on the full set of data[186]. This obtained the model constants presented in Table 4.1.

$$pH = A + B\sqrt{\mu_I} + (C + D\sqrt{\mu_I}) \log((1 - a)/a) \tag{4.4}$$

,

For accurate modeling of the PMAA · Na, the molar concentration and salt substitution of the polyacid needed to be determined. A specimen of the stock PMAA solution was carefully weighed into a cleaned and pre-weighed 20 mL glass scintillation vial, and dried under 32 in-Hg vacuum at 80 °C for 24 hours. Once dried, the vial was sealed and re-weighed, to determine that the stock solution contained 40.01 wt% dissolved PMAA/PMAA · Na. A 19 mg specimen of this dried material was then placed in a TA Instruments Q500 TGA, degraded at 10 °C/min to 700 °C under nitrogen, cooled to 390 °C, then reheated at 10 °C/min under air flow to 900 °C to drive off the carbon content, leaving only white ash. A molar analysis of the masses determined that the sodium salt substitution of the PMAA carboxylic acid groups was 86.86 mol%. This was treated in the model as 0.8686 mol NaOH strong base being added alongside each mol of PMAA.

To utilize the model, the user provided the ingredient amounts intended in the two reactants solutions, the ratio of the two solutions, and a list of desired degrees of silver conversion that the model equations are to be evaluated for. From these, the program calculates the total concentration of each species present at the degree of conversion being solved. The estimates of pH and the degree of dissociation of ascorbic and PMAA species were initialized at 12 and 0.5, respectively, and the initial ionic strength estimate is calculated. The program then solves for equilibrium pH at this degree of conversion by repeatedly alternating between recalculating the ionization strength and dissociation constants of each buffer species under the current species concentration estimates, and iteratively solving for the current pH estimate based on recalculations of the buffer dissociation from the last estimates of pH, μ_I, and dissociation constants. The pH was estimated based on the current estimated concentration of hydronium ions, obtained by summation of estimated concentrations for all hydrogen-dissociated species and subtracting the concentration of strong base. The convergence criteria used was that an acceptable pH estimate had been found for that degree of conversion when the difference between two consecutive

Table 4.1: Linear model constants for dissociation of Poly(methacrylic) acid

	A	B	C	D
Values	6.33324	-1.32015	-1.80890	0.37048
Linearized using:	X_1 $\sqrt{\mu_I}$	X_2 $\log((1 - a)/a)$	X_3 $X_1 X_2$	

pH estimates was < 0.001 and the difference between two consecutive μ_I estimates was < 0.0001, concurrently. Once converged, the model would recalculate concentrations based on the next degree of conversion, and reinitialize the estimates as before.

Using estimates from the above pH model, relative reaction kinetics were calculated for recipes 1-6, based on data reported by Kimura et al., and Moya et al, for the reduction of tris(oxa1ato)-cobaltate(III) by L-ascorbic acid[187, 188]. This makes the assumption that the pH and ionic strength scaling for the two systems is similar, and allows us to compare relative rates on an arbitrary timescale. In accordance with Kimura et al., the rate model equation 4.5 was used, where K_0 was dependent on pH and ionic strength, and calculated by equation 4.6 in the range of pH < 4.5. In accordance with the findings by Moya et al., K_0 was considered constant at K_0 = -2.69 for $4.5 <$ pH < 7.5. This relationship was found by comparing the two published datasets, and determining that Ionic Strength had an insignificant effect in the studied range.

$$\dot{\alpha}_{L-ASB} = k_0[AgNO_3][L - ASB] \tag{4.5}$$

$$k_0 = 0,42\,(pH) - 4.6 \tag{4.6}$$

4.1.3 Results

To investigate the effect of $AgNO_3$ / L-ASB molar ratio on the shape of silver supercrystals, six different recipes were selected (Table 4.2). Five replicates of each recipe were performed, both with and without the addition of balance water used to maintain constant final volume (4^{th} column of Table 4.2). The addition of water had minimal effect of the resulting nanoparticles, which otherwise exhibited repeatable morphologies specific to each recipe, providing ten replicates per recipe. Figure 4.1 demonstrates the synthesized nanostructures. Recipe 1 used a very low $AgNO_3$ / L-ASB molar ratio (0.05) which leads to ball-like nanoparticles, which are actually disordered clusters of very small structural blocks (inset of Figure 4.1-a). Increasing the $AgNO_3$ / L-ASB ratio in recipe 2 changes the supercrystals to flower-shaped particles composed of short wavy ribbon-like structural blocks (inset of Figure 4.1-b). Recipes 3 and 4 produced small porous nanosheets of silver (Figure 4.1-c and d). Inset image of Figure 4.1-d reveals the thickness of the sheets is about 25 nm. Finally, high $AgNO_3$ / L-ASB molar ratios in recipes 5 and 6 produced one-dimensional silver nanobelts (Figure 4.1-e and f).

Careful examination of the SEM images of Figure 4.1 reveals a clear trend in the synthesized nanoparticles. Recipes 2 through 6 produced nanostructures composed of short nanobelt segments that have undergone a second stage of assembly with a progression in preferred joining site. Recipe 2 displays extensive joining along all segment faces, producing

flower-like clusters. Recipes 3 through 6 display joining that is highly selective to the narrow edges of the short segments. This progresses from long-edge-to-long-edge "lateral joining dominating (recipe 3), to tip-to-long-edge "branching joining dominating (recipes 4 and 5), with tip-to-tip "linear joining becoming more frequent in the progression from recipe 5 to 6. This is either due to an increasing preference towards linear joining, or an increasing aversion to long-edge joining. Recipe 1 appears to be consistent with this progression, representing clusters of particles that have joined indiscriminately.

All recipes have the same initial ascorbic acid and PMAA concentration. What varies across recipes is the silver content of the final mixture. This is accomplished by adding differing volumes of 220 mM silver nitrate solution (Solution A). As the reduction reaction progresses ascorbic acid (weak) is converted into nitric acid (strong), lowering mixture pH. Therefore pH and molar ratio are correlated in these first six recipes. For this reason modeling work was carried out in an attempt to delineate the two effects, but failing that to help plan further experiments.

The primary effect of molar ratio is expected to be on reaction kinetics, which are also affected by pH[187, 188]. For each recipe, pH evolution versus reduction reaction progress was calculated using the proposed model (Figure 4.2-a). To examine the model accuracy, the pH of the reactor was measured for all recipes after reaction completion (Figure 4.2-b). As can be seen, very good agreement was obtained. Precise measurement of the pH during the reaction was not practical due to the response time of conventional pH meters. Using the pH model results and data from Kimura et al., and Moya et al it is possible to estimate the relative reaction rates for each recipe (Figure 4.2-c)[187, 188]. This allows us to assume that the pH and ionic strength scaling for the reduction of Ag^+ is similar to that tris(oxalato)-cobaltate(III) , and thus compare relative rates on an arbitrary timescale. In examining Figure 4.2, it is apparent that both pH and reaction rate change monotonically across recipes 1 to 6. Had pH dominated, leading to a reversal in predicted rate, it would have been possible to rule out a rate effect and by extension direct molar ratio effects. As it stands, more experiments are necessary. Two observations of significance can be

Table 4.2: Recipes of the synthesis with different concentration of silver ion

Recipe	Solution A	Solution B	H_2O (mL)	$\frac{AgNO_3}{L-Asb}$
Number	220 mM $AgNO_3$	22 mM L-ASB + PMMA		mol/mol
1	1	200	59	0.05
2	5	200	55	0.27
3	10	200	50	0.53
4	20	200	40	1.00
5	30	200	30	1.60
6	60	200	0	3.20

made when the rates are integrated numerically to estimate relative reaction times as in Figure 4.2-d. First, due to a crossover in stoichiometric ratio though rates increase monotonically, predicted times do not. Second, though recipes 4 and 6 have very different rates they have similar times to completion as they are equidistant from the stoichiometry crossover point.

To distinguish between the effect of pH and $AgNO_3$ / L-ASB molar ratio on the morphology of the products, pH was adjusted by adding NaOH or HNO_3 to solution B (Table 4.3). Recipes 7 and 8 are predicted to have a pH above that of recipe 1 for the bulk of the reaction (Figure 4.3-a) and silver content identical to recipe 6. Recipe 9 has a pH closer to recipe 6 (Figure 4.3-a), but its silver content is identical to recipe 3. Figure 4.3-b to d show the SEM images of the nanoparticles synthesized. In recipe 7 (high initial pH) the product is wavy silver nanobelts and individual overgrown hexagonal and triangular silver particles (Figure 4.3-b). In recipe 8 (the highest initial pH investigated), assembly of the structural blocks was eliminated, allowing the silver to grow as individual particles (Figure 4.3-c). Low pH in recipe 9 resulted in a combination of wavy and straight one-dimensional silver nanostructures (Figure 4.3-d). Although the silver content of this recipe is almost the same as recipe 3, and the conversion time is most similar to recipes 4 and 6, the resultant silver nanostructure is most similar to recipes 5 and 6.

While performing the above studies, it was observed that the size of the silver nanobelts synthesized by recipe 6 is very sensitive to preparation method of the silver nitrate solution. To investigate this phenomenon, the results from two methods of precursor solution preparation were compared. In the first, silver nitrate was dissolved at the same concentration investigated thus far using 5 minutes of severe shaking, and the resulting solution used for synthesis. Figure 4.4-a shows the synthesized sliver nanobelts after severe shaking of silver nitrate solution. Comparison between Figure 4.4-a and Figure 4.1-d clearly demonstrates that shaking of silver nitrate solution is able to reduce the length of the synthesized silver nanobelts. On the other hand, it is reported in the literature that dissolution of the silver nitrate is not a simple one-step process[78], but that the silver nitrate dissolves through some intermediate stages such as silver trimers (Ag_3^{3+} and Ag_3^{+}) and these silver trimers can be considered as nucleation site for nanoplates[78]. Therefore, it can be hypothesized that silver trimers play the role of precursor for silver hexagonal and triangular nanoplates,

Table 4.3: Recipes of the syntheses adjusting pH using NaOH or HNO_3

Recipe	Solution	Modified reducing	solution	$\frac{AgNO_3}{L-ASB}$
Number	A (mL)	Solution B (mL)	Adjusted pH	mol/mol
7	60	200	5.70	3.20
8	60	200	7.40	3.20
9	10	200	1.85	0.53

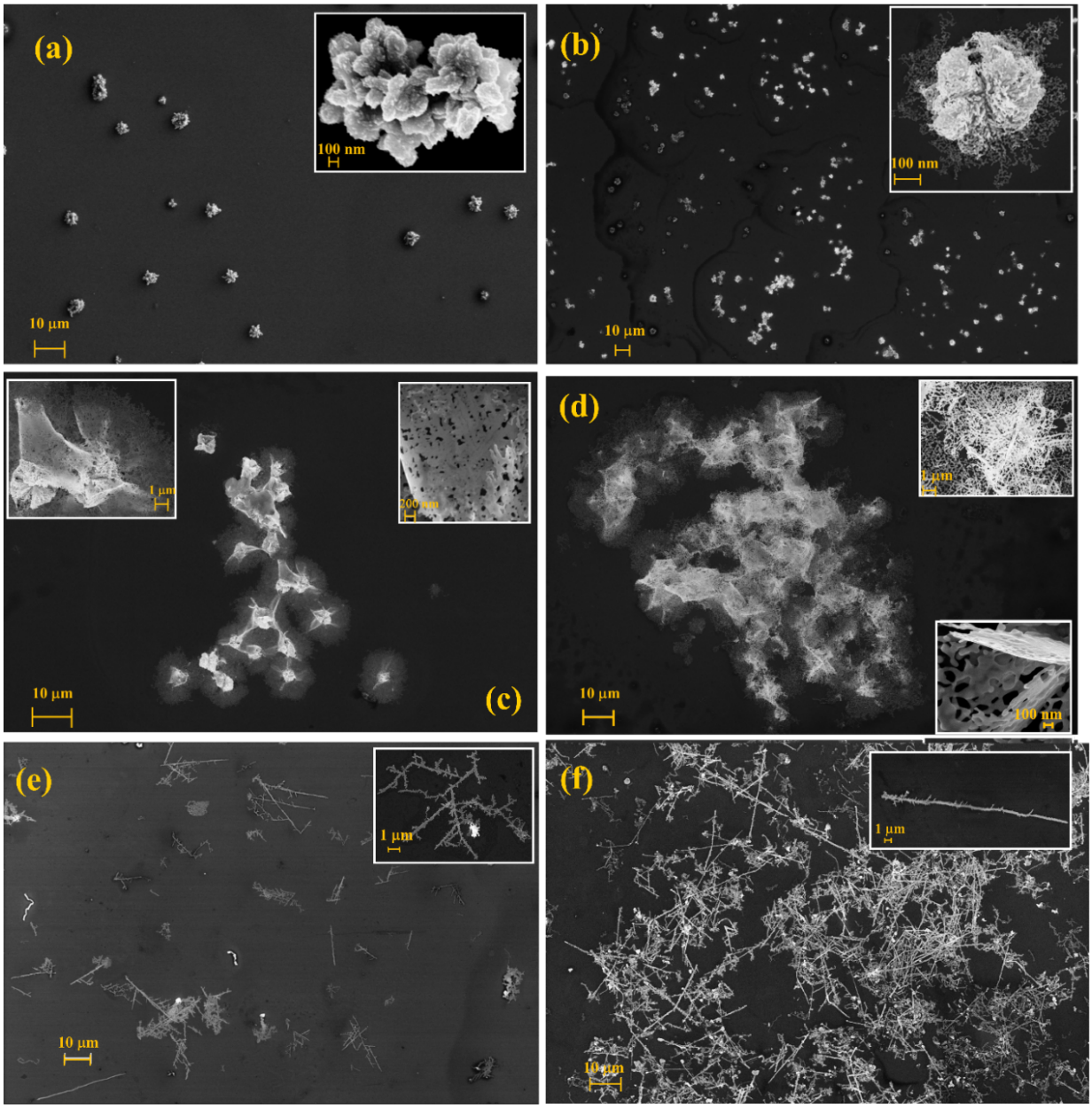

Figure 4.1: SEM images of the silver supercrystals synthesized by recipe 1 to 6 (a to f, respectively).

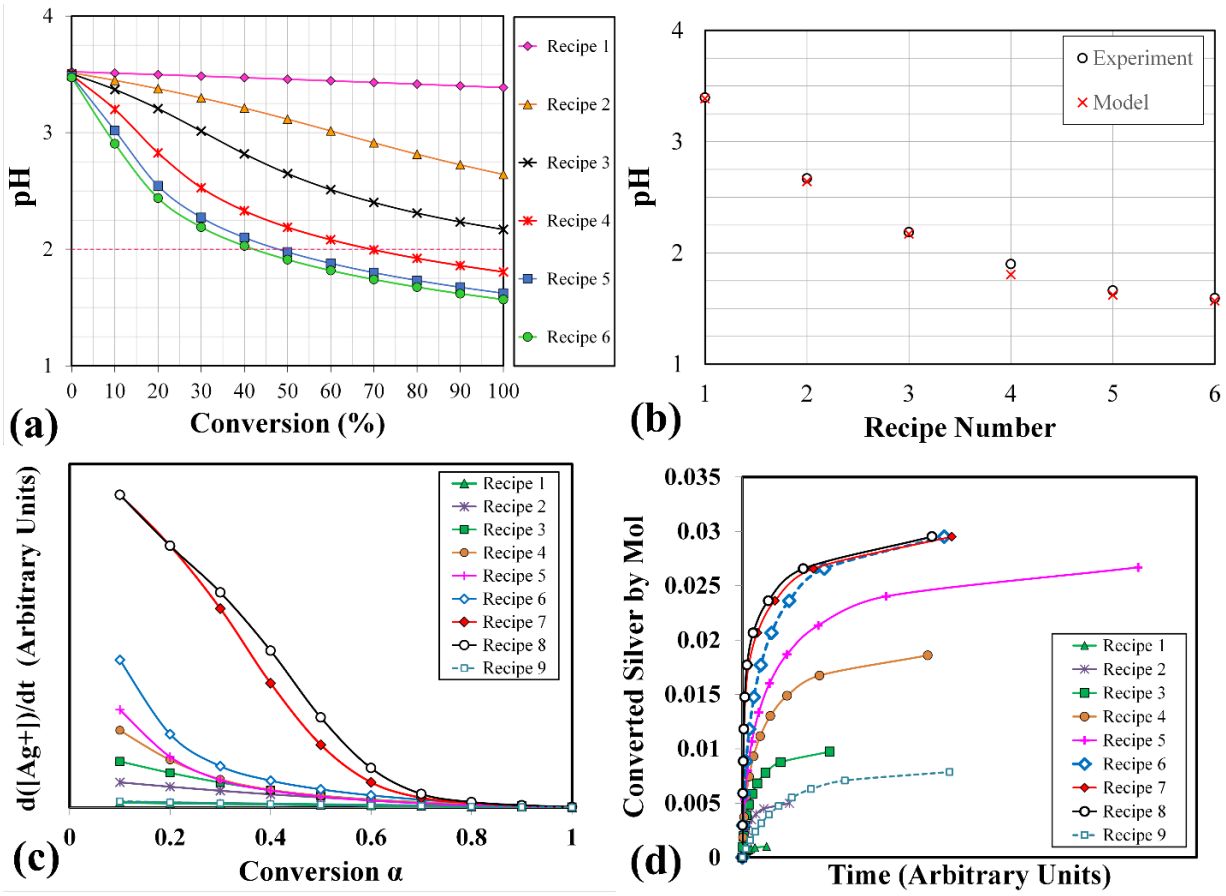

Figure 4.2: a) pH change during progression of synthesis redox reaction for recipe 1 to 6; b) Comparison between predicted final pH of the recipe 1 to 6 and experimental final pH; c) The reaction rate of recipe 1 to 9 versus conversion; d) Calculated molarity of silver converted for recipe 1 to 9 versus time.

and that aggressive mixing decreases the number of silver precursors available in the reactor. To examine this idea, the second precursor solution experiment was designed, recipe 10, in which 2.1 g $AgNO_3$ was slowly dissolved in 10 mL water by very gentle movement of the container to minimize mixing. The concentration of this solution is 6 times higher than recipe 6, and displayed two liquid phases, the denser of which was believed to be near the solubility limit. Under those conditions, it is likely that equilibrium reactions in the dissolution of the silver nitrate and silver timers means that the the silver trimers would be more stable than at lower silver nitrate concentrations, and therefore a greater fraction would survive until mixed with the reducing agent. To keep total concentration of the system same as recipe 6, 50 mL water was added to the reactor simultaneously with reducing solution (Table 4.4). Figure 4.4-b demonstrates the synthesized silver nanobelts and the inset of this image demonstrates the thickness of the nanobelts. The nanobelts synthesized

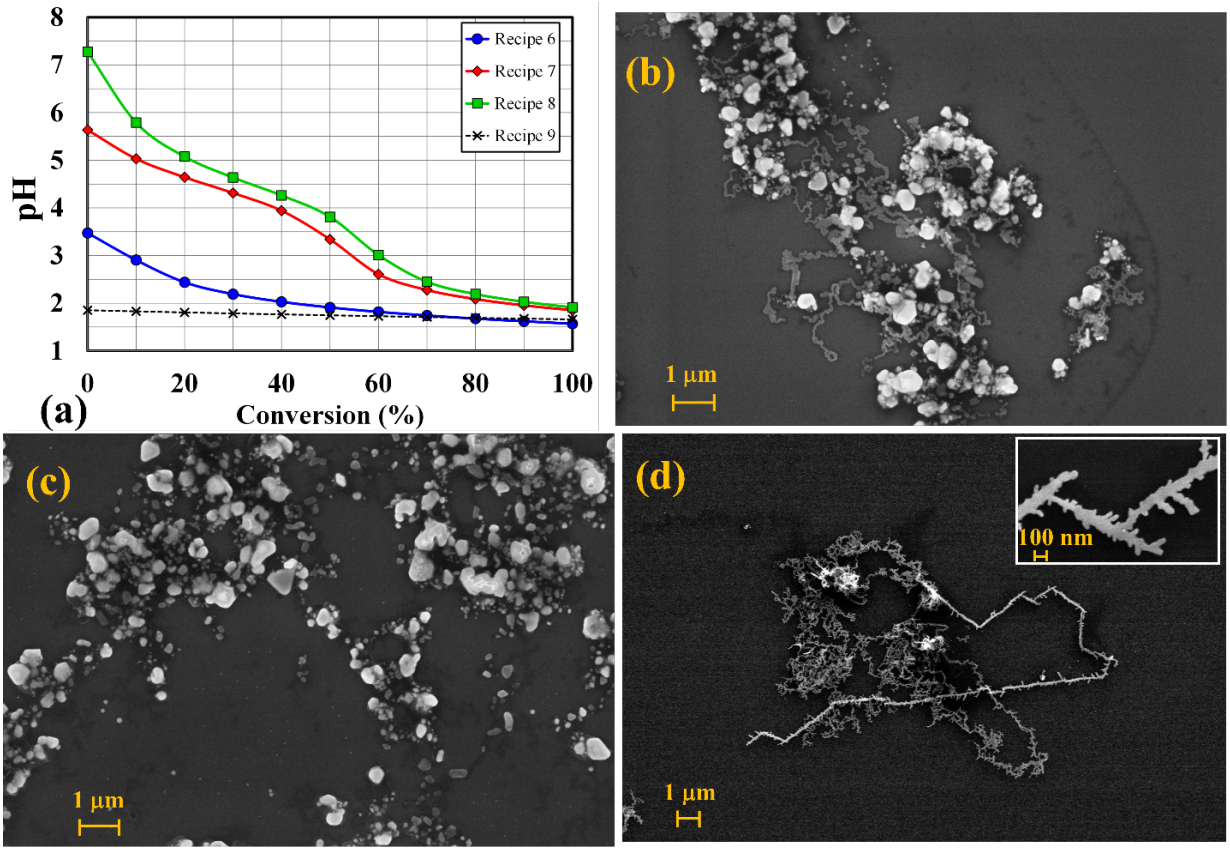

Figure 4.3: a) pH changes during synthesis of supercrystals by recipe 6 to 9; SEM image of the synthesized particles by pH manipulated in: b) Recipe 7; c) Recipe 8; d) Recipe 9.

by recipe 10 are much longer than recipe 6. Figure 4.4-c shows one of the synthesized nanobelts, which is around 95 μm in length. Insets of Figure 4.4 contain high-resolution views of two assembly locations, and confirm continuity of the nanobelt.

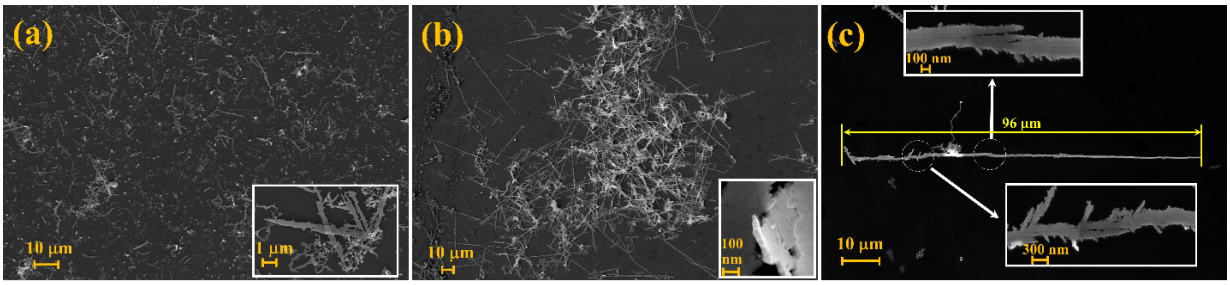

Figure 4.4: a) Short nanobelts, synthesized by recipe 6 by using aggressively shaken silver nitrate solution; b) Long nanobelts, synthesized by recipe 10; c) High magnification SEM image of a long belt-shape supercrystal synthesized by recipe 10.

Table 4.4: Recipe of the synthesis with high silver nitrate concentration

Recipe Number	Silver nitrate solution	Solution B (mL)	H_2O (mL)	$\frac{AgNO_3}{L-ASB}$ mol/mol
10	2.1 g $AgNO_3$ + 10 mL H_2O	200	50	3.2

It is noted that the differing reaction rates among the recipes were not negligible and can be visibly differentiated by changing color of the solution from a clear solution to black. Therefore, the optical transmittance of the solutions during synthesis was measured. The results of these measurements for recipe 6, 8, and 10 are presented in Figure 4.5. In addition, it was possible to record the changing pH of the solution during synthesis for recipe 10, due to its exceptionally slow reaction rate, and the results have been superimposed. Figure 4.5 demonstrates that the synthesis with recipe 8, in which the addition of NaOH raised the pH of the solution above the pKa value of the ascorbic acid and PMAA, displayed a reaction rate higher than recipe 6. More interestingly, recipe 10 has a very low reaction rate, even though the fully-mixed concentration, pH, and $AgNO_3$ / L-ASB molar ratio of these two recipes were similar. The only difference between these two recipes was higher concentration of the precursor silver nitrate solution, and the preparation method of this solution.

4.1.4 Discussion

Literature would argue that the type of nanoparticle growth and assembly observed here achieves varying morphologies through kinetically controlled processes[74, 103]. However, in this system the kinetics of the process was determined to not be the controlling factor. The reduction reaction appears to be the rate-limiting step, as evidenced by the agreement between light-transmission and pH data for recipe 10, and the general agreement between light-transmission and kinetic predictions for recipes 6 through 8. Based on morphology, recipes 6 and 10 were the most similar, and yet their reduction kinetics differ by orders of magnitude. Meanwhile, recipe 4 had a transmittance plot most similar to recipe 6, though the two display significantly different morphology. Similarly, recipes 9 and 10 were both observed to significantly deviate from their predicted kinetics due to long incubation times. Although they displayed similar incubation times and reaction durations, recipe 9 and 10 produced significantly different final morphologies. This insensitivity to kinetics appears to be why the repeatable synthesis of these nanostructures can be completed so rapidly. A working hypothesis on why the morphologies display such insensitivity to kinetics is that they each represent a local equilibrium under their experimental conditions.

Comparing the morphologies of recipes 1 through 6, 9, and 10, it can be seen that the progression in preference for lateral, branching, or linear joining correlates either with the

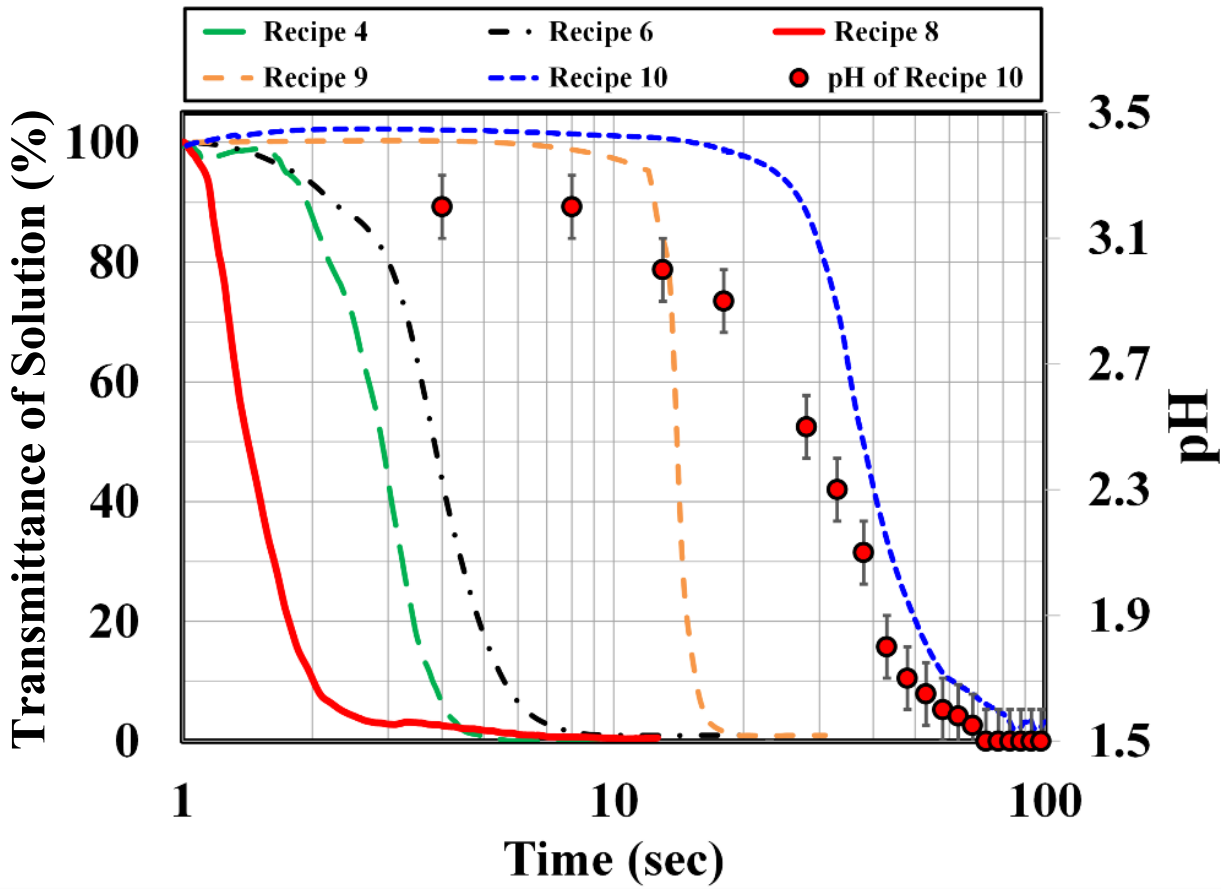

Figure 4.5: Kinetic of synthesis reaction measured by light-transmission for recipe 6, 8, and 10. Evolution of pH during synthesis by recipe 10 is superimposed on the graph. The presented pH data is the average of 6 replicates.

final pH or with the concentration of nitrate ions. Based on the constructed pH model, correlation with final pH may be due to the changing ionization of PMAA from 3% to 0.4% as the pH dropped from approximately 4 to 1.5. This is a relatively small change, and so this having such a significant effect would be surprising, though possible. This would be in agreement with published papers, in which the alignment and assembly of their particles was influenced by columbic interaction between the particles and effect of solvation forces in a collision recrystallization growth process[189–191]. These mechanisms were influenced by the geometry of their particles, and the local charges associated with them, generally agreeing with the pH sensitivity reported here. However, those studies were modelled with highly-idealized radially symmetric particle geometries representing simplified cases, and so more work would be necessary to verify this is applicable to the nano-structures studied here.

Another potential source of the pH sensitivity is the unreacted L-(+)-ascorbic acid,

which changes ionization from 19% to 0.3% across this pH regime as predicted by model. However, for most recipes investigated the lowering pH throughout the reaction is caused by the consumption of the ascorbic acid, in some cases to completion (recipes 6, 10). Therefore, another reasonable hypothesis is that it may be either the uncharged L-(+)-ascorbic acid or the dehydroascorbic acid product of the reduction that is involved in this process. From this data set, the correlation of the nitrate ion with the morphology cannot be ruled out; however, I do not have a hypothesis of a nitrate-controlled joining selectivity mechanism at this time.

It should be noted that Recipe 7 and 8 represent a different regime in the PMAA ionization. In recipe 7, where the high pH value produced initial PMAA ionization of 38% as predicted by the pH model, the majority of the silver is in the form of prismatic crystals, hypothesized to be overgrown primary structural blocks accompanied by limited quantities of assembled nanostructures. In recipe 8, where the PMAA initial ionization was 85% (calculated by model), the assembled nanostructures are absent. Therefore, highly ionized PMAA may be inhibiting assembly, due to charge repulsion between the coated silver nanoparticles.

There is an indication that the silver ion concentration may affect the length of the short secondary nanobelt segments prior to their final assembly, based on comparison within Figure 4.1. If this is the case, the trend may be related to the increasing concentration of primary silver nanoplates. However, silver content is partially correlated with the trend in linear joining, complicating analysis of the length of secondary segments. Recipe 10 displays exceptionally long and linear nanobelts, at the same silver concentration as recipe 6, and differs only in the $AgNO_3$ dissolving procedure. The long reaction time of recipe 10 may indicate a change in the nucleation characteristics caused by this gentle mixing, believed to be an increase in the number-concentration of the silver trimer seeds and correspondingly a decrease in the availability of the silver ions for reduction by the L-ascorbic acid. It is believed that this has impacted the manner in which the primary nanoplates assemble into the secondary nanobelt segments, leading to a smaller number of longer secondary segments which, in turn, are able assemble into the achieved very long and linear tertiary nanobelts.

4.1.5 Summary

Repeatable and fast synthesis of one- and two- dimensional silver nanostructures, constructed from highly stable hexagonal and triangular nanoplates, has been achieved by controlling the reactant concentrations and handling. It was found that the primary nanoplate structural blocks will assemble into secondary 1-dimensional belt-shaped segments, followed by secondary assembly and joining into various larger scale tertiary structures. The selectivity of preferred joint locations during this secondary assembly directed the development of the final morphology. It was also demonstrated that these are not kinetically controlled

processes, and that the selectivity of joining location during secondary assembly correlated with pH and the concentration of nitrate ions in solution. There were some indications that the concentration of silver ions correlated with the developed length of the secondary belt segments, however this was correlated with the factors that also selected for more linear secondary assembly modes, complicating analysis. Altering the methods used to dissolve silver nitrate in the precursor solution resulted in notable improvements to nanobelt linearity and size compared to earlier methods, and so nanobelts produced by these means are now considered "Generation 2" nanobelts.

4.2 PMAA Capping Agent Influence on Synthesis Assembly and Morphology

4.2.1 Overview

As discussed earlier in Sections 2.4, silver nanobelts are part of a family of 1- and 2-dimensional nanosilvers, all synthesized through the same general reduction of $AgNO_3$ by L-Ascorbic acid in the presence of PMAA capping agent *via* the exothermic melding of the contact faces when they are not yet adequately protected by the accumulating PMAA capping agent. Section 4.1 demonstrated that this site selectivity, and thus the final particle morphology, is sensitive to reaction mixture pH. The physical mechanism involved in this pH sensitivity is not well understood, and the experiments in Section 4.1 did not vary the concentration of PMAA.

Section 4.2 presents a study to investigate the influence of PMAA concentration during nanosilver synthesis on final morphology, and are adapted from a research abstract and poster presented at the 3^{rd} International Conference on Nanojoining and Microjoining. That abstract and poster was co-authored by G. Rivers (presenter), P. Lee-Sullivan, and B. Zhao.

In this work, the PMAA capping agent concentration in the synthesis mixture was varied, to investigate the resulting morphology and extent of synthesis joining. It was determined that the PMAA concentration and pH act as counter-factors, having opposite effects on the morphology, and provide arguments that it is the pH-sensitive nature of the PMAA capping agent that produces the final morphology.

4.2.2 Experimental Methods

Nanosilvers were synthesized according to procedures modified from those previously reported in Section 4.1[2, 192]. Formulations were modified to adjust the molar concentration of the PMAA capping agent in the final synthesis mixture, with the planned formulations

listed in Table 4.5. Concentrations were selected below the range where PMAA has an effect on the pH, based on model simulations using the same pH model as was reported in Section 4.1.

Formed nanobelts were dispersed in water at reduced concentration and dried on clean silicon substrates for SEM imaging. SEM imaging of was performed in a Zeiss Leo 1530 field emission SEM at 10KeV and a JSM 6460 SEM (CFI) at 10KeV.

4.2.3 Results

Figure 4.6 a-d) presents the variant morphologies developed as PMAA content increases, all displayed at the same scale. The typical nanobelt synthesis is performed at 2.9 mM PMAA (Fig 4a). There is no significant change in morphology using 4.0 mM (Figure 4.6 b). It is notable that the 4.0 mM formulation dispersed more poorly than the 2.9 mM composition, as did the 9.0 mM formulation.

At higher PMAA concentrations the nanostructures become smaller and far less linear (Fig. 4.6 c), with a greater frequency of the long-edge-to-long-edge "lateral joining and to tip-to-long-edge "branching joining occurring during the site-selective secondary assembly. The developed clusters are relatively small, implying an early end to the joining process compared to formulations with lower PMAA concentrations. At even higher concentrations, the clusters are disorganized "nano-granola clusters (Fig. 4.6 d), implying limited joining, and a disorganized site-selection.

4.2.4 Discussion

Previous work, discussed in Section 4.1, demonstrated the nanosilvers differ based on the site-selectivity of the secondary-assembly stage of particle growth with respect to pH, as summarized in Figure 4.7. In the work presented here, site-selectivity was demonstrated

Table 4.5: Recipes of the synthesis with different concentration of PMAA while all other factors are the same as Recipe 6 Table 4.2

Formulation Number	Solution A 220 mM $AgNO_3$ (ml)	Solution B_x 22 mM L-ASB +X PMAA (ml)	PMAA Concentration In Final Mixture (mM)
PMAA-1	60	200	2.9
PMAA-2	60	200	4.0
PMAA-3	60	200	9.0
PMAA-4	60	200	14.2

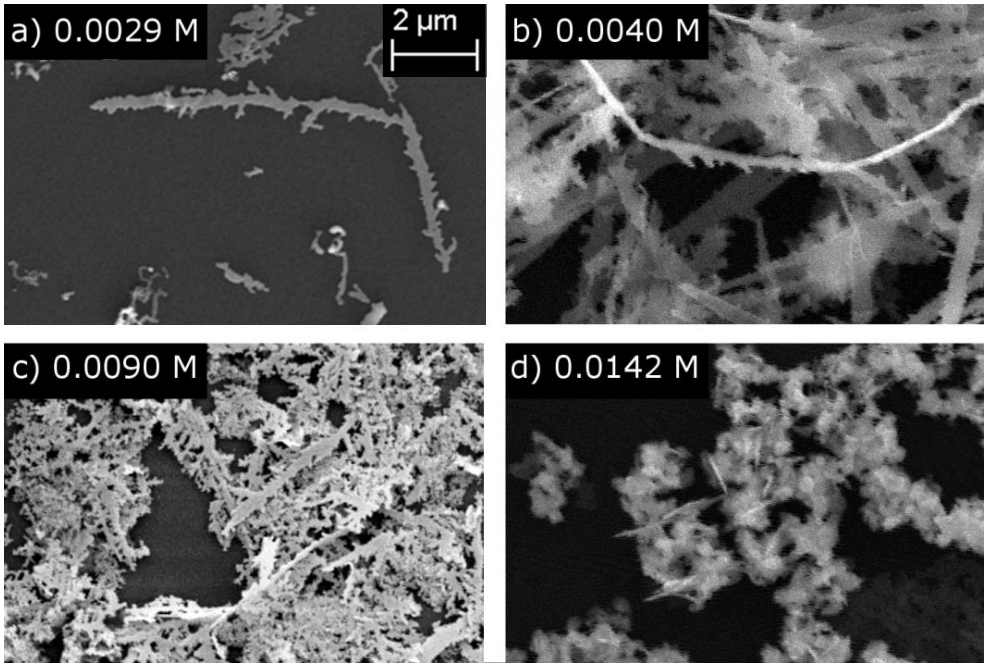

Figure 4.6: SEM Micrographs of nanosilver particles produced using different capping agent concentrations. Molarity of PMAA in final mixture is presented in insets. All micrographs presented at the same magnification.

to be altered by adjustments to the concentration of PMAA·Na, in an effect independent of the influence of pH.

Interestingly, the trend as PMAA increases was the opposite of that reported when pH was reduced in Section 4.1, as summarized in Figure 4.8. Increased PMAA appears to generally reduce the selectivity of the secondary assembly process, and also appears to reduce the extent to which joining during synthesis occurred. This implies that both the PMAA concentration and pH are capable of influencing the site-selection during secondary assembly, and perhaps the extent of joining, through some shared mechanism.

As a capping agent, PMAA governs the suppression of continued joining. As PMAA accumulates on the nanoparticle surfaces throughout the synthesis, the particle surfaces become increasingly protected, and eventually unable to join. This accumulation is thought to be through a combination of adsorption on the high energy nanoparticle surface, and by the coordination-bonding of the PMAA carboxylic repeat units on the nanoparticle surface[39, 193]. As discussed in Section 2.3.3 and in Chapter 4, PMAA is also a weak acid polyelectrolyte, and thus is sensitive to pH: as the pH lowers, the carboxylic acid groups of the PMAA repeat units become increasingly protonated, going from 3% dissociated to 0.4%. This holds true for the formulations with increased PMAA, since the experiments are performed in a concentration regime where the PMAA does not have the capacity to buffer the pH. This degree of dissociation should impact the ability for PMAA to bond to

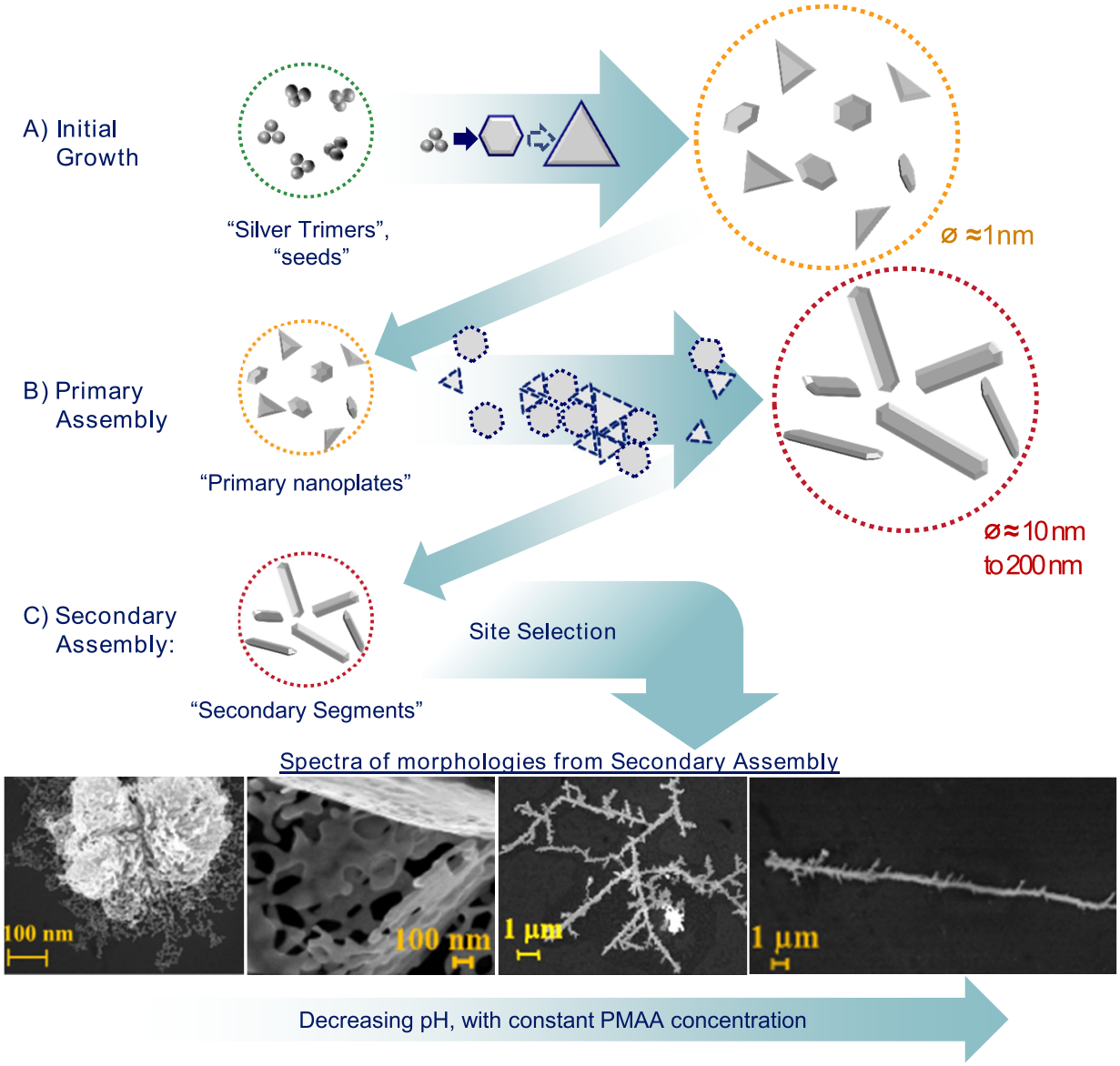

Figure 4.7: Summary of synthesis process of nanobelts and associated nanosilver family. A) Initial growth of silver nanoplates by PMAA-mediated classical crystallization. B) Assembly of nanoplates into small secondary segments. C) Assembly of segments into larger structures by site-selective assembly.

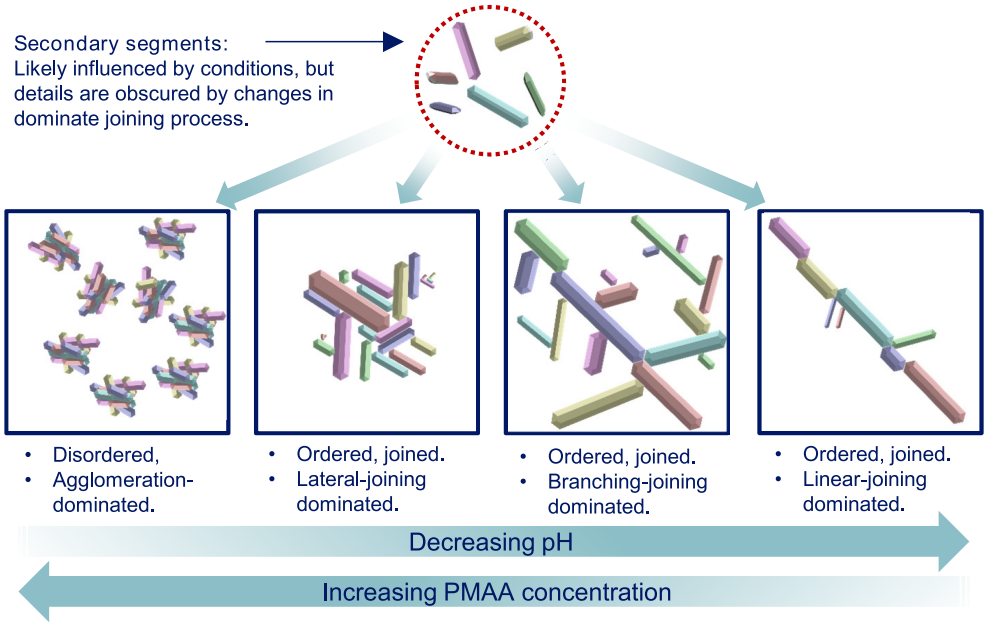

Figure 4.8: Simplified illustration of the influence that PMAA concentration and mixture pH have on the site-selective secondary assembly and final nanoparticle morphology.

the surface by chelation[39], or to interact with Ag^+ ions in solution. Similarly, work by Shiratori and Rubner demonstrated that the thickness of layers of polyelectrolytes, such as poly(acrylic acid) ("PAA"), are pH dependent, with lower pH producing a thicker layer through this mechanism[194].

However, the means of producing site-selectivity in the synthesis joining is unclear: why would PMAA prefer some surfaces over others for joining? Similarly, why would *increasing* the PMAA content produce an apparent *reduction* in site selectivity, if it were preferentially preventing certain assembly modes? It would seem that geometric aspects of the particle morphologies must be a factor as well, on the scale that the narrow tips and straight sides of the short secondary segments can differentiate from one another. Considering this is several times larger than a single PMAA chain, there must be some group-action or long-range mechanism.

One speculative explanation is an electrostatic charge-field built up on the nanoparticles during synthesis. Such a charge field would accumulate mostly at the sharp tips, and to a lesser degree at the straight edges of the nanobelts, due to the conductive nature of the silver. This would repel PMAA from those regions, with an effectiveness that would be based on the strength of the field and the concentration and degree of dissociation of the PMAA. This proposed mechanism is similar to the polyelectrolyte-mediated shape selection and mesocrystal assembly reported by Niederberger *et al.* and *et al.*, for ionic-crystals of $CaCO_3$[103, 195, 196]. An interesting note is that a source of this charge accumulation

could be PMAA forming insoluble salt complexes with Ag^+ ions, which would deposit on the nanoparticle surfaces leaving the charge to be balanced by ions in solution[39].

4.2.5 Summary

The multi-scale assembly during synthesis of silver nanostructures, including nanobelts, is sensitive to PMAA concentration and pH, as counter-factors to one another. This is reasonable due to the pH-sensitive nature of PMAA, and support from literature. Further research is needed to understand the physical mechanism of the PMAA's influence over the site-selective secondary assembly process and resulting final morphology.

However, the determination of the physical-chemical nature of the site selective behavior is beyond the scope of this thesis, and the results of this study provide further insight to the work performed in Chapter 4. With these results, synthesis can be performed to provide sufficiently consistent nanobelts for the studies in Chapters 5 and 7.

Future work that is suggested by these results include investigation of the physical mechanism of the site-selectivity of secondary joining, whether joining can be reactivated chemically at room temperature in aqueous solution, and the effect of varying the PMAA chain length on the developed nanoparticles.

4.3 Concluding Remarks

Investigations of the synthesis and behavior of nanobelts have been performed, and have characterized their behavior independent of a composite. Synthesis has been made repeatable and well understood, identifying the major factors controlling the synthesized morphology as mixing methodology ($AgNO_3$ concentration), pH, and PMAA concentration. This provides the capacity to synthesize sufficient quantities of silver nanobelts for the other planned studies. This study also provides proof that the PMAA capping agent accumulation on the surface is responsible for the control and cessation of room-temperature joining. The next chapter will present an investigation of whether this capping agent protection can be deactivated by heat treatment, similar to that discussed in Section 2.3.2, which may allow the nanobelts to continue their joining, which would be beneficial for device manufacture and ECA production.

Chapter 5

Diffusion-Free Joining of Deposited Nanobelts Resulting in Electrical Resistance Reductions

5.1 Overview

In Section 4.1, it was shown that the nanobelt synthesis occurs while the nanoplate and primary-segment surfaces are not yet fully protected by the accumulating PMAA capping agent, and that the nanobelt growth occurs *via* a very rapid room-temperature non-classical crystallization process similar to the results reported by Kim *et al.* and He *et al.*[72–74]. Prior to the complete protection by PMAA, the partially-effective PMAA still allows some quantity of joining to continue, leading to the site- and morphology-selective synthesis behaviors.

Similar to during synthesis, disabling or diminishing the capacity of the PMAA to protect the surfaces nanobelts after synthesis might allow joining to reactivate under favorable processing conditions, reducing the inter-particle contact resistance as discussed in Section 2.3.2. It is also hypothesized that the high stability of nanobelts will allow the protective PMAA capping agent to be disabled thermally, either by PMAA degradation or by increased PMAA mobility without activating the potentially detrimental diffusional mobility of the silver that was discussed in Section 2.3.2. Thus, it is further hypothesized that nanobelts are metastable, and that it is thermodynamically possible to reactivate their nanojoining to a degree that will sufficiently reduce the network resistance at low enough temperatures to be effectively implemented in conductive functional materials such as epoxy-based ECA nanocomposites.

Sections 5.2 to 5.5 present investigations of these hypotheses, and are taken from a manuscript published in the Journal of Nanotechnology, as listed in Table 1.1. That

manuscript is co-authored by G. Rivers, E. Marzbanrad, M. D. Hook, P. Lee-Sullivan, Y. N. Zhou, and B. Zhao[4].

In this work, *in-situ* methods are utilized to observe the effects of thermal annealing on electrical resistance and exothermic heat flow in nanobelts networks. The purpose is to identify whether the networks of highly-stable nanobelts will exhibit a tendency to join, thus reducing bulk electrical resistance at useful temperatures (< 200 °C). Very sparsely connected networks with high resistances have been selected, to ensure a large signal-to-noise ratio of resistance reduction from the joining process. The results demonstrate that observed reductions in network resistance are the result of temperature-dependent and time-independent exothermic oriented attachment of the nanobelts, occurring below the capping agent degradation temperature. To determine this, *in-situ* properties including electrical resistance measurement, calorimetry, and mass loss have been measured for different ramps and isothermal annealing conditions. Post-heating microstructural analysis was also conducted using microscopy.

5.2 Experimental Methods

Silver nanobelts were produced by the reduction of silver nitrate (AgNO3, Sigma Aldrich, ACS 99+%, 209139) in aqueous solution by ascorbic acid (L-(+)-Ascorbic acid, ACS 99+%, Alfa Aesar, 36237), in the presence of poly(methacrylic acid) (PMAA sodium salt, Sigma Aldrich, 674044 Aldrich) included as a capping agent. All water used was ultrapure deionized water (≥ 17 MΩ· cm). The water, reagents, and glassware were at room temperature for synthesis, which was recorded by k-type thermocouple to range between 20 °C and 25 °C. The formulation and synthesis method have been previously detailed by Marzbanrad *et al*[72]. The reaction time was consistently less than 2 minutes. After synthesis, the suspended product was collected by vacuum filtration onto filter paper (Whatman #5, GE Health Care and Life Sciences), mildly rinsing with deionized water. The collected nanobelt cake was dried in room temperature air, then stored in a desiccator at ambient pressure and temperature for a minimum of two days before further analysis. At this point, the dark grey dried nanobelt "cake can easily be separated from the filter paper by gentle peeling.

All differential scanning calorimetry (DSC) measurements were performed using a TA4600 modulated temperature differential scanning calorimeter. Specimens were prepared by first obtaining a small section of a nanobelt cake by gently breaking into small granules on weigh paper using the tip of a fine stainless steel wire. Care was taken to ensure the crumbling was performed by flaking and cracking of flakes, avoiding compaction of the granules. Approximately 5.5 mg (± 0.5 mg) of the resulting powder was then weighed into hermetically sealed aluminum pans (T131121 and T131219, TA Instruments) and encapsulated.

Dynamic temperature DSC experiments were conducted by heating from 20 °C to 300 °C using a modulation of ± 0.477 °C every 60 seconds and an underlying heating rate of 3 °C/min. Specimens were then rapidly cooled to 20 °C, and the first heating scan was repeated. The modulation in heat-only mode separates the reversing heat capacity (*Rev Cp*) from the non-reversing heat-flow signals, where the non-reversing heat-flow of both heating cycles was used for analysis.

Isothermal DSC studies were performed by heating the specimen from 20 °C to the set isothermal temperature (Tiso) using the same modulation and underlying heating rate as in the continuous heating studies. The specimen was then held at T_{iso} for a selected isothermal dwell time (t_{iso}), then cooled at 20 °C/min to 40 °C. The second heating of the sample was then performed to 300 °C using the same modulation and heating rate as before. The set of T_{iso} and t_{iso} conditions for this study are presented in Table 5.1.

Electrical resistance measurements of nanobelt thin-film coatings were performed *in-situ* to characterize the development of network conductivity during heating. Specimens were prepared by drop-casting sparsely percolated nanobelt networks onto experimental substrates. Nanobelts from dried nanobelt cake were dispersed by bath ultrasonication for 30 minutes (FS20, Fisher Scientific) in deionized water at a concentration of 0.4 mg/ml. Substrates were prepared from high-temperature laminate PCB prototyping blanks (Rogers Corporation R04835, 1 oz copper clad). Masked etching of the PBC blank removed a 7.5 mm wide strip of copper through the center of each slide to form two contact pads. The masking material was removed from the conductive contact pads by washing multiple times with acetone.

Substrates were washed with acetone, followed by washing with ethanol before drying in air. To deposit the nanobelt network, multiple additions of suspension were applied and dried. For each application 20 L of nanobelt suspension drop-cast by micropipette and gently spread using the pipette tip to form a rectangle. The slide was dried in room air while partially covered, and the process repeated until a desired surface coating developed.

Table 5.1: Isothermal treatment conditions for isothermal dwell studies of dry nanobelt coating

Treatment Name	Isothermal Temperature T_{iso} (°C)	Isothermal Time t_{iso} (min)	Square Root Iso Time $t_{iso}^{0.5}$ ($min^{0.5}$)
W	135	40	6.32
X	150	40	6.32
Y	135	160	12.65
Z	150	160	12.65

A slide coated with a nanobelt network using this method is shown in Figure 5.1(a). Photographs of each slide with a calibration scale were recorded to allow measurement of the deposited area by image analysis (ImageJ) for later calculation of the sheet resistance as described in Equation 5.1, based on the dimensions defined in Figure 5.1 (b). All samples were stored in a 35 °C convection drying oven (Binder FD53-UL) for at least 24 hours before being tested.

$$R_s = R_{2\Omega} \frac{W}{L} \tag{5.1}$$

Coated resistance slides were mounted inside the high-precision forced-convection furnace of a TA Instruments DMA-2980 Dynamic Mechanical Analyzer, and connected to both a K-type thermocouple and the measurement leads of a Keithley 2700 source-meter in auto-ranging 4-wire resistance measure mode. *In-situ* measurement of temperature and nanobelt network resistance was performed for dynamic heating and isothermal conditions. Dynamic experiments were performed from 30 °C to 190 °C at a heating rate of 1 °C/min. Isothermal experiments were heated from 30 °C to T_{iso} at 1 °C/min, held isothermal for a duration of t_{iso}, then heated to 190 °C at 1 °C/min. The isothermal treatment conditions used were W and X, as listed in Table 5.1. The temperature range used in the resistance study was limited by the maximum temperature of the resistance leads.

Thermo-Gravimetric Analysis (TGA) was performed to characterize the mass loss of the nanoparticles at elevated temperature using a TA Instruments Q500. Experiments were performed with approximately 15 mg specimens of nanobelt cakes in alumina TGA pans (T141229, TA Instruments). The specimens were prepared using the same crumbling process described in the production of DSC specimens. Specimens were heated from 30 °C to 500 °C at a heating rate of 5 °C/min under nitrogen atmosphere.

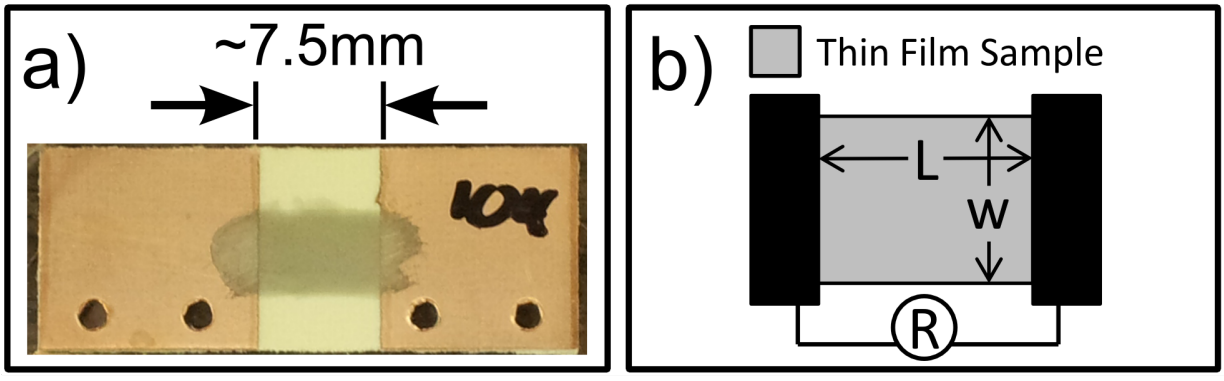

Figure 5.1: (a) Photograph of a typical resistance experiment slide with a coating of silver nanobelts across its center. (b) Schematic representation of the silver nanobelt network coated sample.

Scanning electron microscopy (SEM) was performed to observe the effect of annealing a specimen of dry nanobelt cake prior to dispersion. To prepare suspensions, two specimens were collected from the same cake: one was dispersed as-dried, while the other nanobelt cake was subjected to a heat treatment of 2 hours at 135 °C prior to dispersal. Both suspensions were prepared in acetone at a concentration of 0.4 mg/ml by bath ultrasonication for 30 minutes. For each, 20 l of the resulting suspension was dispensed onto the substrate and allowed to dry at room temperature. Substrates used were 1 cm square sections of P-type silicon wafer. These were cleaned in the following sequence: water, ethanol, then acetone, and dried in room air. A resistance specimen was imaged after coating with gold by plasma vapor deposition (Denton Vacuum Desk II, 120 seconds at 15 mA). SEM was performed in a Zeiss Ultra Plus at 10 kV.

5.3 Results

Figure 5.2(a) shows a representative SEM image of a sample of unaltered nanobelts that were dispersed in water from a dried cake by ultrasonication, then deposited onto a silicon wafer. This demonstrates that the nanobelts are easily re-dispersed after storage at room temperature in a dry state. Figure 5.2 (b) shows SEMs taken at the same magnification of a sample that was heat treated at 135 °C for two hours as the dried cake prior to ultrasonic dispersion and deposition. Clusters of material are visible in the heat-treated sample, implying the nanobelts had joined due to the thermal processing.

To monitor the nanobelt sintering/joining process, *in-situ* resistance measurements were made on a thin deposited layer of nanobelts, under constant heating conditions. For these studies, specimens were purposely produced to be sparsely connected to guarantee a high resistance, in order to aid analysis by maximizing the amplitude of the resistance change at the expense of the final conductivity. Two examples of the typical behaviour of the sheet resistance as a function of temperature are plotted together, with the average of the sheet resistances of six specimens, in Figure 5.3(a). SEM observation of Specimen I is presented in Figure 5.3(b), taken after the completion of the resistance experiment and showing the nanobelt network deposited on the rough surface of the composite test substrate, showing no apparent structures from diffusional sintering between nanoparticles.

Variation between specimens is likely due to small variations in the density of the deposited nanobelt coatings. In most of the silver nanobelt specimens the initial resistance exceeded the maximum detection limit of the source-meter (10 Mohm), and displayed a sharp drop in resistance as the temperature approached 100 °C. These are represented by Specimen II of Figure 5.3(a), which is representative of that group, but was selected for this figure because it exhibited the highest resistance of the specimens. Two specimens did not display this initial behaviour, and are represented by Specimen I in Figure 5.3(a). Specimen I is representative of the two specimens, but also represents the lowest resistance specimen

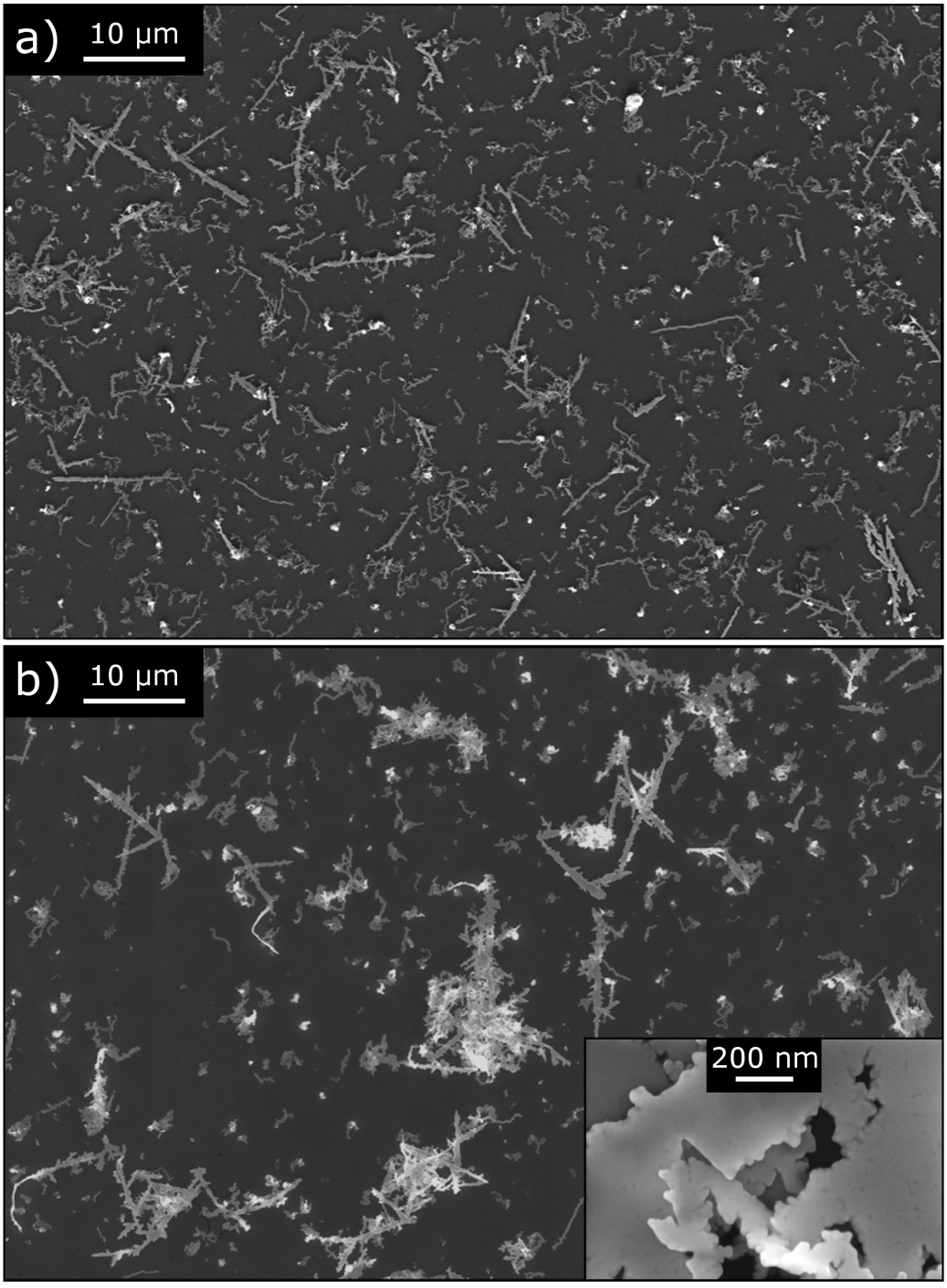

Figure 5.2: SEM images at the same scale, showing (a) nanobelts dispersed without annealing and (b) nanobelts dispersed after annealing for 2 hours at 135 °C. The inset presets a magnified view of the central cluster from (b), showing nanobelts in contact on their thinnest edges, and a lack of diffusional sintering beads.

observed. As such, Specimen I and II represent the envelope of observed behaviors, while being representative of other specimens within the envelope. As such the presented average is strongly influenced by Specimen II, but nonetheless is a fair representation of the average behavior of the observed specimens.

The initial drop in resistance, seen in specimens similar to Specimen II, is believed to be due to small amounts of residual water from specimen preparation drying upon heating. Therefore, the initial resistance drop from the highly variable drying behaviour is considered to be an artifact of the sample preparation. Similar resistance losses from drying of deposited nanoparticle networks were reported by Langley *et al*[92]. Between 110 °C and 180 °C, there exists a reduction in resistance such that the average sheet resistance at 180 °C is 5% that of the resistance at 110 °C, implying that the cluster formation seen in Figure 5.2 represents a joining process applicable to conductive networks. Interestingly, this dramatic drop in resistance is comparable to that reported by Langley *et al.*[92] for the diffusional sintering of silver nanowire networks, even though it was achieved here by a different joining mechanism, which will be discussed below.

DSC studies of the silver nanobelts were performed under modulated continuous heating conditions, to observe exothermal signals related to either joining or diffusional sintering processes expected for silver nanoparticles. The baselines for the scans were accounted for and the resulting normalized non-reversing heat flows were averaged together, as presented in Figure 5.4. The DSC reveals three exothermal peaks: Peak A spanning the 75 °C 200 °C range, and the overlapped Peak B and C spanning the 200 °C 280 °C range. Second heating scans did not detect any peaks, suggesting that the processes responsible for the peaks in the first scan had come to completion. Therefore, Peak A is thought to represent the exothermal heat of the joining process responsible for the network resistance drop across that temperature range.

For comparison, TGA was performed under dynamic heating, with the averaged data of three tests presented in Figure 5.5. The majority of mass loss from the nanobelts occurred between 200 °C and 350 °C, with an onset temperature of 195 °C. Only 15% of the mass lost occurs below 195 °C, and no apparent mass loss is visible below 150 °C. This mass loss corresponds with exothermal Peaks B and C from the DSC. Based on the literature[146], this appears to represent the first-stage thermal degradation of the PMAA capping agent into shorter chains of poly(methacrylic anhydride) (PMAN) through the release of methacrylic acid, water, and carbon dioxide. Therefore, the thermally-activated joining process captured in the resistance study and DSC Peak A is occurring below the PMAA degradation onset, implying that the joining is occurring as the protective capabilities of the capping agent decreases due to its increasing mobility with increasing temperature. This is similar to the behavior of a polyvinylpyrrolidone (PVP) capping agent during diffusional sintering studies reported by both Pashayi *et al.*[29] and Langley *et al.*[92], described as the PVP "melting, losing its stabilizing properties, and allowing the activation of diffusional sintering.

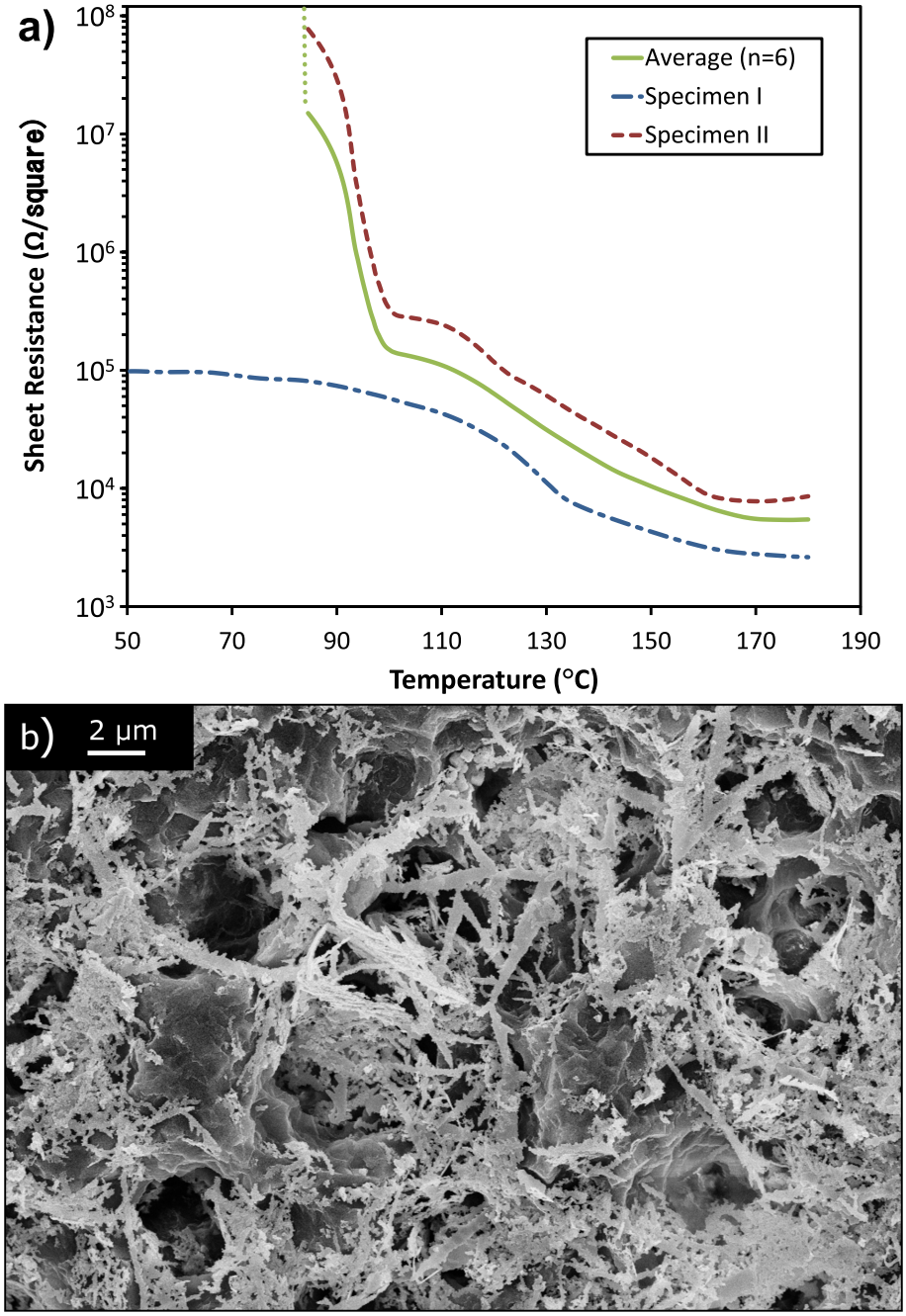

Figure 5.3: (a) Resistance vs temperature measurements for silver nanobelt surface coatings. Two specimens and the average of six are shown. In specimen II, the resistance below 90 °C exceeded the maximum detection limit of the source-meter. The average line starts at the highest temperature at which a specimen established a measurable resistance. (b) SEM of specimen I after continuous heating to 185 °C, displaying the nanobelts on the surface of a rough test slide substrate, with no signs of bead structures or degradation.

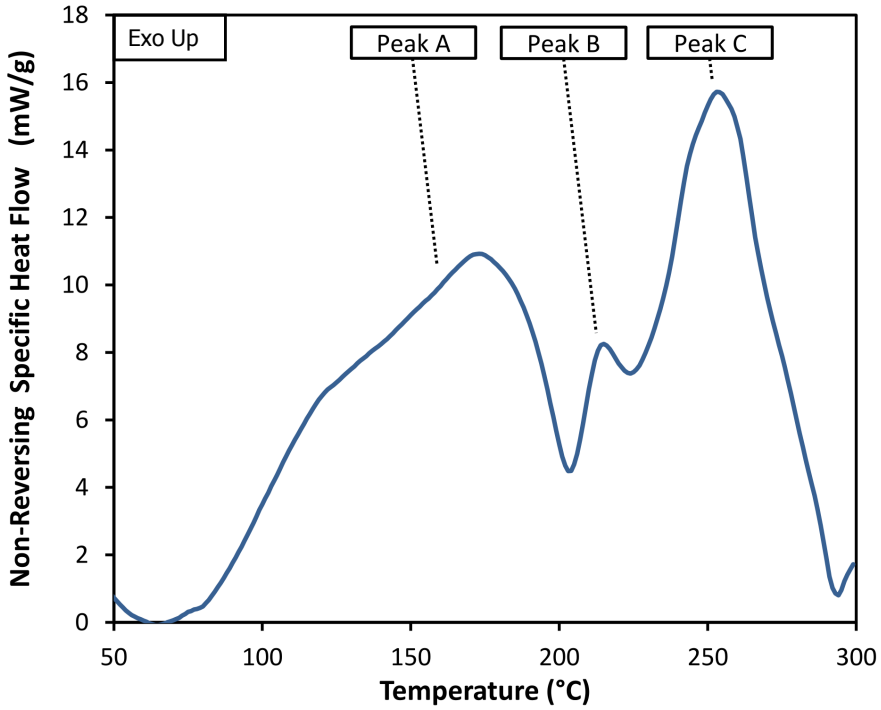

Figure 5.4: DSC plot of baseline-subtracted non-reversing specific heat flow for silver nanobelts. Note that the temperature scale is different than that in Figure 5.3(a).

To observe the time-dependency of the nanobelt joining process, which is related to the kinetics of the joining process, resistance and DSC experiments were repeated with the inclusion of isothermal segments. Due to the nature of these experiments involving a mixture of ramped heating and isothermal temperature modes, it is necessary to present the resistance and DSC data with respect to time, rather than temperature as before. Temperature versus time was also recorded, allowing the datasets to be correlated. Resistance versus time and temperature versus time were measured under the Treatment W and Treatment X conditions. An example of this is presented in Figure 5.6. Both temperature and resistance data were analyzed to obtain the onset times of the transition between the first heating and isothermal periods, and likewise for the transition between the isothermal and the second heating period ($t_{o1\,R}$, $t_{o1\,T}$,$t_{o2\,R}$, $t_{o2\,T}$, respectively). The average time lags between the temperature onset and the resistance onset at 1 °C/min ($t_{o1\,R}, -, t_{o1\,T}$ and $t_{o2\,R}, -, t_{o2\,T}$) for each treatment have been collected in Table 5.2. It should be noted here that the network resistance is expected to be very sensitive to the network connectivity near the percolation threshold, and therefore the low rate of resistance reduction during the isothermal period should represent a very low rate of increasing connectivity.[197] This highlights the sensitivity of the joining progression to the increase of temperature, as opposed to the temperature itself, though further analysis is difficult from this data alone.

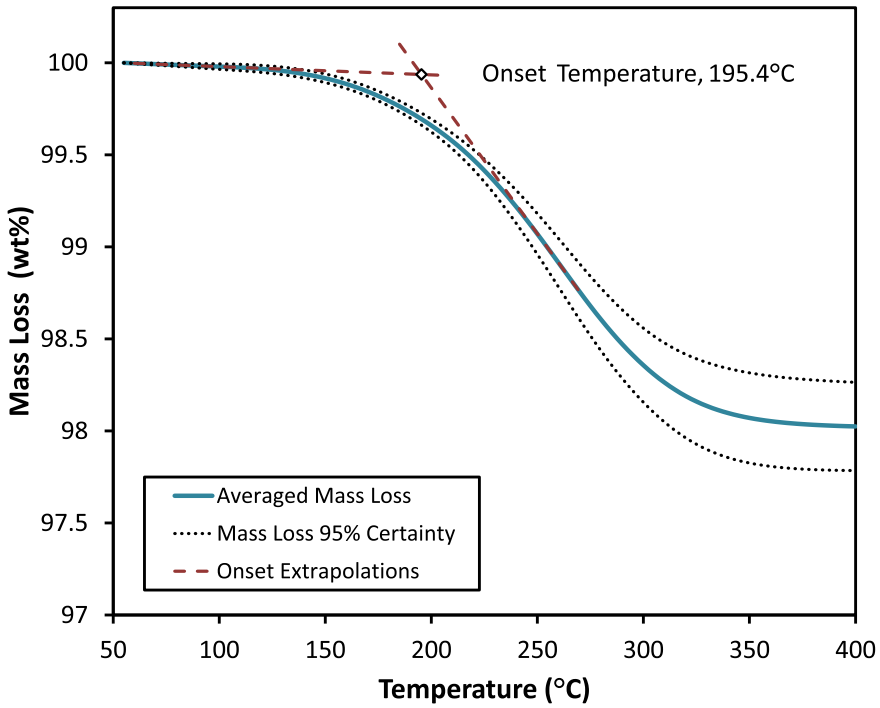

Figure 5.5: Average mass loss of silver nanobelts due to degradation during heating at 5 °C/min, as collected by TGA (n=3). Onset of degradation is 195.4 °C, with 15% of the mass loss occurring before the onset point. Note that the temperature scale is different than those in Figure 5.3 (a) and Figure 5.4.

Table 5.2: Average time lags between the temperature onset and the resistance onset for isothermal treatments W and X. Standard deviation observed is included in brackets.

Treatment	W	X
$t_{o1\,R} - t_{o1\,T}$	4.4 (3.2)	1.5 (1.3)
$t_{o2\,R} - t_{o2\,T}$	7.3 (3.6)	5.3 (2.4)

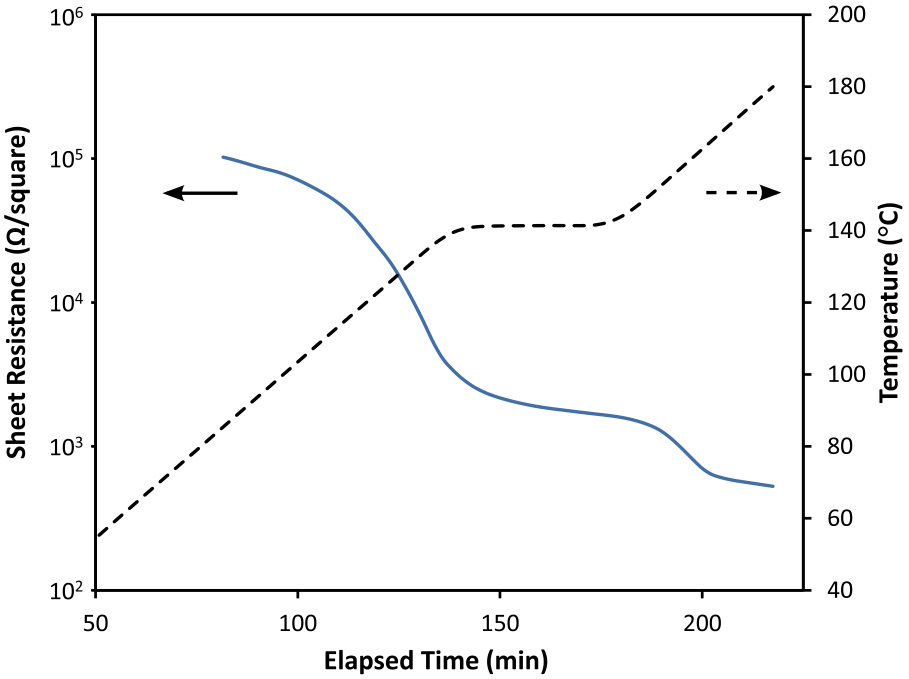

Figure 5.6: Sheet resistance vs time alongside temperature vs time for an example of silver nanobelt network coatings undergoing isothermal treatment X.

An example of the DSC data for one specimen is presented in Figure 5.7 (Treatment X from Table 5.1). Each of the DSC raw data segments (first heat ramp, isothermal soak, and second heat ramp) has a different baseline, and is separated by segments of noise in the data where the sample signal was overwhelmed by heat flow instability signals. These signals were produced by the DSC while it was performing transitioning processes such as equilibrating temperature, rapidly cooling, and establishing stable heating conditions. The transitional instability segments have been presented in grey, to distinguish them from the stable-operation data.

Figure 5.7 demonstrates that during the first heating regime, the exothermic signal of the joining process rises in agreement with earlier heat ramps. This will be referred to as the initial peak. When the isothermal condition is established the exothermal heat flow drops sharply and rapidly flattens out, even though the nanobelts are still at elevated temperature. The disruption of the DSC signal caused by the transition from heat ramp to isothermal mode prevents direct observation of the joining exotherm within the initial portion of the isothermal period, but the sharp drop in heat flow amplitude is apparent from the scan data.

While undergoing the second heating ramp to higher temperatures, the exothermic signal of the remaining joining process is rapidly detected as a relatively large residual DSC peak. This residual peak is of similar amplitude to that of the initial peak. This

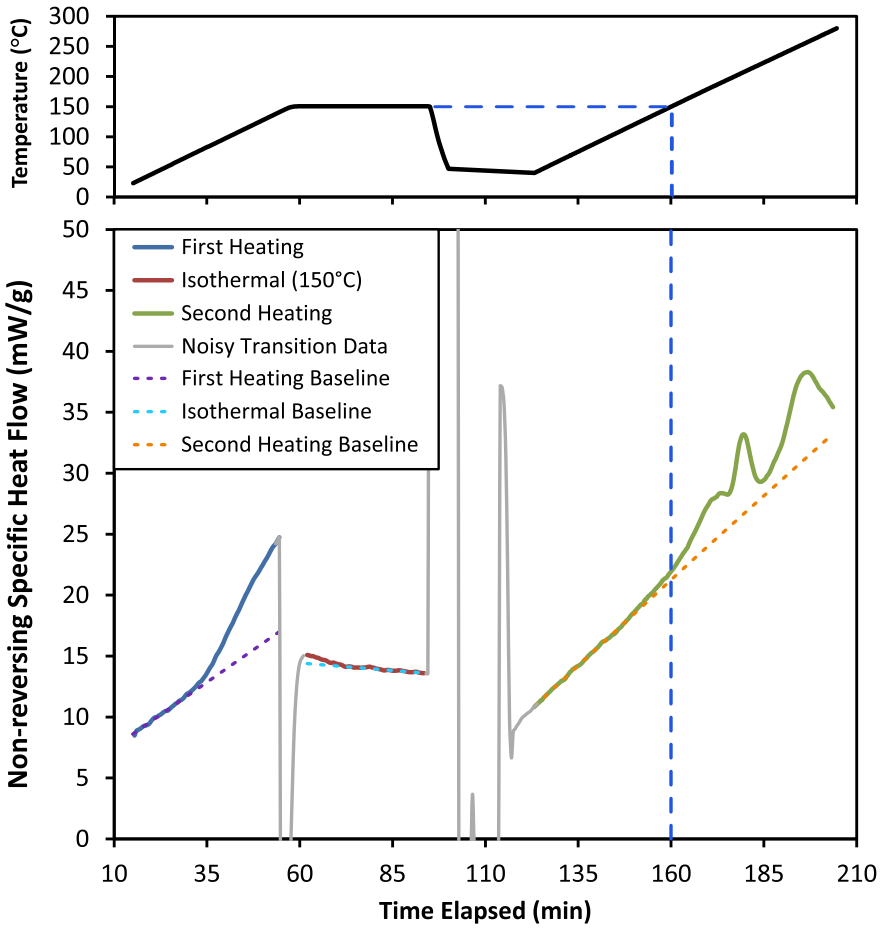

Figure 5.7: DSC heat flows and associated temperature vs time plots for an example of silver nanobelts undergoing isothermal treatment X. DSC segments containing noise due to heating mode transitions have been removed.

demonstrates that significant joining activity is still possible, in spite of the long isothermal soak at elevated temperatures. This and the above mentioned sharp drop in exothermal signal at the start of the isothermal period are significant, implying that the exothermic joining process has little in common with the known behaviour of diffusional sintering.

To investigate this further, all samples tested under the conditions described in Table 5.1 were analyzed to determine the onset temperatures of the second heating residual peak ($T_{o2\,DSC}$). The difference between this and the applied isothermal temperature (T_{iso}), was taken as a measure of the progression of the exothermic joining process during the isothermal period. Simply, the greater the value of the difference between $T_{o2\,DSC}$ and T_{iso}, the greater the progression of joining during the isothermal period. Those values are presented in Table 5.3, organized by treatment conditions from Table 5.1. The raw data was then pooled, and used for an ANOVA analysis of $T_{o2\,DSC} - T_{iso}$ with respect to treatment

isothermal temperature and time. The result found the progression of the joining was only temperature dependent (P=0.0016), and not time dependent (P=0.2115). The implications of this will be discussed below. Interestingly, the effect of increased temperature was to reduce the apparent progression of joining during the isothermal period, suggesting that as temperature was increased, the specificity of the temperature required for further joining to proceed also increased.

5.4 Discussion

Viewing all results together, it is clear that the dried network of surface-deposited silver nanobelts have undergone exothermic particle-particle joining via oriented attachment. This joining has achieved meaningful reductions in network sheet resistance, comparable in the temperature range studied (75 °C to 180 °C) and proportional reduction of resistance (95% reduction) as those reported in literature18 for pentagonal silver nanowires joining by diffusional sintering. The joining observed is identifiable as oriented attachment by lack of time dependency, as determined by statistical analysis of the isothermal data. This is supported by SEMs of the joined material containing no structures associated with diffusional sintering, such as necking or beads (Figure 5.3b). Unlike the diffusion processes at work in sintering, oriented attachment reaches completion very rapidly at each joint once activated[72], and then is expected to progress no further for that joint. Therefore, as observed in this work, under isothermal conditions the progression and rate of progression of oriented attachment would not be expected to be significantly influenced by time.

The literature has reported that unrestricted oriented attachment is a non-thermal process that can occur at very low temperature[69, 101, 102]. However, in this study, the total joining process of the nanobelt network is observed to be temperature dependent, and behaves as the superposition of a heterogeneous population of independent joining events each with a narrowly defined activation temperature. Therefore, there is a temperature-dependent energy barrier inhibiting the joining process. The PMAA capping agent is credited with inhibiting oriented attachment below the onset temperature of 75 °C, allowing dry storage and easy dispersion at room temperature. Degradation of the PMAA

Table 5.3: Average time lags between the temperature onset and the resistance onset for isothermal treatments W and X. Standard deviation observed is included in brackets.

Treatment	Average $T_{o2\,DSC}$ (°C)	$T_{o2\,DSC}$ T_{iso} (°C)
W	149.7	16.1
X	161.6	11.7
Y	153.1	16.95
Z	163.5	13.5

can be ruled out as the loss of protection, based on the lack mass loss observed in the joining temperature range (195 °C onset), from Figure 5.5. Noting that the mobility of a polymer at a free surface is significantly higher than in the bulk, the high bulk glass transition temperature of PMAA (225 °C) would not be applicable to the very thin capping agent layer[198, 199]. The protective capabilities of the PMAA are expected to be temperature dependent due to increases in the mobility of the capping agent with temperature. Once the mobility increases sufficiently at any particular site, the PMAA can no longer resist displacement, allowing oriented attachment[103]. As temperature is increased, the reducing protection would allow oriented attachment at sites with less favorable conditions. The random relative orientations of adjoining nanobelts are likely the source of the variation in the joining sites. Unlike the suspension conditions studied in the literature[102], under the dry conditions in this study these apparent misorientations cannot be easily resolved. Therefore it is believed that the observed temperature dependence is the result of interaction between the random relative orientations of the nanobelts and the temperature-dependent PMAA capping agent.

5.5 Summary

Silver nanobelts show potential as a highly stable alternative to pentagonal silver nanowires for high-temperature or long lifetime applications, without requiring higher processing temperatures to achieve a joined network. It is demonstrated that dry conductive networks of silver nanobelts can undergo inter-particle joining between 75 °C and 200 °C, achieving 95% reductions in the sheet resistance below 180 °C. This joining is identified as a form of oriented attachment, based on its time-independent behaviour under isothermal annealing conditions. The distribution of joining across the 75 °C to 200 °C range, and analysis indicating a diverse population of independent temperature-sensitive joining events, indicates that the nanobelt oriented attachment is being inhibited by the PMAA capping agent, until sufficient thermal energy is available to overcome an energetic boundary. It is believed that the distribution of joining temperatures within the nanobelt networks is result of an interaction between: 1) the reduction of surface protection by the PMAA as temperature increases due to increased polymer mobility; and 2) the variation in the initial condition of joining sites related to the randomly-oriented and mobility-constrained state of the nanobelts in the dried network. The 75 °C onset temperature demonstrates that at room temperature the PMAA capping of the nanobelts is sufficiently stable for dry storage and extensive handling, including dispersion.

5.6 Concluding Remarks

With proof from Chapter 4 that the PMAA is responsible for the control and cessation of room-temperature joining, it was then demonstrated that heat treatment between 80 °C and 180 °C is sufficient to deactivate the protective layer and reactivate the non-diffusional merging of the nanobelts. Provides proof of concept has been provided that nanobelts are capable of the < 200 °C joining behavior that is desirable in device manufacturing to reduce network sheet resistance, without reaching temperatures capable of activating destructive diffusion of the silver atoms. Later, in Chapter 7, this knowledge will be used to examine the behavior of silver nanobelts in a thermosetting conductive adhesive that cures within the range of temperatures that was demonstrated here to promote this beneficial joining.

Chapter 6

In-Situ Investigation of Conductivity Establishment During Cure of Silver-Epoxy Microcomposite

6.1 Overview

In Section 2.5.3, it was discussed that thermosetting conductive composites are known to often rely on the cure of the matrix to establish the conductive filler network through the contraction of the matrix throughout the cross-linking process[117]. Also, in Section 3.1, the analysis of the literature underscored the importance of a) baseline studies, b) awareness of solvent content in tested composites, and c) comparing measured properties to other measured properties within a composite to obtain internally supported analysis. Furthermore, based on the results of Chapter 5, it is known that the nanobelts join and reduce their network electrical resistance within the temperature range that epoxy cures, and it is hoped that a demonstration of this beneficial joining can be made in a prepared composite undergoing cure.

To that end, Chapter 6 investigate the change in conductivity throughout the cure of silver micro-flake filled composites. Preliminary results of this work were presented at the 2016 International Conference on Soldering and Reliability, and have been submitted to the associated Journal of Surface Mount Technology as part of a proof of concept publication for the custom *in-situ* probe. However, the majority of the data is as yet un-published.

In this work, I compare *in-situ* resistance measurements obtained by a custom mold-probe to the calorimetric heat flow and conversion data obtained *via* DSC. The intent was for this set of data to provide baselines of the approximately power-law change in conductivity of a curing microcomposite, based on expectations from the literature review of the subject, for comparison to nanobelt-containing compositions that will be presented later in Chapter 7. However, as will be discussed below, this analysis also obtained novel

results of an unexpected behavior midway through the cure process. This path-dependent disruption to the establishment of conductivity is related to the thermo-mechanical state of the composite throughout curing. This mechanism may be negatively impacting the final conductivities of conductive adhesives cured using multi-step pre- and post- cure methods, and therefore is significant to the scientific body of knowledge for ECAs, and significant to the practical industrial usage of ECAs. A review of the open literature has found no other reports of this repeatable behavior.

6.2 Experimental Methods

Cure of an epoxy-based isotropic ECA was characterized by calorimetry and electrical resistance measurement. These were performed simultaneously in two instruments using the same time-temperature heating procedures between the two devices. The simultaneous measurements were made on specimens of the same composite batch that had been cryogenically stored at -80 °C between tests and loaded simultaneously, to ensure the same thermal history and no significant differences in progression of curing until the test started. The time-temperature procedures used are listed in Table 6.1, where all heating was performed with the average heating rate of 1 °C/min.

Calorimetry was performed using a Modulated Temperature Differential Scanning calorimeter (MTDSC, TA Instruments TA DSC 2920). Multiple DSC specimens of freshly mixed composite batches were encapsulated in hermetically sealed aluminum pans then cryogenically stored. Heating of DSC specimens was performed with a modulation of ±0.159 °C every 60 seconds, with an underlying heating rate of 1 °C/min, to obtain the signals of reversing specific heat capacity (*RevCp*) and non-reversing specific heat flow. Conversion was calculated as degree of cure, α, the release of specific enthalpy at each point in time expressed as a fraction of the total specific enthalpy released over the cure process. Specific enthalpy was calculated as the integration of the non-reversing specific heatflow with baselines calculated and subtracted. Final glass transition temperature ($T_{g\infty}$) was calculated from the RevCp of the second heating performed after cure.

Table 6.1: Applied first-heating treatments for microcomposite cure-conductivity study

	Heating	Isothermal	Dwell	End
Treatment Name	Rate (°C/min)	Temperature (T_{iso}) (°C)	Time (t_{iso}) (min)	Temperature (°C)
Ramp	1	N/A	N/A	175
Iso 75	1	75	300	175
Iso 135	1	135	60	175

In-situ resistance measurements were performed in a custom-designed mold with in-laid 4-wire resistance probe, installed in a dynamic mechanical analyzer (TA Instruments 2980 DMA), used for temperature control, and electrical resistance measurements were recorded from a Kiethley-2400 source meter in automatic ranging 4-wire mode every 15 seconds. Specimens were dispensed into the mold from composite batches stored at -80 °C until testing. Non-electrical contact surfaces of the probe-mold are machined from Teflon, while the electrical components are standard gold-plated pins and receptacles. Geometry of the specimen mold, with in-set electrical probe connectors are presented in Figure 6.1, along with the applicable correction factor relationship. Geometry of the electrical components and a cross section of one probe contact point in operation are presented in Figure 6.2. An overview of the probe-mold assembly is shown in Figure 6.3. Sheet resistance was calculated based on Equation 6.1, where $C_{square} = \pi / \ln 2$ based on the ratio of pin diameter to pin spacing being $d_p/L = 0.069$ [143].

$$\rho = t_s \, R_s = t_s \, (C_{square}) \, \frac{V_{3,4}}{I_{1,2}} = t_s \, (\frac{\pi}{\ln 2}) \, \frac{V_{3,4}}{I_{1,2}} \tag{6.1}$$

Based on Equation 6.1 and the range vs resolution behavior of the source-meter, the sensitivity vs range for this probe is plotted in Figure 6.4, in terms of sheet resistance. Potential sources of error of this probe comes primarily from inhomogeneity and anisotropy: alignment of the fillers, regions deficient in fillers, large voids from entrapped air, or substantial variations in thickness will distort the electric field, potentially altering the R_{obs} by violating these assumptions.

Another potential source of systematic error is poor or intermittent contact between the probes and specimen, potentially varying with temperature due to the cure shrinkage

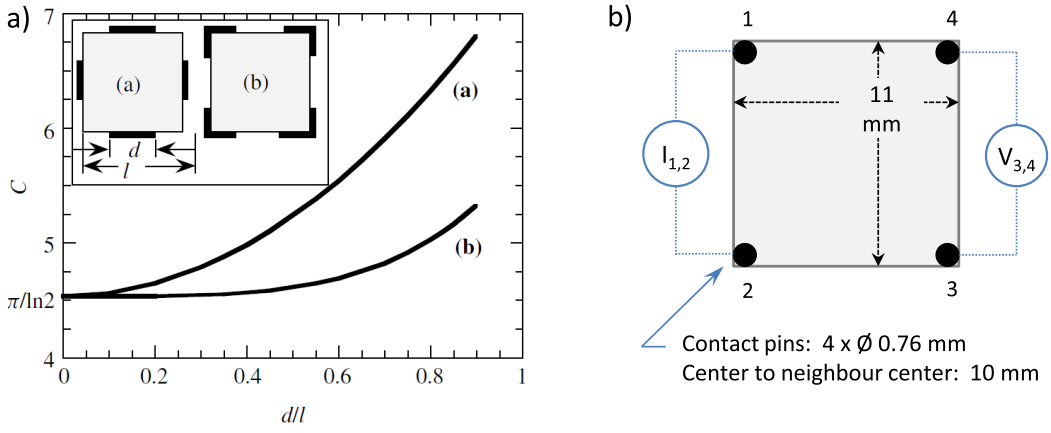

Figure 6.1: 4-Wire probe and specimen geometry. a) Configurations and associated C_{square} correction factors, presented with permission from reference [143], and b) Pin-and-specimen geometry used for this probe design.

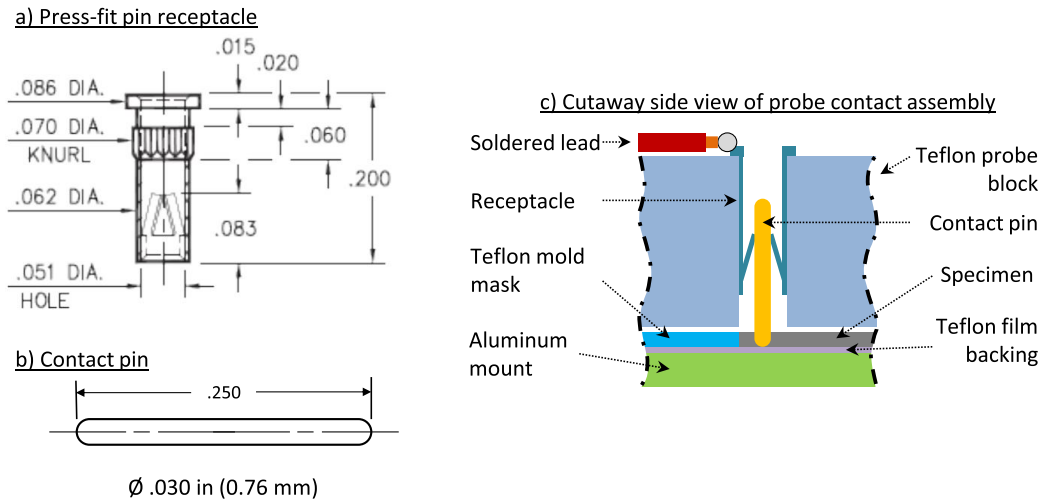

Figure 6.2: Components used in 4-wire probe. a) Press-fit pin receptacle, b) electrical contact pin, c) cut-away side-view of assembly of electrical contact components and teflon body and mold components. Receptacle schematic provided for public use by manufacturer.

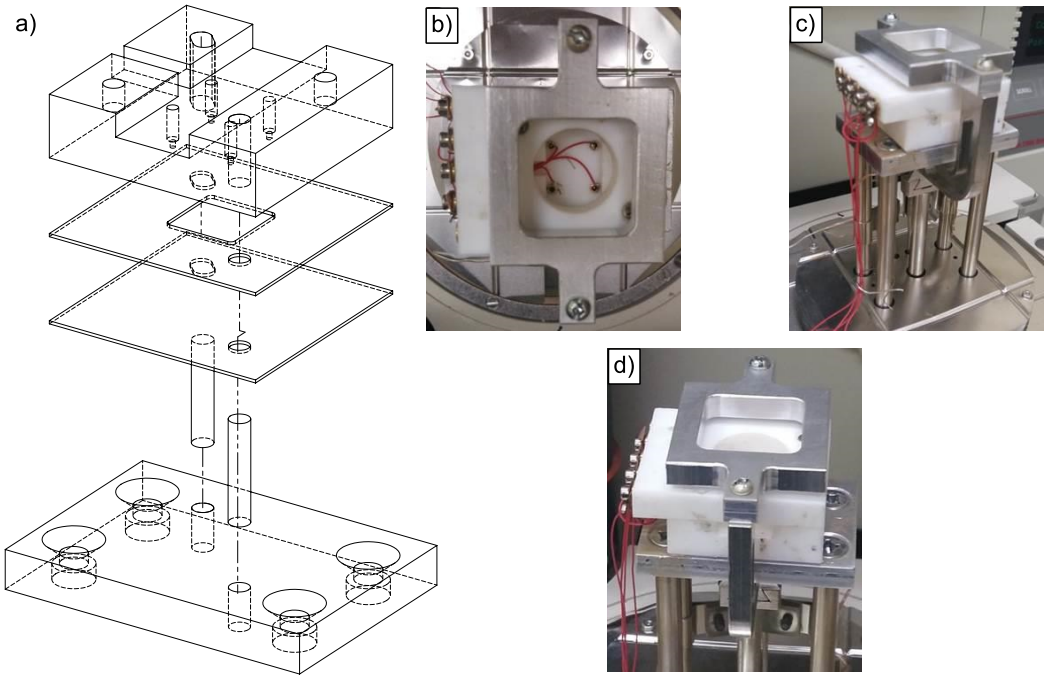

Figure 6.3: Diagram of designed probe. a) Exploded assembly view of designed probe-mold, b) top-view of assembled real device mounted in DMA, b) isometric view, c) side view.

or probe thermal expansion. This is unlikely: when the specimens were removed from the mold the pins were still adhered to and embedded inside the sample, demonstrating a well-developed physical connection (see Figure 6.5).

Four composites were investigated, consisting of 60 wt% (169.5 *phr*) silver microflake (327077, Sigma-Aldrich) dispersed in DGEBA epoxy (Dow D.E.R. 331) hardened by 13 *phr* triethylenetetramine (TETA, Dow D.E.H. 24). Compositions differed with regard to the solvent concentrations added, listed in Table 6.2. All *phr* values are presented as "per 100g neat resin". The desired ethanol addition was incorporated with the resin in advance by vortex mixer, and left to sit at room temperature overnight to simulate epoxy compositions that contain small quantities of reactive solvents as an industrial impurity. Silver microflake (and any desired acetone) was weighed into the resin together, and thoroughly dispersed by a planetary centrifugal mixer (Thinky ARE-310) at 2000 RPM for 5 minutes. The mixture was cooled to room temperature, then hardener was incorporated using the same mixing conditions. To minimize curing before experimentation, the glass vial of mixed composite was immediately placed in carrying container machined from an aluminum block, 11.5 cm^3 on a side, that had been pre-cooled to -80 °C and insulated. This rapidly chilled the specimen while it was transferred to the -80 °C storage freezer and stored until further use.

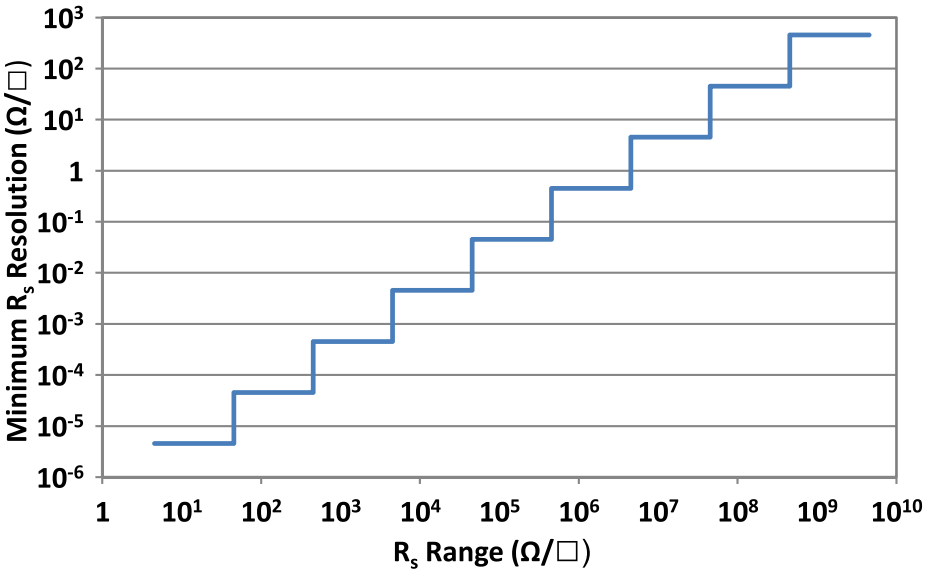

Figure 6.4: Plot of range vs resolution of Rs for Probe-Mold.

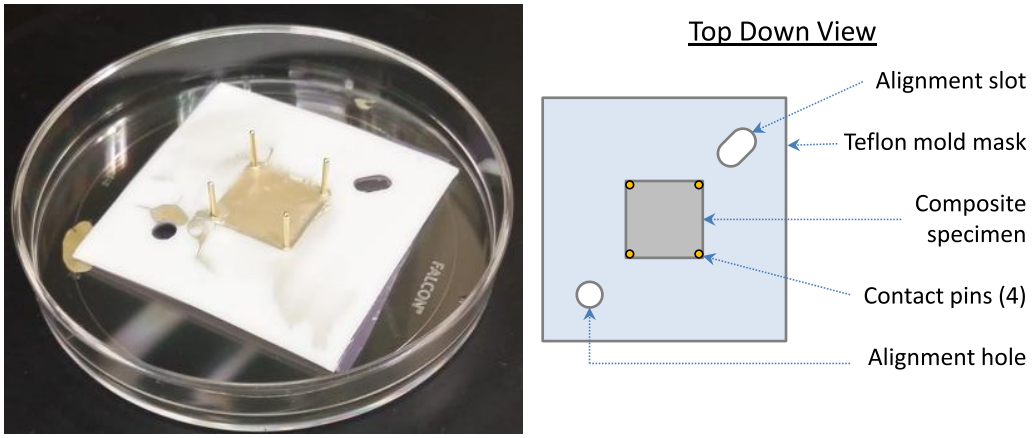

Figure 6.5: Photograph of specimen after cure in probe mold, with top-down view of arrangement of specimen, pins, and Teflon mold mask.

Table 6.2: Prepared Microcomposite ECA Compositions

Composition Label	Silver Wt% / *phr*	Acetone *phr*	Ethanol *phr*	TETA *phr*
Ac0	60 / 169.5	0	0	13
Ac3	60 / 169.5	3	0	13
Ac2E1	60 / 169.5	2	1	13
Ag90	90 / 1017.0	0	0	13

6.3 Results

A typical non-reversing heat flow data from MTDSC, during continuous heating for the solvent-free "Ac0" composition, is displayed in Figure 6.6 a). Figure 6.6 b) presents the corresponding degree of conversion, annotated with $T_{g\infty}$. Reversing specific heat capacity (*RevCp*) during cure is available from the modulated continuous heating program, and is cross-plotted with the conversion graph in Figure 6.6 b). This initial data was collected during development of the probe-mold for *in-situ* resistance measurements, and was originally published in a preliminary study focused reporting the probe development in the proceedings of ICSR, in review for publication in the Journal of SMT, republished here with permission[5].

The shape of the cure exothermal signal in Figure 6.6 a) is a single bell-curve with a shoulder between 75 °C and 125 °C. This corresponds to a segment of the conversion in Figure 6.6 b) that approaches a constant slope, and both correspond to a trough section of the RevCp, with all three features ending when the test temperature approached the $T_{g\infty}$. This demonstrates there was partial vitrification of the composite during cure, when the increas-

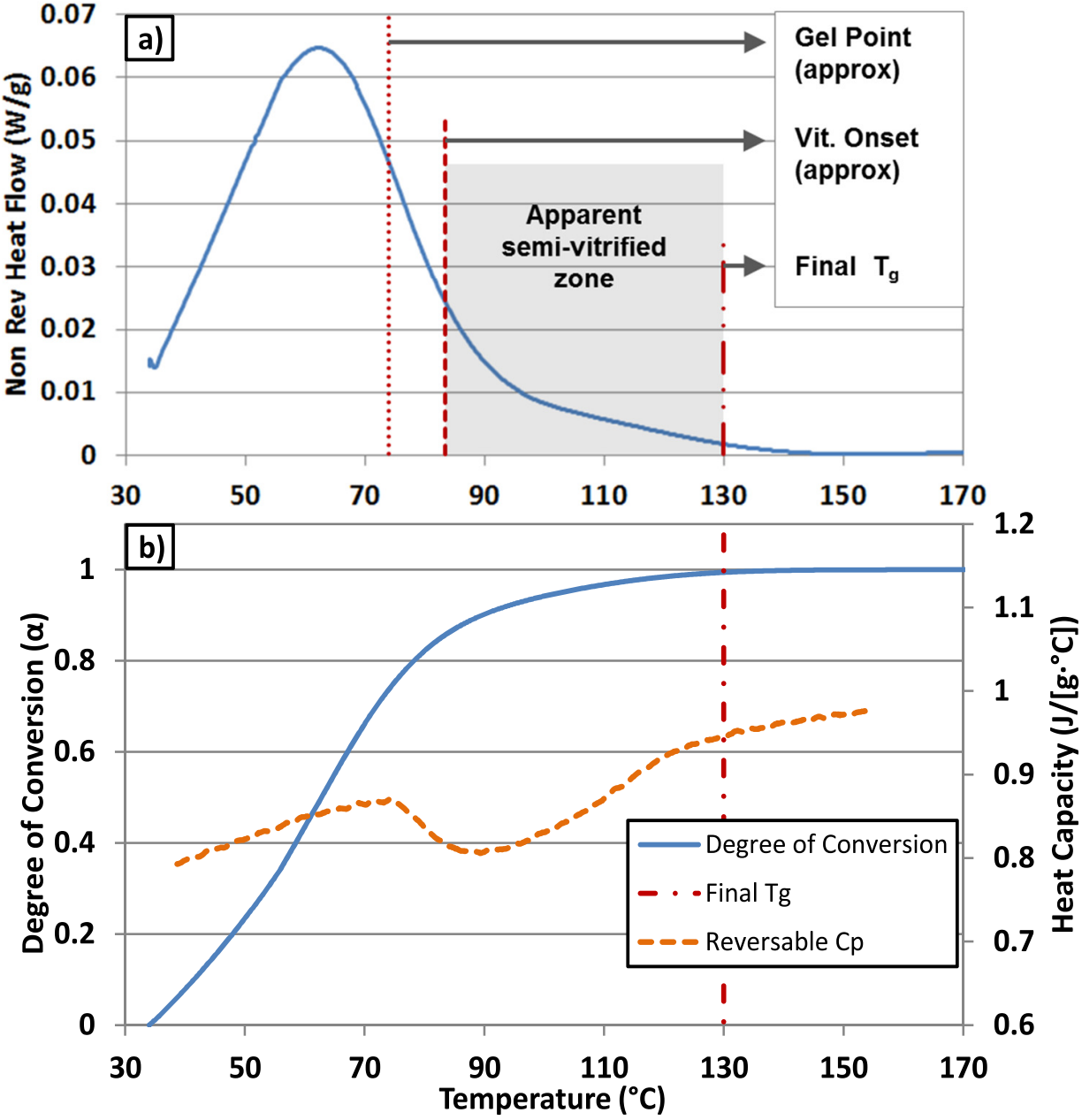

Figure 6.6: Examples of a) non-Reversing heat flow of solvent-free 60 wt% silver-epoxy microcomposite cure, annotated with regions of interest. B) Cure conversion calculated from data in a), with $T_{g\infty}$ and the reversing heat capacity included. Originally published in the proceedings of ICSR, in review for publication in the Journal of SMT, republished with permission [5].

ing $T_{g\,\alpha}$ approached the experimental temperature at that time. For continuously-heated conditions, this is the analogue to an isothermal segment: the partially cured material vitrifies partially or fully, reducing the cure rate, due to the $T_{g\,\alpha}$ and test temperature.

Figure 6.7 presents the cure conversion of three compositions (Ac0, Ac3, and Ac2E1) under all three heating programs in the left-hand column of graphs, with the corresponding electrical resistivity measured under the same conditions in the fight-hand column of graphs. The three rows in Figure 6.7 correspond to the three heating conditions previously listed in Table 6.1. Continuously-heated programs are plotted with respect to temperature, while heating programs containing isothermal segments are plotted in time-domain and include a trace of the temperature at each time. Lines have been included in the continuously heated conditions to identify the $T_{g\,\infty}$ measured during second heating scans. The maximum detection threshold for the resistance mold-probe is $10^9\,\pi\,/\,\ln(2)$ $[\Omega/square]$, and so "overflow" measurements have been treated as this value. These three compositions have the same filler content, and differ based on solvent content.

Before this full set of resistance data is discussed, it is useful to consider in detail one example of the resistance change throughout curing. For the resistance measurements of the Ac0 composition under continuous heating, presented in Figure 6.7 d), the calculated resistivity initially begins to drop at approximately 70 °C. This temperature corresponds with the temperature quoted in the supplier product information as the approximate onset of gelation[119]. Therefore, as expected, this reduction in resistivity is likely related to the beginning of the significant contraction and solidification of the epoxy, although separate measurements would be needed to verify this. Around 80 °C, the resistivity begins to climb back to above the maximum detection range of the device, contrary to the expectation that the resistance reduction and cure progression is related approximately by a power-law[130]. By approximately 100 °C the material is fully insulating again. Then, starting at approximately 130 °C, the resistivity then sharply drops again, producing the final resistivity value of the composite of 7.53 $\Omega \cdot cm$. Features similar to this "partial-cure resistance peak", in the form of peaks, shoulders, and extended plateaus, can be seen in the other compositions and heating conditions.

This partial-cure peak or shoulder varies between composite compositions and the applied heating conditions, but is highly consistent within replicate sets, indicating this is not a random error. Likewise, the final developed resistivity is significantly different between compositions and heat-treatments, spanning from 46.6 $\Omega \cdot cm$ to 0.03 $\Omega \cdot cm$, even though the conductive filler content is constant. Similarly, within a single composition (Ac3), differences in the heat treatment produced a 67× change in resistivity, while another composition displayed a 37× change. This significant difference also appears to be complex: a heat-treatment that improves one composition's conductivity results in conductivity reductions for other compositions, seen in the high-temperature isotherms when comparing the solvent-free and solvent-containing compositions. This leaves the possibility of either an inherent repeatable fault in the design and operation of the resistance-measurement

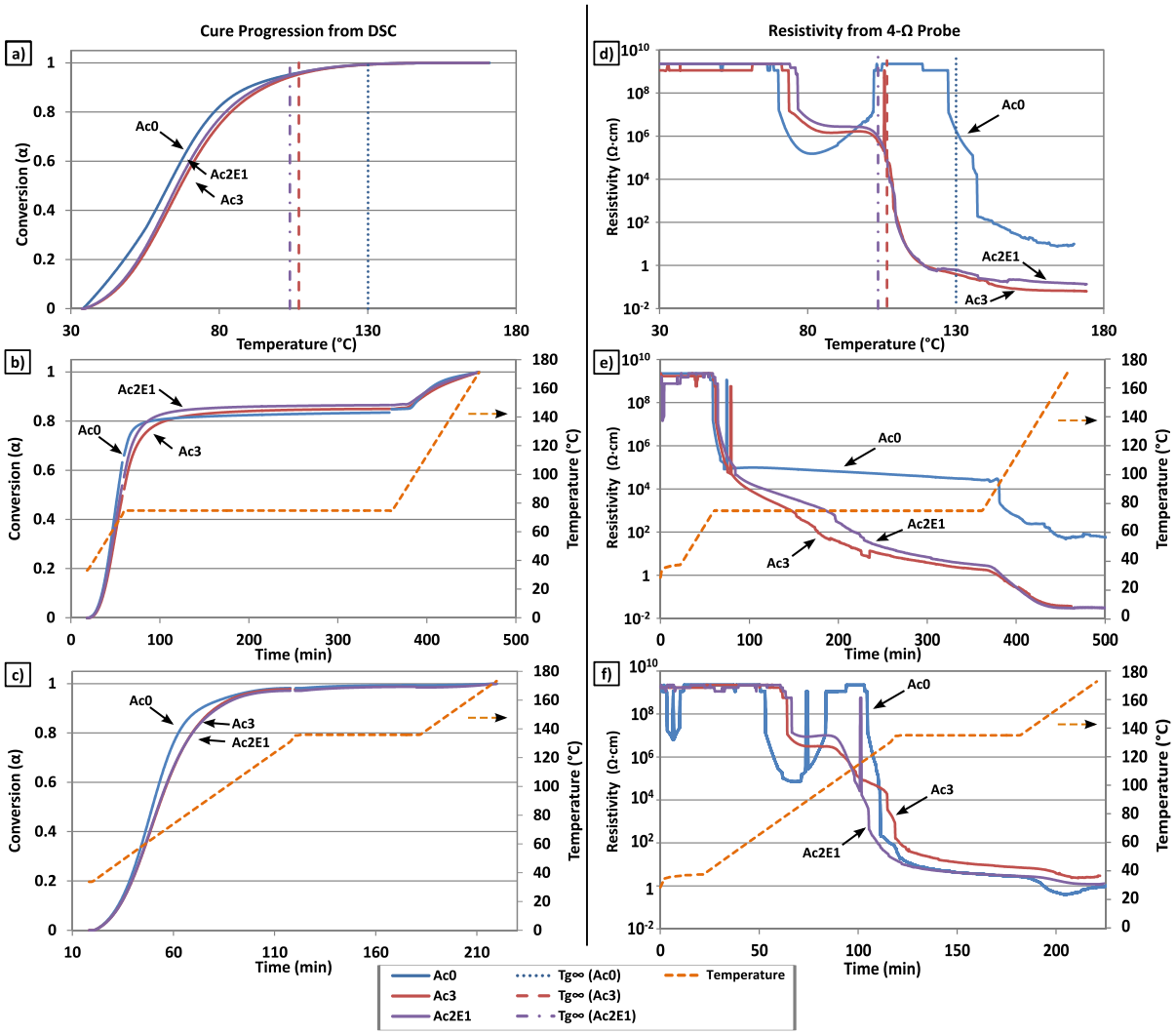

Figure 6.7: Collected conversion and resistivity plots for 60wt% Ag microcomposites listed in Table 6.2. a-c) are cure conversion for microcomposites under heat treatments "Ramp", "Iso 75", and "Iso 135", respectively. d-f) are respectively corresponding resistivity measurements. Each curve is average of 3 replicates.

probe-mold equipment, or it is actually real behavior produced by the cure of the composite.

If the resistance peaks and shoulders are an operational fault, the mechanism would need to in some way be related to both the temperature of the test at any moment, and the adhesive composition. The probe-mold's design is such that it is extremely unlikely that this is an operational fault: relative changes in dimensions due to thermal expansion and cure contraction should not be sufficient to produce intermittent connection between the embedded pins and surrounding specimen, and the spring-contact between pins and receptacles tolerate much larger angular changes without intermittent connection. Additionally, after the experiment the pins were well adhered and embedded inside the sample, demonstrating a well-developed physical connection. Therefore it is highly unlikely that a loss of connection is responsible for the unexpected resistance peak, and instead that this is a real phenomena within the composites.

In several of the *in-situ* resistance scans presented in Figure 6.7 there are short-duration spikes of increased resistivity. It is important to note that these were not seen in all replicates: each spike occurred in only one replicate of the specimen set, and is clearly visible in the presented averaged resistivity scans due to the high amplitude of the resistivity spike. This is unlike the resistivity peak and shoulder behaviors, which occurred consistently in each replicate in each set. These single-specimen resistivity spikes were seen in each composite formulation and in each heating rate, though they were not seen under all heating conditions for all formulations. Although these resistivity spikes were not representative of the other replicates, it was decided to include the single-specimen resistivity spikes in the final averaged data set and not to smooth the inconsistent data. The reasoning for this is that, upon close inspection, these do not appear to be intermittent noise originating from the test equipment, and appears to be a real process within the composites. The spikes have a duration that lasts several resistance measurements (typically 4 to 8 measurements, equivalent to approximately 60 to 120 seconds), and are not simply an "overflow" measurement, which would be the sign of a single-point data recording error. In Figure 6.7 e, the two spikes displayed by single specimens of two differing formulations are occurring at very similar time and temperature histories, and likewise very similar cure conversions ($\approx$ 80%). In Figure 6.7 d the single-specimen resistivity spike displayed by the Ac3 formulation coincides with the $T_{g,\infty}$ of that formulation. These details point to a real process that is occurring sporadically, and for a short duration, related in some way to the cure and temperature processes. Also, these short spikes did not appear to have a significant effect on the resistivity of the replicates they occurred in, unlike the apparent effect of the larger peaks and shoulders observed consistently across all replicates in a set. Also of note, all the observed single-replicate resistivity spikes occurred when the composites were at approximately $10^5\ \Omega \cdot cm$.

Once these results were observed for the sparsely-filled 60 wt% formulations, the experiment was repeated using a 90 wt% composite containing zero solvent, under the "Ramp"

and "Iso 75" heating conditions. The results of this, in terms of the cure conversion calculated from DSC, and resistivity obtained by the probe-mold, are displayed in Figure 6.8. The left-hand column of graphs is the cure conversion under the two heating conditions, while the right hand column is the corresponding resistivity. The ramped heating data is plotted with respect to temperature, while the Iso 75 data is plotted with respect to time and includes a separate curve denoting the test temperature. Each curve is the average of 3 replicates. The DSC behavior reveals that the same dynamically-vitrified cure occurs, denoted by the trough in the reversing heat capacity. It can be seen that in the case of a highly-filled composite, the resistance peak behavior is not seen, and no significant change in resistance occurs as the cure proceeds. This composition also appears to have poorer signal reproduction than the other compositions, and displays a significant random scatter throughout the heating. It was observed that the consistency of the 90 wt% composite was more akin to a damp and crumbly sediment than a flowable adhesive. Therefore it is likely that the microparticles were at a high enough volume fraction that too little epoxy matrix was present to prevent particle-particle electrical and physical contact, even prior to contraction during cure.

Tables 6.3 and 6.4 are collected summaries of the data presented in Figure 6.7 for each composition and heating procedure, including the $T_{g\infty}$, the degree of conversion reached when the first heating reached $T_{g\infty}$ ($\alpha_{T_{g\infty}}$), and the final resistivity developed ρ_{∞}. It can be seen that the $T_{g\infty}$ values of the solvent-containing compositions are considerably lower than those of the Ac0 composition, as expected from literature [128, 181, 200, 201].

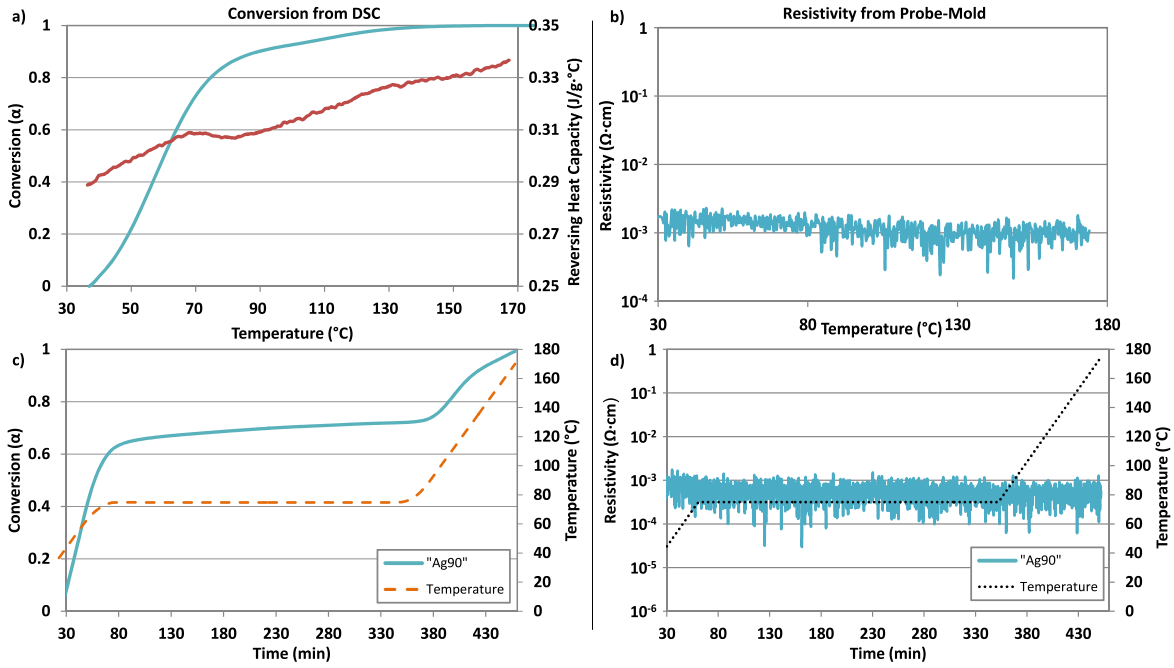

Figure 6.8: Plots of a) DSC and b) electrical resistivity for 90 wt% microcomposite.

Table 6.3: Key values from continuous heating calorimetry and resistance measurements of microcomposites during first heating

Composition	Ramp 1C/min		
	$T_{g\infty}$ °C	$\alpha_{T_{g\infty}}$	Avg ρ_∞ $\Omega \cdot cm$
Ac0	130.1	99.4%	34.7
Ac3	106.8	95.3%	0.19
Ac2E1	103.8	94.9%	0.12
Ag90	108.3	94.4%	0.0009

Table 6.4: Key values from isothermal calorimetry and resistance measurements of microcomposites during first heating

Composition	Iso 75 75c Iso, 5hr			Iso 135 135c Iso, 1 hr		
	$T_{g\infty}$ °C	$\alpha_{T_{g\infty}}$	Avg ρ_∞ $\Omega \cdot cm$	$T_{g\infty}$ °C	$\alpha_{T_{g\infty}}$	Avg ρ_∞ $\Omega \cdot cm$
Ac0	126.7	95.6%	46.6	124.0	98.0%	1.25
Ac3	105.9	89.1%	0.03	102.7	94.0%	2.00
Ac2E1	104.4	90.0%	0.03	107.1	94.7%	0.98
Ag90	109.4	81.1%	0.0006	—	—	—

6.4 Discussion

Literature has reported that the conductivity of a curing thermoset composite should roughly obey a power-law reduction in resistivity as the polymer matrix conversion progresses[130]. However, the data gathered by in-situ measurement demonstrates that the process of resistance reduction is much more complex: peaks or plateaus are observed in the resistance scan, occurring after the resistance has begun significantly reducing. This points to a disruption in the conductive filler network that had been established by that point. Later, the conductive network re-establishes itself and the composite approaches its final resistivity. To the knowledge of the author, this reversing or stalling resistance development has not been reported elsewhere in the open literature.

For all compositions under continuous heating conditions, the end of the partial-cure resistance peak or shoulder corresponds closely with the $T_{g\infty}$, which is measured upon second heating. The shapes and heights of the resistance peaks were strongly affected by

the differing solvent contents of the composites, as well as the heating conditions. The addition of solvent lowered the $T_{g\infty}$, and similarly known to lower the instantaneous T_g ($T_{g\alpha}$) throughout the cure progression [128, 181, 200, 201]. The onset of partial-vitrification during ongoing cure, caused by $T_{g\alpha}$ rising and approaching the test temperature at that time, can be seen to correspond to the onset of the resistance peak or resistance shoulders in all compositions under continuous heating.

The literature states that development of conductivity during ECA cure is primarily controlled by the polymer contraction, producing compaction of the conductive fillers and polymer movement out of the inter-particle spaces, allowing filler-filler contact. Therefore the existence of the partial-cure resistance peak demonstrates that a thermo-physical process is occurring during the semi-vitrified region of the cure that physically separates (or otherwise interferes with) the partially-formed conductive filler network.

Lange *et al.* has discussed the formation of internal stresses at the onset of dynamic vitrification when curing below $T_{g\infty}$, caused by the polymer curing while being unable to easily deform to relieve internal stress against itself and the filler particles, due to the onset of the glassy state[114, 116]. Similarly, Erinc *et al.* discussed how the presence and distribution of filler particles, in that case spheroid nano-silver, produced internal stresses in a modeled epoxy-matrix composite during curing and cool-down[202]. In the current work, this process appears to be capable of increasing the distance between the conductive fillers or otherwise interfering with their connections during semi-vitrified cure. Once the temperature rises and sufficiently exceeds the $T_{g\alpha}$, the thermo-physical state reverts or relaxes and the conductive filler network continues to develop once those stresses are relieved.

This has implications for the final composite conductivity. Although the conductive particles have been separated by the onset of this semi-vitrified state, the epoxy is continuing to cure during the partial-cure peaks and shoulders[114, 116]. Thus, the polymer network is continuing to develop based on the configuration and mobility at that time. Continuous curing during this vitrified and particle-separated state, albeit small scale, may be causing the polymer near the separated filler joints to sufficiently cross-link in a configuration that permanently separates those fillers, even once the temperature rises and the composite continues establishing the conductive network. It is notable at this time that, as a rough metric of this, the Ac0 composition showed the most anomalous behaviour, and correspondingly presented the highest final resistivity. It may be that greater quantities of completed cure under these semi-vitrified and particle-separated conditions may result in a lower fraction of potential filler contact points that develop into a contributing part of the filler network.

The process could cause the final developed resistance of thermosetting conductive adhesives to be path-dependent, sensitive to the temperature and thermo-physical state of the composite throughout the cure. A diagram illustrating this hypothesis is shown in Figure 6.9. Note that the large displacements and spacing between non-contacted particles

in the diagram are an exaggeration, to aid the reader, and are not to be considered accurate of the actual materials. Isothermal heat treatment at $T_{g\alpha}$ improved the final conductivity for the Ac0 compositions, while isothermal heat treatment above $T_{g\alpha}$ degraded conductivity for the solvent-containing compositions. From this it appears that the final stress state of the microcomposite, and subsequent relaxation or thermal aging, is a factor. It is interesting that these two compositions converged on a shared intermediate resistivity from opposing effects.

However, vitrification effects alone are not appropriate to also explain the short-duration single-replicate resistivity spikes, since these features are far more inconsistent than the peak and shoulder behaviours, and are not closely tied to vitrification periods. Since the resistivity spikes are occurring only occasionally in single-replicates, it is reasonable to expect that they require special circumstances. As mentioned earlier, these short-duration

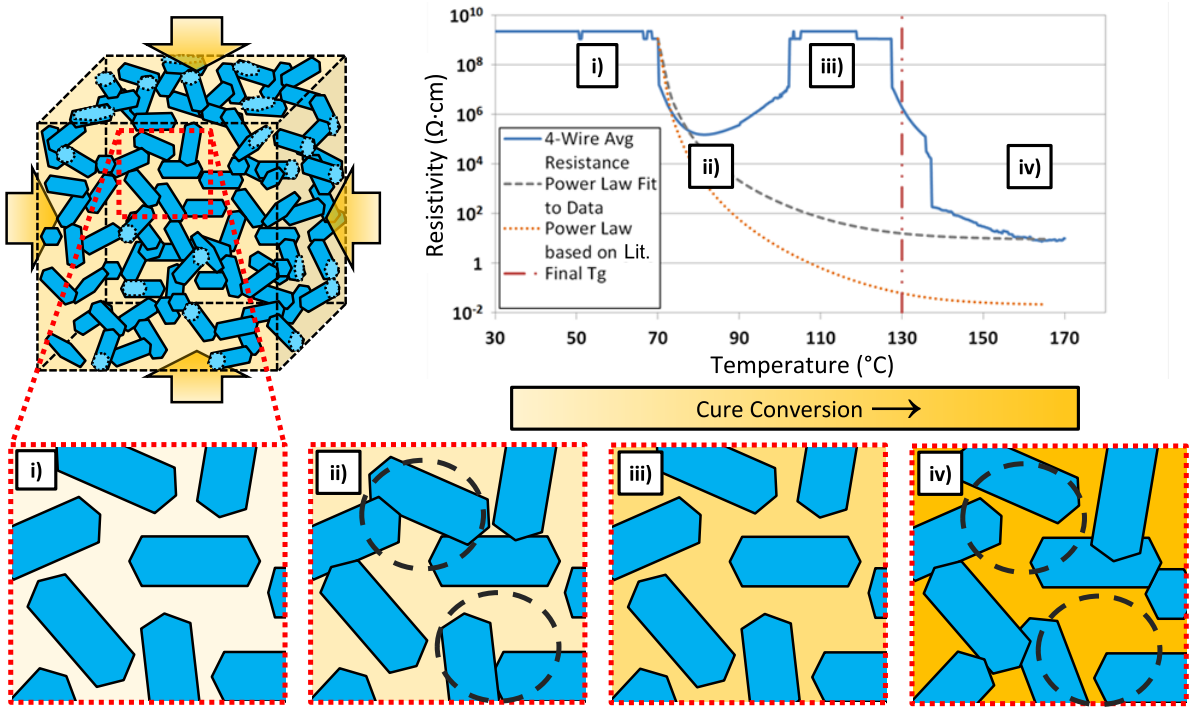

Figure 6.9: Cartoon representing a proposed mechanism of temporary loss of conductivity after initial establishment during microcomposite cure. Progression in cure from i) to ii) produces initial particle-contact and conductivity. Thermophysical stresses developed due to partial vitrification during cure between ii) and iii) separates some initial conductive pathways. Continuing cure between iii) and iv) prevents some original pathways (highlighted in ii) and iv) by dashed circles) from re-establishing as contraction progresses, limiting final conductivity. Orange line is based on power-law fit of comparable literature data [203].

resistivity spikes consistently appear when the resistivity of the composite is approximately $10^5\ \Omega \cdot cm$, which implies that the environment conducive to a spike is when the conductive filler network is in a narrow window of sparse connectivity, and likewise physical contact. The fillers are rigid, and are being brought into contact by the contraction of the epoxy, which is in a rubbery state during each observed instance of these resistivity spikes.

Therefore, I hypothesize that the a single-replicate resistivity spikes are occurring when there are very few conductive pathways, a condition that makes each pathway's contribution to the conductivity very significant. The microflakes at these early pathways have come into physical contact relatively early in the cure process compared to the majority of the eventual filler-filler contacts that are not yet established. Therefore, as the ECA continues to cure and contract, these few early pathways will have a greater amount of pressure applied to their contact point than the conductive pathways that form later. If one of thos filler-filler contact points is not favorable to supporting the applied pressure, the fillers may shift a small amount, and temporarily lose contact. For example, if the contact between particles is a glancing contact, or if the contact point is off-center such that the contact applies a rotational torque to the particles, the rubbery epoxy may allow the microflakes to shear or rotate against one another to relieve the local stresses, causing a thin layer of epoxy or a newly formed void to separate the microflakes. This would produce a sharp spike in ECA resistivity when that highly significant conductive path is lost. Continued contraction from the composite would then bring the microflakes back into contact, or produce the formation of a replacement conductive pathway elsewhere in the specimen, ending the resistivity spike. Therefore, the single-replicate resistivity spikes are likely caused by the continuing contraction of the cure acting unfavorably, thought temporarily, on a particular sub-set of the developed conductive filler contact points.

A 90 wt% silver microcomposite was also prepared and tested in the same manner as the other compositions. At 90 wt% the composite is well above the percolation threshold, and so the microparticles are already in significant contact prior to curing, to the extent that the resulting paste does not flow or slump. This composition did not display the resistance reduction, or the mid-cure peak.

This cure-related process has significant negative implications for the use of minimally-filled ECAs in practical applications. Typically multi-stage curing using isothermal conditions are used to control self-heating, shrinkage, and adhesion of the composite, and also to reduce thermal stresses on sensitive electronic components. Therefore, vitrification during cure is commonplace in practical usage of ECAs, and it can now be seen that the anomalous behaviour reported here is likely producing reduced and inconsistent conductivity in finished parts.

Unfortunately, this process is likely very complex. Physical properties that can be expected to contribute to this process, throughout curing at each at α_i, include the viscoelastic properties, the coefficient of thermal expansion of all components, the cross-link density of the matrix (at all degrees of conversion, and as-influenced by the heating con-

ditions at that time), the duration of the semi-vitrified state in terms of the degree of conversion, and how close T_i is to $T_{g\alpha}$. A complete description would also likely require interface interactions between the filler and matrix, the morphology and distribution of the fillers, and whether fillers can resist separation by the formation of permanent bonds (for example by diffusional sintering, or oriented-attachment-like bonding of the particles).

6.5 Concluding Remarks

Silver microcomposites measured by *in-situ* 4-wire resistance methods throughout their epoxy cure exhibit shoulders and peaks in their resistivity. This is related to the developing thermo-mechanical properties of the thermoset composite, and the stress-development of the composite when cured below the $T_{g\infty}$. Variations in heating programs and $T_{g\infty}$ altered by solvents produced differing final resistances. This is contrary to the general literature belief that conductivity develops approximating a power-law; the final resistance is path-dependent, based on the instantaneous conditions and properties throughout the cure. To the knowledge of the author, there is no report of this detrimental behavior in the open literature. Better understanding of the effect may allow composite curing to be optimized to obtain high conductivity without losing the practical advantages of multi-stage curing, and to obtain more consistent final resistances in complex electronic packaging where many composite joints are being cured.

This study has provided baseline comparisons for nanocomposite studies that will follow, improving the chances of identifying the signal of silver nanobelts undergoing joining in a hybrid nanocomposite during cure. However, this also raises several questions. For example, how will the much thinner nanoparticles respond to the stesses in a near-vitrified curing composite? If the resistance peaks are caused by particles being separated, potentially permanently due to the ongoing cure, will the nanobelts that meet have the opportunity to join and resist separation? These concerns will be investigated in Chapter 7.

Chapter 7

Cure and Conductivity in a Nanocomposite Containing Silver Nanobelts

7.1 Overview

In Chapter 4 the nanobelt synthesis was improved to obtain more consistent batches and a more desirable high-aspect ratio Generation 2 ("G2") morphology. In Chapter 5 it was shown that silver nanobelts are able to join to one another when exposed to temperatures between 70 °C and 180 °C, lowering their network electrical resistance. As seen in Chapters 3 and 6 this temperature range partially corresponds to the range of temperatures that the selected epoxy thermoset cures at. Therefore, additions of small quantities of nanobelts to a microcomposite may obtain significant improvements to conductivity at reduced total filler contents, due to the synergistic interactions of the filler particles and because of the potential for nanobelts to undergo joining during cure. This would be analogous to the in-cure diffusional sintering discussed in Section 2.3.2. However, it is unknown how the mechanisms discussed in Chapter 6 may effect a hybrid nanocomposite containing silver nanobelts, both in terms of the effect of the cure contraction establishing conductivity, and the semi-vitrified regime's opposition to it.

To that end, Chapter 7 will investigate the change in conductivity throughout cure of a hybrid nanocomposite ECA containing silver microflakes and Generation 2 silver nanobelts. These results are as-yet unpublished, and these sections will be prepared for publication in the near future.

In this work *in-situ* resistance measurements are correlated with calorimetric heat flow and polymer cure conversion data. Resistance data is obtained by a custom mold with inlaid resistance probe, and calorimetry by modulated temperature differential scanning calorimetry, collected under matching heating conditions. Both of these will be compared

to dimensional-change measurements made on a specimen of the composite *via* dilatometry, using a thermomechanical analyzer (TMA). Results determine that the addition of silver nanobelts to silver microflake ECAs produce reductions in the ECA resistivity, but also cause the ECA to be more sensitive to glass-transition related behaviour, even after the cure has completed. This will substantially influence future ECA optimization, as it may be possible to reduce silver filler contents necessary for low resistivity by lowering the glass transition temperature. This defines a possible trade-off between maximum service temperature and filler content, and thus expense.

7.2 Methodology

Epoxy-based isotropic ECAs containing silver nanobelts and silver microflakes were characterized during cure by calorimetry, *in-situ* electrical resistance measurement, and linear dilatometry. These experiments were performed simultaneously on specimens drawn from a shared batch with a shared thermal history, and each device used the same time-temperature heating conditions for the experiment. Samples were produced as batches to minimize variation in chemistry and filler content between specimens, and were stored at -80 °C between tests to prevent onset of cure. The time-temperature conditions are listed in Table 7.1, where the isothermal conditions were adjusted based on the $T_{g\infty}$ observed for each formulation during the continuous ramp experiments. All heating was performed with the average heating rate of 1 °C/min. Three replicates of each combination of formulation and heat treatment was performed.

Calorimetry was performed using modulated heating (±0.159 °C, 60 second period) to obtain the non-reversing heat flow and reversing heat capacity of the specimens during heating, using a TA instruments TA DSC 2920 modulated temperature differential scanning calorimeter. Analysis of the heat flow to obtain conversion and glass transition data was performed according to the methods discussed in Section 2.6.1. After the first scan under each condition, a second scan was performed to confirm complete curing.

Table 7.1: Applied first-heating treatments for hybrid nanocomposite cure-conductivity study

	Heating	Isothermal	End
Treatment Label	Rate (°C/min)	Temperature (T_{iso}) (°C)	Temperature (°C)
Ramp	1	N/A	175
$T_{g\infty} - 30$	1	$T_{g\infty,X} - 30$	175
$T_{g\infty} - 15$	1	$T_{g\infty,X} - 15$	175

In-situ resistance measurements were performed in the custom-designed electrical probe-mold, discussed in Section 6.2. After cure was complete, the specimens were removed and measurements of thickness were made by micrometer, for use in the calculation of resistivity.

Dilatometry measurements were performed by curing composite specimens in a thermo-mechanical analyzer (TMA) probe, using the same heating conditions applied in the other instruments. The probe contact components were protected from the composite adhesive by sandwiching the composite between two glass microscope slide covers, as discussed in Section 2.6.5, and shown in detail in Figure 7.1. The initial thickness of each pair of slide covers (denoted by $y_{g,1}$) was measured at room temperature *via* TMA, prior to dispensing the composite specimen. Using these initial measurements, the thickness of the glass slides at each temperature (denoted by $y_{g,2}$) was calculated based on the glass coefficient of thermal expansion. These values were subtracted from the total thickness measurements obtained by the TMA (y_1 and y_2), to obtain the composite thicknesses at each condition ($y_{c,1}$ and $y_{c,2}$). Changes in linear dimension are collected, and analyzed in terms of "percent change" from initial composite thickness, as discussed in Section 2.6.5.

Due to pinning of the composite on the slide cover surface during cure the contraction of the specimen is not isotropic, and therefore the measured change in thickness is not able to be converted to volume contraction. However due to the low fractional volume change expected during cure, and the low thickness of the specimens, it is expected that the measured change in thickness is representative of the cure and thermal expansion processes occurring in the sample. In the interest of clarity, the dilatometry data is presented as the percent linear change in thickness. After curing the specimens were measured throughout cooling and reheating, to characterize the as-cured dimension changes.

7.2.1 Nanocomposite Production

Four composites were investigated, containing silver microflake and silver nanobelts in the proportions listed in Table 7.2. Formulations are named based on the weight percentages of silver microflakes and nanobelts: "505" refers to a composite with 50 wt% silver microflake, with 5 wt% silver nanobelts. Similarly, "603" contains 60 wt% microflake, and 3 wt% nanobelts.

Nanobelts were dispersed into acetone from filter-dried cakes *via* repeated aggressive vortex shear mixing. The dispersed suspensions were transferred into pre-weighed epoxy, and continuously mixed during vacuum solvent extraction. Custom tabletop equipment was developed to allow simultaneous mixing and vacuum solvent extraction. The vacuum mixing chamber is mounted on a Corning LSE 6775 Vortex Mixer, using a custom designed 3-D printed adapter, and a 64 cm$\cdot$Hg vacuum vacuum is drawn. Specimen and glassware masses were weighed throughout the mixing process to track the solvent content. Once the desired nanobelt mass was dispersed into epoxy in the form of a concentrated mixture,

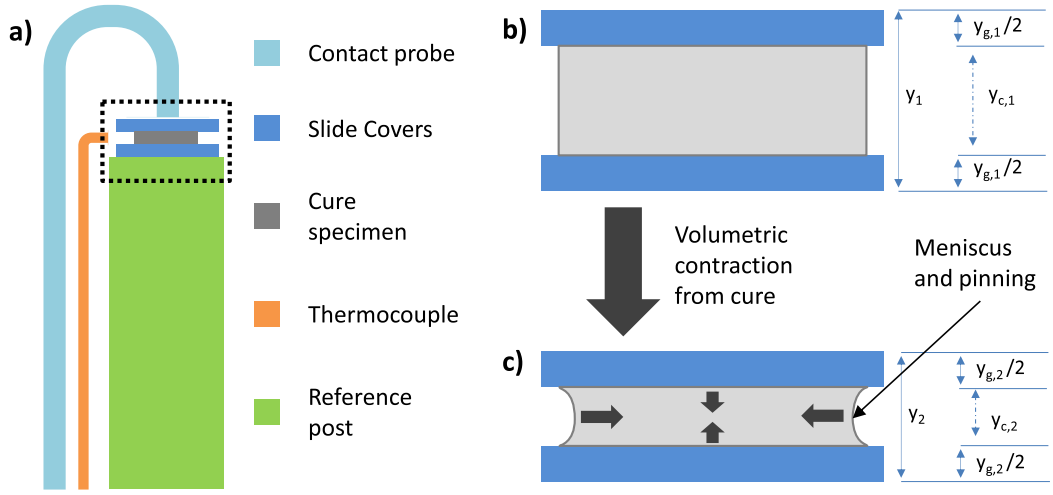

Figure 7.1: Measurement of composite dimension change *via* TMA. a) Side-view of specimen and TMA equipment setup. Measurements of composite and glass slides prior to cure (b), and after volumetric contraction by curing (c).

was added to dilute the residual solvent and nanobelts, and mixed using a planetary centrifugal mixer ("PCM", Thinky ARE-310) at 2000 RPM for 20 minutes. After this, silver microflakes were added in appropriate concentrations, and mixed using the PCM for 5 minutes. The mixture was cooled to room temperature, then the desired amine hardener was added using the PCM. To minimize curing, the vial of composite was placed in a pre-chilled (-80 °C) aluminum holder carried in an insulating styrofoam cooler. The specimen was then quickly transferred to the -80 °C storage freezer and stored until further use.

Table 7.2: Prepared hybrid nanocomposite ECA formulations named after weight percentages

Formulation Label	Silver Microflake	Silver Nanobelts
	Wt% / *phr*	Wt% / *phr*
401	40 / 75.22	1 / 3.16
505	50 / 112.8	5 / 25.1
601	60 / 169.5	1 / 6.72
603	60 / 169.5	3 / 18.63

7.3 Results

Measurements of the changing electrical resistivity of all four composites during cure, for continuous ramp conditions, are presented in Figure 7.2. A close-up of only the first-heating cure segment is presented in 7.2 a, while an overview of the full heating and cooling cycle is presented in 7.2 b. To accommodate the cooling and second heating cycles, this data is plotted with respect to time. The cure conversion of the composites obtained by calorimetry, and the dimensional change *via* linear dilatometry during cure are presented in Figure 7.3 a and b, respectively. Key values of the data obtained presented in these figures are collected in Tables 7.3 and 7.4, presenting the resistance and glass transition data, respectively. Cursory observation of the 401 formulation made during testing appeared to indicate that this formulation remained non-conductive throughout cure, and the brief period of measurable conductivity was not observed until the data was fully analyzed. This lead to the 401 formulation being removed from the remainder of the study.

Measurements made of electrical resistivity, cure conversion, and dimensional change during cure for the isothermal conditions are presented below, grouped by formulation. Figures 7.4 and 7.5 present this data for formulation 505, respectively. Similarly, the

Table 7.3: Key resistance data for hybrid nanocomposites under continuous heating

Formulation Label	1(°C)/min Ramp Minimum ρ $\Omega \cdot cm$	Condition 1st Cycle ρ_∞ $\Omega \cdot cm$	2nd Cycle ρ_∞ $\Omega \cdot cm$
401	4.88	1.45×10^6	1.9×10^9
505	5.34	1033	1222
601	0.32	1.09	12.84
603	0.017	0.017	0.022

Table 7.4: Key glass transition and conversion data for hybrid nanocomposites under continuous heating

Formulation Label	1(°C)/min Ramp $T_{g\infty}$ (°C)	Condition $\alpha_{T_{g\infty}}$ %
401	122	98.9
505	134	99.2
601	126	99.2
603	120	98.8

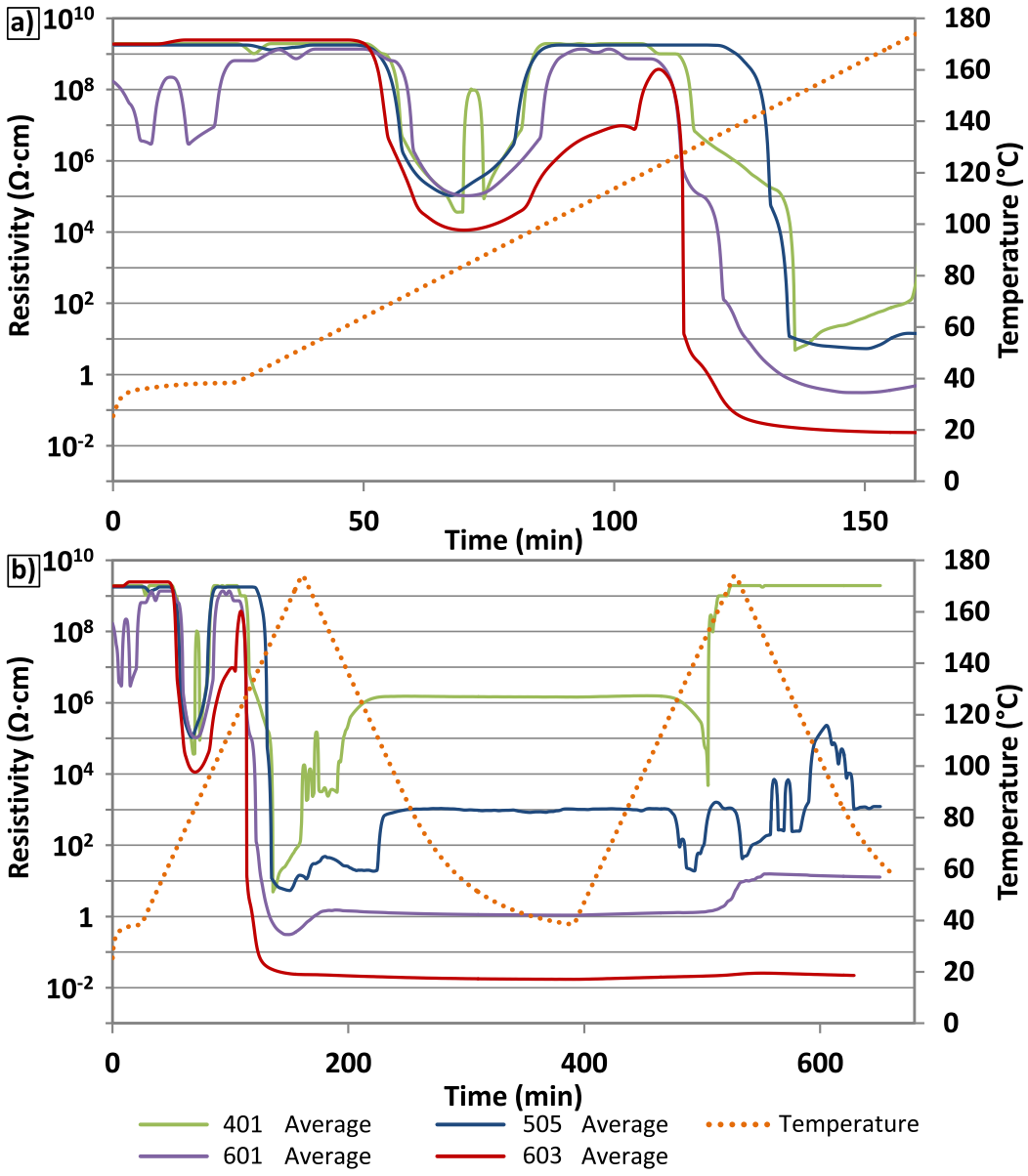

Figure 7.2: Resistivity data for four hybrid nanocomposites obtained during cure under continuous heating. a) detailed section showing resistivity changes during only the cure segment. b) Resistivity changes over the entirety of the two heating and cooling cycles, including after the completion of cure.

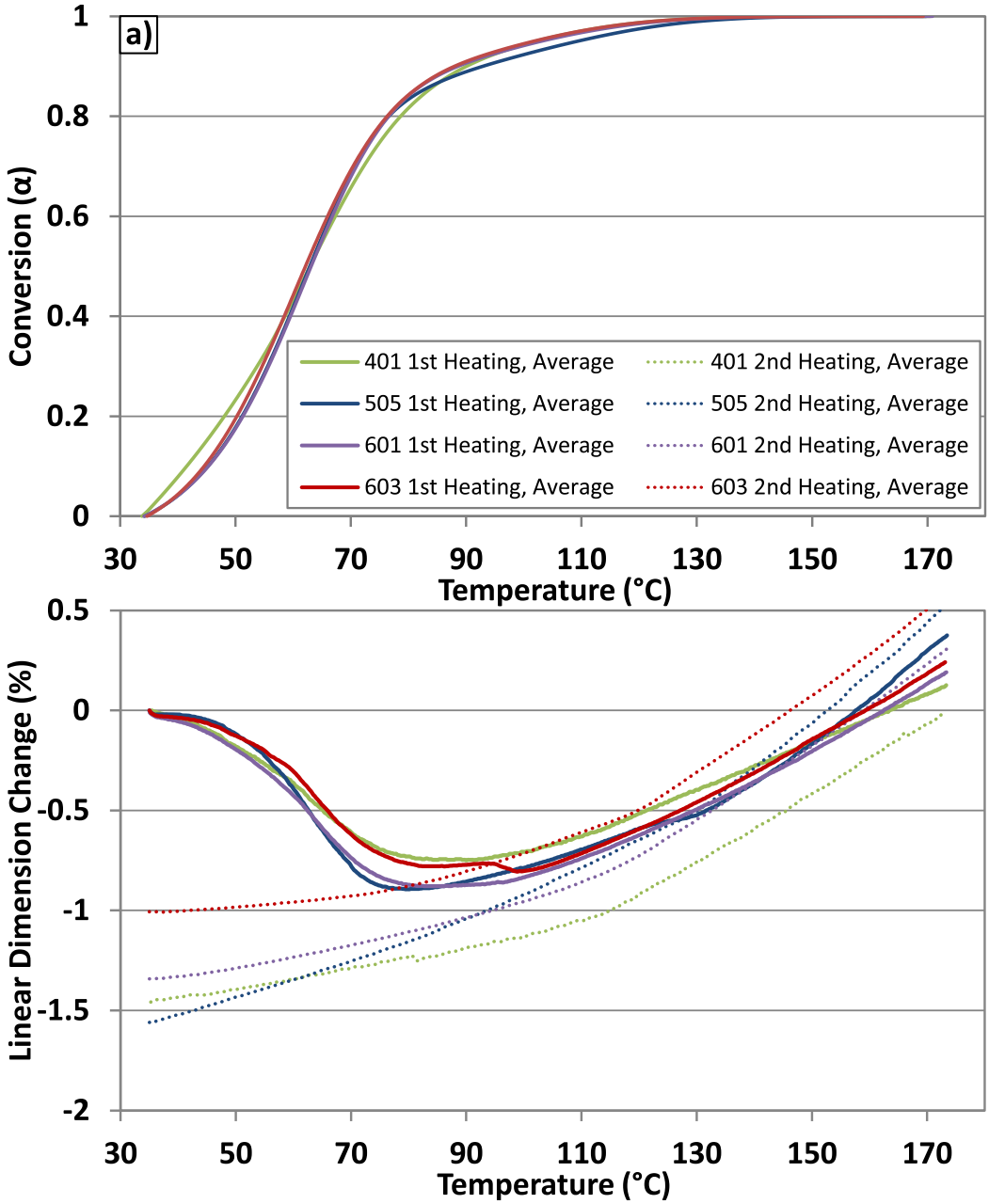

Figure 7.3: a) Cure completion from calorimetry, and b) cure contraction *via* TMA, for four hybrid nanocomposites obtained during cure under continuous heating.

results for the 601 formulation are presented in Figures 7.6 and 7.7, and results for the 603 formulation are presented in Figures 7.8 and 7.9. Note that the start time presented differs between plots, due to the different experiment start times used by the measurement equipment.

Figure 7.4 b presents the resistivity of an exceptional specimen from the 505 formulation alongside the average that was observed, for the "Iso $(T_{g\infty} - 15)$" heating condition. Similarly, Figure 7.8 b presents the resistivity of an exceptional specimen from the 603 formulation alongside the average that was observed, which was also from the "Iso $(T_{g\infty} - 15)$" heating condition. Key values of the data obtained in the isothermal conditions are collected in Tables 7.5 and 7.6, presenting the resistance and glass transition data, respectively.

Each of the formulations studied display mid-cure resistance peaks similar to those observed in the microflake-only formulations studied in Chapter 6. From the resistance data, a strong correlation between the minimum resistivity achieved and the silver content is observed, as expected from theory. It is also observed that heating or cooling the composite through the ultimate glass transition temperature often produces significant increases in resistivity, with the severity of these changes decreasing as the silver content is increased. Formulation 603 has almost insignificant changes in resistivity once it has

Table 7.5: Key resistance data for hybrid nanocomposites under isothermal heating treatments

Formulation Label	Iso Minimum ρ $\Omega \cdot cm$	$(T_{g\infty} - 30)$ 1st Cycle ρ_∞ $\Omega \cdot cm$	2nd Cycle ρ_∞ $\Omega \cdot cm$	Iso Minimum ρ $\Omega \cdot cm$	$(T_{g\infty} - 15)$ 1st Cycle ρ_∞ $\Omega \cdot cm$	2nd Cycle ρ_∞ $\Omega \cdot cm$
505	2.1	12.4	164.8	5.6	5.6	106.9
601	1.05	52.3	324.4	11.96	447.6	435.3
603	0.23	2.64	0.6	0.38	0.38	1.45

Table 7.6: Key glass transition and conversion data for hybrid nanocomposites under isothermal heating treatments

Formulation Label	Iso $(T_{g\infty} - 30)$ $\alpha_{T_{g\infty}}$ %	Iso $(T_{g\infty} - 15)$ $\alpha_{T_{g\infty}}$ %
505	97.8	97.7
601	96.9	99.6
603	94.7	95.3

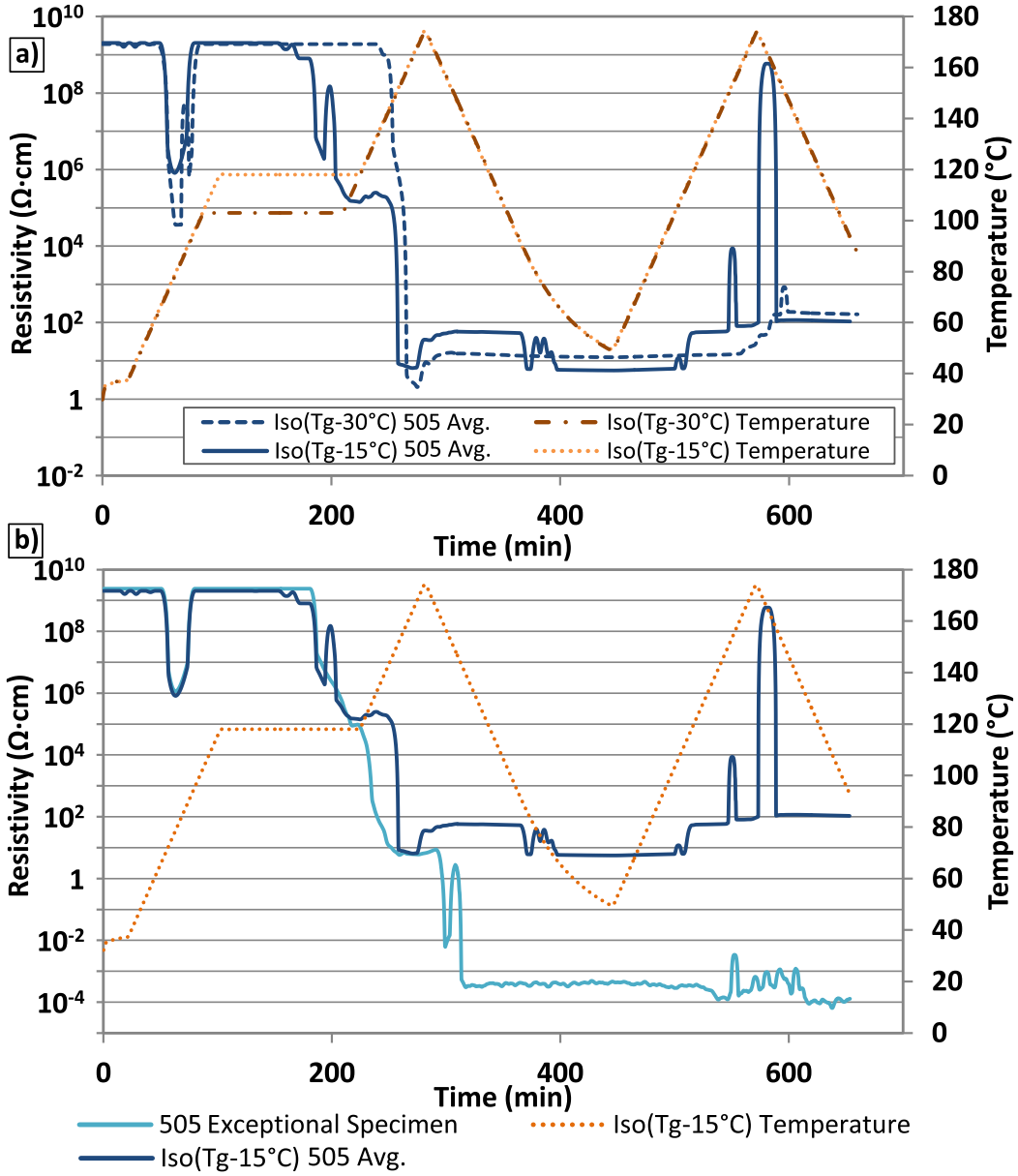

Figure 7.4: a) Average resistivity data for 505 hybrid nanocomposite, obtained during cure and subsequent thermal cycling from two isothermal heat treatments. b) Average resistivity of the composite for the $T_{g\infty} - 15$ isothermal treatment, presented with one exceptional replicate that was not well represented by the average.

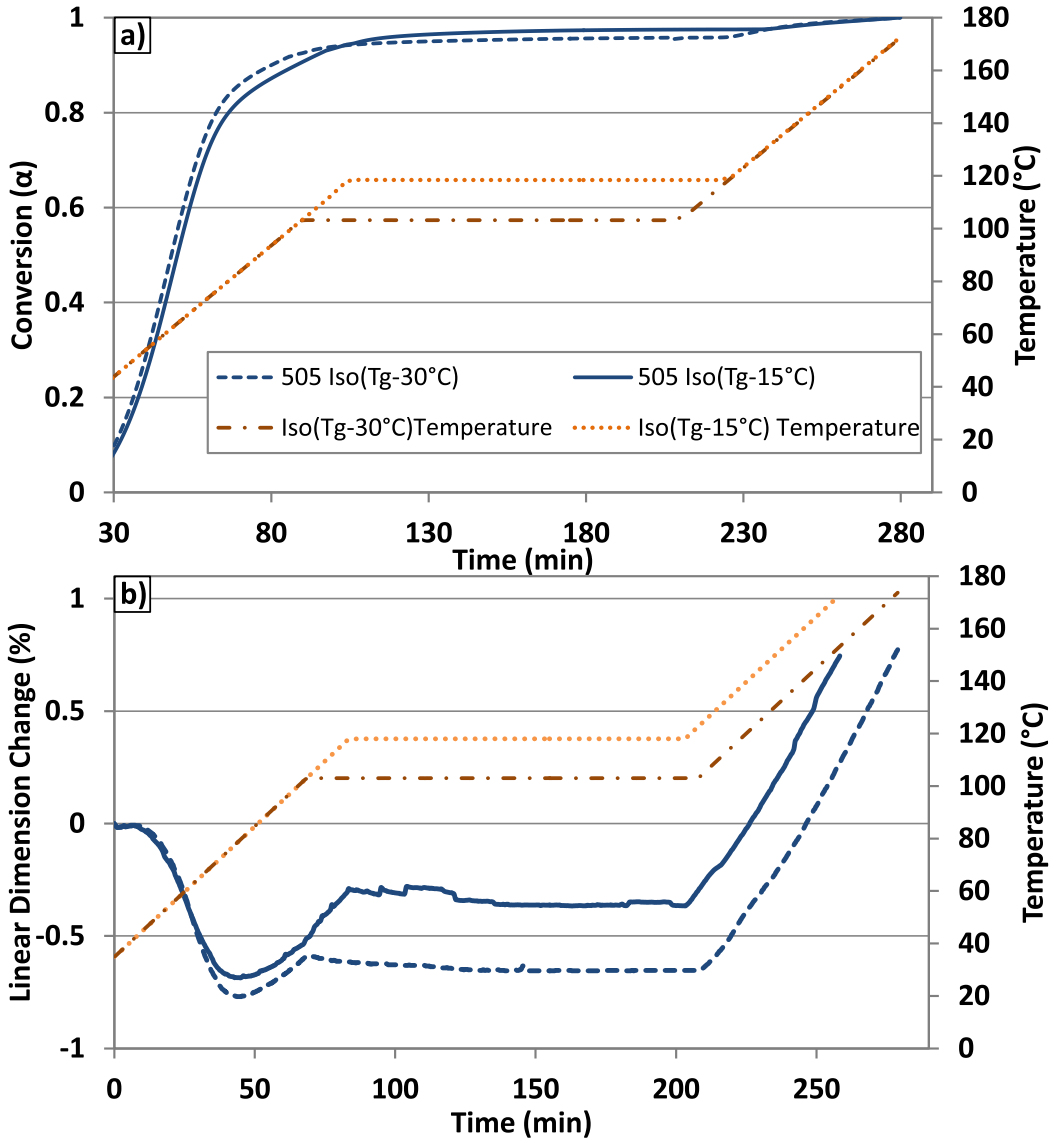

Figure 7.5: a) Cure completion from calorimetry, and b) cure contraction *via* TMA, a hybrid nanocomposite (505) obtained during cure under two isothermal heat treatments.

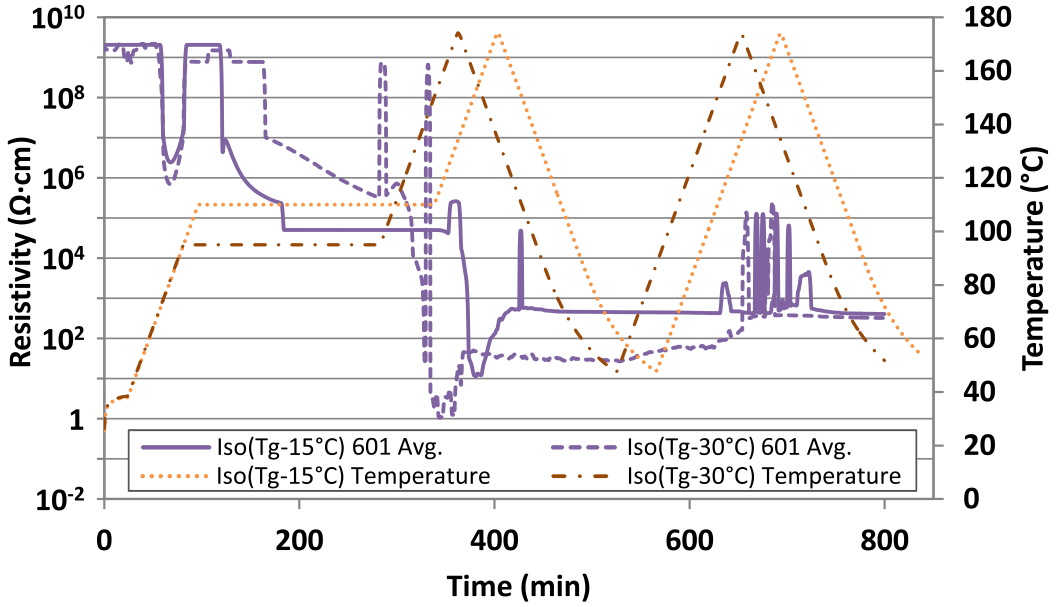

Figure 7.6: Average resistivity data for 601 hybrid nanocomposite, obtained during cure and subsequent thermal cycling from two isothermal heat treatments.

completed curing, and is strikingly different from Formulation 601 in this regard, despite the relatively small difference in silver nanobelt content between the two formulations. In several formulations there are momentary losses of conductivity during the cooling and heating cycles. Interestingly, for any particular composite formulation, these momentary losses occurred in all replicates, and appear to be a characteristic resistivity "fingerprint" of the formulations.

Two replicates, presented in Figures 7.4 b and 7.8 b, displayed significantly different behaviour compared to the other replicates of their formulation and heating condition. Any replicates not presented individually are well represented by the average value that has been plotted.

The calorimetry data obtained demonstrates that all specimens were cured to an extent that no further non-reversing heat flow could be detected during the residual heating cycle, and the final glass transition temperatures ($T_{g\infty}$) demonstrate that there is little residual solvent remaining from composite preparation. Similarly, based on the minor differences in $T_{g\infty}$ and the degree of conversion obtained by the time that the first heating cycle reached the final glass transition temperature ($\alpha_{T_{g\infty}}$), it is reasonable to expect the evolved thermoset polymer to be fairly similar in its properties between formulations and heating conditions.

Contraction and dilation of the composites during cure and heating, based on the linear change in dimension obtained by TMA, led to a net 1% contraction of the composites during the first half of curing. As the cure progressed the contraction slowed, and eventually

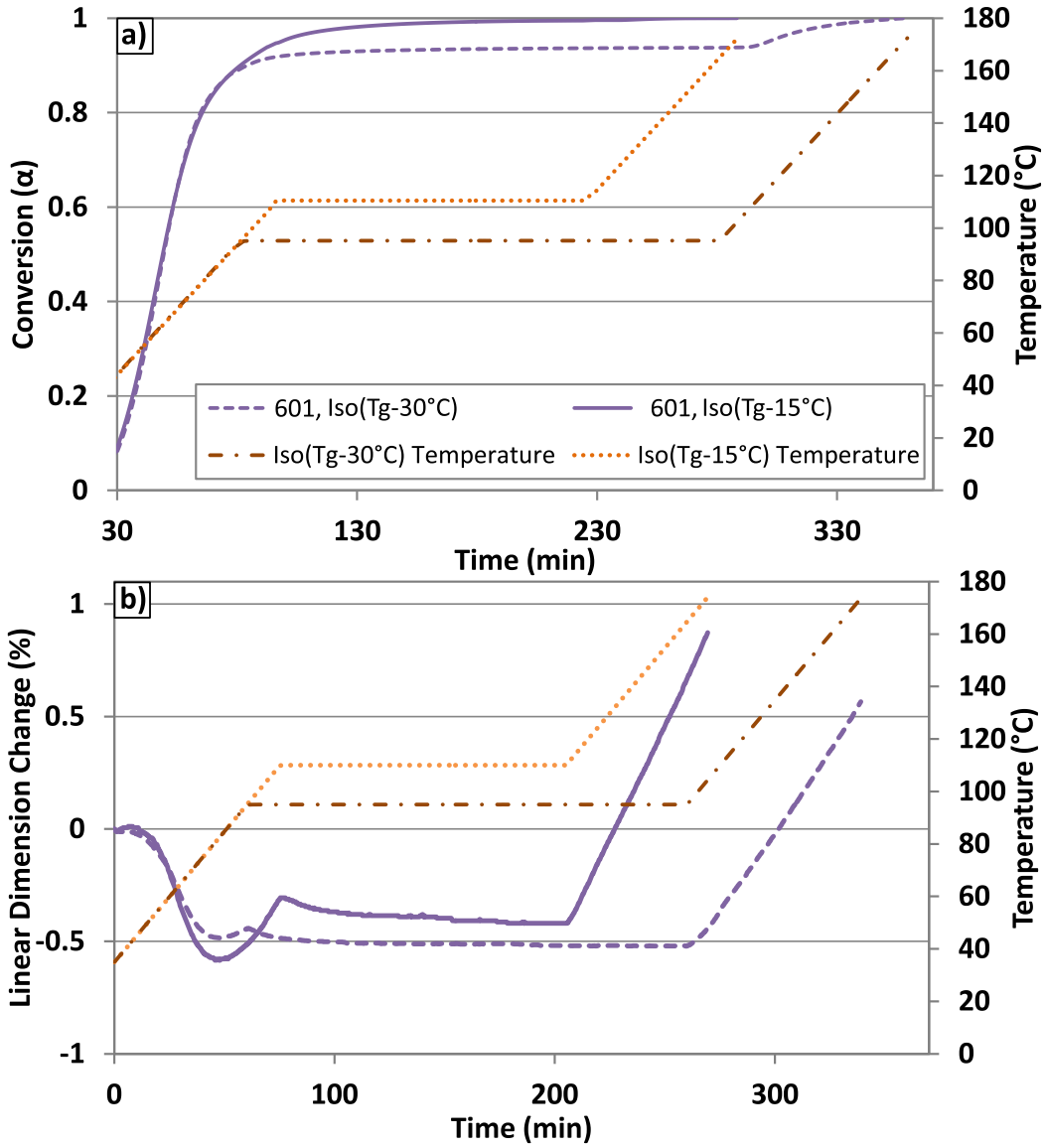

Figure 7.7: a) Cure completion from calorimetry, and b) cure contraction *via* TMA, a hybrid nanocomposite 601 obtained during cure under two isothermal heat treatments.

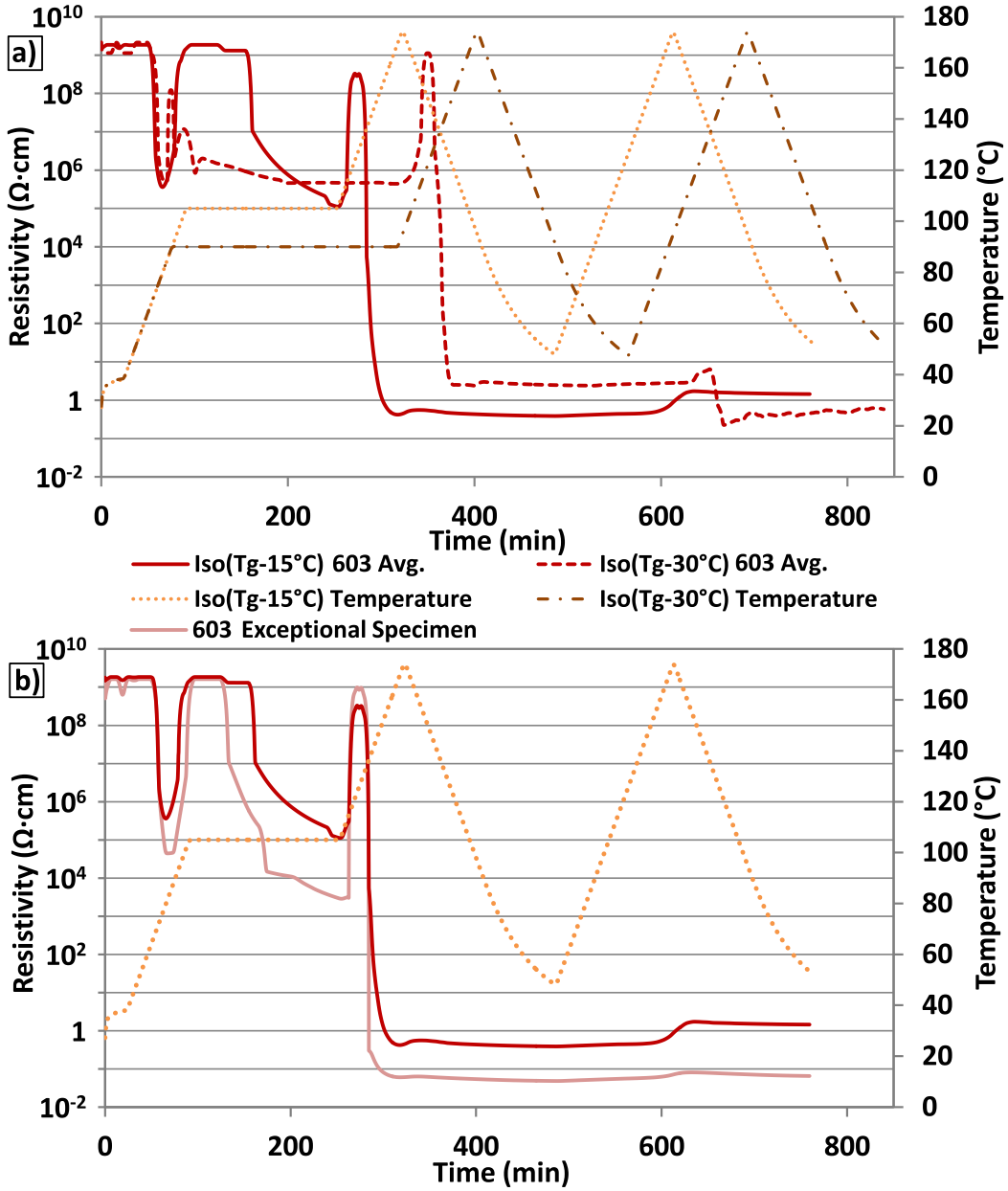

Figure 7.8: a) Average resistivity data for 603 hybrid nanocomposite, obtained during cure and subsequent thermal cycling from two isothermal heat treatments. b) Average resistivity of the composite for the $T_{g\infty} - 15$ isothermal treatment, presented with one exceptional replicate that was not well represented by the average.

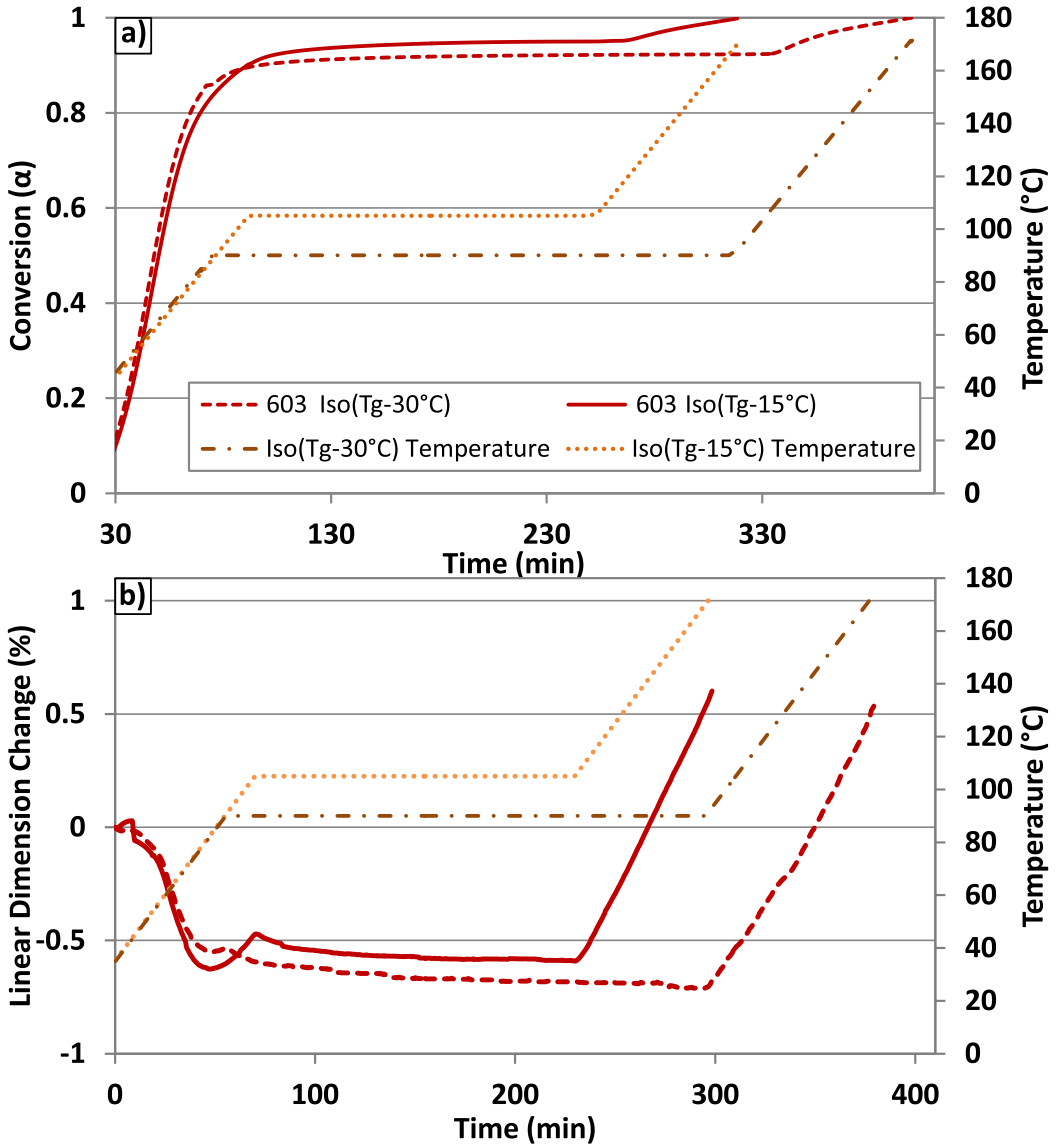

Figure 7.9: a) Cure completion from calorimetry, and b) cure contraction *via* TMA, a hybrid nanocomposite 603 obtained during cure under two isothermal heat treatments.

was overcome by the thermal expansion of the composite. Often, small steps or kinks in the curve are present in the period prior to the test temperature reaching the $T_{g\infty}$ of the composite (as determined by calorimetry). For the isothermal tests, the higher-temperature isothermal conditions produced greater expansion in the last-half of the cure. This is likely due to the influence of larger quantities of thermal expansion prior to curing under isothermal conditions.

However, two possible biases in this TMA test methodology must be addressed. First, the specimens are confined between two flat surfaces, and therefore are constrained by their wetting (and later their adhesive bonding) to the surface. Therefore it is noted that these specimens are not undergoing unconstrained thermal expansion, and the confining forces of the glass may distort the cure contraction. It can be expected that this produces a linear scaling of the response compared to an unconstrained specimen; trends within a specimen scan are reliable, but the absolute value is likely not representative. Secondly, the difference in contraction and expansion presented by some of the specimens tested under differing isothermal heating conditions becomes apparent before the applied heating conditions diverges. This implies that there may be some systematic error in the calculation of dimension change by the TMA equipment when measuring deflections on this scale. However, the differences in outcome between formulations and heating conditions are significant enough (compared to the possible error) to warrant their consideration here. In all cases, subsequent cooling and reheating of the composite produced curves with no further signs of cure progression, with the thermal expansion overlapping the last segment of the curves presented above.

7.4 Discussion

It was reported in the literature that conductive composites are expected to attain conductivity as the cure progresses, in a manner that approximates a power-law[130]. Chapter 6 presented evidence that this was not necessarily accurate for a minimally-filled microcomposite, with the vitrification during cure playing a significant role in both the mid-cure and final resistivities. In the hybrid-nanocomposites studied here, the influence of vitrification on the evolved resistivity is observed during cure and also during the subsequent cooling and re-heat cycles. Addition of silver produced lower resistivities, and also assisted in preventing loss of conductivity once cure was complete. For example, in Formulation 401, the minimum resistivity achieved is comparable to that achieved by the 505 Formulation, but the sensitivity of formulation 401 to the temperature caused the composite's conductivity to degrade far more than other formulations when cyclically heated.

Similarly, the resistivity in all of the formulations tend to change with temperature conditions. Heating after an isothermal period produced a sharp and temporary increase in resistivity, even in the most highly filled composite tested (603). Crossing the glass

transition temperature, either while heating or cooling, often displayed either a sharp momentary spike or a step-change in resistivity. Transitioning from heating to cooling consistently was accompanied by sharp shifts in resistivity, but transitioning from cooling to heating did not. The difference between the last two is likely because heat-to-cool transitions only occurred above the final glass transition temperature ($T_{g\infty}$) in the rubbery state. After cure completion, periods within the rubbery state exhibited intermittent rapid spikes in resistivity, especially during the second heating cycle, with the severity of this reduced when the silver content was increased. For the most highly-filled composite, 603, the most significant effect is the change in resistance peaks from vitrification during cure or the transition from isothermal to heating conditions (which corresponds to de-vitirification while partially cured).

It is interesting to compare the results of the Formulation 601 hybrid nanocomposite to those of the 60 wt% microcomposite studied previously in Chapter 6. The 60 wt% microcomposite did not display any of the features other than the mid-cure resistivity peak produced by the vitrification during cure. While the step-wise changes in 601 led to the resistivity sequentially reducing to the final resistivity of the 60 wt% microcomposite. This shows that a low resistivity was temporarily achieved *via* the addition of nanobelts, and that the resistance was subsequently increased during repeated transitions between glassy and rubbery states during cooling and re-heating. Therefore it is likely that transitioning across the glass transition, in either direction, produces stresses that reduces the connectivity in the conductive filler network. Adding more nanobelts, such as in the 603 formulation, prevents the increases in resistance during re-heating and cooling cycles, indicating that increasing the filler content allows the nanobelts to resist or reduce the stresses, maintaining their connectivity and the resulting conductivity. Thus the benefit of adding the nanobelts, and their limitations, have been identified. Small additions of nanobelts improve conductivity as expected, but appear to be far more substantially impacted by the changes in the polymer matrix during cure and vitrification transitions than microflakes. This is likely due to the large aspect ratio and small minimum dimension of silver nanobelts compared to the micro-flakes, making their conductive network more sensitive to small relative displacements. This also indicates that the nanobelts in the composite were often not able to bond permanently to one another, either due to polymer interference or too-few nanobelt-nanobelt contacts. It also indicates that the nanobelts likely were not forming bonds with the microflakes. Since microflakes are polycrystalline, they are not expected to have readily-available flat surfaces of [111] crystal texture. Thus it is unlikely that the nanobelts can easily bond to them, since nanobelts join to one another without significant diffusion and therefore the joining is expected to be influenced strongly by mismatches in surface crystal texture and orientation, as discussed in Chapter 5.

To gain a better understanding of the mid-cure resistivity peak, previously attributed to the vitrification of the composite during cure, the *in-situ* resistivity, dimensional change, and cure conversion data for the composites are compared. When viewed together, the onset of the mid-cure resistivity peak corresponds to the minimum point of the dimensional

data; the apparent point where the thermal expansion of the material overcame the cure contraction. Factoring in vitrification effects, this can also be interpreted as the point in the cure where the material transitioned from a contracting fluid or gel behavior to a glassy solid. Isothermal conditions ease the thermal expansion of the material, allowing measurement of the the contraction from cure that is still occurring, as seen in Figures 7.5 b), 7.7 b), and 7.9 b). This also correlates to the re-establishment of minimal conductivity during the isothermal period.

Re-heating after the isothermal period de-vitrifies the composite, corresponding to a sharp temporary spike in resistivity without an accompanying sharp change in specimen dimensions. This points to a complex relationship between the conductive filler network, and the contraction and relaxation processes in the composite. This behavior is strikingly similar to the "single-replicate resistivity spikes" seen in Chapter 6, except in this case they exhibit a longer duration and are seen in all replicates. This implies that the addition of nanobelts to the system has drastically increased the likelyhood of particle-particle junctions being intolerant to polymer relaxation processes. This may be due to the nanobelts having small contact areas or glancing contact angles, increasing the likelyhood that relaxation of the epoxy when entering the rubbery state induces temporary particle separation. The step-wise and complex increases in resistivity displayed during subsequent cooling and heating cycles indicates that relaxation of the composite plays a significant role even after the cure of a minimally-filled ECA has completed.

Another important feature is the resistivity spikes displayed by 601 during its second heating cycle from the isothermal cure treatments, which rose as high as $10^5\ \Omega \cdot cm$. This is of importance, because this is as much as 3 orders of magnitude higher than the resistivity displayed by the 60 wt% microcomposite under the same conditions, where there were no spikes. This indicates that one of the simplifications of hybrid nanocomposite theory may not be applicable to the silver nanobelt/microflake system: namely that adding nanoparticles to a microcomposite does not significantly disrupt or alter the amount or nature of the expected microparticle-only network[26]. Figure 7.10 presents a comparison of pure micro- or nano-particle composites to two hybrid composites produced by the particles, demonstrating the subtle difference between the two systems. In the second system pictured, the addition of the silver nanobelts has caused them to act as spacers between poorly-connected clusters of microflakes. As such, the nanobelts appear to have become the primary critical component of the network at low filler contents, causing the 601 formulation to be strongly affected by their losses in connectivity when the composite was in the rubbery state. In the 603 formulation, there appear to be sufficient fillers that the effects of cure and vitrification are not able to reduce their connectivity by a significant degree.

The 505 and 401 composites emphasize this further, and also highlight the significance of vitrification effects on hybrid ECA composites. Based on hybrid percolation models discussed in Section 2.3, the 401 formulation should be above the percolation threshold[24–

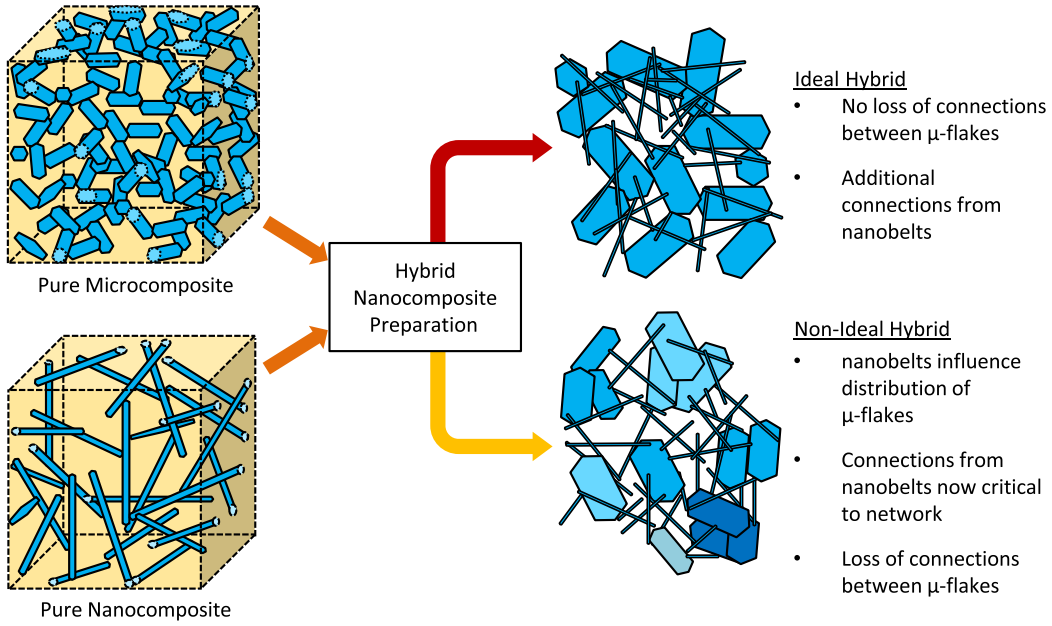

Figure 7.10: Comparison of an ideally simplified hybrid filler network to a hypothesized hybrid with discrete separations between microfillers caused by the addition of silver nanobelts.

28]. Thus this composite should be sufficiently filled, such that additional fillers would have a minimal net improvement on its conductivity. Instead, formulation 401 initially establishes a conductivity nearly identical to the 505 formulation, and then both undergo successive losses of conductivity from processes within the polymer matrix.

Interestingly, the 505 and 603 formulations each demonstrated a single replicate that achieved exceptional conductivity. The 505 formulation's exceptional specimen had the highest conductivity of all the specimens. At the point in the experiment where the other specimens of the same formulation underwent an increase in resistivity at the glass transition, the exceptional 505 specimen underwent a sharp drop of resistivity of several orders of magnitude. Also of note, both the 505 and 603 exceptional specimens did not display the same scale of random resistance spikes displayed by the other replicates and formulations during the cycling of heating and cooling. Instead, once the exceptionally low resistance was established it appeared to be highly stable, with some small spikes that correspond to the same temperatures as the far larger spikes seen in other replicates. Thus, the exceptional specimens had significant portions of their conductive filler networks that were more extensively and more stably connected than the other replicates. These behaviors imply that the nanobelts in the exceptional specimens were able to join often enough to significantly lower and stabilize the composite's resistance beyond that of the specimens with less joining. A significant detail is that the 505 and 603 formulations are the two compositions with the highest ratio of silver nanobelts to their total silver content. Fur-

thermore, the 505 formulation has the highest nanobelt fraction and the most exceptional specimen. Thus, the 505 and 603 formulations were more likely to have opportunities for stable nanobelt-nanobelt connections to form and permanently join. It is likely that the nanobelt contents and filler fractions used in this study are below some critical threshold where nanobelt-nanobelt contacts are reliably plentiful. As such, in the studies formulations such a configuration is less probable, and subject to the random distribution of the particles, and thus most likely in the formulations with the highest fractions of nanobelts. This suggests that one avenue for improvement may be to increase the nanobelt fraction of the silver content to improve the availability of nanobelt-nanobelt contacts beyond some critical threshold. The limitation to this is the significant, though not yet quantified, increase to mixture viscosity that nanobelts impart to the epoxy mixture, which reduces workability and flowability during mixing and dispensing.

Based on the previous work discussed in Chapter 6, I suggest that the conductivity of these composites may also be further improved by reducing the strong glass transition behavior of these composites, *via* the addition of a small quantity of solvent to reduce the glass transition temperatures. The current formulations have high glass transition temperatures, and are most accurately compared to the solvent-free "Ac0" formulation from Chapter 6. Addition of solvent to that system reduced the effects of vitrification, removing the mid-cure resistance peak and reducing the final conductivity. However, lowering the glass transition temperature reduces the range of operational temperatures that a composite can be practically used. Thus for low-temperature operations this provides a potential avenue for filler reductions and cost savings.

7.5 Concluding Remarks

The present hybrid nanocomposite work demonstrates that the silver nanobelts have improved the conductivity of the silver-filled ECA. It is believed that the addition of nanobelts alters the distribution and packing of silver microflakes, causing the nanobelts to be the critical component in the filler network at most filler contents. The nanobelts appear to be joining by oriented attachment to one another and thereby improving their conductivity, but are not doing so with the microflakes. For the formulations investigated, it appears that the ratio of nanobelts to total silver fillers was below some critical value that allows the nanobelt-nanobelt joints to be commonplace.

As a result, the silver nanobelt connections with the microflakes were the most common particle-particle contact, and these appear to be highly sensitive to the polymer matrix as it undergoes cure contraction, thermal expansion, and glass/rubber transitions. This produces reductions in conductivity as the composite is heated and cooled cyclically in most specimens. Exceptional specimens in the formulations with the highest, but still subcritical, nanobelt fractions exhibited sharp improvements in conductivity and improved

stability, implying that in those specimens the distribution of the particles was conducive to forming a larger number of permanent nanobelt connections.

These results indicate three potential avenues for achieving improved conductivity in the future: 1) increasing the total silver content to the $60\mu + 3\eta$ range in exchange for higher costs, 2) increasing the fraction of the total silver content that is composed of silver nanobelts, and 3) lowering the glass transition temperature to reduce disruption from the polymers as discussed in Chapter 6, at the cost of a lower range of operational temperatures. Thus, future work will be needed to investigate these relationships further, and to optimize low-cost silver nanobelt hybrid ECAs for particular operational conditions.

Chapter 8

Conclusions and Future Work

8.1 Summary

This dissertation focused on investigating epoxy-based conductive adhesive composites containing newly-developed silver nanobelts as conductive fillers. The high filler contents required in ECAs containing microparticle-only or spherical nanoparticles, and the poor stability of previous high-aspect ratio silver nanoparticles (pentagonal silver nanowires), provided an opportunity to develop and investigate better options. To do so, the synthesis methods of highly-stable silver nanobelts was investigated, obtaining better repeatability between batches. The characterization of the relationship between mixing procedures and final particle morphology achieved the capacity to select between useful morphologies, and an increase in the aspect ratio of nanobelts intended for use in ECAs. An investigation of the nanobelts as a deposited coating, outside of an ECA via calorimetry and electrical resistance measurement, revealed that the particles could be induced to undergo merging of their surfaces to form a conductive network. Studies of microcomposite-based ECAs studied the relationship between the cure process, glass transition properties, and the evolved electrical properties. They were performed using *in-situ* electrical resistance measurements in a newly developed probe-mold and comparing the results to calorimetry measurements. Following this, similar investigations of hybrid nanocomposites containing silver nanobelts were performed. For the latter study, measurements of the composite contraction taken by thermo-mechanical analyzer were included, and a variety of ECA formulations and heat treatments were compared. This study also included the heating and cooling processes after cure was complete, from which additional vital data was collected. The specific conclusions of the thesis are listed in the following section.

8.2 Thesis Conclusions

The following conclusions can be drawn from this thesis:

1) The addition of silver nanobelts to epoxy does not appear to have a significant or practical influence on the cure behaviour or glass transition temperature. Although changes to these properties were measurable when nanobelts were added at high filler contents, the changes observed were of the same size as those produced by the addition of much smaller concentrations of solvent. Additionally, these nanobelt concentrations necessary to produce these observable changes were far greater than those that would be practical for use.

2) I suggest that comparing nanocomposite filler content to cure or glass transition properties obtained by traditional methods of cure analysis is not as informative as typically considered in the literature. Comparing $T_{g\infty}$ or cure rate to as-mixed composition did not reliably provide useful results, due to complications introduced by other factors, such as residual solvent. Instead it is demonstrated that effective analysis is better obtained by varying the composition and test conditions, while comparing several properties to one another, such as the $T_{g\infty}$, cure rate, temperature conditions, and independently measured *in-situ* conductivity or dimensional change. Correlating these various properties to one another allowed identification of complex behaviors which would have been overlooked if the final properties were only correlated with the composition.

3) I report for the first time that, contrary to the previous reports by the literature, the resistivity of a curing thermoset ECA does not necessarily follow a power-law reduction throughout the composite curing. Instead the evolving resistivity is sensitive to the cure process and glass transition properties of the composite throughout cure. This can drastically influence the evolution of final conductivity: a) The mid-cure vitrification, and its associated loss of conductivity during continuing cure, disrupts the conductive filler network and produces lasting reductions in conductivity. b) Reductions to glass transition temperature throughout cure (and thus a reduction to the magnitude of the in-cure vitrification effect) typically reduced the final resistivity of the composite. This can be achieved using small concentrations of solvent in the ECA, added prior to curing. However, such a reduction will reduce the maximum operating temperature of that ECA. c) Conductive networks composed of silver nanobelts are significantly more sensitive to crossing the composite glass transition than silver microparticle, likely owing to the smaller contact areas between particles, and reduced pinning by other particles. The anomalies in conductivity caused by this can be suppressed by increasing silver filler content, likely confining nanobelt mobility.

4) As expected, the addition of small weight fractions of silver nanobelts to a silver microflake ECA reduced the resistivity of the ECA: a) The sensitivity of the nanobelts' connectivity allowed the observation that the addition of nanobelts affected the distribution of filler particles, such that the hybrid composite was not an un-biased super-position of two conductive filler networks. Instead, the nanobelts acted as spacers, reducing the likelihood

of direct contact between microparticle clusters. In turn, the silver nanobelts acted as the critical conductive pathway in the hybrid composite. b) In a minimally filled (401) formulation, predicted to be percolated based on literature models, the resistivity is initially equivalent to a more highly filled formulation, until the glass transition behavior negatively impacted the connectivity of the filler network: the two formulations present differing degrees of conductivity reduction associated with the glass transition. This indicates that the silver content required to obtain acceptable conductivity in silver nanobelt hybrid ECAs may be substantially reduced if this disruptive polymer effect can be reduced.

5) Silver nanobelts have the capacity to merge and establish conductive connections at temperatures below 180°C, analogous to resistance reductions *via* sintering but without instability from diffusion. Outside of ECA mixtures this produces significant ($> 95\%$) reductions in resistivity, indicating that silver nanobelts can be expected to produce similar reductions during the cure of an ECA with favorable conditions. When this was investigated in hybrid nanocomposites, it was determined: a) In most cases the disruptive effect of the ECA cure and vitrification appears to strongly influence the network when nanobelts are included, likely because nanobelts are unable to easily join to silver microflakes; b) In two replicates, the hybrid composite underwent a large reduction of resistance at a temperature where all others of similar composition underwent an increase due to glass-transition and cure related disruptive effects. After this, no further disruptions from changing temperatures were seen. These composites contained the highest ratio of silver nanobelts compared to total silver content of the formulations studied. This implies that, in those specimens, the nanobelt content and their distribution in the composite were randomly favorable for forming permanent nanobelt-nanobelt connections than the other formulations. However, that this happened in only one replicate indicates the nanobelt content is below a critical threshold that would achieve this result reliably. The nanobelt-nanobelt joints appear to prevent the loss of connectivity associated with the anomaly-producing polymer-related behaviors, and substantially improve final conductivity. Increasing the nanobelt fraction of the filler content filler may increase the probability of achieving plentiful nanobelt joining in all specimens.

6) The family of nanoparticles closely related to silver nanobelts have a shape-selective assembly process governing their final morphology. This is dependent on the interaction of the PMAA capping agent with the surfaces of the growing particles and their reaction solution, sensitive to pH and mixing conditions: a) In contrast to the literature, silver nanobelts produced by the studied process are very rapidly synthesized in process that is not kinetically controlled; b) various other useful morphologies are possible for other applications; and c) the developed understanding and control of the relationship between mixing conditions and final morphology produced an order of magnitude improvement in the aspect ratio of silver nanobelts intended for ECA use.

8.3 Recommendations and Future Work

The following future work can be done to further improve the developed materials and the scientific knowledge of their surrounding fields. Briefly:

In Chapter 6 it was seen that the effect of the mid-cure vitrification on the evolving resistivity could be reduced by lowering the glass transition *via* solvents. In Chapter 7, it was seen that this is also true for the hybrid nanocomposites, alongside indications that the nanocomposites may be capable of significantly improved conductivities at low silver content if this disruption were minimized. Similarly, it was hypothesized that the nanobelts were typically unable to join during curing due to this disruption by the matrix glass transitions. Therefore it is recommended to characterize the hypothesized relationship between $T_{g\infty}$ (which governs maximum operational temperature as approximately $T_{g\infty} - 50$ °C to $T_{g\infty} - 40$ °C), with respect to conductivity. This may also be done comparing glass transition to the filler content required to reach a desired conductivity. Durability testing by temperature cycling, and electron microscopy, can be used to determine if the nanobelts are undergoing joining during the cure of these modified epoxies.

Commercially available ECAs, and those in development containing other nanofillers or other polymers, are likely influenced by processes similar to those characterized in this thesis. Therefore, it would be of value to apply the developed methodologies to a wide variety of composites, both from the market and from the scientific literature. Characterizing the evolving conductivity in relationship to the applied conditions and material properties of various composites can lead to a wider model of the processes under study. This may lead to further optimization of the cure treatments applied to commercial ECAs, improving their conductivity, and a better understanding of the underlying material physics.

In Chapter 4, it was noted that the physical mixing process of the silver nitrate solution had a large influence on the rate of reaction and obtained morphology of the nanobelts. It has been hypothesized that minimal mixing promoted the formation of a saturated solution phase. In comparison to the well mixed condition, it is hypothesized that the resulting equilibrium kinetics in the saturated solution caused a higher fraction of the silver ions to be sequestered as silver trimer clusters. If this is the case, it is hypothesized that a similar effect can be achieved in a well-mixed solution by introducing sufficient co-ions to keep the silver ions (such as sodium) at their saturation point. Future work on this topic may lead to stable enough stock solutions that scaling and industrialization of the nanobelt synthesis is affordable.

In Chapter 7 it was seen that the hybrid nanocomposite of silver nanobelts and microflakes was not ideally distributed, in spite of the carefully controlled dispersion methods. Instead, the nanobelts and microflakes appear to have undergone a small degree of sequestration, leaving one of them the critical component of the conductive network. Based on

the hybrid percolation theory this is a potential limitation, and it should be possible to improve the synergy of the hybrid. One option of doing so is to replace the silver microflakes with a nanomaterial of different morphology (or chemistry) than the nanobelts. For example, in Chapter 4 it was demonstrated that porous 2-dimensional sheets of nanobelt-like "nanosheets" could be manufactured. These have the same crystallography and thickness as a silver nanobelt, and therefore would likely be more available than the silver microflakes to join to the nanobelts during cure. This may lead to further improvements in conductivity, reliability, reductions in total filler content.

References

[1] G. Rivers, A. Rogalsky, P. Lee-Sullivan, and B. Zhao, "Thermal analysis of epoxy-based nanocomposites: Have solvent effects been overlooked?" *Journal of Thermal Analysis and Calorimetry*, 2nd ser., vol. 119, pp. 797–805, 2015.

[2] A. E. Marzbanrad, G. Rivers, A. Rogalsky, P. Lee-Sullivan, B. Zhao, and N. Y. Zhou, "Highly repeatable kinetically-independent synthesis of one- and two-dimensional silver nanostructures by oriented attachment," *RSC Adv*, vol. 6, pp. 61 641–61 649, 2016. DOI: 10.1039/C6RA08031F.

[3] G. Rivers, P. Lee-Sullivan, and B. Zhao, "Silver nanobelts: Capping agent influence on synthesis assembly and annealed joining," in *2016 International Conference on Nanojoining and Microjoining*, 2016.

[4] G. Rivers, E. Marzbanrad, M. D. Hook, P. Lee-Sullivan, Y. N. Zhou, and B. Zhao, "Highly-stable silver nanobelts joined via diffusion-free attachment," *Nanotechnology*, vol. 27, no. 29, Jun. 2016.

[5] G. Rivers, P. Lee-Sullivan, B. Zhao, A. Chen, J. Persic, and R. Lyn, "In-situ resistance characterization during cure progression of a conductive adhesive," in *ICSR (Soldering and Reliability) 2016 Conference Proceedings*, 2016.

[6] J. C. Agar, K. J. Lin, R. Zhang, J. Durden, K. Lawrence, K. S. Moon, and C. P. Wong, "Deconstructing the myth of percolation in electrically conductive adhesives and its implications," in *2010 Proceedings 60th Electronic Components and Technology Conference (ECTC)*, 2010, pp. 1713–1718. DOI: 10.1109/ECTC.2010.5490742.

[7] H. Jiang, K.-S. Moon, J. Lu, and C. Wong, "Conductivity enhancement of nano silver-filled conductive adhesives by particle surface functionalization," *Journal of electronic materials*, vol. 34, no. 11, pp. 1432–1439, 2005.

[8] S. Fenglian, L. Yang, and W. Jiabing, "Improving the solderability and electromigration behavior of low-ag snagcu soldering," in *Thermal, Mechanical and Multi-Physics Simulation and Experiments in Microelectronics and Microsystems (EuroSimE), 2011 12th International Conference on*, 2011, pp. 1/5–5/5. DOI: 10.1109/ESIME.2011.5765807.

[9] C. E. Ho, S. C. Yang, and C. R. Kao, "Interfacial reaction issues for lead-free electronic solders," *Journal of Materials Science: Materials in Electronics*, vol. 18, no. 1, pp. 155–174, 2007. DOI: 10.1007/s10854-006-9031-5.

[10] K. I. Winey and V. Ra., "Polymer nanocomposites," *MRS Bull*, vol. 32, pp. 314–9, 2007.

[11] F. Hussain, M. Hojjati, M. Okamoto, and R. E. Gorga, "Review article: Polymer-matrix nanocomposites, processing, manufacturing, and application: An overview," *Journal of Composite Materials*, vol. 40, no. 17, pp. 1511–1575, 2006. DOI: 10.1177/0021998306067321.

[12] O. Breuer and U. Sundararaj, "Big returns from small fibers: A review of polymer/carbon nanotube composites," *Polymer Composites*, vol. 25, no. 6, pp. 630–645, 2004. DOI: 10.1002/pc.20058.

[13] M. Moniruzzaman and K. I. Winey, "Polymer nanocomposites containing carbon nanotubes," *Macromolecules*, vol. 39, no. 16, pp. 5194–5205, 2006. DOI: 10.1021/ma060733p.

[14] N. G. Sahoo, S. Rana, J. W. Cho, L. Li, and C. S. H., "Polymer nanocomposites based on functionalized carbon nanotubes," *Prog in Polym Sci*, vol. 35, pp. 837–67, 2010.

[15] H. Kim, A. A. Abdala, and M. Cw., "Graphene/polymer nanocomposites," *Macromolecules*, vol. 43, pp. 6515–30, 2010.

[16] J. R. Potts, D. R. Dreyer, C. W. Bielawski, and R. Rs., "Graphene-based polymer nanocomposites," *Polymer*, vol. 52, pp. 5–25, 2011.

[17] T. Ramanathan, A. AbdalaA, S. Stankovich, D. A. Dikin, M. Herrera-Alonso, R. D. Pinerm, D. H. Adamson, H. C. Schniepp, X. Chen, R. S. Ruoff, S. T. Nguyen, I. A. Aksay, R. K. Prud'Homme, and L. C. Brinson, "Functionalized graphene sheets for polymer nanocomposites," *Nat Nano*, vol. 3, no. 6, pp. 327–331, 2008. DOI: 10.1038/nnano.2008.96.

[18] R. N. Das, F. D. Egitto, and V. R. Markovich, "Nano and microfilled conducting adhesives for zaxis interconnections: New direction for highspeed, highdensity, organic microelectronics packaging," *Circuit World*, vol. 34, no. 1, pp. 3–12, 2008. DOI: 10.1108/03056120810848743.

[19] M. Fang, K. Wang, H. Lu, Y. Yang, and S. Nutt, "Covalent polymer functionalization of graphene nanosheets and mechanical properties of composites," *J. Mater. Chem.*, vol. 19, pp. 7098–7105, 38 2009. DOI: 10.1039/B908220D.

[20] Y. Li, D. Lu, and C. Wong, *Electrical Conductive Adhesives with Nanotechnologies*. Springer US, 2009.

[21] F. L. Matthews and R. D. Rawlings, *Composite Materials: Engineering and Science*. Chapman & Hall, 1994.

[22] F. L. Matthews and R. D. Rawlings, *Composite Materials: Engineering and Science*. Chapman & Hall, 1994.

[23] M. E. AZIZ, "A study on the effect of hardener on the mechanical properties of epoxy resin," Master's thesis, University of Technology, 2010.

[24] R. Taherian, "Development of an equation to model electrical conductivity of polymer-based carbon nanocomposites," *ECS Journal of Solid State Science and Technology*, vol. 3, no. 6, pp. M26–M38, 2014. DOI: 10.1149/2.023406jss.

[25] E. J. Garboczi, K. A. Snyder, J. F. Douglas, and M. F. Thorpe, "Geometrical percolation threshold of overlapping ellipsoids," *Phys. Rev. E*, vol. 52, pp. 819–828, 1 1995. DOI: 10.1103/PhysRevE.52.819.

[26] Y. Chen, S. Wang, F. Pan, and J. Zhang, "A numerical study on electrical percolation of polymer-matrix composites with hybrid fillers of carbon nanotubes and carbon black," *Journal of Nanomaterials*, vol. 2014, no. 25, p. 9, 2014. DOI: http://dx.doi.org/10.1155/2014/614797.

[27] S. Sreenivasan, D. R. Baker, G. Paul, and H. E. Stanley, "Discrepancy between monte-carlo results and analytic values for the average excluded volume of rectangular prisms," *Eprint arXiv:cond-mat/0208145*, Aug. 2002.

[28] M. O. Saar and M. Manga, "Continuum percolation for randomly oriented soft-core prisms," *Phys. Rev. E*, vol. 65, p. 056 131, 5 2002. DOI: 10.1103/PhysRevE.65.056131.

[29] K. Pashayi, H. R. Fard, F. Lai, S. Iruvanti, J. Plawsky, and et al., "High thermal conductivity epoxy-silver composites based on self constructed nanostructured metallic networks," *J Appl Phys*, vol. 111, no. 10, 104310 [6pp.] May 2012.

[30] W. J. Jeong, H. Nishikawa, D. Itou, and T. Takemoto, "Electrical characteristics of a new class of conductive adhesive," *Mater Trans*, vol. 46, no. 10, pp. 2276–2281, Oct. 2005.

[31] H. Jiang, K. S. Moon, Y. Li, and W. Cp., "Surface functionalized silver nanoparticles for ultrahigh conductive polymer composites," *Chem Mater*, vol. 18, p. 2969, 2006.

[32] J. Bai and A. Allaoui, "Effect of the length and the aggregate size of {mwnts} on the improvement efficiency of the mechanical and electrical properties of nanocomposite-sexperimental investigation," *Composites Part A: Applied Science and Manufacturing*, vol. 34, no. 8, pp. 689 –694, 2003. DOI: http://dx.doi.org/10.1016/S1359-835X(03)00140-4.

[33] R. Gangopadhyay and A. De, "Conducting polymer nanocomposites: A brief overview," *Chemistry of Materials*, vol. 12, no. 3, pp. 608–622, 2000. DOI: 10.1021/cm990537f.

[34] D. Chen, X. Qiao, X. Qiu, F. Tan, J. Chen, and R. Jiang, "Effect of silver nanostructures on the resistivity of electrically conductive adhesives composed of silver flakes," *Journal of Materials Science: Materials in Electronics*, vol. 21, no. 5, pp. 486–490, 2010. DOI: 10.1007/s10854-009-9943-y.

[35] A. Yu, P. Ramesh, X. Sun, E. Bekyarova, M. E. Itkis, and R. C. Haddon, "Enhanced thermal conductivity in a hybrid graphite nanoplatelet carbon nanotube filler for epoxy composites," *Advanced Materials*, vol. 20, no. 24, pp. 4740–4744, 2008. DOI: 10.1002/adma.200800401.

[36] I. Balberg, C. H. Anderson, S. Alexander, and N. Wagner, "Excluded volume and its relation to the onset of percolation," *Phys. Rev. B*, vol. 30, pp. 3933–3943, 7 1984. DOI: 10.1103/PhysRevB.30.3933.

[37] B. M. Amoli, E. Marzbanrad, A. Hu, Y. Zhou, and B. Zhao, "Electrical conductive adhesives enhanced with high-aspect-ratio silver nanobelts," *Macromol Mater Eng*, vol. 299, no. 6, pp. 739–747, Jun. 2014.

[38] B. Meschi Amoli, A. Hu, N. Y. Zhou, and B. Zhao, "Recent progresses on hybrid micro–nano filler systems for electrically conductive adhesives (ecas) applications," *Journal of Materials Science: Materials in Electronics*, vol. 26, no. 7, pp. 4730–4745, 2015. DOI: 10.1007/s10854-015-3016-1.

[39] Y. Li and W. C. P., "Monolayer protection for eletrochemical migration control in silver nanocomposite," *Appl Phys Lett*, vol. 89, no. 11, 112112 [3pp.] Sep. 2006.

[40] G. Suriati, M. Mariatti, and A. Azizan, "Silver-filled epoxy composites: Effect of hybrid and silane treatment on thermal properties," *Polymer Bulletin*, vol. 70, no. 1, pp. 311–323, 2013. DOI: 10.1007/s00289-012-0808-9.

[41] K. Sanada, Y. Tada, and Y. Shindo, "Thermal conductivity of polymer composites with close-packed structure of nano and micro fillers," English, *Composites Part A*, vol. 40, no. 6-7, pp. 724–730, 2009. DOI: 10.1016/j.compositesa.2009.02.024.

[42] G. Zheming, L. Chunzhong, W. Gengchao, Z. Ling, C. Qilin, L. Xiaohui, W. Wendong, and J. Shilei, "Electrical properties and morphology of highly conductive composites based on polypropylene and hybrid fillers," *Journal of Industrial and Engineering Chemistry*, vol. 16, no. 1, pp. 10 –14, 2010. DOI: http://dx.doi.org/10.1016/j.jiec.2010.01.028.

[43] K. L. Chan, M. Mariatti, Z. Lockman, and S. L. C., "Effects of the size and filler loading on the properties of copper- and silver-nanoparticlefilled epoxy composites," *J Appl Polym Sci*, vol. 121, pp. 3145–52, 2011.

[44] D. Chen, X. Qiao, X. Qiu, F. Tan, J. Chen, and R. Jiang, "Effect of silver nanostructures on the resistivity of electrically conductive adhesives composed of silver flakes," *J Mater Sci: Mater Electron*, vol. 21, no. 5, pp. 486–490, May 2009.

[45] H. W. Cui, Q. Fan, D. S. Li, and T. X., "Formulation and characterization of electrically conductive adhesives for electronic packaging," *J Adhes.*, vol. 89, pp. 19–36, 2013.

[46] H.-w. Cui, Q. Fan, and D.-s. Li, "Novel flexible electrically conductive adhesives from functional epoxy, flexibilizers, micro-silver flakes and nano-silver spheres for electronic packaging," *Polymer International*, vol. 62, no. 11, pp. 1644–1651, 2013. DOI: 10.1002/pi.4461.

[47] R. N. Das, J. M. Lauffer, K. Knadle, M. Vincent, M. D. Poliks, and M. V. R., "Nano and and micro materials in a pb-free world," *IEEE Electron Compon and Tech Conf.*, pp. 1228–33, 2011.

[48] J. Jordan, K. I. Jacob, R. Tannenbaum, M. A. Sharaf, and I. Jasiuk, "Experimental trends in polymer nanocomposites-a review," *Mater Sci Eng A*, vol. 393, pp. 1–11, 2005.

[49] T. b. Song, Y. Chen, C. h. Chung, Y. M. Yang, B. Bob, H. s. Duan, G. Li, K. n. Tu, Y. Huang, and Y. Yang, "Nanoscale joule heating and electromigration enhanced ripening of silver nanowire contacts," *ACSnano*, vol. 8, pp. 2804–2811, 2014.

[50] Y. H. Wang, N. N. Xiong, H. Xie, Y. Z. Zhao, and J. Li, "New insights into silver nanowires filled electrically conductive adhesives," *Journal of Materials Science: Materials in Electronics*, vol. 26, no. 2, pp. 621–629, 2015. DOI: 10.1007/s10854-014-2475-0.

[51] L. Ye, Z. Lai, and J. Liu, "Effect of ag particle size on electrical conductivity of isotropically conductive adhesives," *IEEE Trans Electron Packag Manuf*, vol. 22, no. 4, pp. 299–302, Oct. 1999.

[52] Y. H. Wang, N. N. Xiong, Z. L. Li, H. Xie, J. Z. Liu, J. Dong, and J. Z. Li, "A comprehensive study of silver nanowires filled electrically conductive adhesives," *Journal of Materials Science: Materials in Electronics*, vol. 26, no. 10, pp. 7927–7935, 2015. DOI: 10.1007/s10854-015-3446-9.

[53] Z. X. Zhang, X. Y. Chen, and F. Xiao, "The sintering behavior of electrically conductive adhesives filled with surface modified silver nanowires," *J Adhes Sci Technol*, vol. 25, no. 13, pp. 1465–1480, Apr. 2011.

[54] R. Zhang, W. Lin, K. S. Moon, and W. C.P., "Fast preparation of printable highly conductive polymer nanocomposites by thermal decomposition of silver carboxylate and sintering of silver nanoparticles," *ACS Appl Matls And Interfaces*, vol. 2, no. 9, pp. 2637–2645, Aug. 2010.

[55] B. M. Amoli, S. Gumfekar, A. Hu, N. Zhou, and B. Zhao, "Thiocarboxylate functionalization of silver nanoparticles: Effect of chain length on the electrical conductivity of nanoparticles and their polymer composites," *J Mater Chem*, vol. 22, pp. 20 048–56, 2012.

[56] Y.-S. Jun, S. Sy, W. Ahn, H. Zarrin, L. Rasen, R. Tjandra, B. M. Amoli, B. Zhao, G. Chiu, and A. Yu, "Highly conductive interconnected graphene foam based polymer composite," *Carbon*, vol. 95, pp. 653 –658, 2015. DOI: http://dx.doi.org/10.1016/j.carbon.2015.08.079.

[57] B. M. Amoli, J. Trinidad, G. Rivers, S. Sy, P. Russo, A. Yu, N. Y. Zhou, and B. Zhao, "Sds-stabilized graphene nanosheets for highly electrically conductive adhesives," *Carbon*, vol. 91, pp. 188–199, 2015.

[58] J. Trinidad, B. M. Amoli, W. Zhang, R. Pal, and B. Zhao, "Effect of sds decoration of graphene on the rheological and electrical properties of graphene-filled epoxy/ag composites," *Journal of Materials Science: Materials in Electronics*, pp. 1–9, 2016. DOI: 10.1007/s10854-016-5434-0.

[59] T. Kuilla, S. Bhadra, D. Yao, N. H. Kim, S. Bose, and J. H. Lee, "Recent advances in graphene based polymer composites," *Progress in Polymer Science*, vol. 35, no. 11, pp. 1350 –1375, 2010. DOI: http://dx.doi.org/10.1016/j.progpolymsci.2010.07.005.

[60] S. G. Miller, J. L. Bauer, M. J. Maryanski, P. J. Heimann, J. P. Barlow, G. J-M, and A. R. E., "Characterization of epoxy functionalized graphite nanoparticles and the physical properties of epoxy matrix nanocomposites," *Compos Sci Tech*, vol. 70, pp. 1120–5, 2010.

[61] O Maxian, D Pedrazzoli, and I Manas-Zloczower, "Modeling the electrical percolation behavior of hybrid nanocomposites based on carbon nanotubes and graphene nanoplatelets," *Materials Research Express*, vol. 2, no. 9, p. 095 013, 2015.

[62] S. P. Gumfekar, A. Chen, and B. Zhao, "Silver-polyaniline-epoxy electrical conductive adhesives - a percolation threshold analysis," in *Electronics Packaging Technology Conference (EPTC), 2011 IEEE 13th*, 2011, pp. 180–184. DOI: 10.1109/EPTC.2011.6184411.

[63] R. C.N.R, A. K. Sood, K. S. Subrahmanyam, and G. A., "Graphene: The new two dimensional nanomaterial," *Angew Chem Int Ed*, vol. 48, pp. 7752–77, 2009.

[64] P. Russo, A. Hu, and G. Compagnini, "Synthesis, properties and potential applications of porous graphene: A review," *Nano-Micro Letters*, vol. 5, no. 4, pp. 260–273, 2013. DOI: 10.1007/BF03353757.

[65] V. Singh, D. Joung, L. Zhai, S. Das, S. I. Khondaker, and S. S., "Graphene based materials: Past, present and future," *Prog Mater Sci*, vol. 56, pp. 1178–271, 2011.

[66] L. M., 3rd. United States: Barrons, 2007.

[67] C. for Physics of the Royal Swedish Academy of Sciences, "Scientific background on the nobel prize in physics 2010 - graphene," in, Royal Swedish Academy of Sciences, 2010.

[68] A. Graff, D. Wagner, H. Ditlbacher, and U. Kreibig, "Silver nanowires," *The European Physical Journal D - Atomic, Molecular, Optical and Plasma Physics*, vol. 34, no. 1, pp. 263–269, 2005. DOI: 10.1140/epjd/e2005-00108-7.

[69] P. Peng, A. Hu, H. Huang, G. A. P., Z. B., and Z. Y. N., "Room-temperature pressureless bonding with silver nanowire paste: Towards organic electronic and heat-sensitive functional devices packaging," *J Mater Chem*, vol. 22, pp. 12 997–13 001, May 2012.

[70] P. Peng, A. Hu, A. P. Gerlich, G. Zou, L. Liu, and Z. Y. N., "Joining of silver nanomaterials at low temperatures: Processes properties, and applications," *ACS Appl Mater Interfaces*, vol. 7, pp. 12 597–12 618, May 2015.

[71] E. Marzbanrad, G. Rivers, P. Peng, B. Zhao, and Z. N. Y., "How morphology and surface crystal texture affect thermal stability of a metallic nanoparticle: The case of silver nanobelts and pentagonal silver nanowires," *Phys Chem Chem Phys*, vol. 17, no. 1, pp. 315–324, Jan. 2015.

[72] M. E, H. A, Z. B., and N. Y. Zhou, "Room temperature nanojoining of triangular and hexagonal silver nanodisks," *J Phys Chem C*, vol. 117, no. 32, pp. 16 665–16 676, Aug. 2013.

[73] X. He, X. Zhao, Y. Li, and X. Sui, "Shape-controlled synthesis for silver: Triangular/hexagonal nanoplates, chain-like nanoplate assemblies, and nanobelts," *J Mater Res*, vol. 24, no. 7, pp. 2200–2209, Jul. 2009.

[74] M. H. Kim, D. K. Yoon, and I. S. H., "Growth pathways of silver nanoplates in kinetically controlled synthesis: Bimodal versus unimodal growth," *RCS Adv*, vol. 5, p. 14 266, Jan. 2015.

[75] X. Tian, K. Chen, and G. Cao, "Seedless, surfactantless photoreduction synthesis of silver nanoplates," *Materials Letters*, vol. 60, no. 6, pp. 828 –830, 2006. DOI: http://dx.doi.org/10.1016/j.matlet.2005.10.025.

[76] X. Tian, W. Wang, and G. Cao, "A facile aqueous-phase route for the synthesis of silver nanoplates," *Materials Letters*, vol. 61, no. 1, pp. 130 –133, 2007. DOI: http://dx.doi.org/10.1016/j.matlet.2006.04.021.

[77] X. Tian, J. Li, and S. Pan, "Facile synthesis of single-crystal silver nanowires through a tannin-reduction process," *Journal of Nanoparticle Research*, vol. 11, no. 7, p. 1839, 2009. DOI: 10.1007/s11051-009-9700-4.

[78] Y. Xiong, I. Washio, J. Chen, M. Sadilek, and Y. Xia, "Trimeric clusters of silver in aqueous agno3 solutions and their role as nuclei in forming triangular nanoplates of silver," *Angew Chem Int Ed*, vol. 46, pp. 4917–4921, 2007.

[79] X. Lu, M. Rycenga, S. E. Skrabalak, B. Wiley, and Y. Xia, "Chemical synthesis of novel plasmonic nanoparticles," *Annual Review of Physical Chemistry*, vol. 60, no. 1, pp. 167–192, 2009, PMID: 18976140. DOI: 10.1146/annurev.physchem.040808.090434.

[80] K. M. A. El-Nour, A. Eftaiha, A. Al-Warthan, and R. A. Ammar, "Synthesis and applications of silver nanoparticles," *Arabian Journal of Chemistry*, vol. 3, no. 3, pp. 135 –140, 2010. DOI: http://dx.doi.org/10.1016/j.arabjc.2010.04.008.

[81] J. Zeng, X. Xia, M. Rycenga, P. Henneghan, Q. Li, and Y. Xia, "Successive deposition of silver on silver nanoplates: Lateral versus vertical growth," *Angewandte Chemie International Edition*, vol. 50, no. 1, pp. 244–249, 2011. DOI: 10.1002/anie.201005549.

[82] H. Huang, C. Zhi, P. Jiang, Y Golberg D. Bando, and T. T., "Polyhedral oligosilsesquioxane-modified boron nitride nanotube based epoxy nanocomposites: An ideal dielectric material with high thermal conductivity," *Adv. Funct. Mater.*, pp.8, 2012. DOI: 10.1002/adfm.201201824.

[83] J. A. Throckmorton, A. L. Watters, X. Geng, and G. R. Palmese, "Room temperature ionic liquids for epoxy nanocomposite synthesis: Direct dispersion and cure," *Composites Science and Technology*, vol. 86, pp. 38 –44, 2013. DOI: http://dx.doi.org/10.1016/j.compscitech.2013.06.016.

[84] Z. Han and A. Fina, "Thermal conductivity of carbon nanotubes and their polymer nanocomposites: A review," *Progress in Polymer Science*, vol. 36, no. 7, pp. 914 –944, 2011, Special Issue on Composites. DOI: http://dx.doi.org/10.1016/j.progpolymsci.2010.11.004.

[85] J. CESARANO, I. A. AKSAY, and A. BLEIER, "Stability of aqueous -al2o3 suspensions with poly(methacrylic acid) polyelectrolyte," *Journal of the American Ceramic Society*, vol. 71, no. 4, pp. 250–255, 1988. DOI: 10.1111/j.1151-2916.1988.tb05855.x.

[86] Y. Long, J. Wu, H. Wang, X. Zhang, N. Zhao, and J. Xu, "Rapid sintering of silver nanoparticles in an electrolyte solution at room temperature and its application to fabricate conductive silver films using polydopamine as adhesive layers," *J Mater Chem*, vol. 21, no. 13, pp. 4875–4881, Feb. 2011.

[87] J. Lee, P. Lee, H. Lee, D. Lee, S. S. Lee, and K. S. H., "Very long ag nanowire synthesis and its application in a highly transparent, conductive and flexible metal electrode touch panel," *Nanoscale*, vol. 4, no. 20, pp. 6408–6414, Aug. 2012.

[88] H. A. Alarifi, M. a. C. Atis, H. A., Y. M., and Z. N. Y., "Molecular dynamics simulation of sintering and surface premelting," *Mater T JIM*, vol. 54, no. 6, pp. 884–889, May 2013.

[89] S. Iwama and K. Hayakawa, "Sintering of ultrafine metal powders ii. neck growth stage of au, al, and cu," *Jpn J Appl Phys*, vol. 20, no. 2, pp. 335–340, Feb. 1981.

[90] J. Sopousek, J. Bursik, J. Zalesak, and Z. Pesina, "Silver nanoparticles sintering at low temperature on a copper substrate: In situ characterization under inert atmosphere and air," *J Min Metall Sect B-Metall*, vol. 48, no. 1, pp. 63–71, Oct. 2012.

[91] K. S. Moon, H. Dong, R. Maric, S. Pothukuchi, A. Hunt, Y. Li, and W. C. P., "Thermal behavior of silver nanoparticles for low-temperature interconnect applications," *J Electron Mater*, vol. 34, no. 2, pp. 168–175, Aug. 2005.

[92] D. P. Langley, M. Lagrange, G. Giusti, C. Jiménez, Y. Bréchet, N. D. Nguyen, and B. D., "Metallic nanowire networks: Effects of thermal annealing on electrical resistance," *Nanoscale*, vol. 6, no. 22, pp. 13 535–13 543, Sep. 2014.

[93] Y. Tao, Y. Tao, L. Wang, B. Wang, Z. Yang, and Y. Tai, "High-reproducibility, flexible conductive patterns fabricated with silver nanowire by drop or fit-to-flow method," *Nanoscale Research Letters*, vol. 8, no. 1, p. 147, 2013. DOI: 10.1186/1556-276X-8-147.

[94] P. Peng, A. Hu, and Z. Y. N., "Laser sintering of silver nanoparticle thin films: Microstructure and optical properties," *Appl Phys A*, vol. 108, pp. 685–691, May 2012.

[95] S. B. Sepulveda-Mora and C. S. G., "Figures of merit for high-performance transparent electrodes using dip-coated silver nanowire networks," *J Nanomater.*, vol. 2012, 286104 [7pp.] Aug. 2012.

[96] Y. Hu, J. Shen, N. Li, H. Ma, M. Shi, B. Yan, W. Huang, W. Wang, and M. Ye, "Comparison of the thermal properties between composites reinforced by raw and amino-functionalized carbon materials," *Comp Sci and Tech*, vol. 70, pp. 2176–82, 2010.

[97] J. Y. Lee, S. T. Connor, Y. Cui, and P. Peumans, "Solution-processed metal nanowire mesh transparent electrodes," *Nano Lett*, vol. 8, no. 2, pp. 689–692, Jan. 2008.

[98] E. C. Garnett, W. Cai, J. J. Cha, F. Mahmood, S. T. Connor, M. G. Christoforo, Y. Cui, M. D. McGehee, and B. M. L., "Self-limited plasmonic welding of silver nanowire junctions," *Nat Mater*, vol. 11, no. 3, pp. 241–249, Mar. 2012.

[99] J. A. Spechler and A. Cb., "Direct-write pulsed laser processed silver nanowire networks for transparent conducting electrodes," *Appl Phys A*, vol. 108, no. 1, pp. 25–28, 2012.

[100] T. Tokuno, M. Nogi, M. Karakawa, J. Jiu, T. T. Nge, Y. Aso, and K. Suganuma, "Fabrication of silver nanowire transparent electrodes at room temperature," *Nano Res*, vol. 4, no. 12, pp. 1215–1222, Dec. 2011.

[101] Y. Lu, J. Y. Huang, C. Wang, S. Sun, and J Lou, "Cold welding of ultrathin gold nanowires," *Nat Nanotechnol*, no. 5, pp. 218–224, Feb. 2010.

[102] P. Peng, L. Liu, A. P. Gerlich, A. Hu, and Z. Y. N., "Self-oriented nanojoining of silver nanowires via surface selective activation," *Part Part Syst Charact*, vol. 30, no. 5, pp. 420–426, May 2013.

[103] M. Niederberger and H. Cölfen, "Oriented attachment in nanocrystals: Non-classical crystallization mechanisms based on nanoparticle assembly," *Phys. Chem. Chem. Phys*, vol. 8, no. 28, pp. 3271–3287, Apr. 2006.

[104] M. Giersig, I. Pastoriza-Santos, and L. M. Liz-Marzán, "Evidence of an aggregative mechanism during the formation of silver nanowires in n,n-dimethylformamide," *J Mater Chem*, vol. 14, no. 4, pp. 607–610, Nov. 2003.

[105] S. Karim, M. E. Toimil-Molares, A. G. Balogh, W. Ensinger, T. W. Cornelius, E. U. Khan, and R. Neumann, "Morphological evolution of au nanowires controlled by rayleigh instability," *Nanotechnology*, vol. 17, no. 24, pp. 5954–5959, Nov. 2006.

[106] P. Xu, S. H. Jeon, H. T. Chen, H. Luo, G. Zou, Q. Jia, M. Anghel, C. Teuscher, D. J. Williams, B. Zhang, X. Han, and W. H. L., "Facile synthesis and electrical properties of silver wires through chemical reduction by polyaniline," *J Phys Chem C*, vol. 114, no. 50, pp. 22 147–22 154, Dec. 2010.

[107] Y. Mei, G. Q. Lu, X. Chen, S. Luo, and D. Ibitayo, "Effect of oxygen partial pressure on silver migration of low-temperature sintered nanosilver die-attach material," *IEEE Trans Device Mat Rel*, vol. 11, no. 2, pp. 312–315, Jun. 2011.

[108] R. Riva, C. Buttay, B. Allard, and P. Bevilacqua, "Migration issues in sintered silver die attaches operating at high temperature," *Microelectron Reliab*, vol. 53, no. 9-11, pp. 1592–1596, Sep. 2013.

[109] G. Q. Lu, W. Yang, Y. H. Mei, X. Li, G. Chen, and X. Chen, "Migration of sintered nanosilver on alumina and aluminum nitride substrates at high temperatures in dry air for electronic packaging," *Trans Device Mat Rel*, vol. 14, no. 2, pp. 600–606, Jun. 2014.

[110] B. Ingham, T. H. Lim, C. J. Dotzler, A. Henning, M. F. Toney, and R. D. Tilley, "How nanoparticles coalesce: An in-situ study of au nanoparticle aggregation and grain growth," *Chem Mater*, vol. 23, no. 14, pp. 3312–3317, Jun. 2011.

[111] P. R. B., "Thermosets," in *Thermal characterization of polymeric materials*, T. E. A., Ed., New York: Academic Press, 1981, pp. 548–53.

[112] D. U. Shah and P. J. Schubel, "Evaluation of cure shrinkage measurement techniques for thermosetting resins," *Polymer Testing*, vol. 29, no. 6, pp. 629 –639, 2010. DOI: http://dx.doi.org/10.1016/j.polymertesting.2010.05.001.

[113] J. Lange, S. Toll, J.-A. E. Mnson, and A. Hult, "Residual stress build-up in thermoset films cured above their ultimate glass transition temperature," *Polymer*, vol. 36, no. 16, pp. 3135 –3141, 1995. DOI: http://dx.doi.org/10.1016/0032-3861(95)97876-H.

[114] J. Lange, S. Toll, J.-A. E. Mnson, and A. Hult, "Residual stress build-up in thermoset films cured below their ultimate glass transition temperature," *Polymer*, vol. 38, no. 4, pp. 809 –815, 1997. DOI: http://dx.doi.org/10.1016/S0032-3861(96)00584-8.

[115] J. Lange, R. Ekelf, and G. A. George, "Indications of micro-vitrification during chainwise cross-linking polymerisation," *Polymer*, vol. 40, no. 12, pp. 3595 –3598, 1999. DOI: http://dx.doi.org/10.1016/S0032-3861(98)00536-9.

[116] J Lange, N Altmann, C. Kelly, and P. Halley, "Understanding vitrification during cure of epoxy resins using dynamic scanning calorimetry and rheological techniques," *Polymer*, vol. 41, no. 15, pp. 5949 –5955, 2000. DOI: http://dx.doi.org/10.1016/S0032-3861(99)00758-2.

[117] L. Fan, C. Tison, and C. P. Wong, "Fundamental understanding of conductivity establishment for electrically conductive adhesives," in *52nd Electronic Components and Technology Conference 2002. (Cat. No.02CH37345)*, 2002, pp. 1154–1157. DOI: 10.1109/ECTC.2002.1008250.

[118] J. Ramos, N. Pagani, C. Riccardi, J. Borrajo, S. Goyanes, and I. Mondragon, "Cure kinetics and shrinkage model for epoxy-amine systems," *Polymer*, vol. 46, no. 10, pp. 3323 –3328, 2005. DOI: http://dx.doi.org/10.1016/j.polymer.2005.02.069.

[119] DOW, "D.e.r. 331 liquid epoxy resin product information," Tech. Rep.

[120] D. Chemicals, "D.e.h. 24 epoxy curing agent product information," Tech. Rep.

[121] T. Liu, Y. Nie, R. Chen, L. Zhang, Y. Meng, and X. Li, "Hyperbranched polyether as an all-purpose epoxy modifier: Controlled synthesis and toughening mechanisms," *J. Mater. Chem. A*, vol. 3, pp. 1188–1198, 3 2015. DOI: 10.1039/C4TA04841E.

[122] N. K. L., *The Glass Transition and the Glassy State*, M. J, K. L. Ngai, W. Graessley, L. Mandelkern, E. Samulksi, J. Koenig, and G. Wignall, Eds. Cambridge: Cambridge Press, 2003, pp. 72–146.

[123] J. Mark, "The rubber elastic state," in *Physical Properties of Polymers. 3rd ed.* J. Mark, K. Ngai, W. Graessley, L. Mandelkern, E. Samulski, J. Koenig, and G. Wignal, Eds. Cambridge: Cambridge University Press, 2004, pp. 3–71.

[124] Q. Liu, X. Zhou, X. Fan, C. Zhu, X. Yao, and L. Z., "Mechanical and thermal properties of epoxy resin nanocomposites reinforced with graphene oxide," *PolymPlast Tech Eng*, vol. 51, pp. 251–6, 2012.

[125] X. J. Shen, X. Q. Pei, S. Y. Fu, and K. Friedrich, "Significantly modified tribological performance of epoxy nanocomposites at very low graphene oxide content," *Polymer.*, vol. 54, pp. 1234–42, 2013.

[126] K. K-S, J. I-Y, A. S-N, K. Y-D, and B. J-B., "Edge-functionalized graphene-like platelets as a co-curing agent and a nanoscale additive to epoxy resin," *J Mater Chem*, vol. 21, p. 7337, 2011.

[127] O. R. E., "Rk-tr-63-20: Kinetics of epoxide-carboxylic reaction.," *Army Missile Research Development and Engineering Laboratory, Redstone Arsenal Al, Propulsion Directorate*, 1963.

[128] I. Mondragon and B. C. B., "Effects of residual dichloromethane solvent on the cure of epoxy resin," *Plast Rubber Compos Process Appl.*, vol. 21, no. 5, pp. 275–81, 1994.

[129] U. L. A., *Polymer alloys and blends: Thermodynamics and rheology*. New York: Hanser Publishers, 1990, p. 93-105.

[130] M. Inoue and K. Suganuma, "Effect of curing conditions on the electrical properties of isotropic conductive adhesives composed of an epoxybased binder," *Soldering & Surface Mount Technology*, vol. 18, no. 2, pp. 40–45, 2006. DOI: 10.1108/09540910610665125.

[131] E. Turi, *Thermal characterization of polymeric materials*. Academic Press, 1981.

[132] J. D. Menczel, L. Judovits, R. B. Prime, H. E. Bair, M. Reading, and S. Swier, "Differential scanning calorimetry (dsc)," in *Thermal analysis of polymers fundamentals*, M. J. D. and P. R. B., Eds., Hoboken: Wiley, 2009, pp. 7–239.

[133] P. S. Gill, S. R. Sauerbrunn, and M. Reading, "Modulated differential scanning calorimetry," *Journal of Thermal Analysis*, vol. 40, no. 3, pp. 931–939, 1993. DOI: 10.1007/BF02546852.

[134] M. R. Kamal and S. Sourour, "Kinetics and thermal characterization of thermoset cure," *Polymer Engineering & Science*, vol. 13, no. 1, pp. 59–64, 1973. DOI: 10.1002/pen.760130110.

[135] S. Sourour and M. Kamal, "Differential scanning calorimetry of epoxy cure: Isothermal cure kinetics," *Thermochimica Acta*, vol. 14, no. 1, pp. 41 –59, 1976. DOI: http://dx.doi.org/10.1016/0040-6031(76)80056-1.

[136] S.-N. Lee, M.-T. Chiu, and H.-S. Lin, "Kinetic model for the curing reaction of a tetraglycidyl diamino diphenyl methane/diamino diphenyl sulfone (tgddm/dds) epoxy resin system," *Polymer Engineering & Science*, vol. 32, no. 15, pp. 1037–1046, 1992. DOI: 10.1002/pen.760321509.

[137] L. Nez, F. Fraga, A. Castro, M. R. Nez, and M. Villanueva, "Effects of diffusion on the kinetic study of an epoxy system diglycidyl ether of bisphenol a/1,2-diamine cyclohexane/calcium carbonate filler," *Journal of Applied Polymer Science*, vol. 77, no. 10, pp. 2285–2295, 2000. DOI: 10.1002/1097-4628(20000906)77:10<2285::AID-APP22>3.0.CO;2-W.

[138] A. D. Rogers and P. Lee-Sullivan, "An alternative model for predicting the cure kinetics of a high temperature cure epoxy adhesive," *Polymer Engineering & Science*, vol. 43, no. 1, pp. 14–25, 2003. DOI: 10.1002/pen.10001.

[139] J. Menczel and R. Prime, *Thermal Analysis of Polymers: Fundamentals and Applications*. Wiley, 2009.

[140] T. Hatakeyama and F. Quinn, *Thermal analysis: Fundamentals and applications to polymer science*. Wiley, 1999.

[141] B. Wunderlich, *Thermal analysis*, ser. Studies in Social Discontinuity. Academic Press, 1990.

[142] *Standard test method for kinetic parameters for thermally unstable materials using differential scanning calorimetry and the flynn/wall/ozawa method*, 2016.

[143] D. K. Schroder, "Resistivity," in *Semiconductor Material and Device Characterization*. John Wiley & Sons, Inc., 2005, pp. 1–59. DOI: 10.1002/0471749095.ch1.

[144] J. D. Weiss, R. J. Kaplar, and K. E. Kambour, "A derivation of the van der pauw formula from electrostatics," *Solid-State Electronics*, vol. 52, no. 1, pp. 91 –98, 2008. DOI: http://dx.doi.org/10.1016/j.sse.2007.07.029.

[145] J. D. Weiss, "Generalization of the van der pauw relationship derived from electrostatics," *Solid-State Electronics*, vol. 62, no. 1, pp. 123 –127, 2011. DOI: http://dx.doi.org/10.1016/j.sse.2011.04.006.

[146] S. H. G., "Thermal degradation of poly (methacrylic acid): Further studies applying tga/ ftlr," *J Polym Sci A Polym Chem*, vol. 31, no. 9, pp. 2403–2405, Mar. 1993.

[147] D. Lu and C. Wong, "Effects of shrinkage on conductivity of isotropic conductive adhesives," *International Journal of Adhesion and Adhesives*, vol. 20, no. 3, pp. 189 –193, 2000. DOI: http://doi.org/10.1016/S0143-7496(99)00039-1.

[148] G. Bai, J. S. Bee, J. G. Biddlecombe, Q. Chen, and W. T. Leach, "Computational fluid dynamics (cfd) insights into agitation stress methods in biopharmaceutical development," *International Journal of Pharmaceutics*, vol. 423, no. 2, pp. 264 – 280, 2012. DOI: http://dx.doi.org/10.1016/j.ijpharm.2011.11.044.

[149] M. Discacciati, D. Hacker, A. Quarteroni, S. Quinodoz, S. Tissot, and F. M. Wurm, "Numerical simulation of orbitally shaken viscous fluids with free surface," *International Journal for Numerical Methods in Fluids*, vol. 71, no. 3, pp. 294–315, 2013. DOI: 10.1002/fld.3658.

[150] A. Ducci and W. H. Weheliye, "Orbitally shaken bioreactorsviscosity effects on flow characteristics," *AIChE Journal*, vol. 60, no. 11, pp. 3951–3968, 2014. DOI: 10.1002/aic.14608.

[151] W. Weheliye, M. Yianneskis, and A. Ducci, "On the fluid dynamics of shaken bioreactors flow characterization and transition," *AIChE Journal*, vol. 59, no. 1, pp. 334–344, 2013. DOI: 10.1002/aic.13943.

[152] H. Zhang, S. R. Lamping, S. C. Pickering, G. J. Lye, and P. A. Shamlou, "Engineering characterisation of a single well from 24-well and 96-well microtitre plates," *Biochemical Engineering Journal*, vol. 40, no. 1, pp. 138 –149, 2008. DOI: http://dx.doi.org/10.1016/j.bej.2007.12.005.

[153] M. L. Gupta, S. A. Sydlik, J. M. Schnorr, D. J. Woo, S. Osswald, T. M. Swager, and D. Raghavan, "The effect of mixing methods on the dispersion of carbon nanotubes during the solvent-free processing of multiwalled carbon nanotube/epoxy composites," *Journal of Polymer Science Part B: Polymer Physics*, vol. 51, no. 6, pp. 410–420, 2013. DOI: 10.1002/polb.23225.

[154] B. Bittmann, F. Haupert, and A. K. Schlarb, "Ultrasonic dispersion of inorganic nanoparticles in epoxy resin," *Ultrasonics Sonochemistry*, vol. 16, no. 5, pp. 622 –628, 2009. DOI: http://dx.doi.org/10.1016/j.ultsonch.2009.01.006.

[155] T. R. Frømyr, F. K. Hansen, and T. Olsen, "The optimum dispersion of carbon nanotubes for epoxy nanocomposites: Evolution of the particle size distribution by ultrasonic treatment," *Journal of Nanotechnology*, vol. 2012, no. 1, pp. 138 –149, 2012. DOI: http://dx.doi.org/10.1155/2012/545930.

[156] M. A. Rafiee, J. Rafiee, I. Srivastava, Z. Wang, H. Song, Z. Z. Yu, and K. N., "Fracture and fatigue in graphene nanocomposites," *Small*, vol. 6, no. 2, pp. 179–83, 2010.

[157] M. Martin-Gallego, R. Verdejo, M. A. Lopez-Manchado, and S. M., "Epoxy-graphene uv-cured nanocomposites," *Polymer.*, vol. 52, pp. 4664–9, 2011.

[158] S. Bose, T. Kuila, M. E. Uddin, N. H. Kim, A. K. Lau, and J. H. Lee, "In-situ synthesis and characterization of electrically conductive polypyrrole/graphene nanocomposites," *Polymer*, vol. 51, no. 25, pp. 5921 –5928, 2010. DOI: http://dx.doi.org/10.1016/j.polymer.2010.10.014.

[159] H. Wu, J. Liu, X. Wu, M. Ge, Y. Wang, G. Zhang, and J. Jiang, "High conductivity of isotropic conductive adhesives filled with silver nanowires," *International Journal of Adhesion and Adhesives*, vol. 26, no. 8, pp. 617 –621, 2006. DOI: http://dx.doi.org/10.1016/j.ijadhadh.2005.10.001.

[160] C. Zhi, Y. Bando, C. Tang, and G. D., "Boron nitride nanotubes," *Mater Sci and Eng R*, vol. 70, pp. 92–111, 2010.

[161] S. Ganguli, A. K. Roy, and A. D. P., "Improved thermal conductivity for chemically functionalized exfoliated graphite/epoxy composites," *Carbon.*, vol. 46, pp. 806–17, 2008.

[162] R. Voo, M. Mariatti, and S. L. C., "Properties of epoxy nanocomposite thin films prepared by spin coating technique," *J Plast Film Sheet*, 2011. DOI: 10.1177/8756087911419745.

[163] H. Liang and Y. D., "Mechanical and thermal properties of (ag/c nanocable)/epoxy resin composites," *Polym Sci Ser B*, vol. 53, no. 11, pp. 601–5, 2011.

[164] G. Suriati, M. Mariatti, and A. Azizan, "Effects of filler shape and size on the properties of silver filled epoxy composite for electronic applications," *Journal of Materials Science: Materials in Electronics*, vol. 22, no. 1, pp. 56–63, 2011. DOI: 10.1007/s10854-010-0082-2.

[165] J. Yu, X. Huang, C. Wu, X. Wu, G. Wang, and P. Jiang, "Interfacial modification of boron nitride nanoplatelets for epoxy composites with improved thermal properties," *Polymer.*, vol. 53, pp. 471–80, 2012.

[166] I. Zaman, T. T. Phan, H. C. Kuan, Q. Meng, L. Ltb, L. Luong, O. Youssf, and J. Maa, "Epoxy/graphene platelets nanocomposites with two levels of interface strength," *Polymer.*, vol. 52, no. 7, pp. 1603–11, 2011.

[167] Y. Guo, C. Bao, L. Song, B. Yuan, and Y. Hu, "In situ polymerization of graphene, graphite oxide, and functionalized graphite oxide into epoxy resin and comparison study of on-the-flame behavior," *Ind Eng Chem Res*, vol. 50, pp. 7772–83, 2011.

[168] D. R. Bortz, E. G. Heras, and I. Martin-Gullon, "Impressive fatigue life and fracture toughness improvements in graphene oxide/epoxy composites," *Macromolecules*, vol. 45, no. 1, pp. 238–245, 2012. DOI: 10.1021/ma201563k.

[169] M. Monti, M. Rallini, D. Puglia, L. Peponi, L. Torre, and K. J. M., "Morphology and electrical properties of graphene-epoxy nanocomposites obtained by different solvent assisted processing methods," *Compos A*, vol. 46, pp. 166–72, 2013.

[170] C. Bao, Y. Guo, L. Song, Y. Kan, X. Qian, and Y. Hu, "In situ preparation of functionalized graphene oxide/epoxy nanocomposites with effective reinforcements," *J Mater Chem*, vol. 21, p. 13 290, 2011.

[171] E. Corcione, F. Freuli, and A. Maffezzoli, "The aspect ratio of epoxy matrix nanocomposites reinforced with graphene stacks," *Polym Eng Sci.*, 2012. DOI: 10.1002/pen.

[172] I. Zaman, H. C. Kuan, Q. Meng, A. Michelmore, N. Kawashima, T. Pitt, L. Zhang, S. Gouda, L. Luong, and J. Ma, "A facile approach to chemically modified graphene and its polymer nanocomposites," *Adv Funct Mater*, vol. 22, pp. 2735–43, 2012.

[173] H. Ren, S. Tang, J. A. Syed, and X. Meng, "Incorporation of silver nanoparticles coated with mercaptosuccinic acid/poly(ethylene glycol) copolymer into epoxy for enhancement of dielectric properties," *Mater Chem and Phys*, vol. 137, pp. 673–80, 2012.

[174] C. C. Teng, M. C. C. M., C. H. Lu, S. Y. Yang, S. H. Lee, M. C. Hsiao, M. Y. Yen, K. C. Chiou, and L. T. M., "Thermal conductivity and structure of non-covalent functionalized graphene/epoxy composites," *Carbon.*, vol. 49, pp. 5107–16, 2011.

[175] Y. Yagci, M. Sangermano, and G. Rizza, "A visible light photochemical route to silver-epoxy nanocomposites by simultaneous polymerization-reduction approach," *Polymer.*, vol. 49, pp. 5195–8, 2008.

[176] B. Guo, J. Wan, Y. Lei, and D. Jia, "Curing behaviour of epoxy resin/ graphite composites containing ionic liquid," *J Phys D*, vol. 42, no. 1, pp. 45 307–14, 2009.

[177] D. A. T., "Prediction of the glass transition temperature of polymers: A model based on the principle of corresponding states," *J Poly Sci B*, vol. 26, pp. 1949–69, 1987.

[178] S. Park and K. D. S., "Preparation and physical properties of an epoxy nanocomposite with amine-functionalized graphenes," *Polym Eng Sci*, 2012. DOI: 10.1002/pen.23368.

[179] S. L. Qiu, C. S. Wand, Y. T. Wang, C. G. Liu, X. Y. Chen, H. F. Xie, Y. A. Huang, and C. Rs., "Effects of graphene oxides on the cure behaviors of a tetrafunctional epoxy resin," *EXPRESS Polym Lett.*, vol. 5, no. 9, pp. 809–18, 2011.

[180] K. C. Yung and H. Liem, "Enhanced thermal conductivity of boron nitride epoxy-matrix composite through multi-modal particle size mixing," *J Appl Polym Sci*, vol. 106, pp. 3587–91, 2007.

[181] M. R. Loos, C. Laf, S. H. Pezzin, and A. S. C., "The effect of acetone addition on the properties of epoxy," *Polym Sci Tech*, vol. 18, no. 1, pp. 76–80, 2008.

[182] N. Lange and J. Dean, *Lange's Handbook of Chemistry*. McGraw-Hill, 1973.

[183] K. Seth, S. R. Roy, D. N. Kommi, B. V. Pipaliya, and A. K. Chakraborti, "Silver nanoparticle-catalysed phenolysis of epoxides under neutral conditions: Scope and limitations of metal nanoparticles and applications towards drug synthesis," *Journal of Molecular Catalysis A: Chemical*, vol. 392, pp. 164 –172, 2014. DOI: http://dx.doi.org/10.1016/j.molcata.2014.05.011.

[184] E. G. Ball, "Studies on oxidation-reduction: Xxiii ascorbic acid," *J. Biol Chem*, vol. 118, pp. 219–239, 1937.

[185] S. E. Kudaibergenov, "Recent advances in the study of synthetic polyampholytes in solutions in: Polymer latexes - epoxide resins polyampholytes," *Advances in Polymer Science*, vol. 144, pp. 115–197, 1999.

[186] A. Katchalsky and P. Spitnik, "Potentiometric titrations of polymethacrylic acid," *Journal of Polymer Science*, vol. 2, pp. 432–446, 1947.

[187] M. Kimura, M. Yamamoto, and S. Yamabe, "Kinetics and mechanism of the oxidation of l-ascorbic acid by tris-(oxalato)cobaltate(111) and tris(1,i0-phenanthroline)iron(111) complexes in aqueous solution," *J. Chem Soc, Dalton Trans*, vol. 2, pp. 423–427, 1982.

[188] H. D. Moya and N. Coichev, "Kinetic studies of the oxidation of l-ascorbic acid by tris(oxalate)cobaltate in the presence of cdta metal ion complexes," *J Braz. Chem. Soc.*, vol. 17, pp. 364–368, 2006.

[189] Y. Pan, W. Lv, Y. Niu, K. Wen, X. Hou, J. Gu, M. Zou, L. Ye, W. Wang, K. H. L. Zhang, and W. He, "Initial-stage oriented-attachment one-dimensional assembly of nanocrystals: Fundamental insight with a collision-recrystallization model," *RSC Adv.*, vol. 5, pp. 54 605–54 612, 67 2015. DOI: 10.1039/C5RA08796A.

[190] W. He, "An insight into the coulombic interaction in the dynamic growth of oriented-attachment nanorods," *CrystEngComm*, vol. 16, pp. 1439–1442, 8 2014. DOI: 10.1039/C3CE40646F.

[191] D. A. Welch, T. J. Woehl, C. Park, R. Faller, J. E. Evans, and N. D. Browning, "Understanding the role of solvation forces on the preferential attachment of nanoparticles in liquid," *ACS Nano*, vol. 10, no. 1, pp. 181–187, 2016, PMID: 26588243. DOI: 10.1021/acsnano.5b06632.

[192] E. Marzbanrad, B. Zhao, and N. Zhou, "Porous silver nanosheets: A novel sensing material for nanoscale and microscale airflow sensors," *Nanotechnology*, vol. 26, p. 445 501, 2015, this is ref 41, 40 is missing.

[193] J.-P. Jalkanen and F. Zerbetto, "Interaction model for the adsorption of organic molecules on the silver surface," *The Journal of Physical Chemistry B*, vol. 110, no. 11, pp. 5595–5601, 2006, PMID: 16539502. DOI: 10.1021/jp055225g.

[194] S. S. Shiratori and M. F. Rubner, "Ph-dependent thickness behavior of sequentially adsorbed layers of weak polyelectrolytes," *Macromolecules*, vol. 33, no. 11, pp. 4213–4219, 2000. DOI: 10.1021/ma991645q.

[195] T. Wang, M. Antonietti, and H. Clfen, "Calcite mesocrystals: morphingi crystals by a polyelectrolyte," *Chemistry A European Journal*, vol. 12, no. 22, pp. 5722–5730, 2006. DOI: 10.1002/chem.200501019.

[196] T. Wang, H. Clfen, and M. Antonietti, "Nonclassical crystallization: mesocrystals and morphology change of caco3 crystals in the presence of a polyelectrolyte additive," *Journal of the American Chemical Society*, vol. 127, no. 10, pp. 3246–3247, 2005. DOI: 10.1021/ja045331g.

[197] L. de Arcangelis, S. Redner, and A. Coniglio, "Anomalous voltage distribution of random resistor networks and a new model for the backbone at the percolation threshold," *Phys Rev B*, vol. 31, no. 7, pp. 4725–4727, Apr. 1985.

[198] M. T. Garay, M. C. Llamas, and E. Iglesias, "Study of polymer-polymer complexes and blends of poly(n-isopropylacrylamide) with poly(carboxylic acid): 1. poly(acrylic acid) and poly(methacrylic acid)," *Polymer*, vol. 38, no. 20, pp. 5091–5096, Sep. 1997.

[199] J. Mark, K. Ngai, W. Graessley, L. Mandelkern, E. Samulski, J. Koenig, and G. Wignal, *Physical Properties of Polymers.* 3rd ed. Cambridge: Cambridge University Press, 2004.

[200] K. tak Lau, M. Lu, C. ki Lam, H. yan Cheung, F.-L. Sheng, and H.-L. Li, "Thermal and mechanical properties of single-walled carbon nanotube bundle-reinforced epoxy nanocomposites: The role of solvent for nanotube dispersion," *Composites Science and Technology*, vol. 65, no. 5, pp. 719 –725, 2005, Papers presented at the European Materials Research Society 2004 Spring Meeting: Nano-Composites for Space and Infrastructure Applications. DOI: http://dx.doi.org/10.1016/j.compscitech.2004.10.005.

[201] S.-G. Hong and C.-S. Wu, "{dsc} and {ftir} analysis of the curing behaviors of epoxy/dicy/solvent open systems," *Thermochimica Acta*, vol. 316, no. 2, pp. 167 –175, 1998. DOI: http://dx.doi.org/10.1016/S0040-6031(98)00356-6.

[202] M. Erinc, M. van Dijk, and V. G. Kouznetsova, "Residual stresses in isotropic conductive adhesives with nano-ag particles," in *Thermal, Mechanical and Multi-Physics Simulation and Experiments in Microelectronics and Microsystems (EuroSimE), 2012 13th International Conference on*, 2012, pp. 1–6. DOI: 10.1109/ESimE.2012.6191707.

[203] N. Xiong, Z. Li, J. Li, H. Xie, and Y. Wang, "Influence of curing procedures on the electrical properties of epoxy-based isotropic conductive adhesives," in *Electronic Packaging Technology (ICEPT), 2014 15th International Conference on*, 2014, pp. 373–377. DOI: 10.1109/ICEPT.2014.6922676.